UNIVERSITY OF PAVIA

Ph.D. SCHOOL IN CHEMICAL AND PHARMACEUTICAL SCIENCES AND INDUSTRIAL INNOVATION (XXXV Cycle)
Coordinator: Chiar.mo Prof. Giorgio Colombo

NEW MATERIALS FOR ELECTROCHEMICAL ENERGY STORAGE:
ADVANCED LITHIUM ION BATTERIES AND BEYOND

Ph.D. Thesis of
Daniele Callegari

Academic Year 2021/2022

Tutor
Chiar.ma Prof.ssa Eliana Quartarone

Abstract

During my PhD research activity, I had the opportunity to explore a huge range of innovative materials for the next generation Li-based batteries.

I started working on anodes active materials for advanced lithium ion batteries considering high entropy oxides (HEO) as possible candidates. High entropy oxides based on transition metals, as $Mg_{0.2}Co_{0.2}Ni_{0.2}Cu_{0.2}Zn_{0.2}O$ (TM-HEO), have recently drawn special attention as potential anodes in lithium-ion batteries, due to high specific capacity and cycling reversibility. However, the lithiation/delithiation mechanism of such systems is still controversial and not clearly addressed. My experimental results allowed to propose a new complex mechanism occurring during the lithiation/delithiation processes in high entropy oxides, based on transition metals with rock-salt structure, as anodes for lithium-ion cells. To this aim, I carried out both *operando* and *ex-situ* XAS investigation on the system $Mg_{0.2}Co_{0.2}Ni_{0.2}Cu_{0.2}Zn_{0.2}O$ (TM-HEO), in combination with electrochemical and microstructural characterization. The spectroscopic results suggest that the redox reaction takes place through a multi-step process depending on the TMs reduction potential. The whole process is incomplete and irreversible, leading to a mixture of M and MO in a variable molar ratio depending on the metal. In addition, contrary to what supposed in literature by XRD analysis, we prove that even ZnO takes part in the conversion mechanism, since a significant fraction of Zn is found in the metallic state at the end of the charging process. Despite the collapsing of the rock-salt structure, a charge/discharge specific capacity higher than 600 mAh g^{-1} at 0.1C has been delivered by the TM-HEO-based cell with coulombic efficiency very close to 1, in particular at higher current density. Taking into account the irreversibility of the redox mechanism, it is reasonable to ascribe such capacity to the alloying/dealloying reaction typical of anodes as ZnO and MgO. Even though the rock salt structure of such a system is intended to collapse, it is maintained up to 60% of charge, when the first traces of metallic Co are apparent (around 0.8V), confirming the stabilising effect of the configurational entropy. Despite the promising performances shown in literature, this kind of systems is not still suitable for use as anode in LIBs. Further strategies of phase stabilization should be therefore investigated, for instance, by properly modulating important key-factors, as type of metal, number of cations, stoichiometry, morphology, and also by exploring other structures as spinel, where a different lithiation/delithiation mechanism

occurs. I strongly believe that such novel understanding is therefore interesting not only *per se*, but also in the design of better materials for the next generation Li$^+$ and Na$^+$ ion batteries.

Another investigated active material for the anode compartment was black phosphorus (BP) that I studied for application in Sodium Ion batteries as potential alternative to the family of Hard Carbons. As known, sodium ion batteries (SIBs) are promising alternative to lithium-ion batteries for massive stationary energy storage. To improve energy density, however, more performing active materials are needed. In order to allow sustainable scale-up, it is also mandatory to develop green products and processes. Herein, I report on anodes of phosphorus/carbon (P/C) nanocomposites prepared via high energy ball milling (HEBM), a simple, powerful and easily scalable synthesis technique. More specifically, P/C composites were successfully synthetized via high energy ball milling at a rate of 500 rpm, spheres/material ratio of 30/1 and two different times: 2 hours (BC_2h) and 54 hours (BC_54h). All the electrochemical characterizations were performed on aluminum current collector thanks to the exclusion of oxygen during aqueous electrode processing. The active materials were investigated by XRD, XPS, SEM-EDS, post-mortem SEM and galvanostatic cycling. A ball milling time of 54h resulted in a phosphorus-carbon composite delivering initial specific charge capacities of around 2250 mAhg$_P^{-1}$ and excellent capacity retention of around 80% at 0.05C after 120 cycles. Three phenomena were identified to synergistically improve the electrochemical performance if compared to a composite ball milled for 2h: (i) longer milling times and, thus, higher energies lead to an almost fully amorphous system which is able to partially buffer the volume expansion, (ii) decrease of the phosphorus particles dimensions (< 500 nm), leading to homogeneous distribution of phosphorus and carbon within the composite secondary particles without isolated P-based domains, and finally (iii) the introduction of defects in the carbon matrix, enabling Na-ion insertion at high potentials and enhancing overall electrochemical performance. The presented phosphorus-carbon composite outperforms state of the art hard carbons in SIBs and graphite in LIBs in terms of specific and volumetric capacity, and the good capacity retention - especially in combination with aluminum current collector - are certainly a major step towards successful future commercialization of SIBs.

One of the main drawbacks of BP is that, similarly to what occurs for silicon-based system, undergoes to irreversible structural modifications upon sodiation/desodiation (and also upon lithiation/delithiation), leading to severe electrode cracking and pulverization. Very recently, it has been demonstrated that the introduction of smart functionalities in the cell components, such as the self-healing ones, may be a successful strategy to buffer this kind

of degradation phenomena. In particular, autonomous self-healing (SH), namely the ability to repair damages from mechanical stress spontaneously, is polarising attention in the field of the new generation electrochemical devices. This property is highly attractive to enhance the durability of rechargeable Li- (LIB) or Na-ion (SIB) batteries, where high-performing anode active materials (Silicon, Phosphorus, etc.) are strongly affected by volume expansion and phase changes upon ion insertion. Here, we applied a self-healing strategy, based on the dynamic quadruple hydrogen bonding, to nanosized black phosphorus (BP) anodes for Na-ion cells. The goal is to overcome drastic capacity decay and short lifetime, resulting from mechanical damages induced by the volumetric expansion/contraction upon sodiation/desodiation. Specifically, we developed novel ureidopyrimidinone (UPy)-telechelic systems and related blends with poly(ethylene oxide) as novel and green binders, alternative to more conventional ones, such as polyacrylic acid (PAA) and carboxymethylcellulose (CMC), which are typically used in SIBs. BP anodes show impressively improved (more than 6 times) capacity retention when employing the new self-healing polymeric blend. In particular, the SH electrode still works at current density higher than 3.5 A g^{-1}, whereas the standard BP electrode exhibits very poor performances already at current densities lower than 0.5 A g^{-1}. This is the result of better adhesion, buffering properties and spontaneous damage reparation.

In a second phase of my research, I was involved in developing innovative Co-free cathodes materials for application in lithium-ion batteries that exhibit promising functional performances in a wide voltage range and high specific capacities. The ever-growing demand for Li-ion batteries, in fact, requires high-capacity electrode materials that should also be environmentally benign, Co-free, secure, and durable, to achieve an optimal compromise between sustainability and functional performances. Spinel $LiMn_2O_4$ (LMO) is a state-of-the-art material, which, in principle, could satisfy such requirements. However, an undesired cubic-tetragonal phase transition favors Jahn-Teller (J-T) spinel distortion, leading to severe capacity reduction upon cycling below 3 V. I analyzed, for the first time, the microstructure, local environment, and electrochemistry of new $LiFe_xMn_{2-x-y}Ti_yO_4$ compositions with different Li/Mn ratios. The redox mechanism of these materials was clarified. An easy and fast sol-gel synthesis produced a family of spinels with Li/Mn ratio ranging between 1.0 and 1.7, all presenting the cubic $\boldsymbol{Fd\bar{3}m}$ structure of $LiMn_2O_4$ with lattice parameter, a, increasing with the Li/Mn ratio. Fe/Ti dual-doped spinels show higher electronic conductivity and electronic transport number than undoped $LiMn_2O_4$, achieving values that exceed 0.2 mS cm^{-1} and 0.7 at 90°C, respectively, in case of compositions

presenting smaller lattice parameters. XAS investigation demonstrated that the only electrochemically active redox couples involves Mn, while both Fe(III) and Ti(IV) do not change their oxidation state upon cycling. Two electrochemical phenomena are clearly observed, one ascribed to Mn(IV)/Mn(III) at around 4 V, and the second one at 3 V, which is assigned to the Mn(III)/Mn(II) transition. The exchange of more than 2 Li ion through the whole Mn(IV)/Mn(II) redox couple is observed in the LFMT spinels during Li intercalation/deintercalation, providing specific capacity significantly higher than what observed for the undoped spinel (> 270 mAh g^{-1} during the first delithiation step). Extensive galvanostatic cycling between 1.5 and 4.8 V also demonstrated the presence of irreversible anion redox activity during the first charge, whose entity increases with the Li/Mn ratio in the spinel.

The disorder induced by multiple doping stabilizes the spinel phase, hindering the cubic-tetragonal transition upon prolonged Li intercalation/deintercalation. Such effect results in an unusual behavior through the modification of the LFMT spinel into two different spinel phases with 3:1 mass ratio. The first phase is electrochemically active and shows Mn-rich domains, while the other, including Ti-rich domains, is electrochemically inert, as proved by the lattice parameter variation and SEM-EDX maps upon cycling. By suppressing the spinel Jahn-Teller distortion, the substitution of Mn(III) with Ti and Fe lowers the concentration of J-T Mn(III), which is responsible for the severe capacity fade in the undoped spinel. Such stabilizing effect, favored by the synergistic presence of Fe and Ti, results in remarkably reduced capacity fade at low current density ($< 28\%$ after 100 cycles at 27 mA g^{-1}) and to an excellent stability and reversibility in case of higher C rate (270 mA g^{-1}). In conclusion, the encouraging functional performances of these new LFMT spinels and the resulting structure-property relationship may be an important guide to design an ever-wider range of spinel materials with enhanced stability against J-T distortion as new cathodes for sustainable, greener, and Co-free Li-ion batteries.

During the last year, my research focus was on improving lithium metal battery (LMB) technology. As well known, LMB is a key enabling technology for sustainable and efficient electric transport thanks to high energy density. However, it suffers detrimental phenomena such as the dendrites formation, causing severe internal short circuits. A first studied solution was the realization of an innovative separator able to block the formation and proliferation of dendrites. Specifically, I developed a Janus separator, which is characterized by two layers with different chemical and physical properties: an electronically insulating one, facing the lithium metal, consisting of a (PVdF-HFP)- LLZO composite membrane; an electronically

conducting layer, facing the cathode, consisting of a (PVdF-HFP)-nitrogen-carbon quantum dots (N-CQDs). The dendrite blocking capability of the Janus separator was investigated by means of electrochemical tests carried out on a NMC811| *Separator* | Li$_{(m)}$ cell. A reference configuration including a neat PVdF-HFP separator was also studied for a sake of comparison. The Janus Separator-based cell delivered a specific capacity of ∼150-160 mAh g^{-1} up to 130 cycles with a capacity loss lower than 10% and coulombic efficiency very close to 100%, contrary to the reference cell whose capacity drop was significantly higher. Also, the analysis concerning the voltage profile showed no evidence of an internal self-discharge due to a short circuit event, which, in contrast, characterises the cell including non-Janus separator. Furthermore, *post mortem* SEM analysis showed that the conductive layer possesses the ability to intercept dendrite growth, which is likely due to the hardness properties of the ceramic (LLZO) filling the polymer. This property makes it possible to improve the safety and performance of the cell.

Remaining in the field of lithium-metal batteries, a further possible alternative is the use of anode-less system cells. One of the solutions recently implemented has been the realisation of anode current collectors based on porous carbon. In my case, the investigated solution was the realisation of copper-based 3D current collectors. The aim was to increase the surface area that led to smaller practical current in order to delay the formation of dendrites. In addition, copper possesses greater electrical conductivity and mechanical strength. The 3D patterned Cu current collectors were easily produced by means of additive manufacturing in different geometries, all of them characterised by an enhanced surface area over the planar current collector, which leads to more sites for a stable lithium nucleation. The electrochemical tests performed on symmetric Li | electrolyte | 3D-Cu@Li cell at a current density of 2 mA cm^{-2} showed a cycle life of more than 300 hours with very low overpotential and an excellent cyclability. The anode-less configuration with 3D current collectors was also successfully tested in full cell configuration LiFePO$_4$|3D-Cu@Li.

Chapter 1:
Introduction

Nowadays, the rising awareness of the climate problems is leading the industrialized countries towards the lowering of polluting emissions.

Since Kyoto Protocol (1997) the world has focused its attention on environmental problems and thus a growing number of countries is now trying to mediate between the need of lowering CO and CO_2 emission levels both from industries and cars, and the will of keeping the inner economy stable besides this action. The solution to this problem is given using renewable sources instead of the mainly employed fossil fuels. Since one of the main drawbacks of using renewable energies is still their inefficient storage into proper devices, the field of Electrochemistry has to search for new active materials for a future generation of batteries with better storage and conversion performances.

To achieve this goal the characteristics that define a good rechargeable battery such as rate capability, raw materials, cycle life, cost, and temperature tolerance must be taken into consideration. However, observing the evolution of rechargeable batteries over time, it is the energy density improvement that has been the pivot that has guided the overall technological evolution in the last 150 years, mainly moving from nickel-cadmium cells (1890) to lead-acid cells in the 1950s and from nickel metal hydride cells (1960) to lithium-ion batteries (LIBs) to present days.

The lithium-ion battery is one of the most promising energy storage technologies currently available and widely used and dominating relatively short-term energy storage field. The remarkable importance of the lithium-ion technology is evidenced through the Nobel Prize in Chemistry in 2019 by John B. Goodenough, M. Stanley Whittingham, and Akira Yoshino for the invention of the first prototype of a lithium-ion battery with a positive electrode made of $LiCoO_2$ and a negative electrode constituted of graphite.[1]

1.1. Lithium Ion Batteries (LIBs): Overview

In this chapter we will describe the state of the art regarding the cathodic and anodic compartment of lithium ion batteries.

1.1.1. Cathodic Materials

Nowadays, the most common positive electrodes for lithium-ion batteries are based on materials working through intercalation or insertion processes. A first subdivision of cathode materials is based on their structure and there are mainly three group of interest: olivine, layered and spinel.

These three model structures can also be linked to the number of dimensions where they allow the lithium ions to move and they are respectively: one-dimensional (1D) for the olivine, two-dimensional (2D) for the layered and three-dimensional (3D) for the spinel structures.

1.1.1.1. Polyanionic Compounds

Polyanionic compounds are 1D materials where lithium ions move in structures tunnel like. Lithium Iron Phosphate-based (LiFePO$_4$, LFP) cathode materials, with orthorhombic olivine structures, are attracting notable relevance in the recent two decades. The main reasons for this interest are due to the exceptionally long-term stability upon cycling, minimum volumetric variation during lithium intercalation and de-intercalation processes, and low cost and low environmental impact which also transpose into a certain intrinsic safety. Together with these factors there is also an excellent thermal stability, at high temperature, versus oxygen release.[2] Despite the many advantages associated with LFP there are several drawbacks like the low intrinsic electric conductivity ($\sim 10^{-9}$ S cm^{-1}), that can be overcome throughout an essential carbon coating of the materials, and a low working potential of 3.5 V that leads to low values of specific energies. A further dualism of this material is represented by the phosphate group, which is the origin of excellent thermal stability but, due to its high molecular weight, it involves a low specific capacity of $\sim$160-170 mAh g^{-1}.[3,4]

1.1.1.2. Layered Type

The evolution of lithium-ion batteries led to the deepening of technology based on 2D cathode materials during the 1980s and 1990s. Currently, in the current widespread

commercial batteries, these materials are transition metal-based oxides with a layered structure that allows the two-dimensional diffusion of the Li^+ ion. In particular, M.S. Whittingham and J.B. Goodenough have distinguished themselves by realizing the most important materials in this category. The former was notable for his research into a new type of cathode, based on the concept of reversible intercalation of Li^+ ions in the crystal structure of such materials during charge and discharge cycle. As he explained, the main characteristics these must have to ensure good electrochemical performance are: i) small structural change following electrode reactions; ii) high diffusivity of Li^+ in the cathode structure; iii) reversibility of electrode reactions; iv) good ionic conductivity; v) insolubility in the electrolyte used. Among all the investigated materials, titanium disulphide turned out to be the best one.[5] In TiS_2, Ti^{4+} is octahedrally coordinated with S^{2-} thus resulting in a compact and separate layered structure, where Li^+ ions can intercalate easily and reversibly. However, due to the problems concerning lithium metal as anode and the low voltage to which the cell can reach overall (< 2.5 V), the battery and cathode devised by Whittingham were not developed further. In order to solve these problems, research turned to the design of new cathode materials that already contained lithium within their structure, so that the use of $Li_{(m)}$ could be definitively eliminated, but still managed to guarantee the presence and consequent movement of the Li^+ ion. Based on the same concept of reversible intercalation, Goodenough's research led to cathode materials still used in common batteries today. His main merit was that he realised that, by using compounds such as oxides and not sulphides, the overall working voltage of batteries could be significantly increased. In order to understand the theory behind this idea, it is necessary to analyse the diagrams of the densities of states of the transition metal oxides and to remember that, for the cathodes, the potential of the redox pair must be as low as possible. From the analysis of the diagram in Figure 1.1, its evident that the 2p band of O^{2-} was at a lower energy than the 3p band of S^{2-}, allowing access to bands with lower energies and consequently increasing the working potential of the battery.[6]
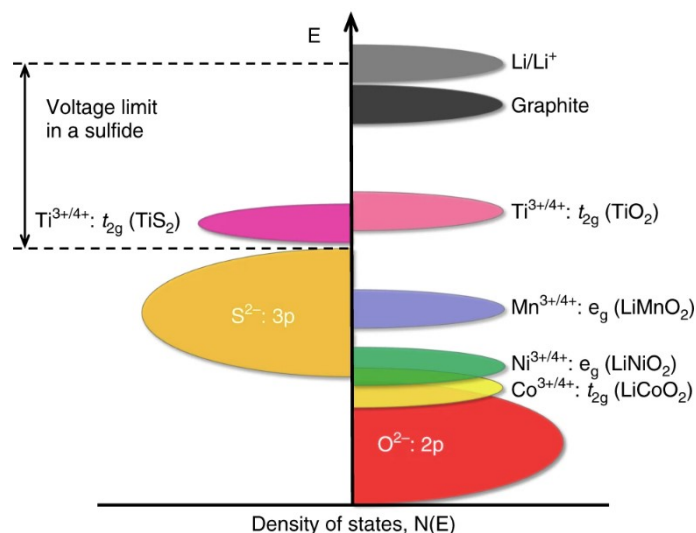
Figure 1.1. Density of states diagram for sulphide- and oxide-based cathodes. Taken from Ref.6.

The first oxide-based cathode to have been studied is LiCoO₂, commonly known as LCO. Its crystal structure is similar to that of the aforementioned TiS₂. The redox reaction describing the operation of an LCO-based cathode is as follows:

$$Li_{(1-x)}CoO_2 + xLi^+ + xe^- \rightleftharpoons LiCoO_2$$
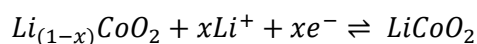
Compared to the very high specific capacitance value (274 mAh g⁻¹), the LCO experimentally recorded, when charged to its threshold potential of 4.2 V, an almost halved capacitance of approximately 140 mAh g⁻¹. The explanation behind the difference between the two values can be deduced by looking again at Figure 1.1 and remembering that the working voltage of the cathodes is limited by the upper energy threshold of the 2p band of the O^{2-}. In this specific case, given the partial overlap between the Co^{3+}/Co^{4+} band and the 2p band of O^{2-}, it is evident that LiCoO₂ does not have the necessary characteristics to work at its maximum capacity; for this reason, it has been possible to estimate that the effective capacity to intercalate reversibly, during charge-discharge cycles, is only limited to about half of the lithium contained in its structure.[7] A further point of criticism related to the use of LCO is economic and ethical: cobalt falls into the category of critical raw materials (CRM) as a consequence of its scarce presence in nature and in limited areas (such as the Democratic Republic of Congo), which leads to its high cost. In addition to the economic issue, there are various ethical aspects associated with the working conditions for its extraction. Despite these problems, however, it is still one of the most widely used cathode materials in common LIBs, especially in those found in small portable devices. In order to

4

limit the use of Co and make the cathodes more high-performance, attempts have been made to design other materials with the general formula $LiMO_2$, simultaneously incorporating more transition metals (M) into the crystal structure. Of particular relevance is the oxide $LiNi_{(1-y-z)} Mn_yCo_zO_2$, also known as NMC. The characteristics of each of the three metals present are exploited to guarantee structural stability and good electrochemical performance: Co, present as Co^{3+}, is reversibly oxidised to Co^{4+} during the charge and discharge processes and, moreover, due to its high charge, succeeds in limiting the so-called Li/Ni ratio; this value indicates the amount of Ni^{2+} that, migrating towards the crystallographic sites where Li^+ is reversibly interspersed, limits the maximum capacity obtainable from the cell. Mn^{4+} provides structural stability and is considered electrochemically inactive. Finally, Ni, due to the favourable position of the Ni^{3+}/Ni^{4+} band with respect to the oxide band (Figure 1.2), is mainly responsible for the high specific capacitance to which the material can attain. There are reports in literature where this cathode is able to achieve, in the potential range of 2.5 V-4.5 V, reversible capacities of even more than 200 mAh g^{-1}.[8] Since it was verified that the capacity of $Li(Ni_{1/3}Mn_{1/3}Co_{1/3})O_2$ is comparable to that of LCO, the commercialisation of the latter, still used as a cathode in some electric vehicles today, began immediately.[9] A further important metal taken into consideration to limit the use of cobalt is aluminium; it has been noted, in fact, that the simultaneous presence of Co^{3+} and Al^{3+} in the $Li(Ni_{0.70}Co_{0.15}Al_{0.15})O_2$ (NCA) structure guarantees good specific capacitance values and excellent structural stability.[10]

1.1.1.3. Spinel Type

Spinel compounds like lithium manganese oxide ($LiMn_2O_4$) and nickel doped lithium manganese oxide ($LiNi_{0.5}Mn_{1.5}O_4$) are example of traditional 3D insertion materials. The space group these materials belong to is $Fd\bar{3}m$ and their general chemical formula is AB_2O_4: the O^{2-} ions are arranged in a compact cubic crystal lattice (*ccp*); the A atoms occupy 1/8 of the tetrahedral sites *8a* and, finally, the B cations occupy half of the octahedral positions *16d*. This category of materials possesses several positive characteristics such as high working potentials, excellent capacities, and relatively low volumetric variations upon cycling. The cubic spinel $LiMn_2O_4$ (LMO) is one of most traditional active materials for cathode in lithium ion batteries. In addition to its excellent performance, LMO immediately

aroused great interest as it does not contain Co and is a stable, non-toxic, sustainable material with much lower production costs than LCO, primarily due to the greater abundance of manganese in nature. In its structure, the Li^+ ion manages to intercalate and de-intercalate reversibly, during charge-discharge cycles, migrating from its position to neighbouring tetrahedral sites, passing through the free octahedral sites (*16c*).[11,12] Studying the intercalation profile, Thackeray *et al.* verified the presence of two reversible redox phenomena.[13] In a typical model, the LMO spinel exhibits a reversible insertion/de-insertion phenomenon from its tetrahedral sites (*8a*) of the lithium ion at ~4 V that induces no phase transition, causing the structure of the $Li_{1-x}Mn_2O_4$ material to be stable from x = 0 up to x = 1. Further intercalation of Li^+ within the material structure would result in a first-order phase transition to give $Li_2Mn_2O_4$ (rock salt), consequent to the lithium ion occupying free octahedral (*16c*) sites. Following this transition, a significant amount of Mn^{4+} ($t_{2g}^3 e_g^0$) tends to reduce to Mn^{3+} ($t_{2g}^3 e_g^1$). By analysing the electronic configuration of these two ions, it is possible to justify the decrease in specific capacitance that the material experiences as the number of cycles increases: Mn^{3+} is, in fact, an ion that generates a strong Jahn-Teller (J-T) effect. For this reason, the distortion due to the J-T effect causes the material structure to undergo a phase transition from cubic to tetragonal, electrochemically inactive. In addition to the aforementioned J-T effect, a further cause of the drop in performance over time is undoubtedly the dissolution of Mn in the electrolyte mixture. Already studied even before the advent of lithium ion batteries, this phenomenon is particularly evident when the electrolyte used is, even slightly, acid. In particular, Mn(III) present in the spinel structure undergoes disproportionation to Mn(II) and Mn(IV). The cation Mn^{2+} proves to be soluble in the electrolyte and, consequently, has the tendency to migrate from the cathode to the anode; here, it is reduced to metallic Mn to form a passivating layer on the electrode surface.[14] To limit capacity fading due to these two factors as much as possible, new materials were sought by varying the stoichiometry and composition of the LMO, with the aim of increasing the cell reversibility and electrochemical performance. The partial replacement of the manganese present with other transition metals (M=Ni, Cr, Co, Fe, Mg) was certainly one of the most interesting lines of research. The synthesis of these new cathodes, having the general formula $LiMn_{2-x}M_xO_4$, is based on the idea of increasing the concentration of Mn^{4+} by inserting other divalent metal cations into the structure, to suppress Mn^{2+} dissolution and J-T elongation due to Mn^{3+}. Some of these also allow the working potential of the cell to be increased by up to 5 V, resulting in so-called high-voltage cathode materials.[15] Among the different materials realized, the most interesting and promising

appears to be $LiNi_{0.5}Mn_{1.5}O_4$ (LMNO). In this cathode two reversible phenomena between 4.4 V and 5 V are visible, corresponding to the redox pairs Ni^{2+}/Ni^{3+} and Ni^{3+}/Ni^{4+}; it is interesting to note that, at 4 V, the Mn^{3+}/Mn^{4+} phenomenon is present but almost completely negligible for the purposes of calculating the specific capacitance.[16] Due to the high work potential, it can reach energy density of 650 Wh kg^{-1}, a value higher than that of the previously mentioned cathodes; for example, 518 Wh kg^{-1} for LCO and 400 Wh kg^{-1} for LMO. The main issue related to these cathodes, however, is dependent on the high working potentials at which common electrolyte mixtures tend to undergo degradation, leading to major drops in capacity and Coulombic efficiency.[17]

1.1.2. Anodic Materials

The request for active systems as anode alternatives for lithium ion batteries is, therefore, strongly compelling. Different innovative materials were consequently proposed in the literature with enhanced electrochemical properties in terms of both potential and capacity, such as graphene, silicon-based systems, and a huge family of metal oxides and oxysalts, typically nanostructured.[18-21]

1.1.2.1. Carbon-based

Carbon materials capable of reversibly intercalating Li^+ ions are of two types: graphitic and disordered (or non-graphitic). The former possesses a layered structure, and both natural graphite and pyrolytic graphite, composed of a set of aggregates of graphite crystals, belong to this category. In these, the intercalation of Li^+ ions occur through a gradual occupation between the different layers.[22] On the other hand, disordered carbons are made up of carbon atoms arranged to form a planar network structure but lacking an extended long-range order. Disordered carbon-based anodes possess high specific capacitance but suffer from huge capacity loss problems during the first cycle and significant fading upon cycling. Graphite is nowadays dominant as an anode in lithium ion batteries. The typical layered structure of this material allows and facilitates the intercalation and deintercalation of Li^+ ions with a high degree of reversibility, resulting in excellent cyclability.[23]

7

Intercalation/Deintercalation mechanism:

$$C_6 + xLi^+ + xe^- \rightleftharpoons Li_xC_6$$
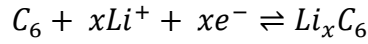
However, a significant negative aspect of such anodes is due to the technological development of recent decades, which has led to their theoretical maximum capacity of 372 mAh g^{-1} being reached. As a result of the demands for increased energy and power densities in modern LIBs, to face the requirements of electric vehicles, it became necessary to investigate alternatives with higher energy density and safety.[24]

1.1.2.2. High Entropy Oxide (HEO)

In recent years, one of the main focuses in the field of material science has been the development of new materials with highly modulable chemical-physical properties capable of supporting continuous technological evolution. Since their discovery, high entropy oxide (HEO) has attracted a great deal of interest. Already known since the early 2000s for metal alloys, the concept of high entropy materials was extended to oxides in 2015, when Rost *et al.* verified the possibility of synthesising at high temperatures an oxide containing five transition metals (Mg, Ni, Co, Cu, Zn) within a rock-salt-like crystalline structure.[25] Analysing the structure and phase diagrams of the precursor oxides, however, one would not expect the formation of a single-phase material but a mixture composed of several phases (P) in equilibrium with each other, as well described by the Gibbs phase rule:

$$P = C + 1 - F$$

where F equals the number of degrees of freedom and C the number of components in the system.[26] To explain this apparent anomaly, one must first resort to the thermodynamic concept of configurational entropy (S_{congif}), defined as the amount of entropic disorder generated by the occupation of the same Wyckoff positions by the different elements in the material under examination. Empirically, it can also be calculated as:

$$S_{config} = -R \sum_i \chi_i \ln \chi_i$$

with χ_i equal to the mole fraction of the *i*-th component and R equal to the universal gas constant (8.314 J mol^{-1} K^{-1}). It is evident that the value of S_{config} increases as the number of

components i in the system increases. In general, a system is considered to have high entropy if $S_{config} \geq 1.5R$, medium entropy if $1R \leq S_{config} < 1.5R$ and low entropy if $S_{config} < 1R$.[27] Now, recalling the definition of Gibbs free energy (ΔG):

$$\Delta G = \Delta H - T\Delta S$$

and considering the very high configurational entropy value, one can indeed thermodynamically justify the formation of a stable single-phase HEO. Indeed, working at high temperatures, the $T\Delta S$ value is very high and can positively compensate for the ΔH, generating a $\Delta G < 0$ (spontaneous process). In conclusion, therefore, a high entropy oxide is only formed spontaneously if the working temperature is above a certain critical temperature, approximately equal to 1000°C. For this reason, following the heat treatment carried out as the last step in the synthesis, the HEO structure is usually quenched by bringing the sample from the heat treatment temperature to room temperature in a few seconds.[28,29] Initially, HEOs were tested as anodic materials for LIBs, as an alternative to graphitic materials. Regarding the mechanism of these materials, to date, materials have been reported that are able to work via simple conversion mechanism, and in some cases via alloying reaction mechanism.

Conversion Reaction mechanism

$$M_X O_y + 2yLi^+ + 2ye^- \rightleftharpoons xM + yLi_2O$$

Alloying Reaction mechanism

$$M_X O_y + 2yLi^+ + 2ye^- \rightarrow xM + yLi_2O$$
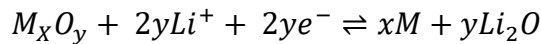
$$M + zLi^+ + ze^- \rightleftharpoons Li_zM$$
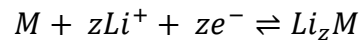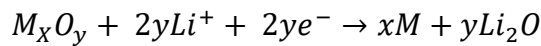
1.2. Lithium Metal Batteries (LMBs): Overview

Lithium metal as an anode for rechargeable batteries has been extensively studied over the past 40 years. The interest in this type of technology is due to the many positive properties of this metal: it has a high theoretical specific capacity (3860 mAh g^{-1}), a low density (0.59 g cm^{-3}) that makes it suitable for use in large devices, and a low electrochemical potential (-3.040 V vs. standard hydrogen electrode).[30,31] The main problems with this type of anode are the growth of dendrites, which can lead to short-circuit phenomena, with consequent

safety risks, and the reduced lifetime. Especially the former mentioned issue has led to fire hazards with sometimes dramatic consequences that have therefore slowed and reduced industrial efforts in the development of lithium-metal battery technology, in addition to the well-known development and progress in the field of lithium-ion batteries. A new and recent interest in the use of lithium metal anodes has arisen from the energy needs of the new generation of rechargeable batteries. The research carried out to make lithium metal batteries available have focused on mitigating and nullifying potential risk phenomena, *i.e.* the growth of dendrites. One of the first attempts concerned the possibility of realising a solid electrolyte interphase (SEI) with greater stability and uniformity by optimising the components of the electrolyte and through the use of appropriate additives.[32-34] Another approach to blocking the proliferation of dendrites is the creation of rigid mechanical barriers consisting of multiple layers of polymer matrix with a high shear modulus.[35] However, the methods just mentioned are based on mechanisms that aim to suppress the penetration of dendrites. Such approaches have proved effective in the short to medium term, but for repeated charging and discharging cycles over long periods of time, they have not yet succeeded in improving Coulombic efficiency and limiting the actual growth of dendrites. Ultimately, in order to actually be able to use these batteries in marketable devices, further studies need to be conducted focusing on the origin of problems such as, for example, the mechanism of dendrite formation and growth during the charging and discharging process and finding solutions that can mitigate these factors.

1.3. Sodium Ion Batteries (SIBs): Overview

Within the periodic table of elements, sodium is placed below lithium, sharing very similar chemical properties with it. Sodium has almost twice the density of lithium, an atomic radius of 180 pm and is usually presented as a silvery, soft and highly reactive metal. The amount of sodium present on the planet is much higher than that of lithium and is evenly distributed, in the form of minerals or NaCl salt dissolved in seawater, making all sodium-based technologies potentially less expensive than LIB technology. Regarding the components and operating mechanism of SIBs and LIBs, they appear to be quite similar. However, there are substantial differences between these two systems due to the different ion carriers. Na^+ ions are larger than Li^+ ions (1.02 Å vs. 0.76 Å), a factor that influences the transport properties

and phase stability used for the different cell components, as well as the formation of interphases.[36] In addition, compared to lithium, sodium is also heavier (23 g mol^{-1} vs. 6.9 g mol^{-1}) and, more importantly, sodium has a higher standard electrode potential (-2.71 V vs. SHE as compared to lithium -3.02 V vs. SHE), thus theoretically leading SIBs to have significantly lower energy density. However, it is important to highlight that the actual mass of Li or Na that contributes to the energy density of the device is only a small fraction of the total, which instead depends more on the composition and stability of the electrode part. Therefore, the differences in energy density may not be so obvious and significant.[37] Considering the cathode compartment, several valuable active materials for SIBs have been realised in recent years, the most famous are based on transition metal oxides, transition metal fluorides, oxyanionic compounds and Prussian blue analogues. On the other hand, the realisation of anode materials with suitable voltage storage, efficient reversible capacity and high structural stability remains one of the main factors that have delayed the development and application of sodium ion batteries. Still considering the technology of LIBs, the most commonly used anode is graphite, which has a moderate lithium storage capacity of ~350 mAh g^{-1} at approximately around 0.1 V vs. Li/Li^{+}.[38] This value cannot be obtained by using the same anode for sodium ion batteries due to a greater difficulty of intercalation.[39,40] As an alternative, anodes that are not graphite-based but are carbonaceous type such as hard carbon, carbon black, carbon fibres that allow Na^{+} ions to be inserted, have been realized.[41-44] In addition, other classes of materials have also been developed but considering different types of mechanisms such as conversion and alloying. Specifically transition metal oxides or transition metal sulphides have been studied regarding the conversion mechanism and elements of group 14 or 15 by alloying reaction.[45-47] Anode materials working by these two mechanisms are known to have high capacitance but suffer from severe volumetric expansion, which leads to considerable degradation and damage of the electrode with consequent significant loss of capacity.[48]

1.4. Smart Materials with Self-Healing Functionalities: Overview

The massive spread of Li-ion batteries for the e-mobility sector asks for a new concept of next generation energy storage devices, which must guarantee improved lifetime, quality, reliability and safety.[49] All these aspects are strictly dependent from several degradation

processes occurring upon continuous cycling, which involve all the cell components, as current collector corrosion/dissolution, anode pulverization and electric contact loss, dendrites and solid electrolyte interface (SEI) growth, gas evolution, leaching of transition metals from cathode, electrode cracks and structure disordering, electrolyte penetration.[50] These ageing phenomena cannot be totally avoided, but rather mitigated through a plethora of strategies that have been widely reviewed in literature during the last decade.[51-55] Very recently, breakthrough research approaches have been presented at European level as a new roadmap which points to develop the future batteries through the integration of artificial intelligence, advanced tools of monitoring, evaluation and diagnosis and the introduction of smart functionalities as sensing and self-healing.[56] Self-healing is a nature-inspiring concept that expresses the ability of a system to repair damage spontaneously and restore its original properties.[57] For this reason, the development of materials for batteries capable to self-repair may be an innovative strategy to exploit higher intrinsic durability and, consequently, prolonged cell lifetime.[58] Self-healing functionalities demonstrated to pave the way for more performing battery cells by improving the durability of materials and components. Basically, the self-healing mechanisms can be divided in: i) intrinsic or autonomous repair of mechanical and structural cracks, chemical composition, thermal stability and also electric properties, and ii) extrinsic or non-autonomous recover of damages triggered by external stimuli such as light, temperature or pressure. In the specific case of Li-ion batteries, the intrinsic self-healing mechanism proved to be successful in the spontaneous repair of failed electrodes or electrolytes through reversible bond reformation in the damaged materials re-activating their original properties.[59-61] In case of anodes, self-healing approaches addressed the issue of physical and mechanical damages in active materials as Silicon or Black Phosphorus induced by irreversible volume expansion and fractures upon Li (or Na) insertion/deinsertion.[62-65] Recovering strategies of chemical failure were discussed for cathodes which undergo leaching of transition metals in presence of byproducts coming from some Li salt degradation (*e.g.* LiPF$_6$), or loss of small molecules as O$_2$ released from sublattice sites.[66] Such approaches considered the use of self-healing binders, based on polymers with ureidopyrrolidone units capable to physically repair cleavages through dynamic multiple Hydrogen bonds or coating layers properly designed to trap detrimental gasses or byproducts.

1.5. Aim of the Thesis

The market for rechargeable lithium-ion batteries has reached world values equal to about 10 billion dollars a year and appears to be in continuous growth. The main reason that justifies these rapid levels of growth is given by the unique characteristics and clearly superior to any other energy storage device, such as the high energy density and the performance obtained during cycling. A further stimulus to the great interest in large-scale lithium-ion battery systems has been given by recent requests in energy and environmental sustainability as in the automotive field and for the storage of energy from renewable resources, such as solar and wind power. There is also an evident interest to improve the energy density of lithium-ion batteries through increasing the operating voltage or the charge-storage capacity or both. The performance required are largely determined by the properties and characteristics of the component materials used in assembling the batteries as well as the cell engineering and system integration involved. At present, the aim of my Ph.D. is not only to improve the already widespread lithium-ion batteries on the market, but also to investigated innovative materials to gain low production costs, higher energy density, safety, biocompatibility and, definitely, better energy storage and conversion efficiency, for moving to the new technology of post-lithium-ion battery (PLIBs).

1.6. Bibliography

1. Zhou, H. New energy storage devices for post lithium-ion batteries. *Energy Environ. Sci.* 2013, **6**, 2256.

2. Padhi, A. K.; Nanjundaswamy, K. S.; Goodenough, J. B. Phospho-olivines as positive-electrode materials for rechargeable lithium batteries. *J. Electrochem. Soc.* 1997, **144**, 1188-1194.

3. Chung, S. Y.; Bloking, J. T.; Chiang, Y. M. Electronically conductive phospho-olivines as lithium storage electrodes. *Nat. Mater.* 2002, **1**, 123-128.

4. Gong, Z.; Yang, Y. Recent advances in the research of polyanion-type cathode materials for Li-ion batteries. *Energy Environ. Sci.* 2011, **4**, 3223-3242

5. Whittingham, M. S. Chemistry of Intercalation Compounds: Metal Guests in Chalcogenide Hosts. *Progress in Solid State Chemistry* 1978, **12**.

6. Manthiram, A. A. Reflection on Lithium-Ion Battery Cathode Chemistry. *Nat. Commun.* 2020, **11 (1)**, 1550.

7. K. Mizushima, K.; Jones, P. C.; Wiseman, P. J.; Goodenough, J. B. LixCoO$_2$ (0 < x < -1): A new cathode material for batteries of high energy density. *Materials Research Bulletin* 1980, **15**, 783-789.

8. Robert, R.; Villevieille, C.; Novák, P. Enhancement of the High Potential Specific Charge in Layered Electrode Materials for Lithium-Ion Batteries. *J. Mater. Chem. A* 2014, **2 (23)**, 8589-8598.

9. Yoshizawa, H.; Ohzuku, T. Prismatic Lithium - Ion Batteries of LiCo$_{1/3}$Ni$_{1/3}$Mn$_{1/3}$O$_2$ with Graphite. *Electrochemistry* 2003, **71**,1177-1181.

10. Guilmard, M.; Pouillerie, C.; Croguennec, L.; Delmas, C. Structural and Electrochemical Properties of LiNi$_{0.70}$Co$_{0.15}$Al$_{0.15}$O$_2$. *Solid State Ionics* 2003, **160 (1-2)**, 39-50.

11. Masquelier, C.; Croguennec, L. Polyanionic (Phosphates, Silicates, Sulfates) Frameworks as Electrode Materials for Rechargeable Li (or Na) Batteries. *Chem. Rev.* 2013, **113 (8)**, 6552-6591.

12. Huang, Y.; Dong, Y.; Li, S.; Lee, J.; Wang, C.; Zhu, Z.; Xue, W.; Li, Y.; Li, J. Lithium Manganese Spinel Cathodes for Lithium-Ion Batteries. *Adv. Energy Mater.* 2021, **11 (2)**, 1-21.

13. Thackeray, M. M.; David, W. I. F.; Bruce, P. G.; Goodenough, J. B. Lithium Insertion into Manganese Spinels. *Mater. Res. Bull.* 1983, **18 (4)**, 461–472.

14. Zhan, C.; Wu, T.; Lu, J.; Amine, K. Dissolution, Migration, and Deposition of Transition Metal Ions in Li-Ion Batteries Exemplified by Mn-Based Cathodes-A Critical Review. *Energy Environ. Sci.* 2018, **11**, 243-257.

15. Yoon, Y. K.; Park, C. W.; Ahn, H. Y.; Kim, D. H.; Lee, Y. S.; Kim, J. Synthesis and Characterization of Spinel Type High-Power Cathode Materials $LiM_xMn_{2-x}O_4$ (M=Ni, Co, Cr). *J. Phys. Chem. Solids* 2007, **68 (5-6)**, 780-784.

16. Markovsky, B.; Talyossef, Y.; Salitra, G.; Aurbach, D.; Kim, H. J.; Choi, S. Cycling and Storage Performance at Elevated Temperatures of $LiNi_{0.5}Mn_{1.5}O_4$ Positive Electrodes for Advanced 5 V Li-Ion Batteries. *Electrochem. commun.* 2004, **6 (8)**, 821-826.

17. Yi, T. F.; Mei, J.; Zhu, Y. R. Key Strategies for Enhancing the Cycling Stability and Rate Capacity of $LiNi_{0.5}Mn_{1.5}O_4$ as High-Voltage Cathode Materials for High Power Lithium-Ion Batteries. *J. Power Sources* 2016, **316**, 85-105.

18. Al Hassan, M. R.; Sen, A.; Zaman, T.; Mostari, M. S. Emergence of Graphene as a Promising Anode Material for Rechargeable Batteries: a review. *Mater. Today Chem*. 2019, **11**, 225-243.

19. Hatchard, T. D.; Dahn, J. R. *In Situ* XRD and Electrochemical Study of the Reaction of Lithium with Amorphous Silicon. *J. Electrochem. Soc.* 2004, **151**, A838.

20. Reddy, M. V.; Subba Rao, G. V.; Chowdari, B. V. R. Metal Oxides and Oxysalts as Anode Materials for Li Ion Batteries. *Chem. Rev.* 2013, **113**, 5364-5457

21. Liu, J.; Liu, X.-W. Two-Dimensional Nanoarchitectures for Lithium Storage. *Adv. Mater.* 2012, **24**, 4097-4111.

22. Winter, M.; Besenhard, J. O.; Spahr, M. E.; Novak, P. Insertion electrode materials for rechargeable lithium batteries. *Adv. Mater.* 1998, **10**, 725-763.

23. Megahed, S.; Scrosati, B. Lithium-ion rechargeable batteries. *J. Power Sources* 1994, **51**, 79-104

24. Deng, D.; Lee, J. Y. Meso-oblate Spheroids of Thermal-Stabile Linker-Free Aggregates with Size Tunable Subunits for Reversible Lithium Storage. *ACS Appl. Mat. Interfac.* 2013, **6**, 1173-1179.

25. Rost, C. M.; Sachet, E.; Borman, T.; Moballegh, A.; Dickey, E. C.; Hou, D.; Jones, J. L.; Curtarolo, S.; Maria, J. P. Entropy-Stabilized Oxides. *Nat. Commun.* 2015, **6**, 8485.

26. Berardan, D.; Meena, A. K.; Franger, S.; Herrero, C.; Dragoe, N. Controlled Jahn-Teller Distortion in (MgCoNiCuZn)O-Based High Entropy Oxides. *J. Alloys Compd.*

2017, **704**, 693-700.

27. Murty, B. S.; Yeh, J. W.; Ranganathan, S. High Entropy Alloys. *Butterworth-Heinemann Ltd (Verlag)* 2014.

28. Sarkar, A.; Wang, Q.; Schiele, A.; Chellali, M. R.; Bhattacharya, S. S.; Wang, D.; Brezesinski, T.; Hahn, H.; Velasco, L.; Breitung, B. High-Entropy Oxides: Fundamental Aspects and Electrochemical Properties. *Adv. Mater.* 2019, **31 (26),** 1806236.

29. McCormack, S. J.; Navrotsky, A. Thermodynamics of High Entropy Oxides. *Acta Mater.* 2021, **202**, 1-21.

30. Whittingham, M. S. History, Evolution, and Future Status of Energy Storage. *Proc. IEEE*, 2012, **100**, 1518-1534.

31. Aurbach, D.; Cohen, Y. The application of atomic force microscopy for the study of Li deposition processes. *J. Electrochem. Soc.* 1996, **143**, 3525-3532.

32. Aurbach, D.; Zinigrad, E.; Cohen, Y.; Teller, H. A short review of failure mechanisms of lithium metal and lithiated graphite anodes in liquid electrolyte solutions. *Solid State Ionics* 2002, **148**, 405-416.

33. Gireaud, L.; Grugeon, S.; Laruelle, S.; Yrieix, B.; Tarascon, J. M. Lithium metal stripping/plating mechanisms studies: A metallurgical approach. *Electrochem. Commun.* 2006, **8**, 1639-1649.

34. Yamaki, J.-i.; Tobishima, S.-i.; Hayashi, K.; Keiichi, S.; Nemoto, Y.; M. Arakawa, M. A consideration of the morphology of electrochemically deposited lithium in an organic electrolyte. *J. Power Sources* 1998, **74**, 219-227.

35. Li, Y.; Fedkiw, P. S.; Khan, S.A. Lithium/V_6O_{13} cells using silica nanoparticle-based composite electrolyte. *Electrochim. Acta* 2002, **47**, 3853-3861.

36. Adelhelm, P.; Hartmann, P.; Bender, C. L.; Busche, M.; Eufinger, C.; Janek, J. *J. Nanotechnol.* 2015, **6**, 1016-1055.

37. M. D. Slater, D. Kim, E. Lee, E.; Johnson, C. S. Sodium-ion batteries. *Adv. Funct. Mater.* 2013, **23**, 947-958.

38. Pan, H.; Hu, Y.-S.; Chen, L. Unlocking sustainable Na-ion batteries into industry. *Energy Environ. Sci.* 2013, **6**, 2338-2360.

39. Divincenzo, D. P.; Mele, E. J. *Phys. Rev. B: Condens. Matter Mater. Phys.* 1985, **32**, 2538-2553.

40. R. Alcántara, R.; Jiménez-Mateos, J. M.; Lavela, P.; Tirado, J. L. Carbon black: a promising electrode material for sodium-ion batteries. *Electrochem. Commun.* 2001, **3**, 639-642.

41. Thomas, P.; Ghanbaja, J.; Billaud, D. Electrochemical insertion of sodium in pitch-based carbon fibres in comparison with graphite in NaClO₄-ethylene carbonate electrolyte. *Electrochim. Acta* 1999, **45**, 423-430.

42. Stevens, D. A.; Dahn, J. R. An *in situ* small-angle X-ray scattering study of sodium insertion into a nanoporous carbon anode material within an operating electrochemical cell. *J. Electrochem. Soc.* 2000, **147**, 4428-4431.

43. - Stevens, D. A.; Dahn, J. R. The mechanisms of lithium and sodium insertion in carbon materials. *J. Electrochem. Soc.* 2001, **148**, A803-A811.

44. Xia, X.; Dahn, J. R. Study of the reactivity of Na/hard carbon with different solvents and electrolytes. *J. Electrochem. Soc.* 2012, **159**, A515-A519.

45. Klein, F.; Jache, B.; Bhide, A.; Adelhelm, P. Conversion reactions for sodium-ion batteries. *Phys. Chem. Chem. Phys.* 2013, **15**, 15876-15887.

46. Chevrier, V. L.; Ceder, G. Challenges for Na-ion negative electrodes. *J. Electrochem. Soc.* 2011, **158**, A1011-A1014.

47. Mortazavi, M.; Ye, Q.; Birbilis, N.; Medhekar, N. V. High capacity group-15 alloy anodes for Na-ion batteries: Electrochemical and mechanical insights. *J. Power Sources* 2015, **285**, 29-36.

48. Kim, Y.; Ha, K. H.; Oh, S. M.; Lee, K. T. High-capacity anode materials for sodium-ion batteries. *Chemistry* 2014, **20**, 11980-11992.

49. Fichtner, M.; Edström, K.; Ayerbe, E.; Berecibar, M.; Bhowmik, A.; Castelli, I. E.; Clark, S.; Dominko, R.; Erakca, M.; Franco, A. A.; Grimaud, A.; Horstmann, B.; Latz, A.; Lorrmann, H.; Meeus, M.; Narayan, R.; Pammer, F.; Ruhland, J.; Stein, H.; Vegge, T.; Weil, M. Rechargeable Batteries of the Future - The State of the Art from a BATTERY 2030+ Perspective. *Adv. Energy Mater.* 2022, **12**, 2102904.

50. Kabir, M. M.; Demirocak, D. E. Degradation Mechanisms in Li-Ion Batteries: A State-of-the-Art Review. *Int. J. Energy Res.* 2017, **41 (14)**, 1963-1986.

51. Booth, S. G.; Nedoma, A. J.; Anthonisamy, N. N.; Baker, P. J.; Boston, R.; Bronstein, H.; Clarke, S. J.; Cussen, E. J.; Daramalla, V.; De Volder, M.; Dutton, S. E.; Falkowski, V.; Fleck, N. A.; Geddes, H. S.; Gollapally, N.; Goodwin, A. L.; Griffin, J. M.; Haworth, A. R.; Hayward, M. A.; Hull, S.; Inkson, B. J.; Johnston, B. J.; Lu, Z.; MacManus-Driscoll, J. L.; Martínez De Irujo Labalde, X.; McClelland, I.;

McCombie, K.; Murdock, B.; Nayak, D.; Park, S.; Pérez, G. E.; Pickard, C. J.; Piper, L. F. J.; Playford, H. Y.; Price, S.; Scanlon, D. O.; Stallard, J. C.; Tapia-Ruiz, N.; West, A. R.; Wheatcroft, L.; Wilson, M.; Zhang, L.; Zhi, X.; Zhu, B.; Cussen, S. A. Perspectives for next Generation Lithium-Ion Battery Cathode Materials. *APL Mater.* 2021, **9 (10)**, 109201.

52. Zhan, C.; Wu, T.; Lu, J.; Amine, K. Dissolution, Migration, and Deposition of Transition Metal Ions in Li-Ion Batteries Exemplified by Mn-Based Cathodes - a Critical Review. *Energy Environ. Sci.* 2018, **11 (2)**, 243-257.

53. Zhao, Q.; Stalin, S.; Archer, L. A. Stabilizing Metal Battery Anodes through the Design of Solid Electrolyte Interphases. *Joule* 2021, **5 (5)**, 1119-1142.

54. Lin, D.; Liu, Y.; Cui, Y. Reviving the Lithium Metal Anode for High-Energy Batteries. *Nat. Nanotechnol.* 2017, **12 (3)**, 194-206.

55. Pender, J. P.; Jha, G.; Youn, D. H.; Ziegler, J. M.; Andoni, I.; Choi, E. J.; Heller, A.; Dunn, B. S.; Weiss, P. S.; Penner, R. M.; Mullins, C. B. Electrode Degradation in Lithium-Ion Batteries. *ACS Nano* 2020, **14 (2)**, 1243-1295.

56. Amici, J.; Asinari, P.; Ayerbe, E.; Barboux, P.; Bayle-Guillemaud, P.; Behm, R. J.; Berecibar, M.; Berg, E.; Bhowmik, A.; Bodoardo, S.; Castelli, I. E.; Cekic-Laskovic, I.; Christensen, R.; Clark, S.; Diehm, R.; Dominko, R.; Fichtner, M.; Franco, A. A.; Grimaud, A.; Guillet, N.; Hahlin, M.; Hartmann, S.; Heiries, V.; Hermansson, K.; Heuer, A.; Jana, S.; Jabbour, L.; Kallo, J.; Latz, A.; Lorrmann, H.; Løvvik, O. M.; Lyonnard, S.; Meeus, M.; Paillard, E.; Perraud, S.; Placke, T.; Punckt, C.; Raccurt, O.; Ruhland, J.; Sheridan, E.; Stein, H.; Tarascon, J.-M.; Trapp, V.; Vegge, T.; Weil, M.; Wenzel, W.; Winter, M.; Wolf, A.; Edström, K. A Roadmap for Transforming Research to Invent the Batteries of the Future Designed within the European Large Scale Research Initiative BATTERY 2030+. *Adv. Energy Mater.* 2022, **12**, 2102785.

57. Wang, S.; Urban, M. W. Self-Healing Polymers. *Nat. Rev. Mater.* 2020, **5 (8)**, 562-583

58. Mezzomo, L.; Ferrara, C.; Brugnetti, G.; Callegari, D.; Quartarone, E.; Mustarelli, P.; Ruffo, R. Exploiting Self-Healing in Lithium Batteries: Strategies for Next-Generation Energy Storage Devices. *Adv. Energy Mater.* 2020, **10 (46)**, 2002815.

59. Mai, W.; Yu, Q.; Han, C.; Kang, F.; Li, B. Self-Healing Materials for Energy-Storage Devices. *Adv. Funct. Mater.* 2020, **30 (24)**, 1909912.

60. Wang, H.; Wang, P.; Feng, Y.; Liu, J.; Wang, J.; Hu, M.; Wei, J.; Huang, Y. Recent Advances on Self-Healing Materials and Batteries. *ChemElectroChem* 2019, **6 (6)**, 1605–1622.

61. Narayan, R.; Laberty-Robert, C.; Pelta, J.; Tarascon, J.-M.; Dominko, R. Self-Healing: An Emerging Technology for Next-Generation Smart Batteries. *Adv. Energy Mater.* 2022, **12**, 2102652.

62. Wang, C.; Wu, H.; Chen, Z.; McDowell, M. T.; Cui, Y.; Bao, Z. Self-Healing Chemistry Enables the Stable Operation of Silicon Microparticle Anodes for High-Energy Lithium-Ion Batteries. *Nat. Chem.* 2013, **5 (12)**, 1042-1048.

63. Munaoka, T.; Yan, X.; Lopez, J.; To, J. W. F.; Park, J.; Tok, J. B. -H.; Cui, Y.; Bao, Z. Ionically Conductive Self-Healing Binder for Low Cost Si Microparticles Anodes in Li-Ion Batteries. *Adv. Energy Mater.* 2018, **8 (14)**, 1703138.

64. Zhang, G.; Yang, Y.; Chen, Y.; Huang, J.; Zhang, T.; Zeng, H.; Wang, C.; Liu, G.; Deng, Y. A Quadruple-Hydrogen-Bonded Supramolecular Binder for High-Performance Silicon Anodes in Lithium-Ion Batteries. *Small* 2018, **14 (29)**, 1801189.

65. Callegari, D.; Colombi, S.; Nitti, A.; Simari, C.; Nicotera, I.; Ferrara, C.; Mustarelli, P.; Pasini, D.; Quartarone, E. Autonomous Self-Healing Strategy for Stable Sodium-Ion Battery: A Case Study of Black Phosphorus Anodes. *ACS Appl. Mater. Interfaces* 2021, **13 (11)**, 13170-13182.

66. Sharifi-Asl, S.; Lu, J.; Amine, K.; Shahbazian-Yassar, R. Oxygen Release Degradation in Li-Ion Battery Cathode Materials: Mechanisms and Mitigating Approaches. *Adv. Energy Mater.* 2019, **9 (22)**, 1900551.

Chapter 2:
Characterization Techniques an Overview

2.1. Physicochemical Techniques

The following chapters will describe the characterisation techniques used to assess the chemical and physical properties of all the realized materials

2.1.1. X-Ray Diffraction (XRD)

X-ray diffraction (XRD) is one of the most widely used structural characterisation technique for determining the crystallographic properties of crystalline solid materials. It is based on the physical phenomenon of diffraction, originating from coherent scattering (or elastic scattering) undergone by X-ray photons as they encounter a crystalline structure. In laboratory, X-rays are produced using metal anticathode radiogenic tubes, consisting of a tungsten (W) filament (cathode) and a metal target (anode). The production mechanism can be schematised as follows: (i) due to the high values of potential difference and current used, the cathode emits electrons because of the thermionic effect; (ii) following the collision with these electrons, the core electrons of the anode material are excited to higher energy levels; (iii) the electronic configuration achieved is unstable, which is why the atom tends to return to their fundamental state by means of electronic relaxation; (iv) the excess energy produced by the relaxation can be released in the form of a X-ray photon or an Auger electron, in different percentages depending on the type of anode used. Since each element has a particular electronic structure, characteristic X-rays will be obtained depending on the metal target used. The X-ray emission spectrum consists of two main components: the radiation in the continuum (Bremsstrahlung), resulting from decelerate those electrons undergo as they encounter the electronic cloud of the target atoms, and the characteristic radiation, visible only if the incident electron succeeds in promoting a metal core electron to higher energy levels. The latter consists of different types of radiation, which can be classified according to the core state from which the metal electron is extracted. For diffraction experiments, radiation $K\alpha_1$ (removal of an extracted electron from the K sphere and replacement by an electron from the L sphere), which is usually the most intense. One of the most commonly

used metal targets is copper (Cu), whose wavelength of $K\alpha_1$ radiation is equal to 1.5405 Å. The radiation of the continuum and all the secondary characteristic radiations are eliminated using special filters or monochromator crystals. For a Cu target (Z=29), the monochromator used is Ni-based (Z=28). Although not completely correct from a physical point of view, Bragg's diffraction law is the basis for the operation of all commercially available diffractometers. This law is based on the concept of diffraction modelled as the simple phenomenon of reflection of X-rays upon interacting grating planes of the sample. The planes are considered semi-reflective, so that the incident X-ray photons are both reflected by the surface lattice planes and transmitted towards the innermost ones. Bragg's law is defined by the following equation:

$$2d\ sin\theta = n\lambda$$

with d equal to the interplanar distance, θ to the angle of incidence and reflection of the X-ray photons and λ to the wavelength of the incident radiation. For a correct interpretation of the results obtained using this formula, it is important to note that the diffraction angles θ at which the peaks fall in the pattern do not depend on the type of atoms that composed the sample but exclusively on their spatial arrangement. In addition to the X-ray tube and filters described above, diffractometers are made up of a number of other elements, *e.g.* slides and slits, whose role is to optimise the focusing of the X-ray beam interacting with the sample, so that a higher quality diffraction pattern can be obtained. A further fundamental component is the detector, whose function is to record the intensity of diffracted radiation. There are two types: point and solid-state. The former can be gas-proportional or scintillation detectors. Solid-state detectors, on the other hand, are composed of a suitably doped semiconductor crystal (usually Si), which produces several electron holes proportional to the energy of the X-ray photons it can absorb. A potential difference is applied to the crystal, so that the holes and electrons are displaced towards opposite regions of the detector and, therefore, a current is created with an intensity proportional to the energy of the X-radiation diffracted by the sample under examination.

2.1.2. Scanning Electron Microscopy and Energy Dispersive X-ray Spectroscopy (SEM-EDX)

The scanning electron microscope (SEM) has been commercialised since the 1960s. The idea behind the design of all electron microscopes is to employ a focused beam of electrons to illuminate the sample, unlike optical microscopes that use a simple light source. The advantages of using electrons are their wavelength, which is much smaller than that of visible light (0.1-0.005 Å vs. 4000-7000 Å), so scanning electron microscopes can perform better than optical. Performance is generally described in terms of: i) resolution, described as the shortest distance between two distinguishable points in the image (5 nm); ii) magnification, defined as the ratio between the distance between two points on the image and the same distance measured on the sample (up to 10^5); iii) depth of field, equal to the maximum distance between two points simultaneously in focus, measured in the direction parallel to that of observation. The values indicated in brackets refer to those possessed by common SEMs. The as obtained image is produced thanks to the signals emitted by the sample upon interaction with the incident electron beam, which is produced using specific electron guns. These latter can either be traditional, *i.e.* exploiting the thermionic effect to extract electrons from a heated W filament or a LaB_6 crystal, or Field Emission Guns (FEG): electrons are extracted, by tunnel effect, from a single crystal of W shaped with a very thin tip (cathode) to which a very high electric field is applied. The generated beam is accelerated and focused on the sample via two anodes. This type of electron source is the best in terms of beam brilliance and energy; however, it is not very stable over time and requires a very high vacuum to function properly, of about 10^{-10} torr. The vacuum is necessary for all electron sources, as the beam produced must arrive at the sample without any obstacles. In addition to the electron gun, the SEM also consists of: i) a system of three electro-magnetic lenses necessary to make the beam hitting the sample as focused as possible; ii) a different detector for each type of secondary electron emitted by the sample; iii) a specimen holder; iv) a software for observing the constructed images of the samples. Before listing the common detectors, it is necessary to describe the different signals that are produced by the sample upon interaction with the incident electron beam. Those most commonly used for SEM analyses are the secondary electrons (SE) and the backscattered electrons (BSE). The formers are produced as a result of the interaction between the incident electrons and the outermost electrons of the sample which are ejected, in this case we are in presence of inelastic scattering. Since they only arise from the most superficial atoms of the sample,

important topographical considerations can be derived from their detection. The emission yield for SEs depends on various factors, the most important are the atomic number (Z) of the atoms present and the local curvature of the surface of the sample; in general, the number of secondary electrons emitted depends on the morphology of the sample. Instead, BSE are generated by the elastic scattering of electrons bouncing back from the sample without passing through it. They have a high energy, close to that of the electrons in the primary beam. They are used to obtain information on the relative atomic density along with information on the topography of the samples. The detectors used for SE are the so-called Everhart-Thornley detectors, scintillator-photomultiplier type, while for BSE, solid-state detectors are used, similar to those previously described for XRD (paragraph 2.2.1). In addition to the above-mentioned SE and BSE detections, further information can be obtained from the interaction between the sample and the incident electron beam by analysing the emitted X-rays, which are usually detected by means of a solid-state detector of Lithium-doped Silicon (Si-Li). The analysis of X-ray photons using an electron microscope is called EDX (energy dispersive X-ray) analysis. By this technique it is possible to obtain qualitative and quantitative analyses of the elemental chemical composition of the sample and obtain the distribution maps of the elements in a specific area.

2.1.3. Thermogravimetric Analysis (TGA)

Thermogravimetric analysis (TGA) consists of recording the variation over time of the mass of a sample subjected to a programmed temperature scan. This measurement is carried out with a microbalance, which is sensitive to changes in mass due to the development or absorption of gases, while the sample is placed in a furnace to control the temperature and atmosphere. The result obtained is a thermogram showing the temperature (or time) in the abscissa and the mass change, as an absolute value or percentage, in the ordinate. Such a graph is often referred to as a thermal decomposition curve. Thermogravimetric analysis can be carried out in different atmospheres, both inert and reactive, obtaining information on the stability and reactivity of materials under different conditions. With reference to polymeric materials, the information that can be obtained with thermogravimetry can therefore be manifold:

- thermal stability;

- thermo-oxidative stability (*e.g.* oxygen induction time, OIT);

- composition in multi-component systems (*e.g.* information on inert filler content);

- stability in corrosive or reactive atmospheres;

- determination of the content of low-boiling substances (monomer residues, solvents, or moisture.

Any chemical or structural changes that do not lead to mass variation (*e.g.* phase changes without transition to the gaseous state) cannot be detected by TGA analysis, or direct information can be obtained on the degradation products and thus the mechanisms of degradation.

2.1.4. Differential Scanning Calorimetry (DSC)

Differential scanning calorimetry is one of the most widely used analytical techniques for the characterisation of polymers and polymeric materials in general, food and pharmaceutical products, glass and ceramics, biological macromolecules such as proteins, etc., due to the amount of information it can provide and the ease with which measurements can be carried out on the sample of interest. DSC calorimeter measures the heat fluxes associated with thermal transitions that occur in a sample when it is heated/cooled (dynamic conditions) or maintained at a constant temperature (isothermal conditions) in a controlled manner. This allows the user to determine at which temperature or temperature range any transitions (melting processes, crystallisation, etc.) occur in the sample and to quantitatively measure the associated energies. In order to measure a heat flow, since it is not an absolute quantity, a reference is required which, when thermally stressed in a similar way to the sample under examination, has a different response, thus enabling us to obtain a differential signal. The differential measurement is important both from a theoretical and practical point of view because the resulting signal can be studied independently from all those thermal effects external to the system that affect the two samples equally, allowing us to obtain at the output the proper behaviour of the material under examination. In the specific case of polymers and polymeric materials in general, DSC calorimetry under dynamic conditions mainly allows the following to be determined:

- glass transition temperature (T_g), melting temperature (T_m), and crystallisation temperature (T_c);

- enthalpy of melting (ΔH_m) and crystallisation (ΔH_c);
- degree of crystallinity (X_c), in the case of semi-crystalline polymers;
- polymorphism, solid-solid transitions;
- temperature of protein denaturation.

Furthermore, it is important to consider that under dynamic conditions, the data obtained (temperatures, enthalpies, and related quantities) are influenced by the kinetics of the processes being investigated. Therefore, the higher the scanning speed, the greater the deviation from thermodynamic equilibrium conditions. By DSC analysis under isothermal conditions, thermal or thermo-oxidative stability tests are carried out, and crystallisation kinetics and phase transition kinetics can be studied, usually of polymerisation, cross-linking and curing, in all cases kinetics of phenomena that do not involve a change in the mass of the sample under investigation. DSC calorimetry, in addition to the advantage of using small sample quantities (a few mg), is a non-destructive technique for which, provided the thermal degradation threshold of the material under examination is not exceeded, it can be exploited to determine the reversibility of a phenomenon following successive thermal cycles or to study natural or accelerated ageing phenomena by means of appropriate heat treatments.

2.1.5. Dynamic Mechanical Analysis (DMA)

Dynamic mechanical analysis is a thermo-analysis technique in which the viscoelastic properties of the sample are analysed by evaluating the deformation or strain generated as a result of the application of a sinusoidal force overtime at a given temperature or temperature interval. Specifically, stress is the deformation force per unit area (usually expressed in Pa), while strain is the apparent change in shape, volume, or length of the sample under examination due to the applied stress. When a material is subjected to small oscillatory stress, it can respond by assuming three different behaviours:

- Perfectly elastic behaviour: a body subjected to stress will undergo instantaneous deformation that is constant over time; when the applied force is removed, the material will tend to immediately and completely recover its original state. Stress and strain are in phase, so the response to a change in one of these parameters immediately influences the other one.

- Purely viscous behaviour: the applied stress will cause a deformation that will increase proportionally in time until the stress is removed; in this case, once the force has ceased, the deformation will stop but there will be no recovery. Deformation is delayed with respect to stress by 90°.
- Viscoelastic behaviour: intermediate between purely elastic and purely viscous behaviour, displaying a strain lag value with respect to stress between 0° and 90°.

From dynamic mechanical analysis, it is therefore possible to measure various viscoelastic properties (storage and loss modulus) and their temperature and frequency dependence. The storage and loss moduli in viscoelastic materials measure the stored energy, representing the elastic component, and the energy dissipated as heat, representing the viscous component. The tensile storage (E') and loss (E") moduli are defined as follows:

$$E' = \frac{\sigma_0}{\varepsilon_0} \cos \delta$$

$$E'' = \frac{\sigma_0}{\varepsilon_0} \sin \delta$$

with σ_0 being the amplitude of stress, ε_0 is the strain amplitude and δ is the phase shift between stress and strain. By performing temperature dispersion measurements, studies of glass transition temperatures and modulus dependence can be carried out. A further possible characterisation is given by performing simultaneous temperature and frequency dispersion measurements, so that relaxation phenomena such as glass transitions, side chain relaxations and local phenomena can be observed, allowing the molecular structure and motions of a polymer to be studied. Similarly, in the case of shearing instead of tensile, it is possible to define the storage and loss modules G' and G", respectively.

2.1.6. Inductively Coupled Plasma - Optical Emission Spectroscopy (ICP-OES)

Inductively coupled plasma optical spectroscopy (ICP-OES) is an important analytical technique employed in qualitative and quantitative analyses of samples in solution. In particular, the determination involves mainly metallic elements. Compared to other analytical techniques, ICP-OES has two major advantages: it allows several elements to be analysed simultaneously and makes it possible to determine concentrations of a few tens of ppb ($\mu g\,L^{-1}$). The basis of ICP spectrometry is the so-called plasma, defined as an electrically

neutral but highly ionised hot gas, *i.e.* composed of positive ions and electrons in the gas phase. The ICP source is commonly referred to as a torch and consists of three concentric quartz tubes, into which argon (Ar) is flushed: in the innermost tube Ar flows at a rate of about 1 L min^{-1}, carrying with it the sample (in the form of an aerosol) from the nebuliser. The gas passing through the central tube serves to keep the hot plasma away from the injection capillary. Finally, in the outermost tube, the gas flow is very fast (10 L min^{-1}) and is essential to isolate the plasma from the external atmosphere and protect the quartz tube. Also, by means of a solenoid powered by a radio frequency generator, located on top of the torch, it is possible to generate the alternating current required to ignite the torch and the subsequent ionisation of the argon. Ar$^+$ and e$^-$ continuously interact with each other and with the oscillating magnetic field formed; they also manage to transmit part of their momentum to the non-ionised Ar particles they collide with. As a result of all these collisions, the plasma can reach very high temperatures (~9000 K). As already mentioned, the sample is introduced into the torch as dispersed micrometric particles (aerosols), obtained through the use of a nebuliser. As they reach the plasma, these particles undergo rapid atomisation and subsequent ionisation, giving rise to several ions that emit electromagnetic radiation at the specific wavelength of the starting element. Through an optical system consisting of a monochromator and lenses, this radiation reaches the detector, which processes the light signal and allows the quantification of the elements present in the sample. The detectors usually used are photodetectors based on semiconductors, which emit a signal proportional to the incident electromagnetic radiation; the most common are the so-called Charge Coupled Devices (CCD) and Charge Injection Devices (CID). The orientation of the torch with respect to the detector can be horizontal (axial) or vertical (radial); the latter arrangement has the lowest detection limit.

2.2. Electrochemical Techniques

Electrochemical characterisations, fundamental during my thesis, will be described below. The techniques used were: potentiodynamic electrochemical impedance spectroscopy (PEIS), galvanostatic cycling with potential limitation (GCPL) and potentiodynamic cycling with galvanostatic acceleration (PCGA).

2.2.1. Potentiodynamic Electrochemical Impedance Spectroscopy (PEIS)

Electrochemical impedance spectroscopy (EIS) is a widely used analysis technique in electrochemistry as it allows the correct operating of batteries to be monitored over time. Performing an EIS measurement in potentiometric mode means applying a sinusoidal potential to a system placed at a fixed potential and analysing its response, in form of impedance, over an extended range of frequencies. The modulus of the imposed signal must be small enough, usually within 10 mV, so that the relationship between the current (I) and the potential (E) can be considered linear. In response to the sinusoidal input potential, E(t), the current response, I(t), will also have a similar pattern; impedance (Z) is defined as the ratio E(t)/I(t). In general, impedance is a physical quantity related to all factors that hinder and limit the passage of current in the system. In the case of batteries, there are numerous components that oppose the passage of current, such as: (i) resistance to charge transport in the electrolyte solution; (ii) diffusion at the electrode of the ion moving in the electrolyte; (iii) capacitance of the double layer formed at the electrode-electrolyte interface; (iv) the resistance of the electrolyte to the charge transporting ion, formed at the electrode-electrolyte interface; iv) the electrolyte's own resistance. The major advantage of this technique is that it allows all these contributions to be separated and analysed from the complex impedance value obtained. To do this, one must imagine the electrochemical system as if it was an electrical circuit consisting of various elements, such as resistors (R) and capacitors (C). The crucial step in EIS measurements consists in modelling the examined electrochemical system in an electrical circuit (known as an ideal equivalent circuit), which must provide a simulated impedance spectrum very similar to that experimentally obtained. The spectra are collected over a wide range of frequencies, usually between 0.1 Hz and 10^4 Hz, as some contributions are visible only at certain frequencies. Inductance contributions cannot be modelled as a simple combination of R and C, and for this reason are known as distributed elements of the equivalent circuit; of these, the most important are the Warburg impedance (W) and the constant phase element (CPE). The Warburg element describes diffusion phenomena to and from the electrode surface and is particularly evident at low frequencies. The CPE element, on the other hand, takes into account the nonideality of the electrodes used. There are several ways to visualise impedance spectra; the most common method is the so-called Nyquist

diagram (as reported in Figure 2.1), in which the real Z' (*x* axis) and imaginary - Z" (*y* axis) components of the impedance are plotted. In this type of graph, it is important to remember that the frequency increases from right to left.
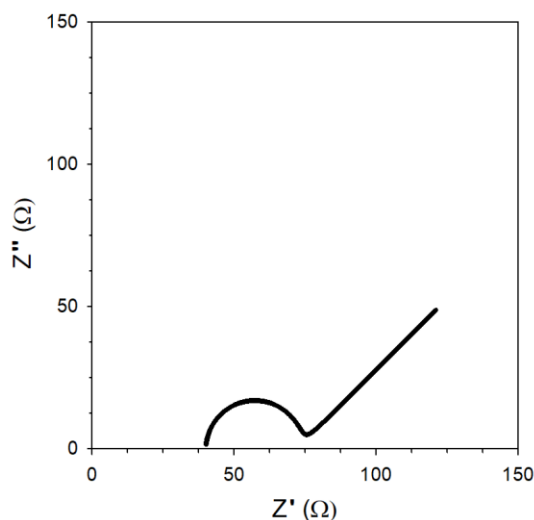
Figure 2.1. Example of Nyquist plot of an EIS spectrum.

The semicircle describes an electronic transfer phenomenon with control over the transfer of matter and charge; the point of intersection of the semicircle with the *x* axis at higher frequencies can be correlated to the ohmic resistance of the electrolyte solution (R_{el}); the point of intersection at lower frequencies, on the other hand, can be easily related to the value of the charge transfer resistance (R_{ct}) at the electrode-electrolyte interface. The 45° straight line is typical of the presence of a Warburg impedance (W).

2.2.2. Galvanostatic Cycling with Potential Limitation (GCPL)

Carrying out galvanostatic cycling means imposing a defined current (both charging and discharging) on the electrochemical system under investigation and recording the potential trend over time. During the charging half-cycle, the voltage of the half-cell increases to a maximum value, V_{max}, and then immediately changes direction of the current and begins the discharge phase, which continues until a minimum value, V_{min}, is reached. These two threshold values are appropriately defined according to the type of electrode to be

investigated (anode or cathode) and its elemental composition. Depending on the potential at which the main redox phenomena occur for each different element in the material, the working potential range is adjusted so that all electrochemically active elements contribute to the specific capacity of the investigated electrodes. From the analysis of the charge-discharge curves obtained, important considerations can be deduced regarding the working mechanism, the reversibility of redox phenomena, Coulombic efficiency, structural stability, and the specific capacitance achieved by the electrode materials at different current values. Measurements performed at different C rates are very significant, as they allow to assess changes in specific capacitance values by varying the charge-discharge rate as a function of the imposed current density. In this regard, so-called rate capability graphs are very common, thanks to it is possible to observe the development of capacitances at different currents. Usually, the early cycles are carried out at slow C rates to allow the material to stabilise; subsequently, the scan rate is gradually increased to also facilitate the study of electrochemical performance under extreme conditions. Finally, to further verify the structural stability of the material and the good reversibility of the electrochemical processes, one or more recovery scans are carried out at C rate intermediate corresponding to moderate current density.

2.2.2.1. Specific Capacity, Theoretical Capacity, and C rate

The term specific capacity represents the maximum gravimetric charge achieved by the electrode in each half-cycle (either in charge or discharge). Concerning the theoretical capacity (Q_T) is the maximum specific capacity that could be obtained as a function of the amount of active material and given a certain number of electrons involved in its reaction. It can be calculated as follows:

$$Q_T = \frac{nF}{3.6M_w}$$

where, n is the number of electrons involved in electrochemical processes, F is the Faraday constant ($\sim$96485 C mol^{-1}), M_w is the molecular weight of the active material and *3.6* is a factor required to convert the number in mAh g^{-1}, traditionally used as a unit of measurement to express capacity in storage systems. Another common term for electrochemical devices

is the C rate. A half-cycle at nC rate means a charging or discharging process corresponding to a sufficiently current to charge/discharge the entire active mass in n hours.

2.2.3. Potentiodynamic Cycling with Galvanostatic Acceleration (PCGA)

Potentiodynamic cycling with galvanostatic acceleration is a widely used technique for the electrochemical characterisation of electrode materials, as it allows the detailed evaluation of the intensity contribution to the total specific capacitance and reversibility of all redox phenomena occurring at the electrode during the charge-discharge cycles. The potential is varied between two extremes V_{min} and V_{max} by means of small potential pulses (typically 5 mV). The potential is maintained for some time until the recorded current falls below a threshold value; following this fall a new pulse is generated until the threshold potential value is reached. Subsequently, it is necessary to calculate the differential capacitance of the material under test, defined as the derivative of the specific capacitance with respect to the potential (dQ/dV) and expressed in mA g^{-1} V^{-1}. From the resulting graph of dQ/dV *vs.* V it is possible to observe curves with maxima of different intensities and shapes depending on the phenomena they represent, at discrete potentials. Also, from the analysis of the shape and position of these peaks, important considerations can be made regarding the working mechanism of electrode materials. Depending on their intensity, the amount of electronic charge involved in each of the observed phenomena can also be calculated. The information that can be deduced from these graphs is the same that can be deduced from GCPLs but enjoys considerably greater precision and sensitivity because it is obtained with a potential scan that is less affected by noise from various contributions, albeit slightly, the data obtained. For example, by means of PCGA, redox processes occurring at neighbouring potentials can be easily separated and thus, in a GCPL, superimposed and contained in the same plateau.

2.3. Synchrotron Light Source

The use of synchrotron light to study the chemical and physical properties of matter has revolutionised material science research. Synchrotron Radiation (SR) is a highly energetic electromagnetic radiation emitted by electrons moving at very high speeds along a circular orbit. The energy of this radiation makes it possible to analyse wavelengths from the so-called Hard X-rays to the near UV. The facilities in which synchrotron radiation is produced consist of three main components: (i) linear particle accelerator, which ensures the transfer of the electrons produced by the cathode ray tubes to the acceleration ring; ii) synchrotron (acceleration ring), with a diameter of tens of metres, where the electrons are accelerated to energies in the order of GeV, by means of a magnetic field; iii) storage ring, with a diameter of hundreds of metres, where the electrons circulate at a speed close to the speed of light while maintaining the same energy. Inside the storage ring, the electrons are deflected by powerful magnets. Upon interaction with these elements, the charged particles lose part of their energy in the form of (synchrotron) light, which will later be used to conduct experiments in appropriate beamlines tangent to the ring. This loss of energy is periodically compensated by the introduction of new electronic charges into the storage ring. The entire production, acceleration and storage system is maintained in a high vacuum condition, which allows measurements to be made with no or little significant background noise.[1] The main characteristics of synchrotron light are:

- Significantly higher intensity than laboratory X-ray sources (more than 10^{15} orders of magnitude);
- high collimation;
- continuous emission spectrum, unlike laboratory sources where there is emission only at the wavelength of the metal used as the electron source;
- high polarisation;
- space- and time-resolved structure.

Specifically, in the field of batteries through synchrotron light source, it is possible to carry out both *ex-situ* and *operando* analyses by coupling electrochemical and physical-structural characterisation. Thus, being able to assess the development of phenomena in active materials upon cycling by means of X-ray diffraction (XRD) and X-ray absorption spectroscopy (XAS).

2.3.1. X-Ray Diffraction (XRD)

In order to increase the intensity of the X-rays produced when the synchrotron light is deflected by the bending magnets in the storage ring, so-called Insertion Devices (Wigglers or ripple magnets) are introduced into the straight sections of the ring. Wigglers produce a continuous emission spectrum, whereas undulators generate a discontinuous spectrum but with higher intensity. Now most synchrotrons exclusively use a silicon photomultiplier detector for diffracted photons. The most important parameter for assessing the intensity of the X-photons produced is the luminance, defined as the number of photons emitted by an X-ray source at a specific wavelength and taking into account the collimation of the beam. Synchrotron light has more than 10^{10} times the brilliance of common laboratory X-ray sources.

2.3.2. X-Ray Absorption Spectroscopy (XAS)

X-ray absorption spectroscopy (XAS) is a structural analysis technique based on evaluating the variation of the absorption coefficient (μ) as a function of the radiation energy used (X-rays). Since it requires a highly energetic X-ray photon beam with a particular geometry, measurements conducted with this technique can only be carried out using synchrotron radiation. During an XAS experiment, the beam energy is varied in a range between -200 eV and +800 eV with respect to the absorption energy of the element whose structural and electronic evolution is to be monitored. This energy range can be divided into three regions, from which important information can be derived:

- pre-edge zone, down to -20 eV relative to threshold energy;
- XANES (X-ray absorption near edge structure), from -20 eV to +30 eV relative to the absorption threshold. By analysing this region, it is possible to obtain information about the coordination geometry, oxidation state and electronic configuration of the elements under investigation;
- EXAFS (extended X-ray absorption spectroscopy fine structure), from +30 eV onwards. By studying the trend of μ in this region, it is possible to assess the bonding distances present between the element under investigation and its respective first neighbours.

The EXAFS analysis requires a lot of data manipulation but also guarantees quantitative results. Regarding XANES, on the other hand, it is very difficult to make a quantitative determination from the spectra; the analysis is carried out by comparing the experimental spectra with others collected on standard or previously characterised materials. In electrochemistry, XAS is also widely used to assess the change in the oxidation state of elements in electrode materials.

2.4. Bibliography

1. Saisho, H.; Gohshi, Y. Application of Synchrotron Radiation to Materials Analysis. 1996.

Chapter 3:
Lithiation Mechanism in High-Entropy Oxides as Anode Materials for Li-Ion Batteries

3.1. Abstract

High-entropy oxides based on transition metals, such as $Mg_{0.2}Co_{0.2}Ni_{0.2}Cu_{0.2}Zn_{0.2}O$ (TM-HEO), have recently drawn special attention as potential anodes in lithium-ion batteries due to high specific capacity and cycling reversibility. However, the lithiation/delithiation mechanism of such systems is still controversial and not clearly addressed. Here, we report on an *operando* XAS investigation into TM-HEO-based anodes for lithium-ion cells during the first lithiation/delithiation cycle. This material showed a high specific capacity exceeding 600 mAh g^{-1} at 0.1C and Coulombic efficiency very close to unity. The combination of functional and advanced spectroscopic studies revealed complex charging mechanisms, developing through the reduction of transition-metal (TM) cations, which triggers the conversion reaction below 1.0 V. The conversion is irreversible and incomplete, leading to the final collapse of the HEO rock-salt structure. Other redox processes are therefore discussed and called to account for the observed cycling behaviour of the TM-HEO-based anode. Despite the irreversible phenomena, the HEO cubic structure remains intact for ~60% of lithiation capacity, so proving the beneficial role of the configuration entropy in enhancing the stability of the HEO rock-salt structure during the redox phenomena.

3.2. Introduction

Lithium metal is an ideal anode for the next-generation Li-ion batteries (LIBs) due to the highest theoretical capacity and lowest electrochemical potential among all of the possible candidate materials.[1] Unfortunately, the safety risk is still a critical issue for practical applications, despite huge progress has been recently made to stabilize the Li-metal anode, thanks to new chemical strategies, advanced investigation tools, and nanotechnology approaches.[1,2] The request for active systems as anode alternatives to Li is, therefore, strongly compelling. The first commercial choice was graphite. However, its low theoretical capacity (372 mAh g^{-1}) and unsafe charging profile at high current densities promoted the

search for alternative negative electrodes. Different innovative materials were consequently proposed in the literature with better electrochemical properties in terms of both potential and capacity, such as graphene,[3] silicon-based systems,[4,5] including Si/C composites,[6] and a huge family of metal oxides and oxysalts,[7] typically nanostructured.[8] As known, research on advanced anodes for LIBs is focused on materials that are electrochemically active through three different mechanisms:[7] (i) intercalation-deintercalation mechanism based on transition-metal (TM) oxides and other compounds with a 2D layered or 3D network structure, where Li can reversibly intercalate without any crystal structure collapse; (ii) metals than can form alloys/intermetallic compounds with Li, whose alloying/dealloying reactions are responsible for the reversible capacity during Li cycling; (iii) conversion mechanism, applicable to TM oxides, fluorides, oxyfluorides, sulfides, etc., which react with Li to give the corresponding reduced metals and Li_2O. Lithium oxide can easily decompose to form metal and oxygen only if the TM oxide is nanosized, thus giving rise to Li cycling and large and reversible capacity at suitable potentials. Very recently, an emerging class of materials is catching on based on the concept of multiple principal elements in equimolar or near-equimolar ratios, whose design can stabilize a single-phase structure of solid solutions by means of rigorous control of the configurational entropy (S_{config}). These kinds of materials, known as high-entropy materials (HEMs), may be properly designed with tailorable properties (for instance, mechanical, thermal, magnetic, dielectric), making them potentially suitable for a wide spectrum of technologies.[9] The high-entropy concept has been first applied to nanostructured alloys[9] and, more recently, also to other systems, like oxides, where up to five cations can be introduced to occupy the same Wyckoff position of the same crystal structure, thus increasing S_{config}.[10] The pioneering system an equimolar solid solution of MgO, CoO, NiO, CuO, and ZnO, yielding the $Mg_{0.2}Co_{0.2}Ni_{0.2}Cu_{0.2}Zn_{0.2}O$ compound with the rock-salt structure,[10] labelled in the following as TM-HEO, transition-metal high-entropy oxide. It was recently shown that not only cation but also anion stoichiometry could be modulated to preserve the rock-salt structure of TM-HEO. Multi-anionic and multi-cationic high-entropy oxyhalides were synthesized by introducing an additional halide (X = F, Cl) into the HEO rock-salt structure, where only oxygen ions occupy the anion site, without any drastic strain. The presence of F^- or Cl^- must be charge compensated by a monovalent cation M^+, as Li^+ or Na^+, to give $M_x(Mg_{0.2}Co_{0.2}Ni_{0.2}Cu_{0.2}Zn_{0.2})OF_x$.[11] Inspired by the well-known electrochemistry of the binary oxides MO (M = Mn, Fe, Co, Ni, Cu), TM-HEO was recently explored as a novel anode material for LIBs. In principle, it was found that entropy

stabilization positively affects the capacity retention of the multicomponent oxide,[12,13] leading to increased cycling stability than the individual MO.[14] Indeed, high process reversibility and long-term cyclability over 900 cycles with a specific capacity higher than 650 mAh g^{-1} were observed in half-cells including conventional liquid electrolytes and microsized HEO as an anode. Such promising performances are evident only if all TMs are present in the structure. Conversely, significant cell failures are observed if one element is removed, especially Co.[14] By considering that TM-HEO contains metal oxides in the rock-salt structure, it plausible to suppose that the mechanism involved during the Li storage and cyclability is the conversion reaction of some of the cations (*e.g.*, Co^{2+}, Ni^{2+}, Cu^{2+}): MO + $2Li^+ + 2e^- \rightarrow$ M + Li_2O. The other cations, as Mg^{2+}, acts as a kind of matrix, stabilizing the rock-salt phase and maintaining intact the structure during the redox process. However, the role of Mg^{2+} in preserving the HEO structure has been explained by considering Mg electrochemically inactive in the given potential window.[13] On the other hand, it should be recalled that a large fraction of Li^+ ions can be easily inserted mostly for two reasons: (i) defects, likely oxygen vacancies, and (ii) charge compensation in the system, achieved through the oxidation of some elements, for instance, Co^{2+} to Co^{3+}.[15] Despite these promising results, the reaction mechanism of TM-HEO as an anode for LIBs is not fully addressed, especially for what concerns the reversibility of the conversion process (decomposition of Li_2O and metal oxidation to TM-HEO). Based on XRD, TEM, and electron diffraction, Sarkar and co-workers recently proposed a lithiation mechanism that significantly differs from the conventional conversion reaction.[13] In that study, it was shown that during the lithiation step, some cations (like Co^{2+} and Cu^{2+}) are reduced to the corresponding metals. This is proved by the gradual disappearance of HEO XRD reflections. However, electron diffraction, performed on the cycled sample, reveals the presence of the rock-salt structure even in the fully lithiated phase, so confirming that other cations, such as Mg^{2+}, stabilize the cubic structure, which is consequently preserved during the electrochemical reaction. The metal nuclei, visible only by SAED due to their sizes smaller than the X-ray coherence length, grow inside the rock-salt structure, introducing defects that suppress the long-range order. The trapped metals can easily diffuse back during the oxidation step to restore the HEO structure after delithiation. However, the final XRD pattern is that of an amorphous system, with no HEO reflection evident after the first lithiation cycle. The presence of the rock-salt structure throughout the conversion mechanism is evident, in fact, only by SAED.[13] However, this is not definitive proof that such a structure could be specifically referred to HEO rather than a single binary oxide such as MgO, CoO, or NiO, all of them having the

same rock-salt crystal structure. In summary, it was concluded that in the conversion reaction of TM-HEO, Mg^{2+} ions contribute to stabilize the phase, whereas the other cations, Co^{2+}, Ni^{2+}, Zn^{2+}, and Cu^{2+}, are responsible for the reversible capacity.[16] Considering the promising functional properties of HEOs in LIBs, a deeper insight into the structural and electronic evolution of the cubic high-entropy oxide during the electrochemical process is fundamental to better clarify the reaction mechanism and to further optimize the system, in terms of structure and composition. A lack of translational order in the products of the conversion reaction asks for the application of a short-range probe. In this respect, X-ray absorption spectroscopy (XAS) is the selection tool, as it is sensitive to the local chemical environment of atoms in terms of both neighbouring and electronic structures (oxidation state). In addition, hard X-rays have a quite large penetration depth in the matter, rendering *in situ* and *operando* experiments possible. Herein, by applying *ex situ* and *in operando* XAS by X-ray absorption near-edge structure (XANES) at the Co, Ni, and Cu K-edges, we investigated the electronic and local structure evolution on the $Mg_{0.2}Co_{0.2}Ni_{0.2}Cu_{0.2}Zn_{0.2}O$ anode in LIBs to detail the reaction mechanism. Our results demonstrate, for the first time to our knowledge, that the lithiation in TM-HEO is irreversible and involves a reactive path where the TMs reduce in sequence to the metallic state: the residual reversible capacity is given by an alloying-dealloying mechanism involving Zn and Mg; we believe that such understanding can advance the development of high-performance HEOs electrodes for Li^+- and Na^+-ion batteries.

3.3. Material and Methods

3.3.1. Synthesis of $(Mg_{0.2}Co_{0.2}Ni_{0.2}Cu_{0.2}Zn_{0.2})O$

$(Mg_{0.2}Co_{0.2}Ni_{0.2}Cu_{0.2}Zn_{0.2})O$ (TM-HEO) was synthesized by a conventional solid-state reaction starting from the commercial metal oxides (MgO, ZnO, CuO, NiO, CoO; Sigma-Aldrich). The starting materials were mixed in the proper stoichiometry and subsequently treated at 1000°C for 6 h, after a temperature ramp of 10°C min^{-1} then cooled to room temperature.

3.3.2. Structural and Morphological Characterization

Powder X-ray diffraction was carried out by using a D8 Advance diffractometer (Bruker). scanning electron microscopy (SEM) and energy-dispersive X-ray spectroscopy (EDX) were performed using a Tescan Mira3XMU microscope operated at 20 kV and equipped with an EDAX EDS analysis system. The samples were coated with a carbon thin film using a Cressington 208 carbon coater.

3.3.3. Anode Preparation and Cell Assembly

The anode slurry was prepared using 70 wt% active material (TM-HEO), 20 wt% conductive carbon black (Timcal-Imerys, Super C65), and 10 wt% binder (poly(vinylidene fluoride), PVdF). The solid content of all slurries was kept between 26 and 28 wt%. HEO and carbon were initially mixed in zirconia jars by a planetary ball mill at 150 rpm for 10 min, followed by a 5 min break and another 10 min of milling in the reverse direction.

Subsequently, it was dispersed in the PVdF solution in N-methylpyrrolidone (NMP) to obtain the slurry, which was cast on a copper foil using a doctor blade with a wet thickness of 100 μm. The anode was finally dried under vacuum at 80°C before the cell assembly.

The same experimental protocol was used to prepare the anodes based on the systems (CoCuMgNi)O and (CoCuNiZn)O. A similar procedure was finally followed to assemble the cell for the *operando* investigation, except for the current collector. In this case, carbon cloth was used instead of copper foil to avoid any interference of Cu from the collector in the XAS spectra. The resulting mass loadings were 1.6 and 7.5 mg cm^{-2} for the Cu-based and carbon cloth-based cells, respectively. Round disc electrodes with 10 mm diameter were cut and dried at 100°C in vacuum for 12 h. All electrochemical measurements were performed in a Swagelok-type three-electrode cell assembled in an Ar-filled glovebox (H_2O and $O_2 < 0.1$ ppm). Metallic Li was used as both reference and counter electrodes. Electrodes were separated with a Whatman glass fiber separator, imbibed by the liquid electrolyte consisting of 1 M $LiPF_6$ solution in ethylene carbonate−dimethyl carbonate (EC:DMC, 50:50 vol%) (200 μL).

3.3.4. Electrochemical Characterization

The electric conductivity of $Mg_{0.2}Co_{0.2}Ni_{0.2}Cu_{0.2}Zn_{0.2}O$ and the four-cation compositions was measured by means of electrochemical impedance spectroscopy on sintered pellets between 100 kHz and 1 Hz at 50 mV amplitude in the temperature range 60-900°C. For what concern the electrochemical performance of the realized active materials, HEO | LP30 | Li$_{(m)}$ configuration cells were galvanostatically cycled using a battery tester from 3.00 to 0.01 V (BioLogic BCS-810). A theoretical capacity of 900 mAh g^{-1} was considered, in agreement with what is typically adopted in the literature for similar TM-HEO-based anodes.[13] The cyclic voltammograms were measured using an electrochemical interface (Solartron 1287) at a scan rate of 0.2 mV s^{-1}. All potentials reported refer to the Li$^+$/Li couple. Two cells were assembled for each system (TM-HEO, (CoCuMgNi)O and (CoCuNiZn)O) and analyzed simultaneously to check the measurement reproducibility. Electrochemical impedance spectroscopy was performed to determine the bulk conductivity of the active materials and the measurement of cell impedance. Nyquist plots were collected in the frequency range between 1 kHz and 0.1 Hz and a voltage amplitude of 50 mV.

3.3.5. *Ex Situ* and *In Operando* and X-Ray Absorption Spectroscopy Measurements

Ex situ XAS experiments were carried out on HEO | 1.0 M LiPF$_6$ EC:DMC (50:50 vol%) | Li$_{(m)}$, frozen at three different potentials, 0.7, 1.9 (in the cathodic branch), and 2.2 V (in the anodic one), corresponding to the main CV peaks. Before measurements, the cells were disassembled and the anode was isolated, washed with ethanol, and dried. Subsequently, the Cu current collector was removed, and the electrode powder was mixed with cellulose (at a ratio of 20:1 cellulose/powder) and finally pressed at 5 ton for 1 min to obtain compact pellets. XAS data were acquired on B18, the Core XAS beamline at Diamond Light Source. Radiation from the bending magnet source was collimated and partially focused with Pt-coated Si mirrors to obtain a beam footprint on the sample of approximately 1×1 mm^2. A double-crystal monochromator was equipped with Si(111) crystals, and higher-order harmonics were removed with the insertion of Pt-coated harmonics rejection mirrors placed at 7 mrad to the incoming beam direction. This setup, with Diamond Light Source operating at 3 GeV and 300 mA, provides ~5×10^{11} monochromatic X-ray photons/s on the sample

with resolution $\Delta E/E$ close to the nominal value for Si(111) of 1.4×10^{-4}. XAS spectra were acquired in the continuous scan mode, with acquisition intervals of 0.25 eV over a range of 1000 eV across the K absorption edges of Co, Ni, and Cu. Several continuous scans of durations of approximately 3 min each were acquired and averaged. Data were acquired in the transmission mode, with three ionization chambers partially filled with 170 mbar (N_2) and 270 mbar (Ar) for the first, second, and third chambers, with pressures adjusted to absorb approximately 10 and 70% of the beam intensity at the Co K-edge. Beam energy calibration was ensured through the simultaneous acquisition of XAS spectra from metal foils of the same elements, inserted between the second and third acquisition chambers. The *operando* XANES spectra were measured at the XAFS beamline operating at the Elettra synchrotron radiation facility in Trieste, Italy. The spectra were acquired at room temperature at the Co, Ni, and Cu K-edges using a silicon drift detector in the fluorescence mode. The ring current and energy were 200 mA and 2.4 GeV, respectively. A Si(111) double-crystal monochromator was used ensuring high-order harmonic rejection by detuning the second crystal. A water-cooled, Pt-coated silicon mirror was used to obtain vertical collimation of the beam. Spectra at the end of the charging process were also collected at the Zn K-edge, in the same experimental conditions. EXAFS spectra of the pristine sample were also collected at the Co, Ni, Cu, and Zn K-edges in the transmission mode. To this aim, an appropriate amount of sample to give one absorption jump in logarithmic units at each of the edges was weighted and thoroughly mixed with cellulose in an agate mortar and pestle and then pressed to pellets. The EXAFS spectra were extracted from the raw data by the Athena code.[18] The operando electrochemical cell was an ECC-Opto-Std test cell (EL-CELL) equipped with an ECC-Opto Polymide window for X-ray experiments. XAS spectra were coupled to electrochemical measurements by the following protocol: (1) GITT performed at a constant current pulse of 1 h and a relaxation time of 10 min, (2) potential electrochemical impedance spectroscopy (PEIS) in the frequency range from 10 kHz to 1 Hz with an amplitude of 10 mV, and (3) equilibration at OCV. The XAS spectra were collected during the GITT and equilibration steps. The resulting GITT is reported in Figure 3.1.
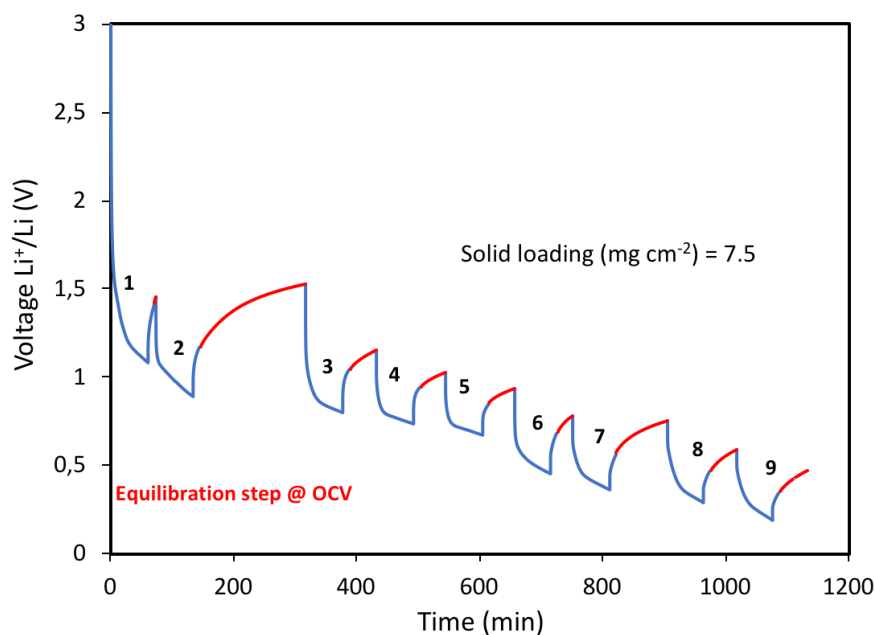
Figure 3.1. GITT plot during the operando XAS experiment.

For the X-ray absorption near-edge structure (XANES) analysis, the spectra were processed by subtracting the smooth pre-edge background fitted with a straight line. The spectra were then normalized at unit absorption at 300 eV above each edge, where the EXAFS oscillations are small enough to be negligible. Linear combination fittings of the *post mortem* XANES spectra were performed by means of the Athena code.[18] A typical fit included more than 200 data points and no more than 2 variables. Successive multivariate curve resolution (MCR) and partial component analysis (PCA) of the whole sets of the operando XAS data[19] confirmed the linear combination fitting results, considering the differences between the two data sets.

3.4. Results

3.4.1. TM-HEO: Morphology, Structure, and Chemical Composition

Highly pure TM-HEO with ~2−5 μm sized particles was produced, as evidenced by the SEM images of Figure 3.2*a*, whose rock-salt structure was confirmed by powder XRD (see Figure 3.2*b*). The EXAFS at the Co, Ni, Cu, and Zn K-edges, reported in Figure 3.2*c*,

suggests that TM-HEO is also homogeneous concerning the chemical composition. The spectra show impressive similarities for all of the four cations (see below for experimental details) and appear extremely similar to those reported by *Rost et al.*[10] Taking into account that EXAFS is sensitive to the radial distribution function around the photo-absorber, this result confirms that the local chemical environment of Co, Ni, Cu, and Zn is very similar.

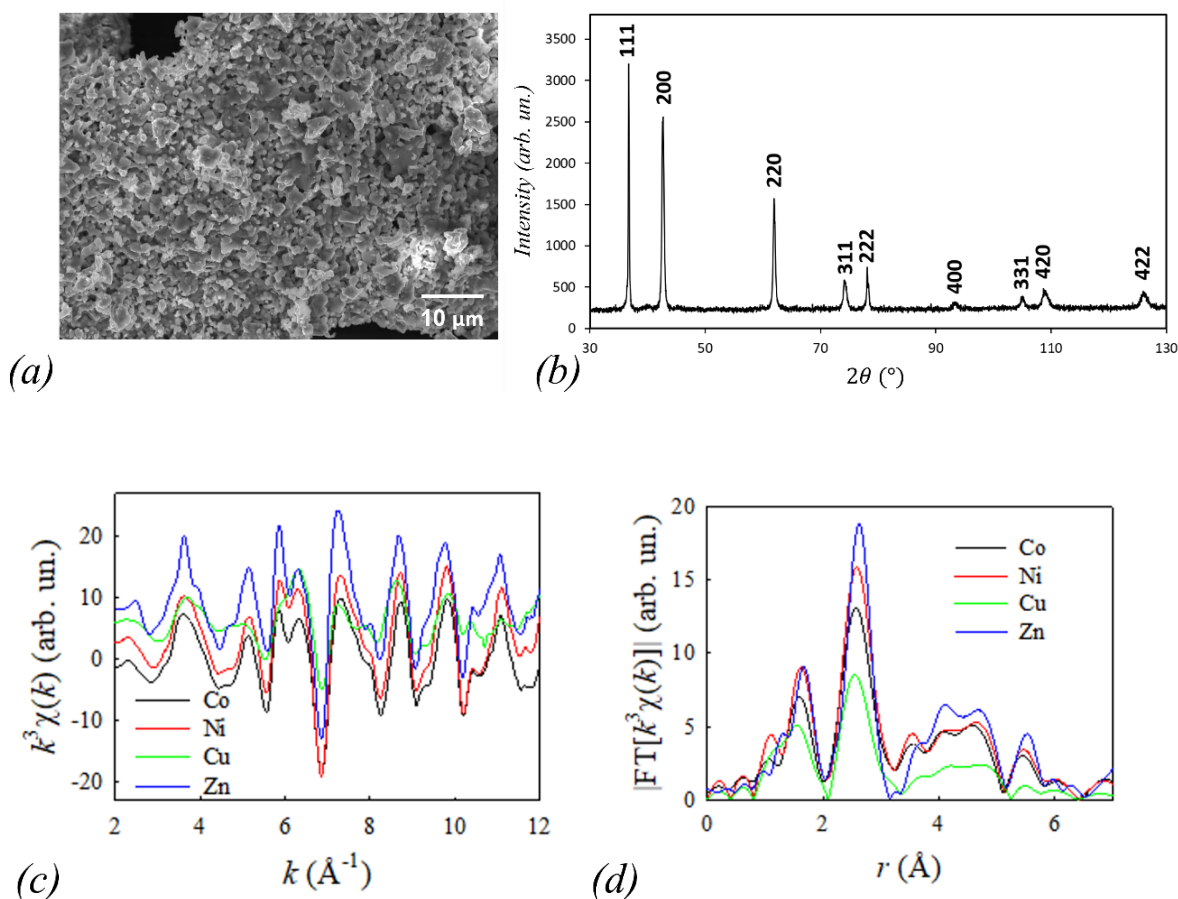***Figure 3.2***. *(a) SEM image of the pristine TM-HEO sample prepared via solid state reaction. (b) XRD pattern of the pristine TM-HEO synthetized via solid state reaction. (c) EXAFS spectra at the Co, Ni, Cu and Zn K-edges of the pristine TM-HEO sample prepared via solid state reaction and (d) the corresponding Fourier Transforms are shown. For the sake of better clarity, the EXAFS spectra have been shifted along the y axis.*

3.4.2. Electrochemical Performance

The resulting Arrhenius plots for the electric conductivity of $Mg_{0.2}Co_{0.2}Ni_{0.2}Cu_{0.2}Zn_{0.2}O$ and the four-cation compositions measured by means of electrochemical impedance spectroscopy are reported in Figure 3.3.
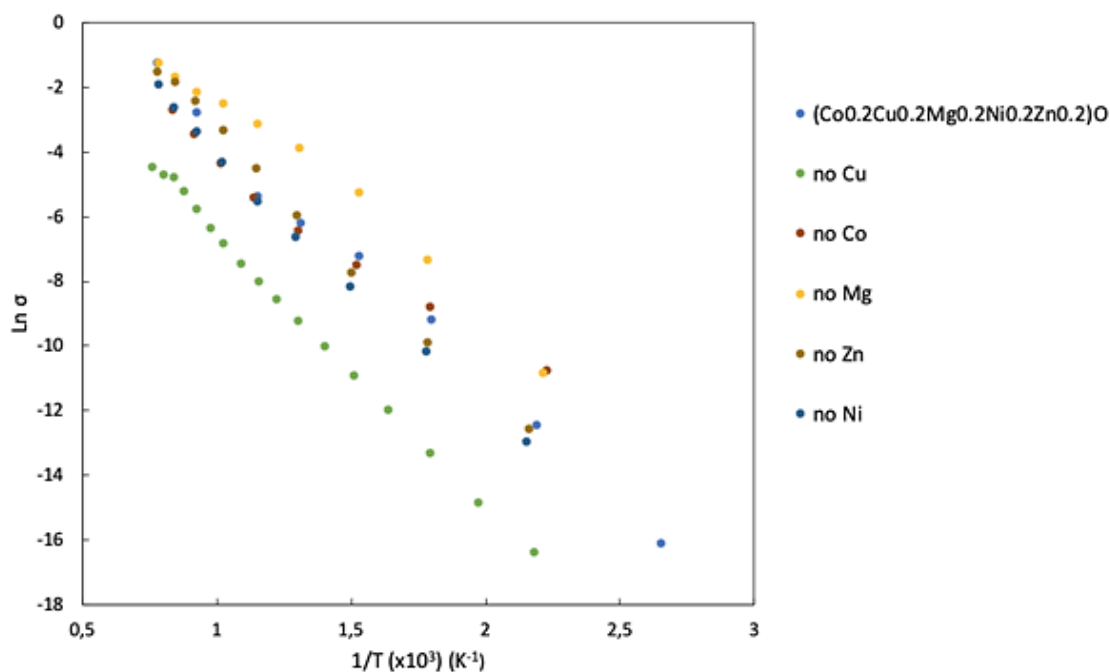

Figure 3.3. Conductivity behaviour vs 1/T for TM-HEO and the 4-cations based systems. The measurement uncertainty is below 5%.

As noticeable from the graphs, conductivities of about 10^{-7} S cm^{-1} are obtained at 60°C for both the high (five cations) and medium (four cations) entropy oxides. These values exceed what is generally observed in the literature for pure NiO and CoO oxides and feel the positive combining effects already observed in the literature in the case of mixed crystals of NiO−CoO mixtures, in a molar composition of at least 25:75 mol %.[17] The electrochemical performance of $Mg_{0.2}Co_{0.2}Ni_{0.2}Cu_{0.2}Zn_{0.2}O$ as the anode in Li-ion cells was studied using metallic Li as the counter electrode. Figure 3.4*a* shows the cyclic voltammetry plots of TM-HEO by sweeping the voltage from 0.01 to 3.0 V vs Li$^+$/Li at a scan rate of 0.2 mV s^{-1}. According to the literature,[7,20–22] the cathodic peaks at a voltage lower than 1.6 V are attributed to the lithiation process with the consequent oxide decomposition to the

44

corresponding metals (like Ni, Co, and Cu) and Li_2O. The intensity of the signal at 0.4 V is significantly reduced under further cycling due to irreversible phenomena during the first lithiation step, such as incomplete Li^+ extraction from Li_2O and the solid electrolyte interphase (SEI) formation. In contrast, two broad and not intense oxidation signals peak at around 0.8 and 1.9 V are notable, which are possibly due to delithiation of Li_2O and consequent phenomena, such as oxidation of M to MO[20–22] and/or Li/M alloying.[7,23]
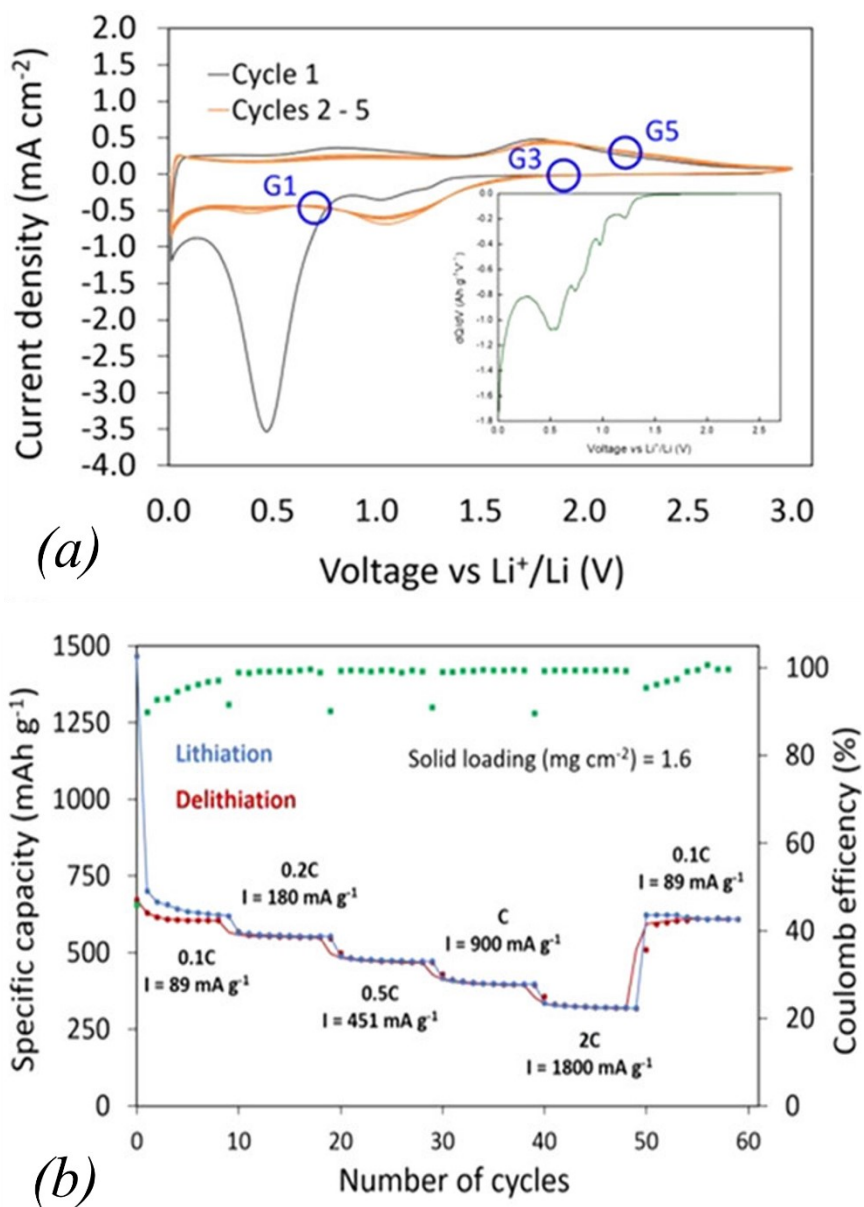
Figure 3.4. Lithiation/delithiation between 0.01 and 3 V of TM-HEO|LiPF$_6$ 1.0M EC:DMC (50:50 vol%)|Li cell in the voltage range 0.01-3 V. (a) Cyclic voltammograms at 0.2 mV s^{-1}. In the inset the differential capacity is reported during the first lithiation step (Points marked with blue circles (Gn) indicate discrete voltage points where anodes were electrochemically frozen for ex situ investigations); (b) galvanostatic cycling at different current density.

In the first cycle, at least three signals between 1.3 and 0.8 V are present, which can be associated with a multistep reaction leading to a Cu^{2+}/Cu^{+} solid solution, to the formation of Cu_2O phase, and to the final decomposition producing metallic Cu.[21,24] Figure 3.4*b* shows the galvanostatic cycling and some voltage discharge-charge profiles at 0.1C of the TM-HEO-Li cell between 0.01 and 3 V vs Li^{+}/Li. The profiles and the related differential capacity plots collected at higher C rates are reported in Figure 3.5*a,b*.
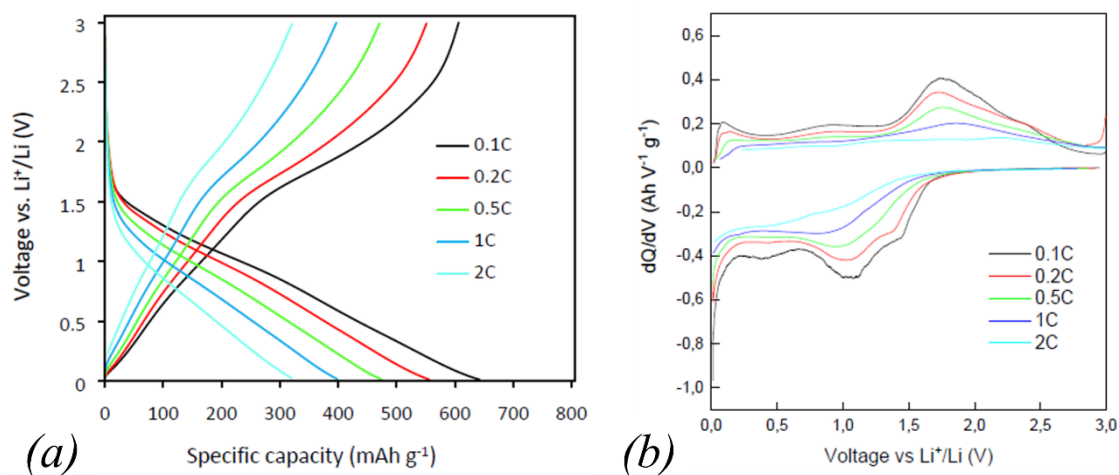

Figure 3.5. *(a) Voltage profile, the lines represent the 5th cycle for each C rate; (b) Differential capacity of the same cycles previously considered.*

Except for the low current region 0.1C (both during the first cycles and at the end of the rate performance experiments), the Coulombic efficiency is very close to 1 and the specific capacity reaches values higher than 300 mAh g^{-1} at 2C, in good agreement with the literature.[13,14] On the other hand, the efficiency increase with the C rate is an expected phenomenon. At low current densities, slow parasitic reactions (*e.g.*, electrolyte consumption in the case of uncomplete SEI) may occur at the expense of the charge. Especially during the first cycles at 0.1C, the delivered capacity is halved during the initial two cycles. Indeed, the first lithiation and delithiation capacities are 1325 and 700 mAh g^{-1}, respectively, with a Coulombic efficiency of about 53% (see Figure 3.6).
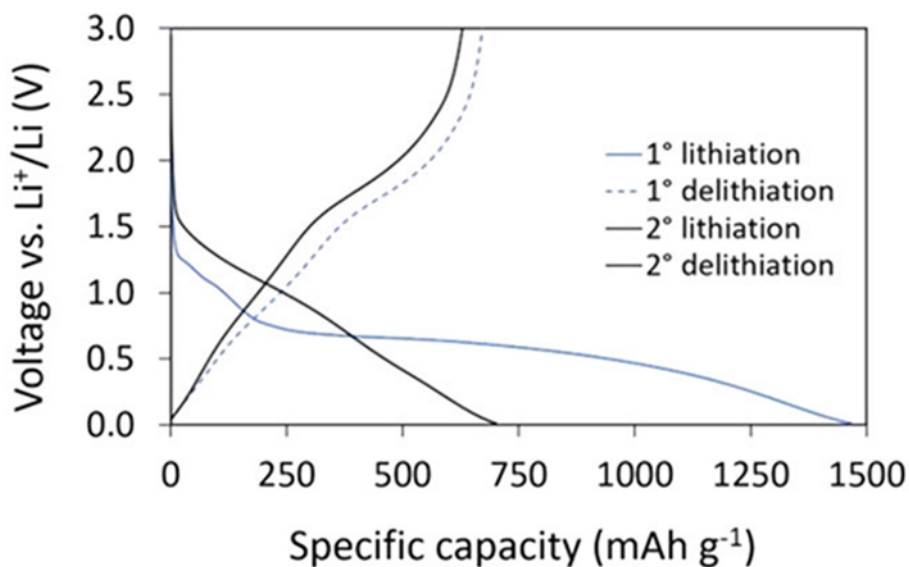
Figure 3.6. *Voltage profiles for the 1ˢᵗ and 2ⁿᵈ cycle.*

This specific value is associated with the formation of an SEI layer and the structural and morphological changes taking place upon (de)lithiation.[25] As observed in the CV plots, the profiles of the second cycle are quite different from those of the first one, with less evident plateaus, suggesting a different reaction mechanism in the case of further cycling.

3.4.3. Spectroscopic Investigation: *In Operando* and *Post Mortem* XAS

Aiming at understanding the actual working mechanisms of $Mg_{0.2}Co_{0.2}Ni_{0.2}Cu_{0.2}Zn_{0.2}O$ TM-HEO as the anode material for Li batteries, we prepared three samples by freezing the HEO-based Li-ion cell at three different voltages (0.7, 1.9, and 2.2 V) during the second lithiation/delithiation cycle (Figure 3.4*a*), two in the cathodic (labelled in the following as G1: Vc = 0.7 and G3: Vc = 1.9 V) and one in the anodic (labelled in the following as G5: Va = 2.2 V) sides, respectively: the potential position of these samples is highlighted with blue circles in Figure 3.4*a*. Such values are the end voltages of the main peaks observed in the cyclic voltammograms and were chosen to identify which ion in $Mg_{0.2}Co_{0.2}Ni_{0.2}Cu_{0.2}Zn_{0.2}O$ is involved in the reduction/oxidation processes. Such three samples were, in fact, subsequently investigated *ex situ* by XAS at the Co, Ni, and Cu K-edges. The application of a local probe such as XAS was dictated by the lack of crystalline order found at the end of the lithiation process; we choose to investigate the Co, Ni, and Cu

K-edges since, according to the standard reduction potentials, these metals are more easily reducible than Zn and Mg and therefore are more likely to participate in the early stages of the lithiation process. In addition, as noted above, the signals in the CV between 1.3 and 0.8 V were assigned to a multistep reduction involving Cu, and this needed further investigation. Further evidence is provided by Figure 3.7 where an XRD pattern of the $Mg_{0.2}Co_{0.2}Ni_{0.2}Cu_{0.2}Zn_{0.2}O$ anode material at the end of the process is shown.
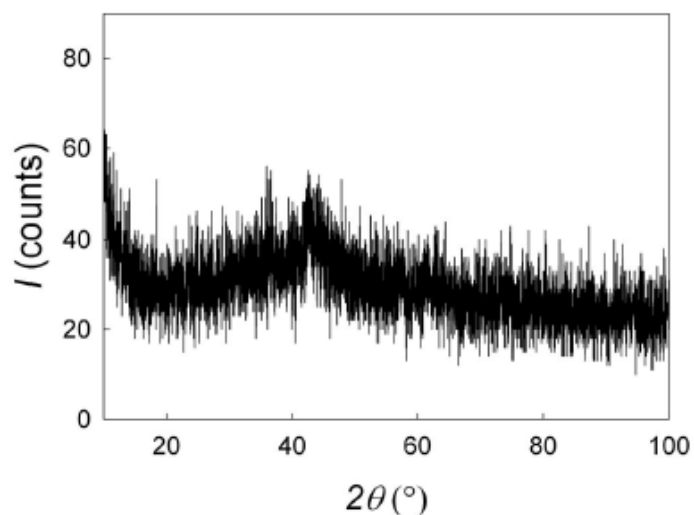
Figure 3.7. *Post-mortem XRD pattern on the TM-HEO based anode after galvanostatic cycling. The diffraction peak around 42° corresponds to the more intense peak of fcc metals and NaCl structure.*

The pattern shows no clear diffraction effects, thus demonstrating that the lithiation process produces an amorphous material. Figure 3.8*a,c,e* shows the XANES spectra of the G1, G3, and G5 samples at the Co, Ni, and Cu K-edges, respectively.
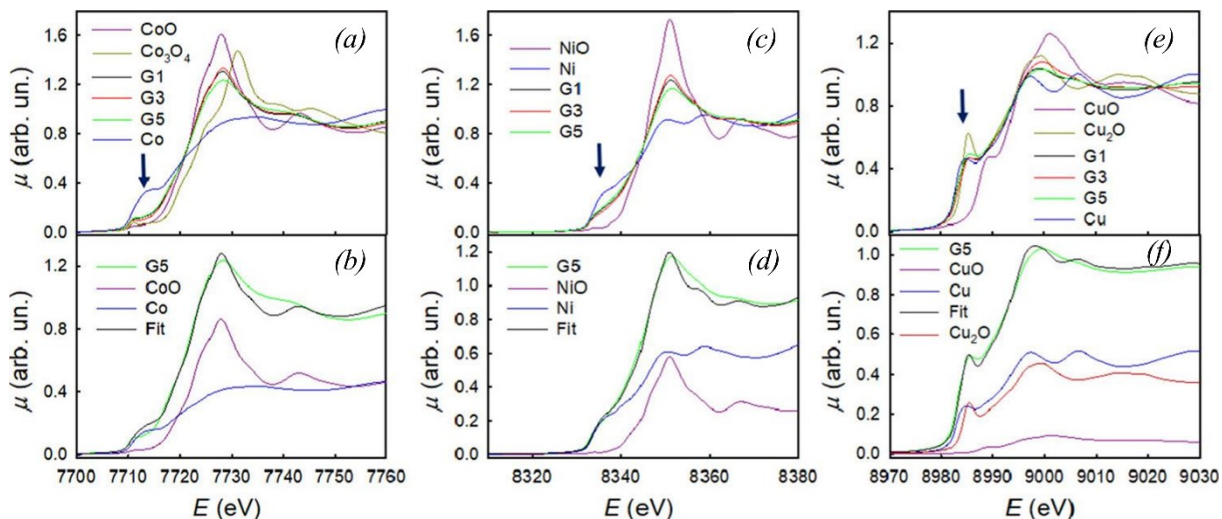
Figure 3.8. *Co K-edge, Ni K-edge and Cu K-edge XANES spectra for sample G1, G3 and G5 (**a**, **c** and **e**). The spectra of Co, Ni and Cu oxides, as well as of Co, Ni and Cu metals, are also shown for reference: the blue arrows mark the position of the metal shoulders on each of the absorption edges. **b**, **d** and **f** show the fits of the spectra of the G5 sample at the Co K, Ni K and Cu K-edges, respectively, with linear combinations of the spectra of the reference compounds, that are also shown in the figure weighted by the coefficients of the linear combinations.*

The spectra of CoO, NiO, CuO, and Cu_2O standards are also shown for comparison, along with the spectra of metallic Co, Ni, and Cu. For each element, the edge energy position is determined by the binding energy of the 1s electrons, which in turn is controlled by the Coulombic potential. This can be screened by the outer (valence) electrons: as a result, the edge shifts at higher energies with increasing oxidation state. At the Co K-edge, the edge energy position of all samples is similar to that of CoO. However, for all of the samples, a tail at lower energy appears. This is at the same energy position of the hump at 7712 eV in the spectrum of metallic Co. In transition metals, this structure is due to the excitation of 1s core electrons to empty states in the conduction band. Looking at the Ni K-edge spectra, quite similar results are found: the edge energy position of all of the samples closely matches that of NiO, but a large spectral intensity is found in the hump region at *ca.* 8335 eV of Ni metal. In this case, this additional spectral intensity is larger than that found at the Co K-edge. At the Cu K-edge, the spectra of all of the samples are in an energy position that closely resembles that of Cu_2O; however, also, in this case, some further spectral intensity is found in the spectral region at *ca.* 8982 eV, where metallic Cu has its first maximum. These results point toward the presence of Co(II), Ni(II), and Cu(I) in all of the samples, together with the presence of Co, Ni, and Cu in a metallic state. This is consistent with the EXAFS spectra and their Fourier transforms shown in Figure 3.9. The presence of both Cu(I) and Cu(0) is in agreement with the equilibrium Cu/O phase diagram.[26]
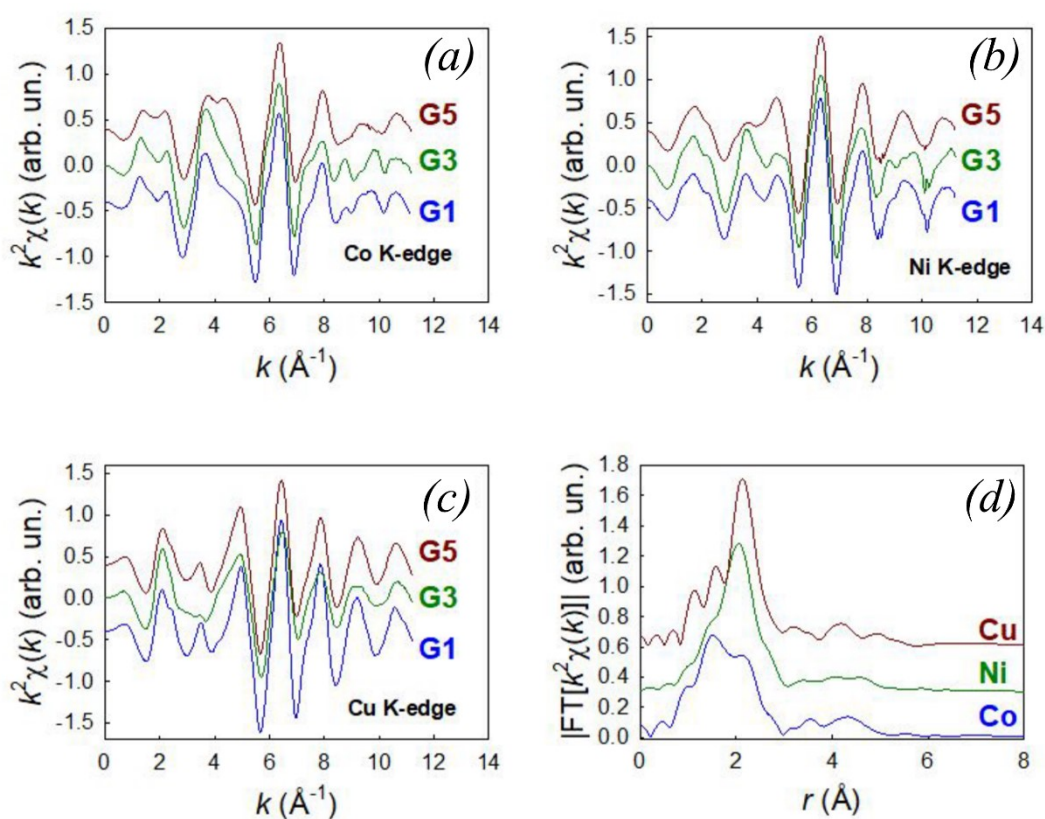
Figure 3.9. *Co K-edge, Ni K-edge and Cu K-edge EXAFS for the G1, G3 and G5 samples (**a**, **b** and **c**, respectively). In **d** the Fourier Transforms of the EXAFS spectra of the G5 sample at all the three edges are compared. Both the EXAFS and FTs were shifted along the y axis for better clarity. The EXAFS spectra at the three edges show impressive similarity in all cases for $k > 4$ Å^{-1}, which is dominated by the scattering by heavy elements. This is reflected by the large peak in all the FTs at ca. 2 Å, which is typical of metallic phases. All this evidence points towards the fact that a large fraction of Co, Ni and Cu is in the metallic state.*

To test this hypothesis, the spectra of the G5 sample, taken as a representative of all of the other samples, were fitted for all of the edges with linear combinations of the spectra of the corresponding metals and oxides. The results are shown in Figure 3.8*b,d,f* for the Co, Ni, and Cu edges, respectively; the results for samples G1 and G3 are shown in Figure 3.10.
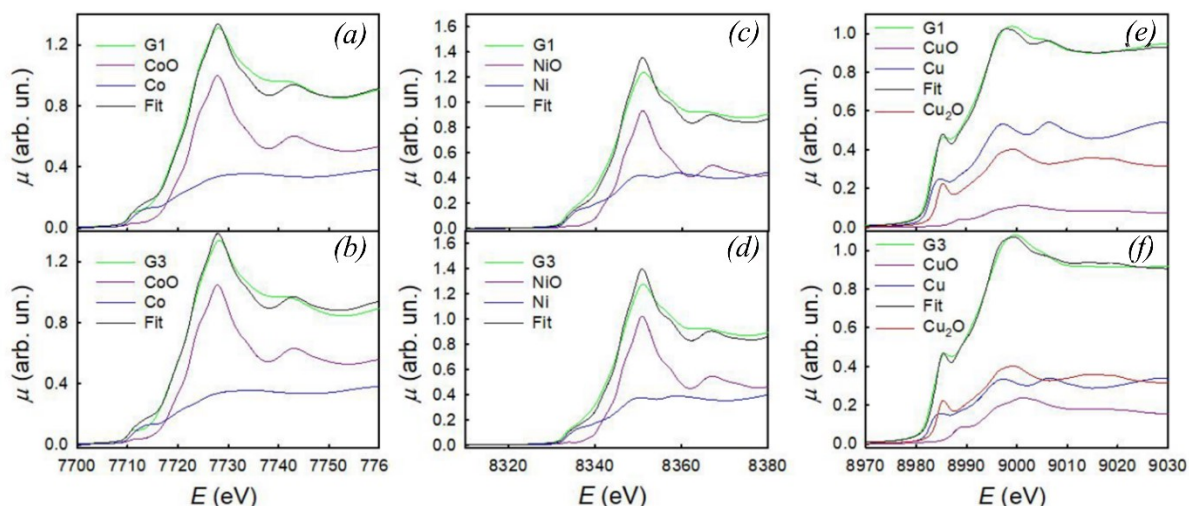
Figure 3.10. ***a***, ***c*** *and* ***e*** *show the fits of the spectra of the G1 sample at the Co K, Ni K and Cu K-edges, respectively, with linear combinations of the spectra of the reference compounds, that are also shown in the figure weighted by the coefficients of the linear combinations.* ***b***, ***d*** *and* ***f*** *show the analogous fits for sample G3.*

The weights for the linear combinations are shown in Table 3.1 and in Table 3.2 for the G1 and G3 samples. The quality of the fits, as measured by the respective R indexes, is quite good in all of the cases: the best agreement was found for the Cu K-edge, where the quality of the fit was reasonably improved by adding to the linear combinations also the spectrum of CuO.

	Co K	Ni K	Cu K
Co	0.464	-	-
CoO	0.536	-	-
Ni	-	0.665	-
NiO	-	0.335	-
Cu	-	-	0.518
CuO	-	-	0.074
Cu_2O	-	-	0.409

Table 3.1. *Linear combination fitting results of the Co, Ni and Cu K-edges XANES spectra of sample G5, expressed as mole fractions. The fit quality is expressed by the R index, equal to 0.0099, 0.0077, 0.0016 for the Co, Ni and Cu K-edge spectra, respectively.*

51

	Co K	Ni K	Cu K
Sample G1			
Co	0.38	-	-
CoO	0.62	-	-
Ni	-	0.41	-
NiO	-	0.59	-
Cu	-	-	0.54
CuO	-	-	0.09
Cu_2O	-	-	0.36
Sample G3			
Co	0.35	-	-
CoO	0.65	-	-
Ni	-	0.46	-
NiO	-	0.54	-
Cu	-	-	0.34
CuO	-	-	0.19
Cu_2O	-	-	0.47

Table 3.2. Linear combination fitting results of the Co, Ni and Cu K-edges XANES spectra of sample G1 and G3, expressed as mole fractions. The fit quality is expressed by the R index: for G1 is equal to 0.0059, 0.0050, 0.0011 for the Co, Ni and Cu K-edge spectra, respectively; for G3 is equal to 0.0075, 0.0059, 0.0011 for the Co, Ni and Cu K-edge spectra, respectively.

This is attributed to the fact that at the end of the lithiation process, a high degree of amorphization was found, which is highly suggestive that the local structure of Co is close to that of the liquid and therefore to that of the metallic *fcc* phase.[27] In the fits, we were obliged to use the experimental XANES of *hcp* Co: therefore, the fact that the worst agreement is obtained in the case of Co is fully sensible. The fraction of metallic Ni is larger than both the fractions of metallic Co and Cu; this may be due to the more easy reducibility of Ni(II) when compared to Co(II) and combined with the fact that Cu(II), which is the more reducible of the three metals, reduces to both Cu(I) and Cu(0). The worst agreement obtained at the Co K-edge may be due to the fact that metallic Co is one of the few metals having a hexagonal close-packed crystal structure. If a metallic alloy is formed during the Li charge-discharge cycles, the crystal structure of the alloy may reasonably differ from *hcp*. In any

case, it is apparent that a large amount of Co, Ni, and Cu is in the metallic state. This amount is the largest for Ni and the smallest for Co. In addition, almost all Cu(II) appears to be reduced, nearly half of which to Cu(I) oxidation state. All of these results point toward the fact that the conversion reaction forming metals and Li_2O is the actual working mechanism for the HEO as the anode. However, the reaction is not completed and totally reversible. In the cathodic region, the reduction of the oxides does not fully occur as the oxidation of metals in the anodic domain, but a coexistence of M and MO is clearly noticeable. Furthermore, both pieces of evidence that the behaviour of the three transition metals is different and that copper is sequentially reduced to Cu(I) and Cu(0) ask for a more detailed investigation. To have a better understanding of the working mechanisms of the HEO anode, we undertook an *operando* XAS investigation on the first lithiation cycle by performing XANES measurements at the Co, Ni, and Cu K-edges on a working cell at different values of capacity delivered by the cell during the lithiation step (Q). The results are shown in Figure 3.11.
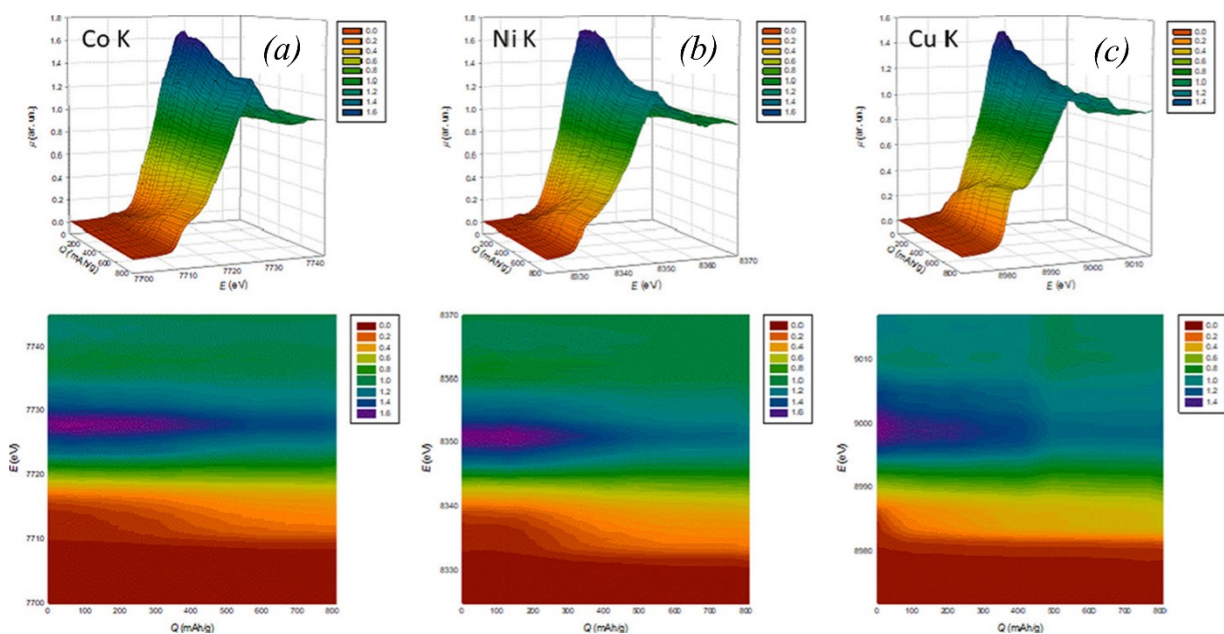
Figure 3.11*. Co K- **(a)**, Ni K- **(b)**, and Cu K- **(c)** edge XANES spectra in a working HEO battery as a function of the delivered capacity during the lithiation, as 3D plots (upper panels) and contour plots (lower panels).*

As in Figure 3.8, the reduction of metals is made evident by the appearance of a shoulder at low energy on the edge, *i.e.*, at *ca.* 7712, 8335, and 8982 eV for Co, Ni, and Cu, respectively, as marked by the blue arrows in Figure 3.8*a,c,e*. It is clearly apparent that the three transition metals have distinct behaviours. The reduction of Cu is the first to be detected, clearly evident at Q = 45 mAh g^{-1}, occurring in the voltage range between 1.2 and 0.9, in very good

53

agreement with the two cathodic peaks observed during CV and galvanostatic cycling (Figure 3.4). At Q = 135 mAh g^{-1} (E ≅ 0.8 V), the first traces of metallic Co become visible, while Ni metal starts to appear at Q = 180 mAh g^{-1} (E ≅ 0.7 V). In addition, the amounts of reduced metals are very different. For Q > 495 mAh g^{-1} (E < 0.5 V), virtually all Cu is in the metallic state, while a relevant fraction of the oxide is present for Co and Ni even at the end of the charging process (*i.e.*, when Q is *ca.* 90% of the theoretical capacity of the battery). The oxide molar fractions are 0.4(1) and 0.3(1) for Co and Ni, respectively, as estimated by fitting the pertinent spectra obtained at the end of the process with linear combinations of the spectra of the metals and those at OCV.[19] The initial lithiation steps are particularly interesting, as only Cu appears to be involved in the reaction. We used the spectrum at the Cu K-edge at Q = 45 mAh g^{-1} to have a closer look at the first steps of the reaction. At Q = 45 mAh g^{-1}, the spectra at both the Co and Ni K-edges remain unchanged, thus proving that the early steps of the reaction involve Cu only. The Cu K-edge spectrum was fitted using linear combinations of the spectra at OCV of metallic Cu and Cu$_2$O. The results are shown in Figure 3.12. It is worth noting that both Cu and Cu$_2$O are needed to obtain a good match of the shoulder at *ca.* 8985 eV.
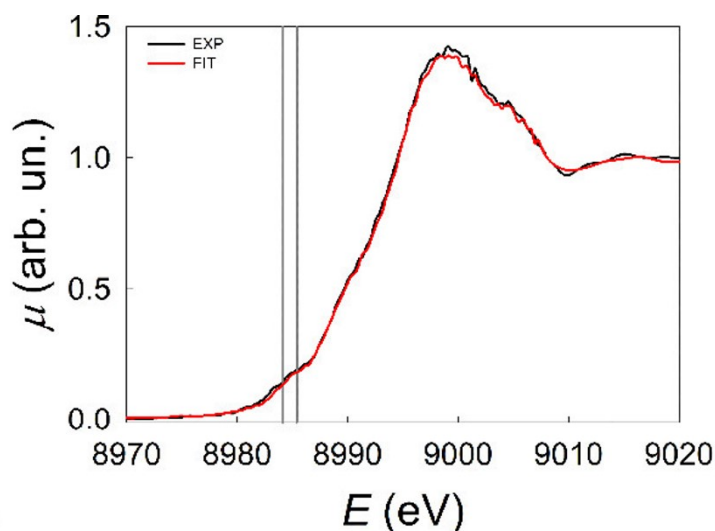
Figure 3.12. *Cu K-edge XANES spectrum for Q=45 mAh g^{-1} (black line) and the fit using a linear combination of the spectra at OCV, of Cu and Cu$_2$O (red line).*

This result, which was confirmed by Multivariant Resolution Curve (MRC) and Principal Component Analysis (PCA) of the whole set of the operando XAS data,[19] is direct proof that the first step of the reaction is the reduction of Cu(II) to Cu(I): we here note incidentally that the MRC and PCA analyses of the whole set of the *operando* XAS data[19] also confirmed the

results of XANES fittings for samples G1, G3, and G5, with the fact that the operando data are taken on the first lithiation step, while the *post mortem* samples refer to the second CV cycle. We also note again that the Co and Ni Kedges remain almost unchanged up to *ca.* Q = 200 mAh g^{-1} (E < 0.7 V), *i.e.*, when *ca.* 60% of Cu is still present as Cu(II) oxide, thus implying that the rock-salt structure of HEO is quite robust toward the reduction of Cu. This is due to the high configurational entropy adding additional stabilizing terms to the Gibbs free energy.[28] However, for Q > 400 mAh g^{-1}, we observe a strong reduction in the amplitude of the main edge peaks (white lines, WLs) at both the Co and Ni Kedges, at *ca.* 7728 and 8351 eV, respectively. In addition, the Cu K-edge seems to be affected as the WL at 8998 eV shows the final decrease for 400 < Q < 600 mAh g^{-1}. We remark here that XANES is a powerful probe of the local order around the photoabsorber: the abrupt change in the WL amplitude at Q > 400 mAh g^{-1} at both the Co and Ni K-edges is therefore related to an abrupt change in the local order around both Ni and Co; for the same reason, also, the local order around Cu is affected. We also observe that the WL amplitudes are never recovered and the XRD pattern at the end of the lithiation process indicates complete amorphization of the material. The combination of these facts allows stating that at Q > 400 mAh g^{-1} the TM-HEO structure collapses.

3.4.4. Morphological and Microstructural Investigation

The morphology of the as-prepared TM-HEO and the HEO-based anode after the galvanostatic cycling was investigated by SEM-EDX analysis. As shown by electron microscopy images (Figure 3.2*a*), HEO particles smaller than 5 μm are obtained by preparing the high-entropy oxide through a solid-state reaction at high temperatures. The microsize of the active material may be responsible for the complex electrochemical mechanisms,[7] proposed by considering the results obtained from XAS investigation. The *post mortem* SEM image (Figure 3.13) shows the presence of irregular grains, presenting an average dimension of about 2 μm. Surprisingly, the EDX analysis gives evidence of a quite inhomogeneous distribution of the component cations.
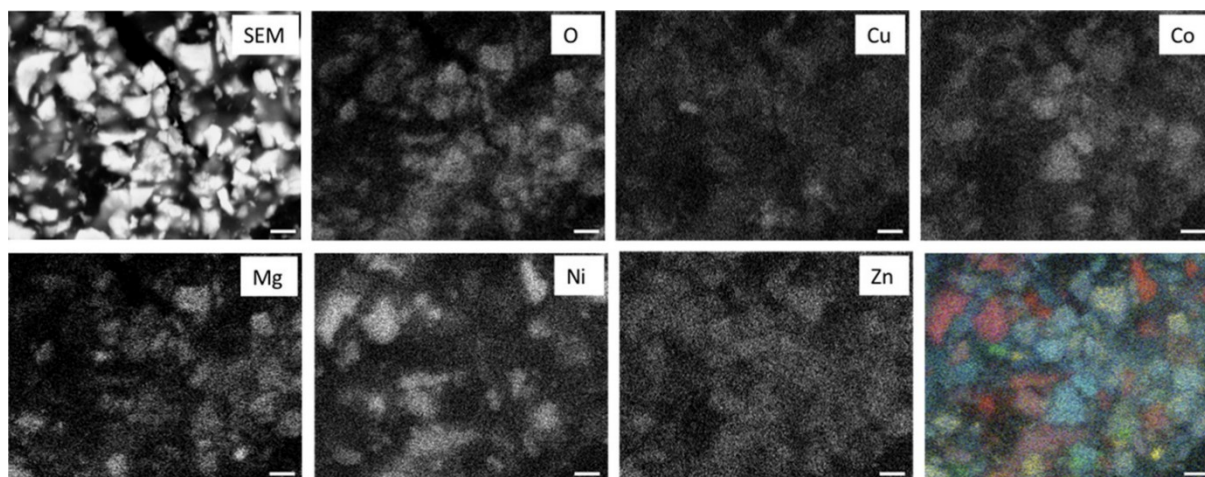
Figure 3.13. Post mortem SEM image of TM-HEO anode (upper left corner) and EDX mapping of the same region for the component cations. The false colours image in the lower right corner has been obtained overlapping all the EDX maps. In this image the blue colour represents Zn, yellow is Mg, red is Ni, green is Cu and cyan is Co.
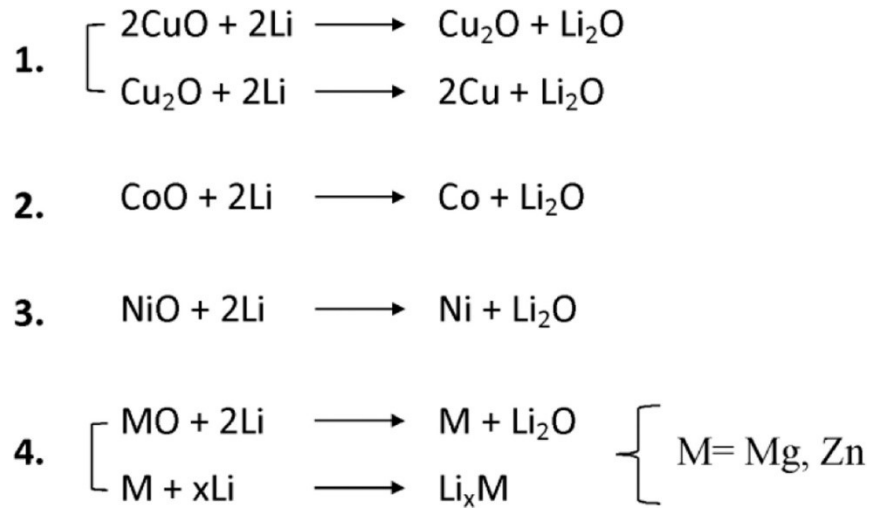*The white bar present on all images is 2 μm in length.*

Each grain presents, indeed, a dominant distribution of one of the cations. This can be observed in the maps relative to the distribution of each metal, but it appears to be even clearer in the false-colour image obtained by overlapping all of the maps; in addition, it is clearly seen by the oxygen map that some grains are oxygen-free or have a low oxygen concentration, and therefore, they can be safely assigned to a metallic phase. Considering that, before the electrochemical treatment, the grains were uniform in composition (Figure 3.2*c,d* and related discussion in paragraph 3.4.1), a possible explanation must consider that galvanostatic cycling collapses the HEO structure with demixing of the original oxide. In this scenario, each grain ends up presenting an inhomogeneous distribution of the cations, resulting in an apparent different composition. Although we have no definitive explanation of this finding, we here note that the lithiation sequence outlined above can give a potential explanation of the observed formation of large grains with segregated composition when the dissolution of the transition-metal ions in the electrolyte (namely, $LiPF_6$ in organic carbonates) is taken into account. This phenomenon is well known in the case of lithium-ion and lithium batteries, both for anodes and cathodes, still representing a critical challenge for the development of next-generation batteries.[29] When Cu starts to reduce, the first Cu(II) cations involved in the reduction are those present in the electrolyte solution. This reduction forms the first nuclei of metallic Cu and lowers the amount of Cu(II) in the solution: additional Cu(II) will then dissolve to restore the equilibrium concentration in the electrolyte. This dissolution-reduction sequence allows the metallic nuclei to grow. When Ni(II) also

starts to be reduced, a lot of Cu is already in the metallic state, outside the HEO structure; therefore, grains of metallic Ni can be formed via the same mechanism. This rationale can be extended also for the other metals. The result is the segregation of the metals at the end of the charging process, as shown by the EDX analysis. The compositional heterogeneity is not so rare in the case of compounds including transition metals as in the cathode systems or metal oxides for anodes. Several articles report on how the compositional and/or structural inhomogeneities of a composite electrode could affect the rate performances of a lithium battery, leading to the loss of capacity and local overcharge or discharge or unsafe conditions, for instance, loss of oxygen in the case of transition-metal oxides at high SOCs. Therefore, an understanding of the formation mechanism during the lithiation/delithiation steps is fundamental from a practical point of view. Focused studies were discussed in the literature investigating the state of charge heterogeneity by means of several techniques, as *in situ* X-ray diffraction (XRD), *ex situ* micro-Raman mapping or synchrotron X-ray imaging, and spectroscopy, of several TM oxides.[30–32] Further insights can be obtained using nanoscale full-field X-ray spectro-microscopy, as recently demonstrated by Wei and co-workers.[33]

3.4.5. TM-HEO Mechanism Investigation

Basically, the lithiation of TM-HEO induces a very complex mechanism involving a two-stage process: (i) the conversion of some cations as Cu^{2+}, Co^{2+}, and Ni^{2+} and (ii) the conversion and subsequent alloying/dealloying of Mg^{2+} and Zn^{2+}, as sketched in the following Scheme 1. Cu is the first element involved in the reduction through a multistep reaction starting at 1.2 V, which leads to Cu^{+} and, finally, to Cu^{0}, storing Li_2O.

$$2CuO + 2Li \longrightarrow Cu_2O + Li_2O$$

1.

$$Cu_2O + 2Li \longrightarrow 2Cu + Li_2O$$

2. $\quad CoO + 2Li \longrightarrow Co + Li_2O$

3. $\quad NiO + 2Li \longrightarrow Ni + Li_2O$

4.

$$MO + 2Li \longrightarrow M + Li_2O$$

$$M + xLi \longrightarrow Li_xM$$

$$M = Mg, Zn$$

Scheme 1. Multiple-Step Mechanism Proposed for TM-HEO Lithiation

At potentials lower than 1.2 V, further Cu reduction gives way to the conversion reaction. The HEO cubic structure remains intact for ~60% of lithiation delivered capacity, thanks to the matrix-stabilizing effects of ZnO and MgO at these potentials, in fair agreement with the literature.[12] Such a result well proves the beneficial role of the configuration entropy in enhancing the stability of the HEO rock-salt structure during the redox phenomena, even if not in the whole explored potential range. By further decreasing the voltages, the Co^{2+} and Ni^{2+} reduction takes place, as evidenced by the appearance of the shoulders at *ca.* 7712 eV at the Co K-edge and at *ca.* 8335 eV at the Ni K-edge. In addition, the intensity of the main peak at both the Co and Ni K-edges considerably lowers. Taking into account that XANES is sensitive to three and four body distribution functions around the photoabsorber, this is unequivocal evidence that Co and Ni are in a chemical environment that is different from that of TM-HEO. While it is possible that MgO and ZnO still form a metastable solid solution in this potential region, the rock-salt structure collapses, leading to a mixture of Co, Ni, and Cu and the corresponding oxides, MO, in a molar ratio as reported in Table 3.1. The conversion reaction is therefore not completed, and the consequent decomposition of Li_2O to reconvert metals into the TM-HEO rock-salt structure is not reversible. Indeed, metals (Ni, Co, Cu) and the corresponding oxides (CoO, NiO, and Cu_2O) remain segregated and are electrochemically inert under further cycling: this is demonstrated by the very close similarity in the spectral shape for samples G1, G3, and G5 at the Co, Ni, and Cu K-edges, both concerning XANES and EXAFS. In addition, the lack of long-range order demonstrated by XRD and the large degree of cation segregation demonstrated by EDX, both at the end

of the lithiation cycle, clearly support the conclusion of a large degree of irreversibility. This spectroscopic result is in very good agreement with the SEM analysis, showing very large aggregates of M and MO particles, as discussed in detail in the previous section. The nonreversibility of the conversion reaction is reasonably related to the morphology of the products resulting from the first lithiation step. It is well known, in fact, that in the case of conversion oxides, the decomposition of the electrochemically inert lithium oxide to Li and MO is allowed only in the presence of metal nanosized nuclei, which are able to catalyse such processes.[22] Concerning Zn, the XAS results show that the Zn K-edge spectra (Figure 3.14), collected before and after the electrochemical experiment, show dramatic changes.
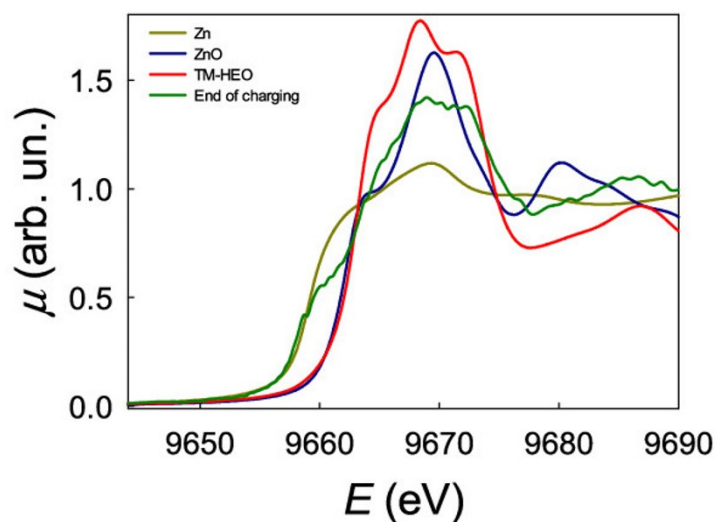

Figure 3.14. *Zn K-edge XANES spectrum for Q=800 mAh g⁻¹ (green line). The spectra of Zn, ZnO and that of the pristine TM-HEO are also shown for reference.*

Indeed, the spectrum of pristine TM-HEO shows a perfect agreement with that of cubic ZnO with the rock-salt structure.[34] On the contrary, at Q = 800 mAh g⁻¹, a marked shoulder is detected at *ca.* 9660 eV, which corresponds to the shoulder of the spectrum of metallic Zn and is due to the electronic transition from the 1s orbital to empty states in the conduction band: this has the obvious meaning that at the end of the charging process, a significant fraction of Zn is found in the metallic state, in contrast with what is reported by *Sarkar et al.*[12] However, the global XANES spectral shapes at the Zn K-edge of pure metallic Zn and of the sample at the end of the lithiation process are considerably different. Bearing in mind that XANES is sensitive not only to the electronic structure as projected onto the photoabsorber but also to the actual atomic local structure around the photoabsorber, this is

strongly suggestive that Zn is indeed not present as pure metallic Zn and, thus, that an alloy (possibly with Li) is formed. Moreover, the presence of a peak in the absorption edge at the same energy as the main peak of ZnO points to the presence of a significant amount of zinc in an oxidic phase. However, the spectroscopic study, showing incomplete and irreversible conversion, does not fit the electrochemical investigation, which, in contrast, shows high specific lithiation/delithiation capacity and rate capability, even at high current densities (see Figure 3.4). Recently, the reversible capacity obtained in similar electrodes was attributed to a mix of pseudocapacitive and faradic contributions, the latter due to the reversible conversion reaction:[35]

$$MO + 2Li^+ = Li_2O + M$$
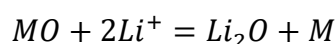
Such data treatment arises from the current peak, i_P, analysis of the cells in the CV plots collected at different scan rates, υ, which follows a power law as in the following equation

$$i_P = a\upsilon^b$$

where b is the slope of the linearized log/log equation, which could provide insight into the charge-storage mechanism. b ranges between 0.5, indicating full faradic intercalation controlled by semi-infinite linear diffusion, and 1, representing a surface capacitive charge storage, free of diffusion control. We analysed the b slope in the HEO CV plots collected between 0.1 and 1.0 mV s^{-1}, obtaining values of about 0.8 (see Figure 3.15), which, in principle, could confirm the mixed faradic/pseudocapacity contribution reported in the literature.
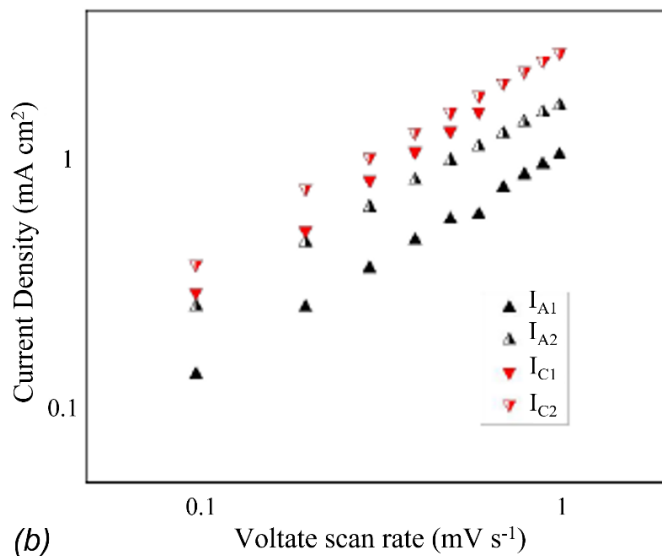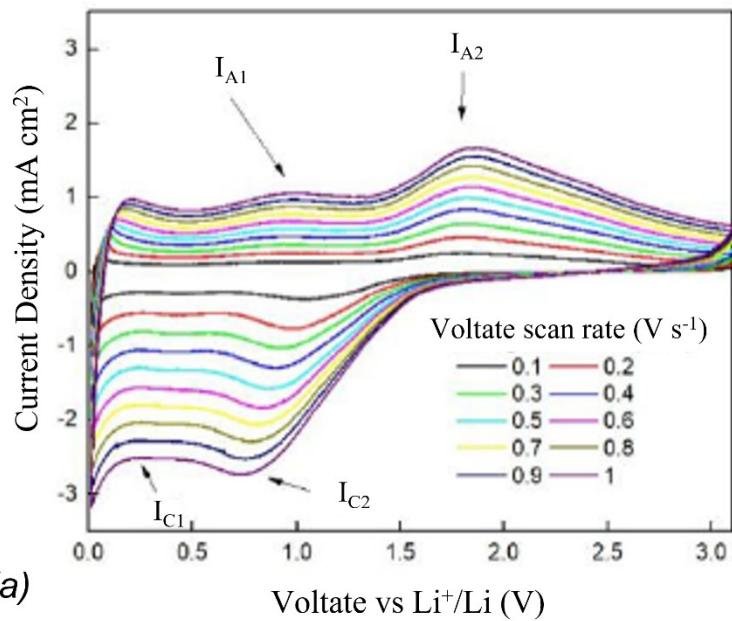
Figure 3.15. *Cyclic voltammetry plots at different scan rate for HEO-based anode (a) and Peak Current Density, I_P, power law and corresponding b parameters (b).*

However, such a hypothesis is not convincing. This linear relationship as well as the fitting parameter *b* strictly, in fact, rules only at the specific potential of the peak current, and accordingly to *Bard* and *Faulkner*,[36] the *b* fitting parameter is equal to 1 only at the potential corresponding to peak current for diffusion-controlled reactions. For this reason, such a procedure has not been validated right now by a more complex treatment, although sometimes used in the literature, and could lead to misleading results, especially in the case of complex electrochemical phenomena. It was also shown that the pseudocapacitive

61

behaviour is proportional to the BET surface area in samples milled for different times and becomes the most important source of charge storage for small particles (up to 90%). However, our spectroscopy measurements demonstrate the irreversibility of the oxide to metal conversion, leaving a mixture of metals and partially reduced oxide at the end of the first cycle, which are not further reconverted over cycling. Moreover, the observed particle size is quite large (Figure 3.4*a*). For all of these reasons, we do not believe that the pseudocapacitive contribution is relevant to justify the delivered capacity observed in such a system. Another consequence of extra capacity could also derive from the reversible electron transfer involving the anions of the liquid electrolyte (*e.g.*, carbonate) during the conversion step to form the corresponding metal salts.[37] However, our XAS measurements provide spectra that are specific for the metal oxides, rather than for carbonates, which, in contrast, are described by significantly different spectroscopic signals. It is then more reasonable discussing these reversible performances in terms of a combination of alloying/dealloying phenomena between two binary systems: (i) Li and Zn and (ii) Li and Mg, whose kinetics (especially in the case of MgO) could be improved by the synergistic catalytic effect of metallic multielements (maybe nanosized), segregated during the first lithiation step. It is well known, for instance, that ZnO is an anode material based on the alloying/dealloying reaction since the respective metal can form alloys with Li, such as LiZn, at potentials lower than 0.7 V. Therefore, large reversible capacities are possible (overall theoretical capacity of 987 mAh g^{-1} [25]). In addition, Li shows very high miscibility in Mg and a wide range of possible binary systems, as shown by the phase diagrams reported in the literature.[38,39] The resulting electrochemical process may occur through two steps: (i) reduction of MO to M and Li$_2$O and (ii) formation of Li/M alloys (M = Zn, Mg). Taking into consideration the reversible charging/discharging processes obtained in the case of HEO-based cells and the molar fraction of ZnO and MgO (x = 0.2) in the TM-HEO, we may speculate that the average specific capacity of 615 mAh g^{-1} observed at 0.1C can explain the concomitance of two phenomena: (i) LiZn alloy formation and (ii) and Li/Mg alloy formation with very high Li at.% (ranging around 80 at.%) (see Figure 3.16).
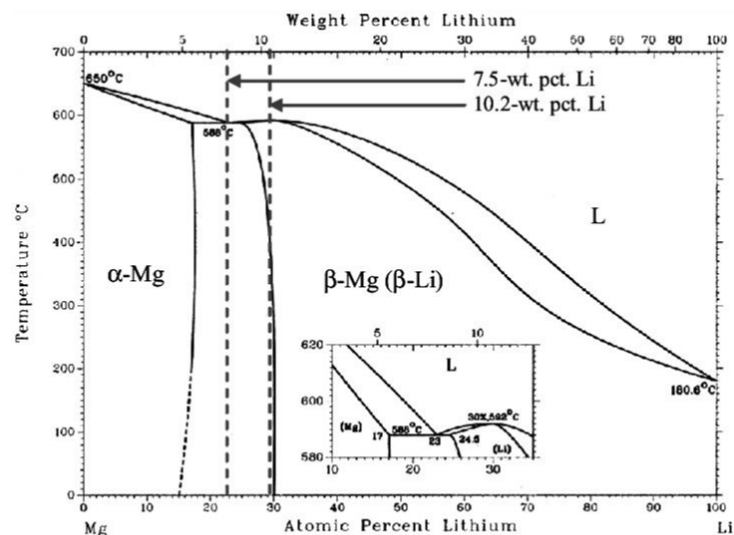
Figure 3.16. *Phase diagram of Mg/Li binary system. Taken from Refs. 38-39.*

The latter compositions are envisaged by the phase diagram of the magnesium−lithium system, which shows a wide range of stable Li solid solutions from 30 to 100 Li at.%, making possible the production of several binary alloys.[38] The delivered capacity is also quite comparable with that reported in the literature for electrodes based on Li/Mg alloys, which show a specific capacity of ~600 mAh g^{-1} in the case of alloys with Li contents of about 70 at.%.[40] To experimentally prove the crucial role of both Mg and Zn in the electrochemical performances of the TM-HEO-based anodes, we investigated the cycling behaviour of HEO-no Zn and HEO-no Mg. Both the pristine materials have rock-salts structures. However, in the case of the (CoCuMgNi)O system, the XRD pattern shows the presence of non-negligible CuO impurities (Figure 3.17*a,b*).
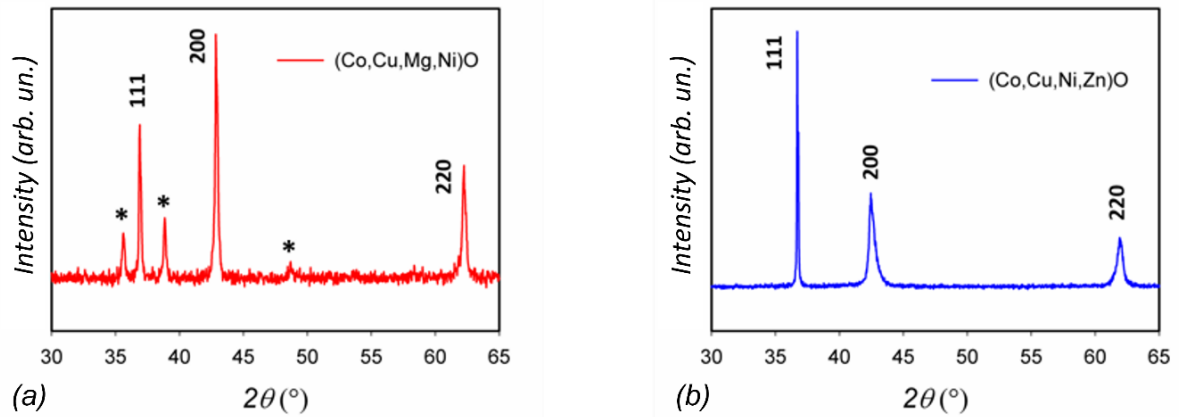
Figure 3.17. XRD pattern of (a) the pristine (CoCuMgNi)O and (b) (CoCuNiZn)O. The star * in plot (a) indicates the CuO signal.

The galvanostatic cycling tests of both the samples have much worse performances than those observed for the TM-HEO-based anode. In the case of (CoCuMgNi)O (Figure 3.18*a-e*), the charge-discharge capacity delivered over cycling rapidly decreases during the first cycles to stabilize around 190 mAh g^{-1} at 0.2C. Such a value is at least a factor of 2.5 lower than $Mg_{0.2}Co_{0.2}Ni_{0.2}Cu_{0.2}Zn_{0.2}O$ at a similar C rate.
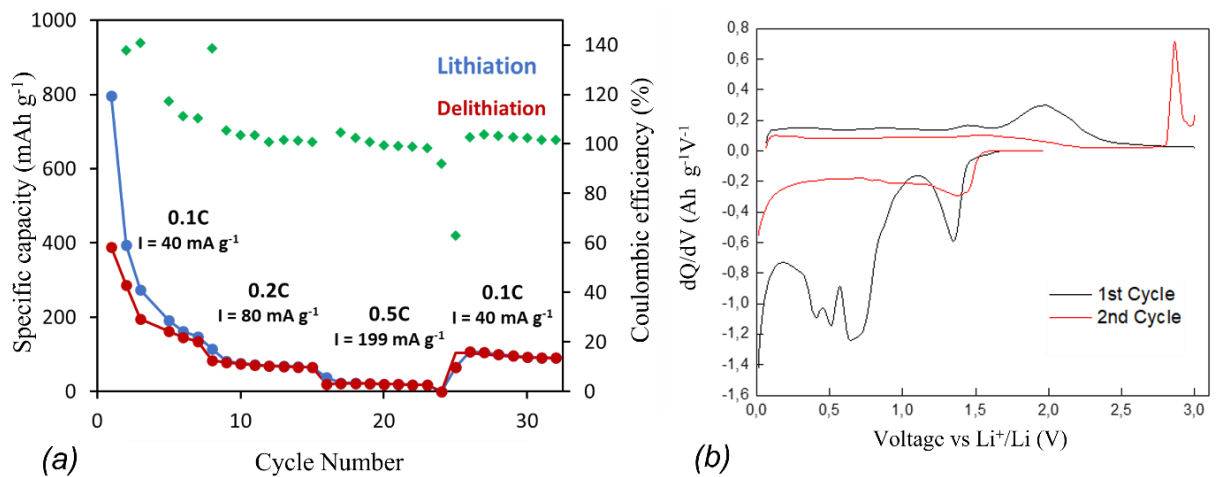
Figure 3.18. **(a)** *Galvanostatic cycling performance.* **(b)** *Differential capacity,* **(c)** *voltage profile and* **(d)** *voltage profiles upon time of the 1st and 2nd cycle.* **(e)** *EIS Nyquist plots of (CoCuMgNi)O-based anode before and after galvanostatic cycling.*

The voltage plateaus are well defined only during the first lithiation cycle and this is clear evidence of highly irreversible phenomena. Such an aspect is better shown in Figure 3.18*b*, which reports the differential capacity for the first and second cycles. During initial lithiation, similar peaks to HEO are noted at comparable voltages, except for the Cu^{2+}/Cu^+ signal, which appears shifted at higher potentials. In the second cycle, the peaks below 1.0 V, mostly ascribed to the reduction of Ni^{2+} and Co^{2+}, disappear, and only the Cu signal is still evident, even if with lower intensity. The (CoCuNiZn)O-based anode shows a significantly different mechanism (Figure 3.19*a-e*). In this case, the delivered capacity is even lower and drastically decreases close to zero during the first six cycles. The differential capacity shows the presence of just one main peak at around 1.1 V both in the anodic and cathodic sides, reversible only during the first lithiation cycle.
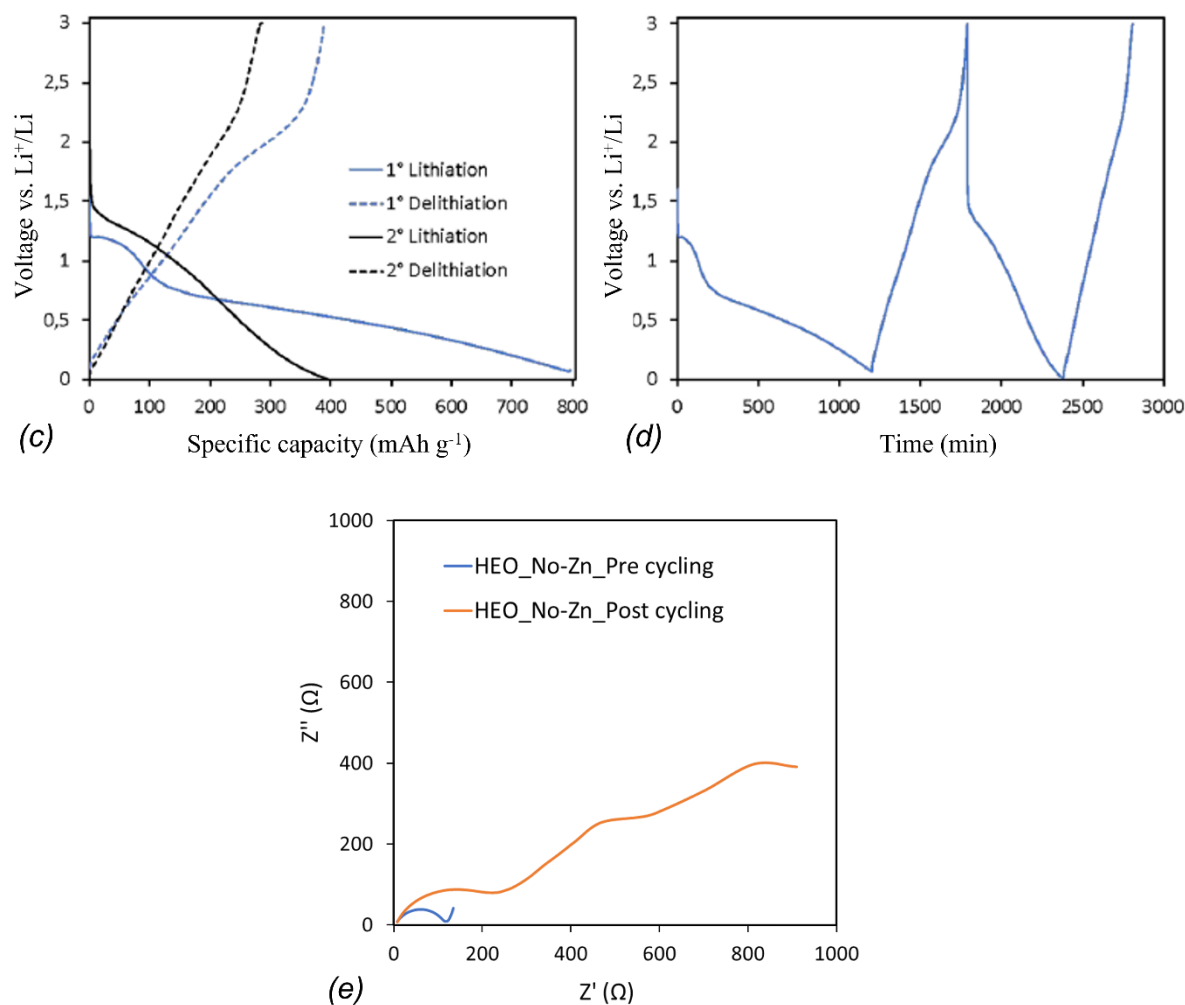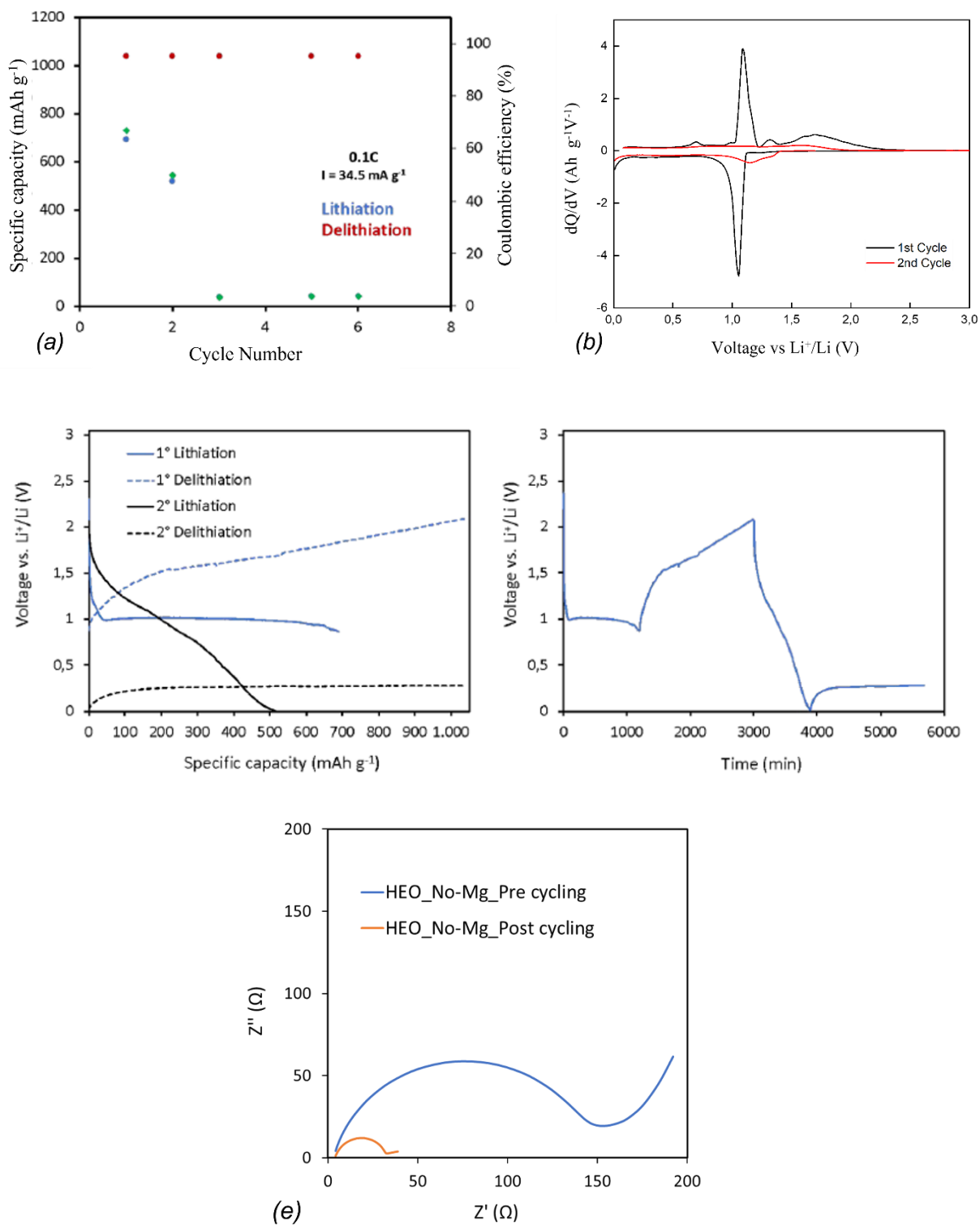
Figure 3.19. *(a) Galvanostatic cycling performance. (b) Differential capacity, (c) voltage profile and (d) voltage profiles upon time of the 1st and 2nd cycle. (e) EIS Nyquist plots of (CoCuNiZn)O-based anode before and after galvanostatic cycling.*

The comparison among the properties of $Mg_{0.2}Co_{0.2}Ni_{0.2}Cu_{0.2}Zn_{0.2}O$, $Co_{0.25}Cu_{0.25}$ $Mg_{0.25}Ni_{0.25}O$, and $Co_{0.25}Cu_{0.25}Ni_{0.25}Zn_{0.25}O$ suggests that both ZnO and MgO, in particular, the latter one, seems to be responsible for the capacity delivered by the TM-HEO-based anode. Very complex phenomena occur, therefore, by changing the number of oxides and the type of metallic cations in the HEO. The entropy-stabilized oxide is a case on his own with its unique thermodynamics, different from the single oxide. Consequently, also, the electrochemistry changes with respect to the individual components. The reason lies in the configurational entropy, which significantly increases with the number of cations in the structure, strongly affecting the functional properties of the system, from the lithiation mechanism to the electrochemical potentials of the M^{2+}/M couples. Regarding the latter aspect, this is particularly evident in the case of copper. Figure 3.20, for instance, compares the first lithiation cycle for all of the analysed samples (*e.g.*, TM-HEO, (CoCuMgNi)O, and (CoCuNiZn)O). The peak above 1.0 V, reasonably assigned to the reduction of CuO, is strongly influenced by the TM-HEO composition, ranging from 1.0 and 1.5 V, depending on the presence or absence of ZnO and MgO.
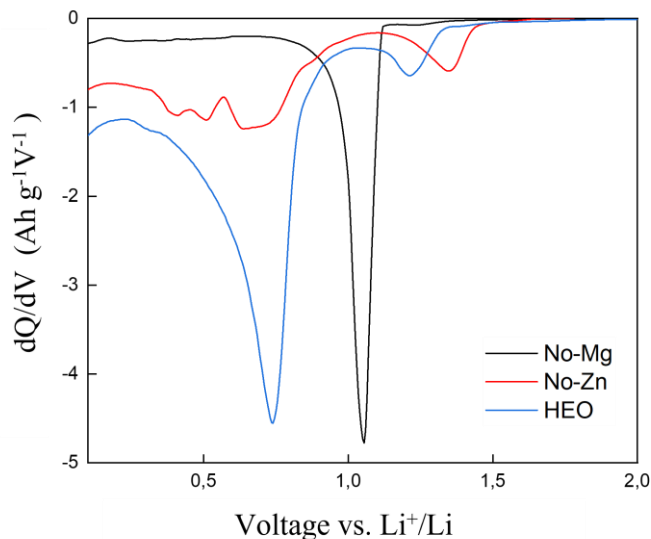
Figure 3.20. Comparison of the Differential Capacity determined TM-HEO-, (CoCuMgNi)O- and (CoCuNiZn)O-based anode.

Another proof (even if indirect) of potential Li/M alloying comes from the poor electrochemical performances of TM-HEO obtained in the case of Na cells (see Figure

3.21*a,b*). From galvanostatic cycling, it is evident the serious inefficiency of the sodiation/desodiation process in this kind of system.
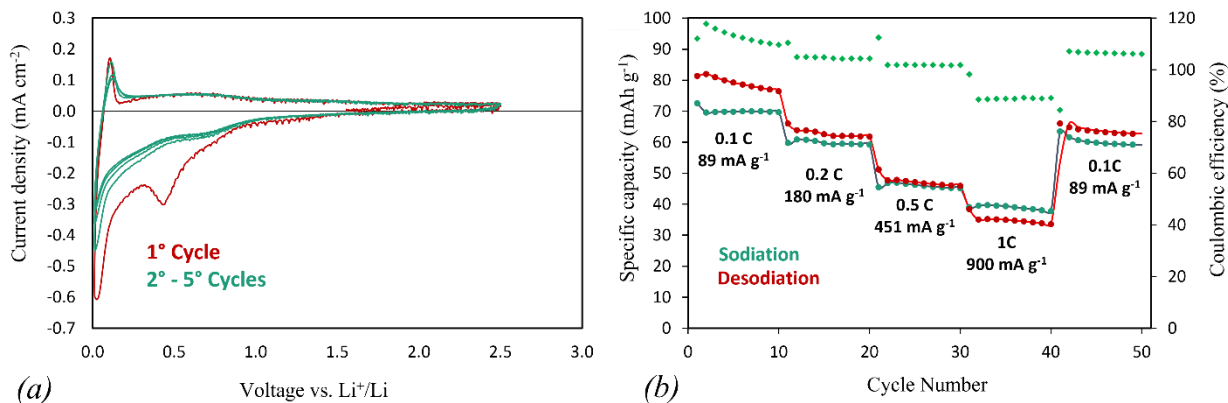
Figure 3.21. *(a) Cyclic voltammograms of TM-HEO-based anodes in a Na-ion cell. Na is the counter electrode and the reference. Scan rate: 0.2 mV s^{-1}. (b) Galvanostatic cycling at different C rate of the cell: TM-HEO|electrolyte|Na. Electrolyte: NaPF$_6$ 1.0M in EC:DEC (50:50 vol%).*

A specific capacity significantly lower than 80 mAh g^{-1} (likely due mostly to the electrochemical activity of the carbonaceous binder fraction in the composite anode) and low Coulombic efficiency are obtained even at a low current density (0.1C). Such worse performances may be likely ascribed, for instance, to the lower solubility of Na in solid M or of M in solid (Na),[41,42] especially in the case of Mg (Figure 3.22), and then to the difficulty or impossibility of forming binary alloys, contrary to what occurs in the case of lithium.
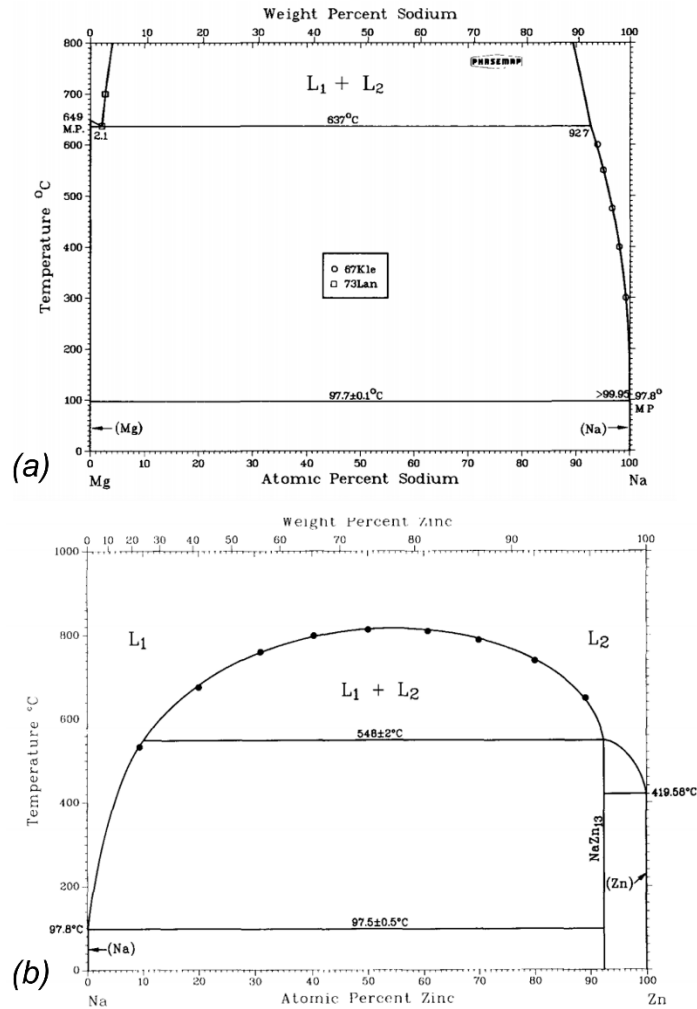
Figure 3.22. *Phase diagram of the (a) Mg/Na and (b) Na/Zn binary system. Taken from Refs. 41 and 42.*

A final comment concerns the lack of crystal order found at the end of the lithiation process. The molar configurational entropy for a high-entropy oxide, S_{config}, with the rock-salt structure and no disorder on the oxygen site is

$$\Delta S_{config} = -R \sum x_i \ln x_i$$

where x_i is the molar fraction of the i element on the cation site.[12] The same relation also applies to an alloy of metals in a crystal structure with just one site, such as *fcc* or *hcp*. Thus, if an alloy of metals with the (say) *fcc* had been formed, no entropy increase would have been expected, and the lithiation process would have been reversible. The experiments show, on the contrary, that (i) the process is highly irreversible, indicating that the entropy production ΔS_i is large and positive, and (ii) the metal distribution shown by the EDX maps

of Figure 3.13 is highly nonhomogeneous, indicating that the configurational entropy of mixing in the final lithiation reaction product is small. The only way that is left to the system to increase the entropy as required by the irreversibility condition ($\Delta S_i > 0$) is to display no crystalline order at the end of the process.

3.5. Conclusion

Here, we proposed a new complex mechanism occurring during the lithiation/delithiation processes in high-entropy oxides based on transition metals with rock-salt structure as anodes for lithium-ion cells. To this aim, we carried out both *operando* and *ex situ* XAS measurements on the system $Mg_{0.2}Co_{0.2}Ni_{0.2}Cu_{0.2}Zn_{0.2}O$ (TM-HEO), in combination with electrochemical and microstructural characterization. The spectroscopic results suggest that the redox reaction takes place through a multistep process depending on the TMs' reduction potential. The whole process is incomplete and irreversible, leading to a mixture of M and MO with a variable molar ratio depending on the metal. In addition, contrary to what is supposed in the literature by XRD analysis, we prove that even ZnO takes part in the conversion mechanism since a significant fraction of Zn is found in the metallic state at the end of the charging process. Despite the collapse of the rock-salt structure, a charge/ discharge specific capacity higher than 600 mAh g^{-1} at 0.1C has been delivered by the TM-HEO-based cell with the Coulombic efficiency very close to 1, in particular, at higher current densities. Taking into account the irreversibility of the redox mechanism, it is reasonable to ascribe such capacity to the alloying/dealloying reaction typical of anodes such as ZnO and MgO. Even though the rock-salt structure of such a system is intended to collapse, it maintains up to 60% of charge, when the first traces of metallic Co are apparent (around 0.8 V), confirming the stabilizing effect of the configurational entropy.

However, our results clearly point out that $Mg_{0.2}Co_{0.2}Ni_{0.2}Cu_{0.2}Zn_{0.2}O$ is not still suitable for use as the anode in LIBs, despite the promising performances shown in the literature. Further strategies of phase stabilization should be therefore investigated, for instance, by properly modulating the important key factors, such as the type of metal, the number of cations, stoichiometry, and morphology, and also by exploring other structures, such as spinel, where a different lithiation/delithiation mechanism occurs. We strongly believe that such a novel

understanding is therefore interesting not only *per se* but also in the design of better materials for the next-generation Li$^+$- and Na$^+$-ion batteries.

3.6. Bibliography

1. Lin, D.; Liu, Y.; Cui, Y. Reviving the Lithium Metal Anode for High-Energy Batteries. *Nat. Nanotechnol*. 2017, **12**, 194−206.

2. Cheng, X.-B.; Zhang, R.; Zhao, C.-Z.; Zhang, Q. Toward Safe Lithium Metal Anode in Rechargeable Batteries: A Review. *Chem. Rev*. 2017, **117**, 10403−10473.

3. Al Hassan, M. R.; Sen, A.; Zaman, T.; Mostari, M. S. Emergence of Graphene as a Promising Anode Material for Rechargeable Batteries: a review. *Mater. Today Chem*. 2019, **11**, 225−243.

4. Jin, Y.; Zhu, B.; Lu, Z.; Liu, N.; Zhu, J. Challenges and Recent Progress in the Development of Si Anodes for Lithium-Ion Battery. *Adv. Energy Mater*. 2017, **7**, No. 1700715.

5. Hatchard, T. D.; Dahn, J. R. In Situ XRD and Electrochemical Study of the Reaction of Lithium with Amorphous Silicon. *J. Electrochem. Soc*. 2004, **151**, A838.

6. Dou, F.; Shi, L.; Chen, G.; Zhang, D. Silicon/Carbon Composite Anode Materials for Lithium-Ion Batteries. *Electrochem. Energy Rev*. 2019, **2**, 149−198.

7. Reddy, M. V.; Subba Rao, G. V.; Chowdari, B. V. R. Metal Oxides and Oxysalts as Anode Materials for Li Ion Batteries. *Chem. Rev*. 2013, **113**, 5364−5457.

8. Liu, J.; Liu, X.-W. Two-Dimensional Nanoarchitectures for Lithium Storage. *Adv. Mater*. 2012, **24**, 4097−4111.

9. Yeh, J.-W.; Chen, S.-K.; Lin, S.-J.; Gan, J.-Y.; Chin, T.-S.; Shun, T.-T.; Tsau, C.-H.; Chang, S.-Y. Nanostructured High-Entropy Alloys with Multiple Principal Elements: Novel Alloy Design Concepts and Outcomes. *Adv. Eng. Mater*. 2004, **6**, 299−303.

10. Rost, C. M.; Sachet, E.; Borman, T.; Moballegh, A.; Dickey, E. C.; Hou, D.; Jones, J. L.; Curtarolo, S.; Maria, J.-P. Entropy-Stabilized Oxides. *Nat. Commun*. 2015, **6**, No. 8485.

11. Wang, Q.; Sarkar, A.; Wang, D.; Velasco, L.; Azmi, R.; Bhattacharya, S. S.; Bergfeldt, T.; Du¨vel, A.; Heitjans, P.; Brezesinski, T.; Hahn, H.; Breitung, B. Multi-Anionic and -Cationic Compounds: New High Entropy Materials for Advanced Li-Ion Batteries. *Energy Environ. Sci*. 2019, **12**, 2433−2442.

12. Sarkar, A.; Wang, Q.; Schiele, A.; Chellali, M. R.; Bhattacharya, S. S.; Wang, D.; Brezesinski, T.; Hahn, H.; Velasco, L.; Breitung, B. High-Entropy Oxides: Fundamental Aspects and Electrochemical Properties. *Adv. Mater*. 2019, **31**, No. 1806236.

13. Sarkar, A.; Velasco, L.; Wang, D.; Wang, Q.; Talasila, G.; de Biasi, L.; Ku¨bel, C.; Brezesinski, T.; Bhattacharya, S. S.; Hahn, H.; Breitung, B. High Entropy Oxides for Reversible Energy Storage. *Nat. Commun*. 2018, **9**, No. 3400.

14. Wang, Q.; Sarkar, A.; Li, Z.; Lu, Y.; Velasco, L.; Bhattacharya, S. S.; Brezesinski, T.; Hahn, H.; Breitung, B. High Entropy Oxides as Anode Material for Li-Ion Battery Applications: A Practical Approach. *Electrochem. Commun*. 2019, **100**, 121−125.

15. Bérardan, D.; Franger, S.; Meena, A. K.; Dragoe, N. Room Temperature Lithium Superionic Conductivity in High Entropy Oxides. *J. Mater. Chem*. 2016, **A 4**, 9536−9541.

16. Qiu, N.; Chen, H.; Yang, Z.; Sun, S.; Wang, Y.; Cui, Y. A High Entropy Oxide (Mg0.2Co0.2Ni0.2Cu0.2Zn0.2O) with Superior Lithium Storage Performance. *J. Alloys Compd*. 2019, **777**, 767−774.

17. Rao, K. V.; Smakula, A. Dielectric Properties of Cobalt Oxide, Nickel Oxide, and their Mixed Crystals. *J. Appl. Phys*. 1965, **36**, 2031.

18. Ravel, B.; Newville, M. ATHENA, ARTEMIS, HEPHAESTUS: Data Analysis for X-ray Absorption Spectroscopy using IFEFFIT. *J. Synchrotron Radiat*. 2005, **12**, 537−541.

19. Tavani, F.; Fracchia, M.; Pianta, N.; Ghigna, P.; Quartarone, E.; D'Angelo, P. Multivariate Curve Resolution Analysis of Operando XAS Data for the Investigation of the Lithiation Mechanism in High Entropy Oxides. *Chem. Phys. Lett*. 2020, **760**, No. 137968.

20. Liu, C.; Li, C.; Ahmed, K.; Mutlu, Z.; Ozkan, C. S.; Ozkan, M. Template Free and Binderless NiO Nanowire Foam for Li-ion Battery Anodes with Long Cycle Life and Ultrahigh Rate Capability. *Sci. Rep*. 2016, **6**, No. 29183.

21. Yuan, Y. F.; Pei, Y. B.; Fang, J.; Zhu, H. L.; Yang, J. L.; Guo, S. Y. Sponge-like Mesoporous CuO Ribbon Clusters as High-Performance Anode Material for Lithium-Ion Batteries. *Mater. Lett*. 2013, **91**, 279−282.

22. Poizot, P.; Laruelle, S.; Grugeon, S.; Dupont, L.; Tarascon, J.- M. Nano-sized Transition-Metal Oxides as Negative-Electrode Materials for Lithium-Ion Batteries. *Nature* 2000, **407**, 496−499.

23. Quartarone, E.; Dall'Asta, V.; Resmini, A.; Tealdi, C.; Tredici, I. G.; Tamburini, U. A.; Mustarelli, P. Graphite-coated ZnO Nanosheets as High-capacity, Highly Stable, and Binder-free Anodes for Lithium-Ion Batteries. *J. Power Sources* 2016, **320**, 314 −321.

24. García-Tamayo, E.; Valvo, M.; Lafont, U.; Locati, C.; Munao, D.; Kelder, E. M. Nanostructured Fe2O3 and CuO Composite Electrodes for Li Ion Batteries Synthesized and Deposited in One Step. *J. Power Sources* 2011, **196**, 6425−6432.

25. Bresser, D.; Mueller, F.; Fiedler, M.; Krueger, S.; Kloepsch, R.; Baither, D.; Winter, M.; Paillard, E.; Passerini, S. Transition-Metal-Doped Zinc Oxide Nanoparticles as a New Lithium-Ion Anode Material. *Chem. Mater.* 2013, **25**, 4977−4985.

26. J.P. Neumann, T. Zhong, Y. A. Chang. The Cu−O (Copper-Oxygen) System. *Bull. Alloy Phase Diagrams* 1984, **5**, 136−140.

27. Lad'yanov, V. I.; Bel'tyukov, A. L.; Tronin, K. G.; Kamaeva, L. V. Structural Transition in Liquid Cobalt. *JETP Lett*. 2000, **72**, 301−303.

28. Fracchia, M.; Ghigna, P.; Pozzi, T.; Anselmi Tamburini, U.; Colombo, V.; Braglia, L.; Torelli, P. Stabilization by Configurational Entropy of the Cu(II) Active Site during CO Oxidation on $Mg_{0.2}Co_{0.2}Ni_{0.2}Cu_{0.2}Zn_{0.2}O$. *J. Phys. Chem. Lett*. 2020, **11**, 3589−3593.

29. Li, W. An Unpredictable Hazard in Lithium-Ion Batteries from Transition Metal Ions: Dissolution from Cathodes, Deposition on Anodes and Elimination Strategies. *J. Electrochem. Soc.* 2020, **167**, No. 090514.

30. Zhang, J.; Li, Q.; Ouyang, C.; Yu, X.; Ge, M.; Huang, X.; Hu, E.; Ma, C.; Li, S.; Xiao, R.; Yang, A.; Chu, Y.; Liu, Y.; Yu, H.; Yang, X.; Huang, X.; Chen, L.; Li, H. Trace Doping of Multiple Elements Enables Stable Battery Cycling of $LiCoO_2$ at 4.6 V. *Nat. Energy* 2019, **4**, 594−603.

31. Tian, C.; Xu, Y.; Nordlund, D.; Lin, L.; Liu, J.; Sun, Z.; Liu, Y.; Doeff, M. Charge Heterogeneity and Surface Chemistry in Polycrystalline Cathode Materials. *Joule* 2018, **2**, 464−477.

32. Nanda, J.; Remillard, J.; O'Neill, A.; Bernardi, D.; Ro, T.; Nietering, K. E.; Go, J.-Y.; Miller, T. J. Local State-of-Charge Mapping of Lithium-Ion Battery Electrodes. *Adv. Funct. Mater*. 2011, **21**, 3282−3290.

33. Wei, C.; Xia, S.; Huang, H.; Mao, Y.; Pianetta, P.; Liu, Y. Mesoscale Battery Science: The Behavior of Electrode Particles Caught on a Multispectral X-ray Camera. *Acc. Chem. Res*. 2018, **51**, 2484−2492.

34. Baranov, A. N.; Sokolov, P. S.; Tafeenko, V. A.; Lathe, C.; Zubavichus, Y. V.; Veligzhanin, A. A.; Chukichev, M. V.; Solozhenko, V. L. Nanocrystallinity as a Route to Metastable Phases: Rock Salt ZnO. *Chem. Mater*. 2013, **25**, 1775−1782.

35. Chen, H.; Qiu, N.; Wu, B.; Yang, Z.; Sun, S.; Wang, Y. Tunable Pseudocapacitive Contribution by Dimension Control in Nanocrystalline- constructed $(Mg_{0.2}Co_{0.2}Ni_{0.2}Cu_{0.2}Zn_{0.2})O$ Solid Solutions to Achieve Superior Lithium-storage Properties. *RSC Adv*. 2019, **9**, 28908−28915.

36. Bard, A. J.; Faulkner, L. R. Electrochemical Methods: Fundamentals and Applications. *John Wiley & Sons, Inc*.: 2011.

37. Su, L.; Zhou, Z.; Qion, X.; Tang, Q.; Wu, D.; Shen, P. $CoCO_3$ Submicrocube/Graphene Composites with High Lithium Storage Capability. *Nano Energy* 2013, **2**, 276−282.

38. Atkins, G.; Marya, M.; Olson, D.; Eliezer, D. Magnesium-Lithium Alloy Weldability: A Microstructural Characterization. *JOM* 2004, **6**.

39. Gasior, W.; Moser, Z.; Zakulski, W.; Schwitzgebel, G. Thermodynamic Studies and the Phase Diagram of the Li-Mg System. *Metall. Mater. Trans. A* 1996, **27**, 2419−2428.

40. Shi, Z.; Liu, M.; Naik, D.; Gole, J. L. Electrochemical Properties of Li-Mg Alloy Electrodes for Lithium Batteries. *J. Power Sources* 2001, **92**, 70−80.

41. Pelton, A. D. The Ba-Rb (Barium-Rubidium) System. *Bull. Alloy Phase Diagrams* 1984, **5**, 454.

42. Wang, J.; Miao, N.; Chartrand, P.; Jung, I.-H. Thermodynamic Evaluation and Optimization of the (Na+X) Binary Systems (X=Ag, Ca, In, Sn, Zn) using Combined Calphad and First-Principles Methods of Calculation. *J. Chem. Thermodyn*. 2013, **66**, 22−33.

Chapter 4:
Towards Advanced Sodium Ion Batteries:
Phosphorus/Carbon Nanocomposite

4.1. Abstract

Sodium-ion batteries (SIBs) are promising alternative to Lithium-ion batteries for massive stationary energy storage. To improve energy density, however, more performing active materials are needed. In order to allow sustainable scale-up, it is also mandatory to develop green products and processes. Herein, we report on anodes of phosphorus/carbon (P/C) nanocomposites prepared via High Energy Ball Milling (HEBM), a simple, powerful, and easily scalable synthesis technique. The electrodes were prepared under oxygen-free atmosphere, using water as solvent, which enabled the use of aluminium (instead of copper) as current collector, implying significant cost reduction. The P/C nanocomposite obtained after 54 h HEBM resulted in excellent cycling stability, delivering very high specific capacity (2200 mAh g^{-1}, 0.05C) and showing good capacity retention after 120 cycles. A careful structural analysis (XRD, FE-SEM/EDX, XPS), revealed that long milling times strongly increased cycling stability due to: (i) significant decrease of P particle size inside the matrix and deep composite amorphization, which alleviates the buffering dimensional issues typical of black phosphorus; (ii) presence of defects in the carbonaceous component, which allows easier Na$^+$ insertion into the anode. Our results show that P/C nanocomposites are very promising anode materials for SIBs, paving the way for further exploitation of nano-architectures in SIBs technology.

4.2. Introduction

Lithium-ion batteries (LIBs) are nowadays the technology of choice for electrochemical energy storage devices because of their high energy density, being one of the key criteria in portable devices and electric vehicles.[1-3] Sodium-ion batteries (SIBs) are considered one of the most promising candidates for stationary energy storage due to high crustal abundance and low cost of sodium resources. In particular, the possibility of using aluminium as current collector has been shown to drastically reduce production cost of SIBs.[4] Nevertheless, active

76

materials need to be improved in terms of specific and volumetric capacity, in order to be compatible with state-of-the-art LIBs. Among a variety of potentially promising anode materials for SIBs, phosphorus (P) is considered particularly attractive because of its high theoretical capacity (2596 mAh g^{-1}) and abundant reserves. Phosphorus possesses three main allotropes: white, red, and black. From an electrochemical point of view, both red P (RP)[5,6] and black P (BP) are attractive,[7,8] but BP generally offers better electrochemical performance due to its higher electronic conductivity compared to RP (10^2 S m^{-1} vs 10^{-12} S m^{-1}).[7,8] Black Phosphorus (BP) has an orthorhombic crystalline structure, consisting of puckered double layers with parallel zig-zag chains of interconnected sp^3 hybridized P atoms. The final structure is made up of P$_6$ rings in a chair conformation. The individual layers are stacked and held together by weak Van der Waals forces creating the bulk BP 2D multilayer structure. This 2D arrangement allows the intercalation of $e.g.$, Li$^+$, Na$^+$ and K$^+$ in the discharge potential range between 1.2 V and 0.4 V. [8] At lower potentials, the high specific capacity is achieved due to the three electron transfer, alloying-like reaction of P with Li$^+$ and Na$^+$ to form Li$_3$P or Na$_3$P in case of LIBs and SIBs, respectively.[6-10] Furthermore, intrinsic anisotropic properties of BP can tune morphological evolution and mitigate strain during sodiation.[11] In case of SIBs, BP based materials have been studied widely as a high capacity alternative to state-of-the-art hard carbons (around 250 - 300 mAh g^{-1}). Some P/C composites described in literature deliver specific capacities exceeding 1500 mAh g^{-1}, depending on the electrolyte composition as well as the type and amount of carbon used.[9-14] However, despite the high initial capacities reported, capacity retentions are poor and the cells show capacity fading already after a few cycles due to severe and irreversible volume expansion (more than 300%) upon cycling. Several attempts were reported to mitigate the degradation of BP and to improve the overall cyclability, as for instance (i) the use of fluoroethylene carbonate (FEC) additive in the electrolyte to form a more stable solid electrolyte interphase (SEI), (ii) an upper cut-off potential of 0.8 V (vs Na$^+$/Na) to enhance reversibility [12-14] or (iii) the use of large amounts of conductive carbon to buffer the volume expansion during cycling. The latter was mostly achieved by producing P/C nanocomposites from red phosphorus and carbon via high energy ball milling, often alongside the direct phase transformation of red to black phosphorus.[7,15,16] The extent of the phase transformation depends on experimental parameters, such as the spheres/material ratio, rotation speed and milling time.[17] The optimized phosphorus/carbon mass ratio was determined to be 7/3 w/w.[7] $G.$-$L.$ Xu et al. prepared nanostructured BP-MWCNT (multi-walled carbon nanotubes) composite anodes for SIB by high energy ball milling which delivered specific capacities of

around 1700 mAh g^{-1} for 100 cycles at relatively high charge/discharge rates.[18] Similar performance was observed in case of other composites such as BP-Super P, BP-graphene[19] or BP-MWCNTs including a cross-linked binary binder (poly acrylic acid-carboxymethyl cellulose sodium salt, PAA-NaCMC).[20] The extent of improved electrochemical performance in these studies is dependent on parameters such as electrode morphology, microstructure, and chemical interactions among the components. It was demonstrated, for instance, that in case of nanostructured composites, the rate capability is significantly improved.[18] Several spectroscopic investigations recently proved the presence of strong P—O—C and even P—C bonds which seems to facilitate the (de-)sodiation in P/C anodes. The proposed mechanism suggests that such stable crosslinking units form three-dimensional networks with well interconnected covalent bonds, which could enhance the anode mechanical properties and create highly conductive pathways. The consequent result is an elastic buffer that accommodates the severe volume expansion during the reversible sodium insertion/extraction process and enhances the electron conduction, thereby delivering better electrochemical performances.[19–21] A much less addressed issue of P-based active materials is their instability towards air/O$_2$ and the release of phosphoric acid,[22,23] making them incompatible with aluminium foil as current collector. However, one of the most significant cost reduction factors of SIBs over conventional LIBs is the possibility of using Al foil as current collector for the anode, due to the slightly higher redox potential of Na/Na$^+$ compared to Li/Li$^+$ and, hence, the prevention of alloy formation.[4] Nevertheless, most studies in common literature report phosphorus-based anode materials for Sodium-ion batteries on copper foil as current collector. To our best knowledge, only one work in literature reports on the electrochemistry on P anodes on Al, describing composite electrodes based on black P/acetylene black. However, this article was not focused on the stability issue and/or optimization aspects concerning the use of Al as current collector.[10] Herein, we investigate the microstructural and electrochemical properties of composite P/C anodes for Na-ion cells, synthetized via high energy ball milling at constant spheres/material ratio and different milling times (2 h and 54 h). The electrochemical performance is compared to the one of pure BP electrodes to determine the role of C in the sodium storage mechanism. To gain insights into the structure-property correlation, the anodes were characterized by X-rays diffraction (XRD), field-emission scanning electron microscopy and energy-dispersive X-ray spectroscopy (FE-SEM/EDX), X-ray photoelectron spectroscopy (XPS) and *post mortem* SEM-FIB/EDX analysis. Finally, electrode processing was performed with

aqueous-based slurries and under exclusion of air, in order to allow the use of aluminium at the current collector.

4.3. Material and Methods

4.3.1. Synthesis of Black Phosphorus

Black Phosphorus (BP) was synthetized starting from commercial Red Phosphorus (RP) (Sigma Aldrich, > 97%) by means of High Energy Ball Milling (HEBM), as described in detail in Ref. 15. In summary, proper amounts of red P were inserted in sealed stainless-steel jars with spheres/powder ratios (ζ) of 40/1 (P-40:1) and 110/1 (P-110:1), and milled at 500 rpm for 2 h. Similarly, composites of phosphorus and conductive Carbon (P/C) were prepared via HEBM of red phosphorus and C-Nergy Super C65 (Imerys) in a weight ratio 7/3. The milling rate and the spheres/powder ratio (ζ) were 500 rpm and 30/1, respectively. Two significantly different milling times were chosen, 2 h (BC_2h) and 54 h (BC_54 h). However, a control sample obtained with an intermediate milling time of 5 h (BC_5h) was also prepared and preliminary characterized to better investigate the mixing time effect on the structure and electrochemistry of P/C composite anodes. The manipulation of the products (jar filling and emptying) before and after the synthetic process was carried out in a glove box under Ar atmosphere (UniLab-MBraum, H_2O and O_2 levels < 0.1ppm).

4.3.2. Structural, Compositional and Morphological Characterization

Powder X-ray diffraction patterns (XRDP) of the active materials (P-40:1, P-110:1, BC_2h and BC_54h) were collected by means of a Bruker Advance D8 diffractometer (Cu-Kα: $\lambda =$ 0.154 nm) using an Al sample holder. The data was acquired in the 2θ range from 10° to 60°, with scan step of 0.02 and a fixed counting time per step of 4 s. XPS spectra were recorded using a modified Omicron NanoTechnology MXPS system equipped with a monochromatic X-ray source (Omicron XM-1000) and an Omicron EA-127 energy analyzer. The exciting radiation was Al Kα (hυ = 1486.7 eV), generated operating the anode at 14-15 kV and 10-20 mA. The experimental spectra were reconstructed by fitting the secondary electrons' background to a Shirley function and the elastic peaks to pseudo–Voigt

functions described by a common set of parameters (position, FWHM, Gaussian-Lorentzian ratio) free to vary within narrow limits. During the fitting procedures the Gaussian–Lorentzian ratio was left free to vary between 0.6 and 0.9. Field Emission-SEM experiments (FE-SEM) were carried out on the active materials (BP and P/C) by a Zeiss Auriga electron microscope equipped with a field emission source and a Bruker energy dispersive X-ray spectroscopy (EDX) probe. SEM experiments were carried out by a PHILIPS-FEI XL 30 ESEM instrument equipped with an EDS probe. Focused-ion beam-scanning electron microscopy (FIB-SEM) of the pristine and cycled electrodes was performed on a Zeiss Crossbeam 340 field-emission electron microscope, equipped with a Capella Focused Ion-Beam (FIB, gallium ion source). EDX maps were acquired with an energy dispersive X-ray (EDX) spectrometer (Oxford Instruments X-Max Xtreme, 100 mm^2, 1-5 kV). Cycled electrodes were recovered in an Ar filled glove box, carefully rinsed with dimethyl carbonate (DMC) and transferred to the microscope under Ar atmosphere in a specially designed transfer box (Sample Transfer Shuttle, SEMILAB). Micrographs were acquired from the top, under a tilt-angle of 54° and in cross-sectional configuration after FIB preparation using smartSEM software for tilt correction to compensate for the image distortion due to the tilt of 54° to the optical axis. To avoid strong curtaining and sample damage, low currents of 15 nA and 1.5 nA at an acceleration voltage of 30 kV were chosen to mill and polish the cross-sections, respectively.

4.3.3. Anode Preparation and Cell Assembly

Electrode slurries were prepared by mixing 50 wt% of active material (BP or P/C), 30 wt% Super C65 and 20wt% binder (Na-CMC and PAA in a weight ratio of 1:1 dissolved in deionized water) in a planetary ball mill at 200 rpm for 2 h, followed by a 10 min break and another 2 h of milling in reverse direction. The solid content of all slurries was kept between 12% and 15%. After ball milling, the slurries were casted on aluminium foil (UACJ) using a doctor blade at the speed of 50 mm s^{-1} and a wet film thickness of 100 μm and immediately dried under vacuum at 80°C for 1 h. The resulting mass loadings ranged between 1.1 mg cm^{-2} and 1.5 mg cm^{-2}. The whole process of electrode preparation was conducted without exposition to O_2, by de-aerating water for the slurry preparation and avoiding ambient atmosphere to reduce any oxygen contamination and to ensure better compatibility with the aluminium current collector.

4.3.4. Electrochemical Characterization

Round disc electrodes with a diameter of 12 mm were cut and dried at 100°C in vacuum for 12 h.

All electrochemical measurements were performed in Swagelok® type three-electrode cells assembled in an Ar-filled glove box (levels for H_2O and O_2 < 0.1 ppm). Na metal was used both as reference and counter electrode. Electrodes were separated with a Whatman glass fiber separator, soaked in a solution of 1M $NaPF_6$ in EC:PC (ethylene carbonate-propylene carbonate, 50:50 wt%) with 2 wt% FEC and 5 wt% NaTFSI (200 μl). Cells were galvanostatically cycled on a Maccor Series 4000 battery cycler from 0.02 V to 2 V. All potentials reported refer to the Na/Na$^+$ quasi-reference couple. Electrochemical Impedance Spectroscopy (EIS) was also carried out on sodium half-cell with P/C composite as anode at OCV before and after the galvanostatic cycling at 0.05C. Nyquist plots were collected in the frequency range 100 KHz - 10 mHz at 50 mV as voltage amplitude and 4 s as integration time.

4.4. Results

4.4.1. Pure BP and P-C Composite: Morphology, Structure, and Chemical Composition

Pure BP and P-C composites were synthetized starting from commercial red phosphorus (RP), which was ball milled as pure or mixed with proper amount of Super C65 (7/3 w/w P/C) at 500 rpm by changing the milling time t and ball/powder ratio ζ. Four samples were produced: (i) two pure phosphorus samples, both milled for t = 2 h with ζ= 40:1 and 110:1, (labelled as P_40:1 and P_110:1, respectively); and P-110:1, respectively); (ii) two P-C composites, obtained at two different milling times (t = 2 h and t = 54 h) and ζ = 30:1 (labelled in the following as BC_2h and BC_54 h).
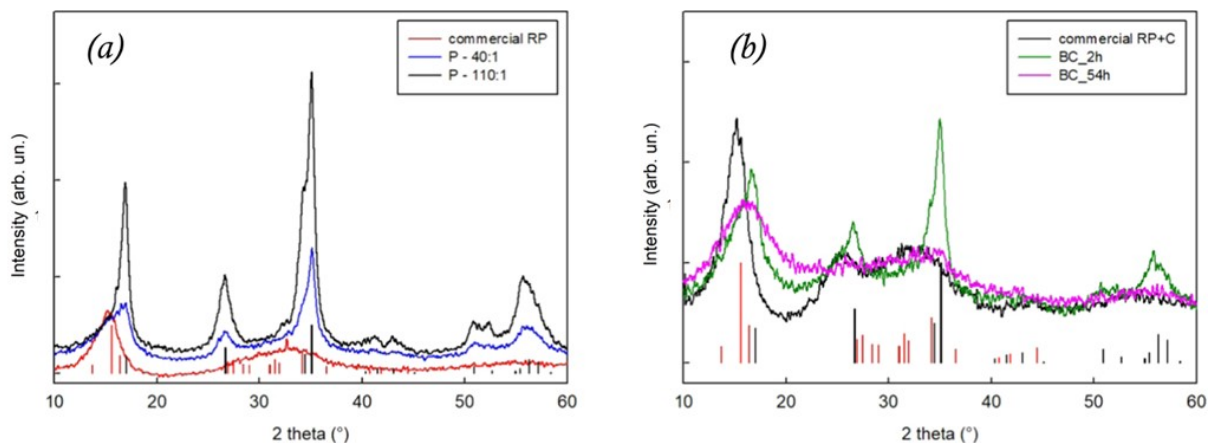
Figure 4.1. Experimental XRDP of pure phosphorus (a) and the P/C composites (b), together with those of commercial RP and a mechanical mixture of RP and C prior to HEBM added for comparison. Vertical bars refer to the Bragg intensities related to RP (red) and BP (black) as reported in the PDF cards 44-0906 and 76-1958, respectively.

Figure 4.1 shows the XRDP acquired on the two BP samples (a) and on the composites P/C (b). For comparison, the XRDP of commercial RP and of the mechanical mixture RP/C prior to HEBM are included in the two panels, respectively. Commercial red phosphorus is characterized by broad peaks centred at around 15° and 32° degrees in 2θ (PDF 44-0906); crystalline black phosphorus can be indexed according to the orthorhombic phase, crystallizing in the *Cmca* space group (PDF 76-1958). RP is famous for its amorphous structure, but it has been shown to adopt also different crystalline modifications.[24] In particular, two crystalline structures are recognized as Hittorf's violet phosphorus and fibrous red phosphorus.[25] The structure reported in PDF card 44-0906 is indexed as monoclinic, in the *P2/c* space group, and has been variously named as "red phosphorus," "violet Hittorf phosphorous," or "red Hittorf phosphorus." In case of pure BP, ball milling conditions were chosen to obtain one sample of fully crystalline BP and a second one containing roughly 20% of unconverted RP.[17] As discussed in detail in our previous work,[17] the HEBM experimental parameters may be varied to modulate the RP-BP conversion. As the balls/powder ratio increases, the degree of RP → BP conversion increases. Figure 4.1*a* depicts this conversion with a decrease of the main reflection of RB (15.61° 2θ) and an increase of the first reflection of BP (17.02° 2θ) for P-110:1, in contrast to P-40:1. A detailed quantification of the RP/BP ratio as a function of HEBM parameters is reported in Ref. 17. Figure 4.1*b* shows the comparison between the XRD patterns of the two P/C composites where a significant difference between the realized samples can be observed. As reported in Figure 4.2*a*, BC_2h depicts a XRD pattern very similar to that of pure BP-40:1, suggesting

that both samples have a similar mixture of RP and BP. The P/C composite ball milled for a longer time (54h, BC_54h), however, shows a very different XRD pattern compared to a pure phosphorus reference sample prepared under the same ball mill conditions (Figure 4.2*b* for a direct comparison).
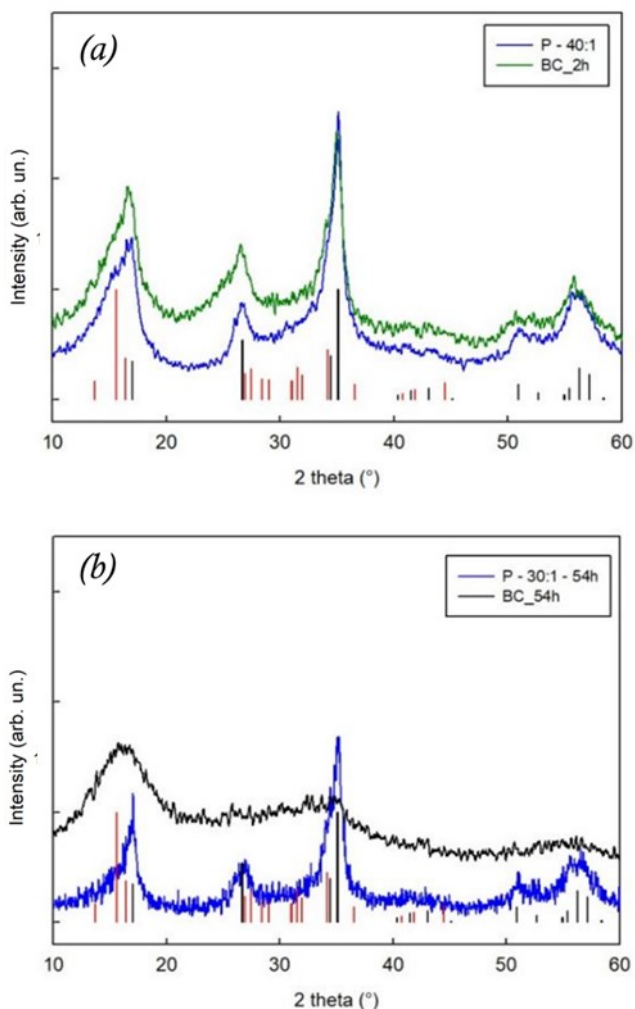

Figure 4.2. *Experimental XRDP of the BP samples obtained at similar milling time: **(a)** pure BP and the corresponding composites BP/C obtained after 2 hours of HEBM; **(b)** pure BP and the corresponding composites BP/C obtained after 54 hours of HEBM. Verticals bars refers to the Bragg intensities related to RP (red) and BP (black) as reported in the PDF cards 44-0906 and 76-1958, respectively.*

While pure phosphorus ball milled for 54 h (P-30:1–54 h) shows the sharp reflections assigned to crystalline BP (again indicating a mixture of RP and BP), they are absent in the pattern of the composite (BC_54h). It is difficult to discern, however, based on the present data, whether the very broad peaks of BC_54h are due to amorphization of the BP component or due to the formation of a novel phase. The morphology and surface composition of the

two P/C composite materials have been investigated by FE-SEM/EDS as shown in the Figure 4.3.
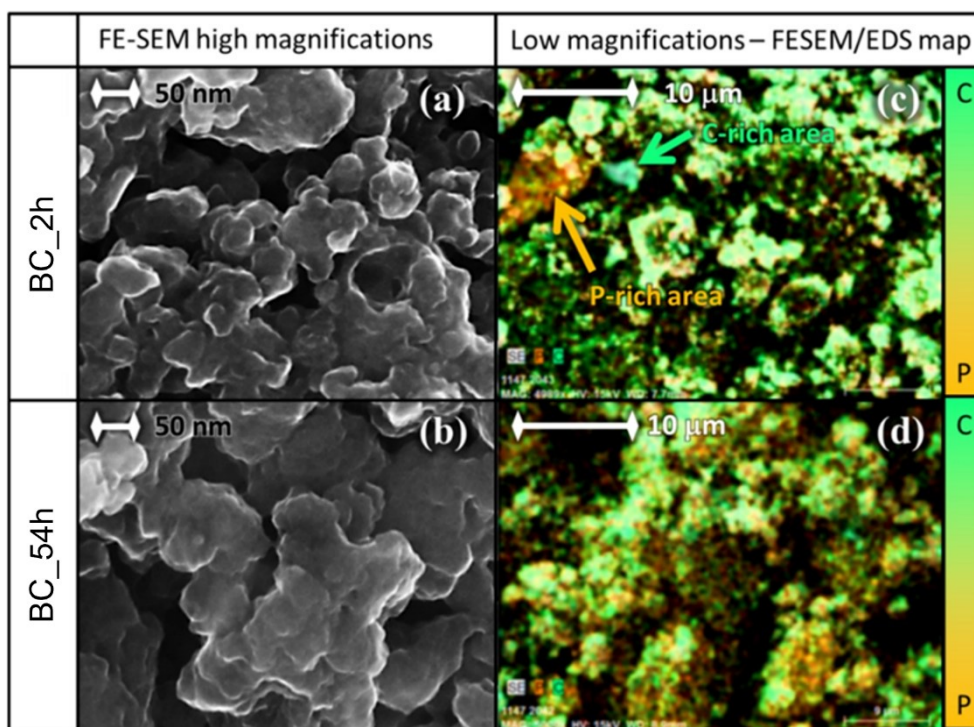

Figure 4.3. *(a, b) FE-SEM micrographs at high magnification and (c, d) combined FE-SEM/EDX areal maps of the two P/C-composite materials ball milled 2 and 54 h, respectively.*

Both SEM micrographs (Figures 4.3*a,b*) show secondary irregular aggregates of linear sizes in the range of 50-300 and 150-500 nm for the two P/C-composite materials ball milled 2 and 54 h, respectively. These secondary aggregates are constituted by similar, smaller nanoparticles of about 10-30 nm, embedded in a smooth outer material. This suggests an increasing agglomeration of primary particles by ball milling and, thus, forming larger secondary aggregates. At low magnification the composition analysis of the materials surfaces by EDX highlights a C/P atomic ratio of 1.5 ± 0.3 and 1.1 ± 0.3 for the two P/C-composite materials ball milled 2 and 54 h, respectively. These values are in good agreement with the expected C/P = 1.1 molar ratio derived from the 3/7 weight ratio used for the synthesis. On the other hand, the FE-SEM/EDX combined areal maps highlight a different dispersion of the elements on the materials surfaces. In fact, the C/P intermixing is much more homogeneous in the sample ball milled for 54 h compared to the one ball milled for 2 h, which shows isolated P-rich and C-rich areas. The outer surfaces of the powder samples have been investigated by XPS as shown in Figure 4.4. The surface of both samples is constituted by a mixture of carbon, phosphorus and oxygen (see Figure 4.4*a*).
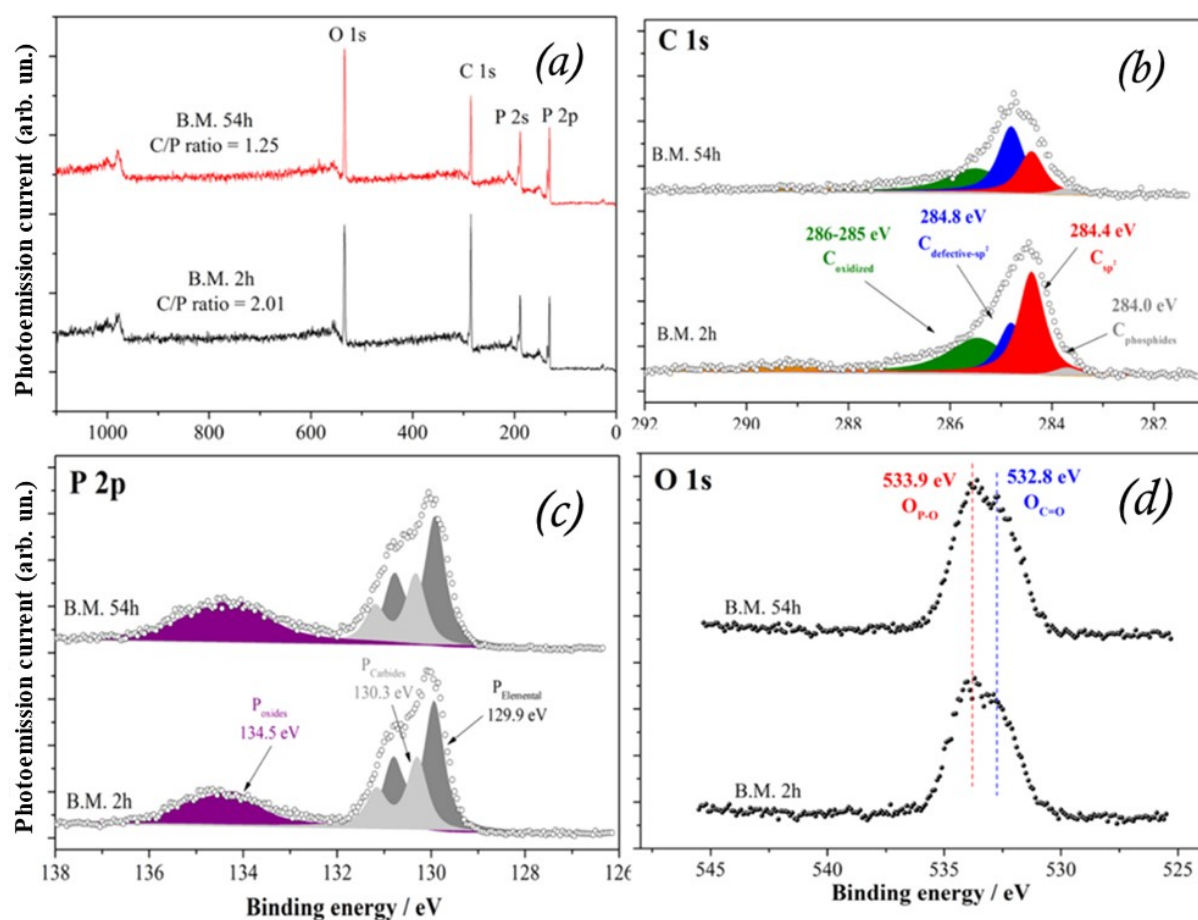
Figure 4.4.. (a) *Wide XPS spectra and details of the **(b)** C 1s, **(c)** P 2p and **(d)** O 1s regions measured for the two P/C-composite materials ball milled 2 and 54 h, respectively.*

In consideration of the limited penetration of the X-ray beam (2-3 nm in carbonaceous materials), the presence of oxygen is likely related to the pristine materials impurities and to the minor, unavoidable contamination of the samples.[26] The C/P atomic ratio derived from the XPS intensities decreases upon increasing the ball milling time, from 2.01 to 1.25 for the two P/C-composite materials ball milled 2 and 54 h, respectively. The C/P value after 54 h of ball milling is in close agreement with the EDX value and the expected 1.1 molar ratio. This trend is likely related to the more intimate mixing of the constituents and to the more extended nanosizing of P particles promoted by ball milling. Experimental XPS spectra and its corresponding theoretical reconstruction in the C 1s, P 2p and O 1s regions are shown in the Figures 4.4*b*, *c* and *d*, respectively. In both cases the C 1s peak can be fitted by two major components centred at 284.4 and 284.8 eV. Their relative intensities, however, are reversed. The component centred at 284.4 eV is typical of sp^2 graphite-like carbons,[27] whereas the signal at slightly higher energy (284.8 eV) is commonly attributed to "defective graphite."[28]

85

Thus, the reversal of the $C_{sp2}/C_{defective\text{-}graph}$ peaks ratio at longer milling time confirms the expected incorporation of defects in the graphitic structure of the pristine Super C carbon particles.[29] Besides these two main components, other minor signals are found and fitted in both samples at 283.7 eV and in the 285-289 eV range. The component at binding energies < 284 eV can be attributed to carbon-phosphides (or phosphorus-carbides, C-P) as already observed by *Capone et al.*[30] and, thus, suggesting the formation of interphases between the phosphorus particles and the surrounding carbon matrix. Remarkably the C-P signal is almost unaltered when the milling time is increased from 2 to 54 h. This trend is in line with the negligible evolution of the components at binding energies >285 eV upon milling due to oxidized carbon species. The reconstructions of the phosphorus 2p peak in the XPS spectra of the two samples match the results in the C 1s region. The P 2p region shows three doublet peaks (*i.e.* 3/2 and 1/2 components of the 2p signal) at 129.9, 130.3 and 134.5 eV. The first doublet can be attributed to elemental phosphorus (P—P direct bonds) whereas the second doublet to the C-P interphases already observed in the C 1s region. The comparison between BC_2h and BC_54h suggests that both components are not modified by extensive ball milling. The third component at binding energies >134 eV is likely due to the overlapping of many peaks related to oxidized phosphorus species (P—O bonds). The O 1s spectral region is unaltered upon ball milling, alike the P 2p one. The O 1s region is constituted by two partially overlapping peaks at 532.8 and 533.9 eV due to C—O and P—O species likely originated by unavoidable impurities and contaminations.[27] Overall the materials surfaces are constituted by elemental phosphorus and graphitic carbon likely interconnected by C-P interphases; minor impurities due to oxidized phosphorus species are also present. The carbon particles incorporate defects upon milling whereas elemental phosphorus remains almost unaltered even after 54 h of ball milling.

4.4.2. Electrochemical Performance

Pure phosphorus and P/C-composite electrodes were cycled in sodium half cells employing an optimized liquid electrolyte solution of 1 M $NaPF_6$ in EC:PC (50:50 wt%) with 2 wt% FEC and 5 wt% NaTFSI. As stated above, Al metal foil was selected as current collector, instead of copper, in order to develop novel P/C-based anodes with reduced cost impact. In order to fit further sustainability requirements, an aqueous electrode processing was conducted by using green binders. As known from the literature,[31] compared to the other allotropes (*e.g.* WP and RP), BP is unaffected by water alone (without O_2), which cannot cause degradation of the black phosphorus since it only weakly physisorbs on the BP surface and does not dissociate on it. In contrast, it has been spectroscopically proved that BP seriously and rapidly degrades in presence of oxygen, because the oxidative process involves an easy dissociative chemisorption of O_2. The oxidation causes two significant phenomena: (i) the turn of the hydrophobic pristine BP surface into hydrophilic; (ii) the change of the black phosphorus electronic structure induced by the O_2 adsorption.[31] The former one causes the release of PH_3 and H_2 and the formation of strong acid as H_3PO_4,[22] with consequent safety issues; the latter leads to the degradation of the electronic properties. Both the phenomena are seriously detrimental for the anode electrochemical behaviour. In order to correlate the influence of the Oxygen environment (air or aerated water) on the electrochemical performance of BP-based anodes, the pH value evolution during the slurry preparation under atmosphere conditions was carefully investigated. Figure 4.5*a* shows the abrupt pH decrease from 8 to 2 when the P/C composite is added to the binder solution, corresponding to a significant acidification of the resulting slurry.
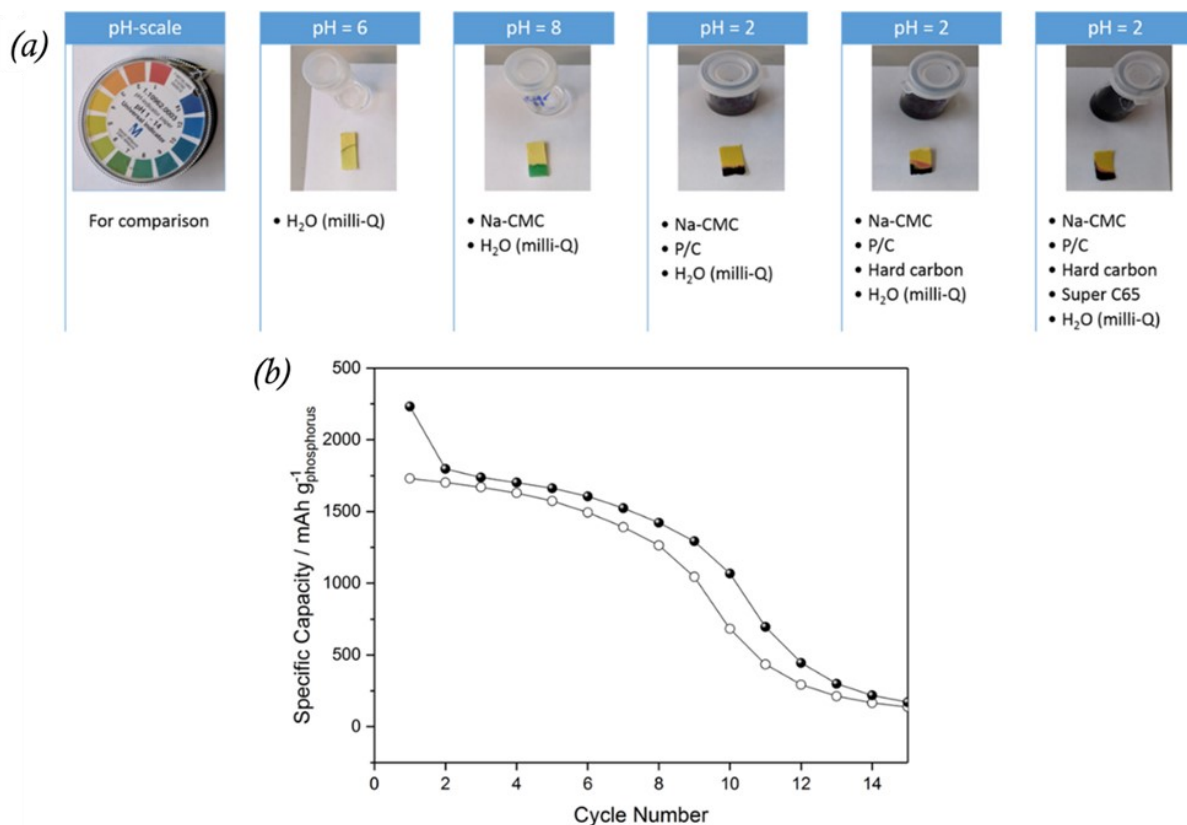
Figure 4.5. (a) pH value evolution upon slurry preparation under ambient atmosphere conditions. The slurry turns highly acidic after addition of P/C-composite exposed to air. (b) Cycling performance of a P/C-composite electrode processed under ambient atmosphere conditions.

Such harsh conditions could favour the corrosion of the current collector with consequent failure of the electrochemical performances. Figure 4.5*b* plots the galvanostatic cycling at 0.05C of a half-cell including a P/C-based anode prepared under ambient condition and exposed to air. It is noticeable that specific capacity higher than 1500 mAh g^{-1} is delivered during the initial charge/discharge process. However, a rapid failure occurs after only 6 cycles of desodiation/sodiation, confirming the strong effect of oxygen on the BP electrochemistry. In the lights of these results, the anodes were processed in O$_2$-free (or very low content) conditions, as described in the experimental section.

Both pure phosphorus and P/C composites were galvanostatically cycled at low currents (0.05C, 1C = 2596 mA g^{-1}). Figure 4.6*a* reports as an example the resulting differential capacity plot for the BC composite (t = 54 h) in the explored voltage range.
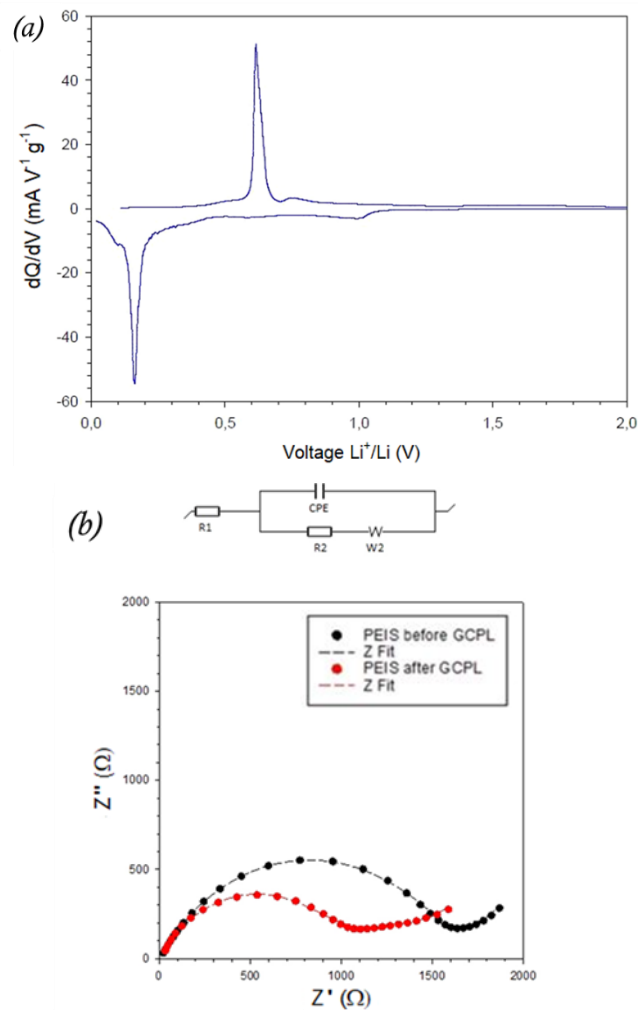
Figure 4.6. **(a)** *Differential capacity behaviour between 0.02 and 2 V obtained from the galvanostatic cycling at 0.02C for the sodium half-cell including BC_54h as composite anode. **(b)** Nyquist plots collected by electrochemical impedance spectroscopy for the sodium half-cell including BC_54h as composite anode at OCV before and after the galvanostatic cycling tests. The inset shows the equivalent circuits model used to fit the plot. R_2 is the charge transfer resistance R_{ct}.*

During the cathodic potential scan, one sharp and intense peak is observed at ~0.65 V, followed by a small signal at 0.75 V, corresponding to the sodiation process of BP, whereas on the reverse anodic process, another well-defined peak is present at 0.15 V, which is ascribed to the desodiation from the reduction products. More precisely, such signals indicate the expected well reversible formation of Na_xP phase (up to x = 3). Figure 4.6*b* shows the Nyquist plots collected for the same sodium half-cell by means of electrochemical impedance spectroscopy at OCV, before and after the galvanostatic cycling tests. The spectra have been fitted by using the equivalent circuits model shown in the figure inset, which allows to determine the interface parameters, in terms of charge transfer and diffusion process. The plots show the typical features of this kind of device, presenting a depressed semicircle in the medium frequency domain that describes the charge transfer at the anode

and a linear region compatible with the Warburg element representative of the Na^+ diffusive process. Compared to the pristine electrode (R_{ct} = 1220 Ω), the charge transfer resistance, R_{ct} at the end of cycling test (after 35 cycles) is lower (R_{ct} = 874 Ω) and this is typically attributed to the increasing of the electrical contact after the activation. Instead, comparable Warburg coefficients, σ_w, (σ_w = 490 Ω s$^{-0.5}$, σ_w = 506 Ω s$^{-0.5}$) are obtained from the spectra before and after the cycling test, respectively. Figure 4.7*a* shows the first cycle potential profiles of electrodes comprising pure phosphorus ball-milled with ball to powder ratios of 40:1 and 110:1, *i.e.*, lower and higher amounts of black phosphorus, respectively. Both samples depict the typical stepwise sodiation (Na_xP species) with a long potential plateau at around 0.3 V vs Na metal due to the final Na_3P formation. The higher specific capacity of P-110:1 at around 0.5 V can be ascribed to more Na^+ being intercalated into black phosphorus sheets due to higher amounts of BP[32] and, eventually, more severe electrolyte decomposition due to smaller particle size. The higher amount of BP in P-110:1 has only a minor effect on the first specific sodiation capacity, which is higher than the theoretical 2596 mAh g^{-1} for both electrodes. The first desodiation capacity, however, is significantly higher for P-110:1 compared to P-40:1, *i.e.*, 1532 mAh g^{-1} and 1127 mAh g^{-1}, respectively. Nonetheless, the cycling performance is not influenced by the amount of BP in the sample, as depicted in Figure 4.7*b*, and both cells show severe capacity fading already in the initial cycles.
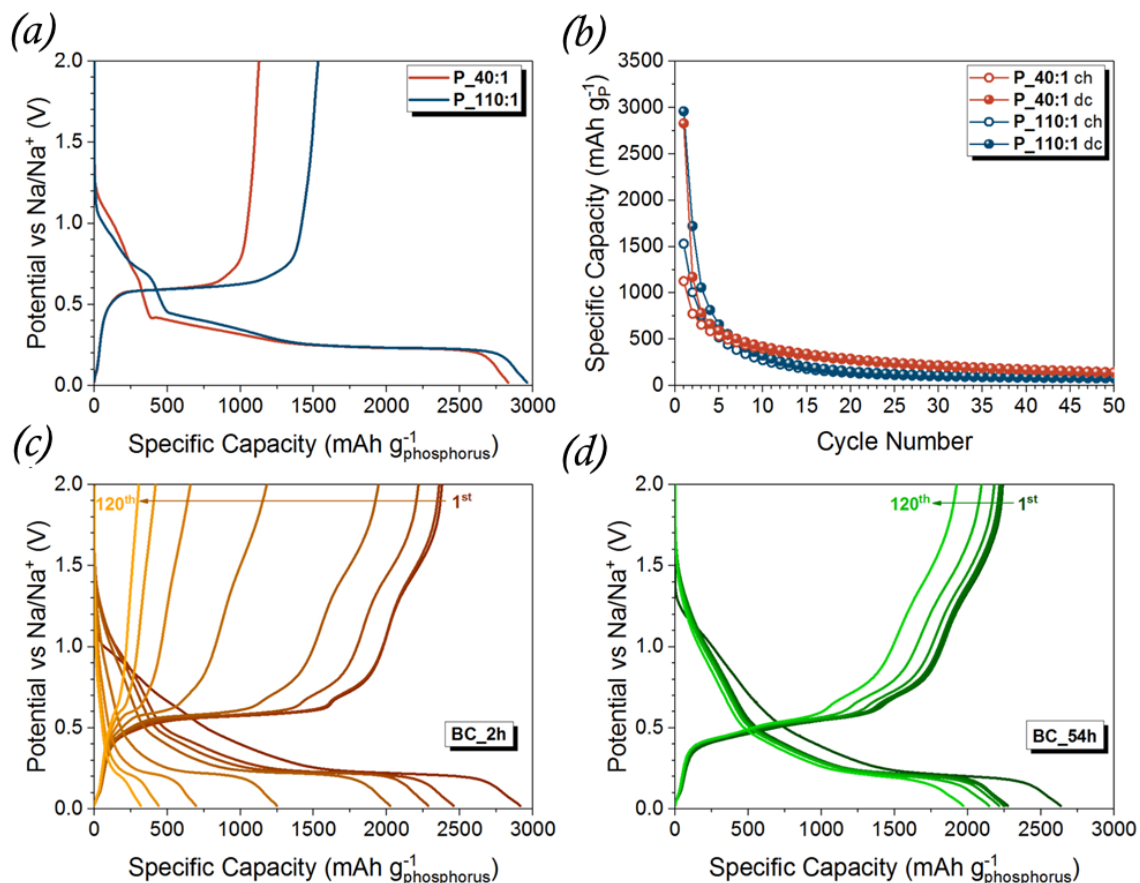
Figure 4.7. *Electrochemical characterization of pure P and the P-C-composite. **(a)** First cycle potential profiles of electrodes with phosphorus ball-milled under different conditions and **(b)** corresponding cycling performance. Potential profiles of the P/C-composite ball-milled for **(c)** 2 h and **(d)** 54 h. Electrolyte: 1 M $NaPF_6$ in EC:PC (50:50 wt%) +5 wt% NaTFSI +2 wt% FEC. Applied current rates: 1st cycle 0.02C, consecutive cycles 0.05C (1C = 2596 m A g^{-1}).*

The capacity retention can be increased when phosphorus is ball-milled with conductive carbon (Super C65). A milling time of 2 h is already sufficient to push the first cycle desodiation capacity to 2378 mAh g^{-1} based on the mass of BP, and the capacity retention in the second cycle to > 99% (Figure 4.7c). In subsequent cycles capacity fades by a shortening of the (de)-alloying plateau, indicating that more and more phosphorus gets inactivated due to active material pulverization. Similar instability is also preliminary observed in case of sodium half-cell including an anode based on P/C composite ball milled for an intermediate time, *e.g.* 5 h (BC_5h). Such composite is not fully amorphous like the BC_54h sample, as shown by the XRD pattern in Figure 4.8, where the main peaks of the BP orthorhombic structure are wider, much less intense but still evident.
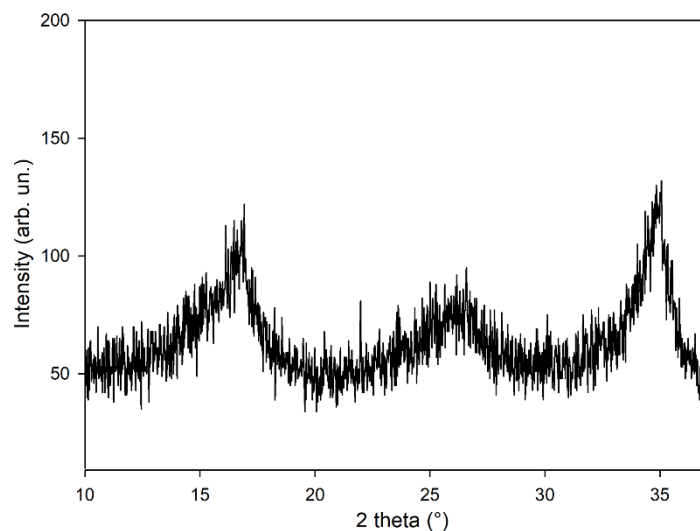
Figure 4.8. *Experimental XRDP of the composite BP/C obtained after 5 hours of HEBM (BC_5h).*

In this case the capacity is higher than 1600 mAh g^{-1} based on the composite mass (about 2293 mAh g^{-1} based on P mass) during the initial cycles. However, it then abruptly decreases to 600 mAh $g_{composite}^{-1}$ (~793 mAh g_P^{-1}) with an overall capacity fading of 64% after 30 cycles as reported in Figures 4.9*a,b*).
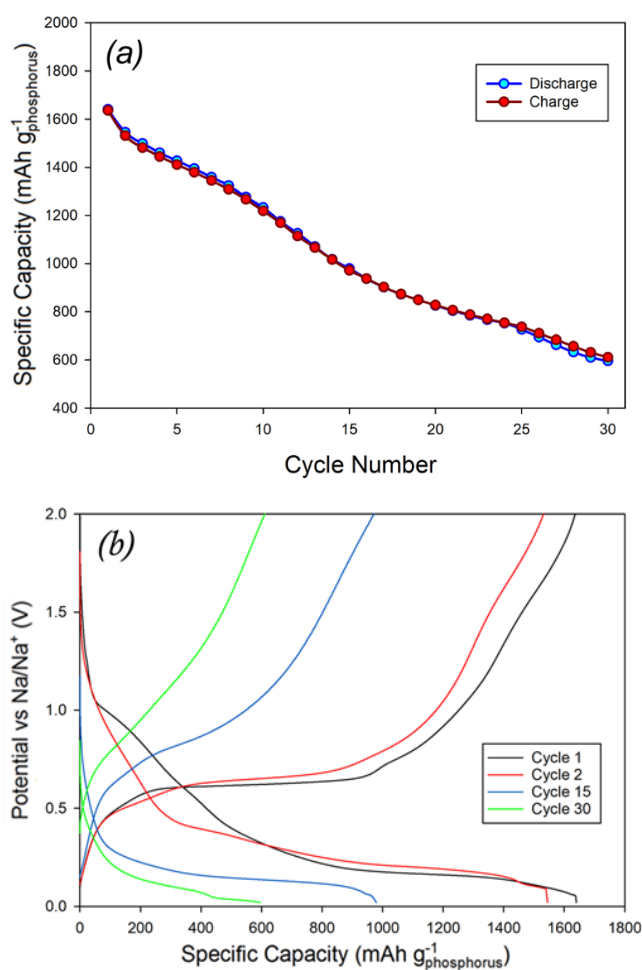
Figure 4.9. *Cycling performance (a) of the P/C-composite ball milled for 5h (BC_5h) based on the mass of the active material (composite) and the corresponding potential profiles (b). Electrolyte: 1 M NaPF$_6$ in EC:PC (50:50 wt%) + 5 wt% NaTFSI + 2 wt% FEC. Applied current rates: 0.05C (1C = 2596 mA g^{-1}).*

It is only the significant increase of the ball-milling time, *t*, to 54 h, which drastically reduces the shortening of the alloying plateau and, thus, the capacity fading (Figure 4.7*d*). All the composites show more slope like potential profiles compared to pure phosphorus electrodes resulting from the carbon matrix. As evidenced from XPS, BC_54h sample shows defective sites in the Carbon (sp^2-defective graphite), which can be a reason for sodiation to start at higher potentials in the BC_54h compared to BC_2h (1.3 V vs 1.0 V). In fact, it has been shown recently that the presence of structural defects in hard carbons significantly improves Na-ion insertion.[30–35] Figure 4.10*a* depicts that stable cycling is possible for up to 80 cycles with a specific capacity of about 2250 mAh g$_P^{-1}$, based on the BP mass (very close to the theoretical value of 2596 mAh g^{-1}) and a desodiation capacity retention of 93.5% (compared to 17.5% in case of the composite balled milled for 2 h).
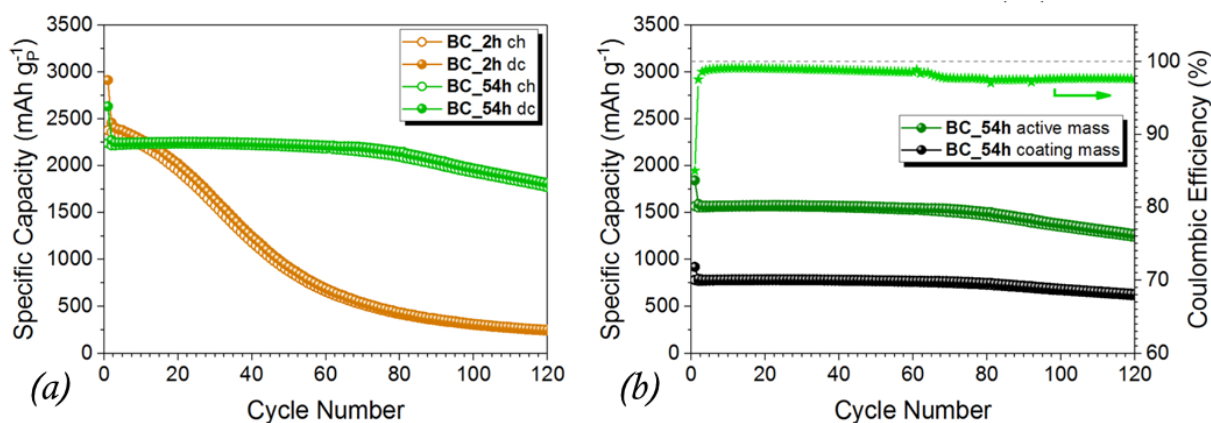
Figure 4.10. Electrochemical characterization of pure P and the P-C-composite. Cycling performance of the P/C-composite ball milled for (a) 2 h and (b) 54 h based on the mass of the active material and the whole electrode coating. Electrolyte: 1 M NaPF$_6$ in EC:PC (50:50 wt%) +5 wt% NaTFSI +2 wt% FEC. Applied current rates: 1st cycle 0.02C, consecutive cycles 0.05C (1C = 2596 mA g^{-1}).

After 120 cycles, the BC_2h and BC_54h show capacity retentions of around 10% and 80%, respectively. The formation of phosphorus-carbides is typically ascribed as the main reason for improved electrochemical performance in the case of P-based composites.[17,19] However, XPS data showed that the amount of carbides in the composites is unaltered when milling times are increased. A different explanation for the enhanced cycling stability might be, for instance, a more homogeneous distribution of carbon and phosphorus in the composite prepared using longer milling times, which is in good agreement with SEM micrographs. In fact, the phosphorus nano-domains allow for a homogeneous embedding into the carbon matrix, which eventually enhances the electronic conductivity of the material and, thus, favours electrochemical insertion of Na$^+$ into the nano-domains. Similar experimental observations were discussed in a recent review.[5,7] The absence of isolated, bulky phosphorus domains as well as the higher degree of amorphization of the BC_54h (as shown by XRD) furthermore prevent excessive volume expansion. First cycle coulombic efficiency of the BC_54h is above 80% and stays above 98% in the first 70 cycles. In subsequent cycles it drops to around 97%, *i.e.*, values which are certainly too low for application in a full cell. When capacities are calculated based on the weight of the P/C composite (active material) and the whole electrode coating, initial desodiation capacities are above 1500 mAh g$_{composite}^{-1}$ and 750 mAh g$_{electrode}^{-1}$, respectively (Figure 4.10*b*). By considering the value based on the composite mass and the P/C ratio, it is possible to isolate the sodiation contribution of BP in the composite, which results to be dominant.[36] As shown in Figure 4.10*a*, capacity higher than 2250 mAh g$_P^{-1}$ based on the BP, is obtained, which is very close to the theoretical value.

94

The Na insertion/deinsertion capacity of Super C65 alone is, in fact, only 100-150 mAh g^{-1} at the same investigate current density[37] and its contribution counts for about 30-45 mAh g^{-1}. Despite a decrease to 97% of the coulombic efficiency, the observed capacity is significantly higher than the ones for graphite in commercial lithium-ion batteries and for hard carbons in state-of-the-art sodium-ion batteries. Furthermore, to the best of our knowledge, such values are unprecedented since achieved on aluminium current collector, while most studies on P-based anodes in common literature show results on copper current collector.[23,38,39,40] Recently, *Dahbi et al.* described a BP/acetylene black composite anode for NIBs, casted on Al foil.[12] The resulting electrode delivered specific capacity of 1500 mAh g^{-1}, based on P mass, which seriously falls to 800 mAh g^{-1} over 25 cycles. Such electrochemical properties were discussed in terms of interface instability and no reference to the slurry optimization with respect to the current collector was discussed. Some improvements were observed by adding proper electrolyte additives, as fluoroethylene carbonate (FEC) or vinylene carbonate (VC), which are particularly efficient for the Na cells by forming more stable SEI. In this case the capacity fading over cycling was limited to 91% for the initial 25 cycles.[12] Figure 4.11 shows *post mortem* SEM-FIB analysis of the BC_54h sample. The cross section of a pristine electrode (Figure 4.11*a*) reveals that the electrode is highly porous, and the coating is around 15 μm thick. The active material particles are rather inhomogeneously distributed in size, with large domains of up to 3 μm. EDX mapping of the cross sections (Figure 4.11*b*) confirms that phosphorus rich domains vary in size from nm to μm scale.
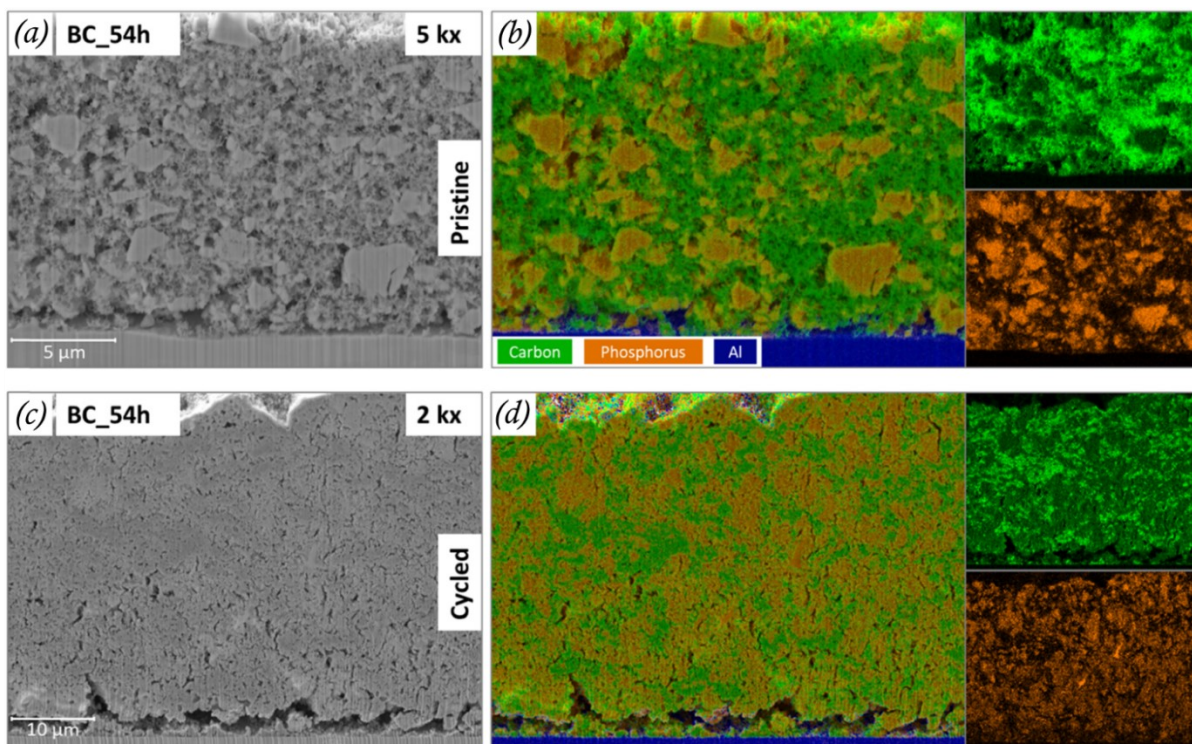
Figure 4.11. *Post mortem SEM-FIB/EDX characterization.* *(a)* *SEM-FIB cross section of a pristine BC_54h composite electrode and* *(b)* *corresponding EDX mapping.* *(c)* *SEM-FIB cross section of a cycled BC_54h composite electrode (after 135 cycles) and* *(d)* *corresponding EDX mapping.*

However, carbon is present in the whole cross section of the electrode, with high signal originating from the conductive additive, and low signal from carbon present in the composite (*i.e.*, in the phosphorus rich domains). This indicates that the composite forms secondary particles composed of phosphorus-carbon composite nanoparticles, which is in good agreement with SEM micrographs (see Figure 4.3). The cycled electrode is much less porous (Figure 4.11*c*), indicating that porosity partially helps to buffer the large volume expansion of phosphorus. Coating thickness of the cycled electrode, however, is > 40 µm and, thus, electrode volume expansion is not fully prevented. This could be an explanation for the rather poor coulombic efficiency (see Figure 4.10*b*), *i.e.*, continuous exposure of fresh electrode surface and, hence, continuous electrolyte decomposition. Furthermore, it appears that the coating layer detaches from the current collector, eventually leading to inactivation of the active material coating layer. On the other hand, EDX maps of the cycled electrode (Figure 4.11*d*) clearly show that the secondary particle structure stays intact even after 135 cycles, which explains the excellent cycling performance of the BC_54h composite.

4.5. Conclusion

P/C composites were successfully synthetized via high energy ball milling at a rate of 500 rpm, spheres/material ratio of 30/1 and two different times: 2 h (BC_2h) and 54 h (BC_54h). All the electrochemical characterizations were performed on aluminium current collector thanks to the exclusion of oxygen during aqueous electrode processing. The active materials were investigated by XRD, XPS, SEM-EDX, *post mortem* SEM and galvanostatic cycling. A ball milling time of 54 h resulted in a phosphorus-carbon composite delivering initial specific charge capacities of around 2250 mAh g_P^{-1} and excellent capacity retention of around 80% at 0.05C after 120 cycles. Three phenomena were identified to synergistically improve the electrochemical performance if compared to a composite ball milled for 2 h: (i) longer milling times and, thus, higher energies lead to an almost fully amorphous system which is able to partially buffer the volume expansion, (ii) decrease of the phosphorus particles dimensions (< 500 nm), leading to homogeneous distribution of phosphorus and carbon within the composite secondary particles without isolated P-based domains, and finally (iii) the introduction of defects in the carbon matrix, enabling Na-ion insertion at high potentials and enhancing overall electrochemical performance. The presented phosphorus-carbon composite outperforms state-of-the-art hard carbons in SIBs and graphite in LIBs in terms of specific and volumetric capacity, and the good capacity retention (especially in combination with aluminium current collector) are certainly a major step towards successful future commercialization of SIBs. In conclusion, the proper design of the composite is a very good strategy to overcome the still open challenges of P-based anodes in SIBs, which are all substantially related to the structural instability of black phosphorus over cycling. Future works to further increase the anode stability, rate capability and, last but not least, the insertion/extraction reversibility might point towards, for instance, the investigation of hard carbons as composite component alternative to carbon black, in order to enhance the surface defective sites, which are beneficial for the Na storage, and the use of other green binders, with self-healing capability to limit the P volume expansion.

4.6. Bibliography

1. Tarascon, J.-M.; Armand, M. Issues and challenges facing rechargeable lithium batteries. *Nature* 2001, **414**, 359.

2. Armand, M.; Tarascon, J.-M. Building better batteries. *Nature* 2008, **451**, 652.

3. Scrosati, B.; Garche, J. Lithium batteries: Status, prospects and future. *J. Power Sources* 2010 **195**, 2419.

4. Vaalma, C.; Buchholz, D.; Weil, M.; Passerini, S. A cost and resource analysis of sodium-ion batteries. *Nat. Rev. Mater.* 2018, **3**, 1.

5. Zhang, S.; Ying, H.; Guo, R.; Tao Yang, W.; Han, W.-Q. Vapor Deposition Red Phosphorus to Prepare Nitrogen-Doped $Ti_3C_2T_x$ MXenes Composites for Lithium-Ion Batteries. *J. Phys. Chem. Lett.* 2019, **10**, 6446.

6. S. Zhang, S.; Li, X.-Y.; Yang, W.; Tian, H.; Han, Z.; Ying, H.; Wang, G.; Han, W.-Q. Novel Synthesis of Red Phosphorus Nanodot/$Ti_3C_2T_x$ MXenes from Low-Cost Ti_3SiC_2 MAX Phases for Superior Lithium- and Sodium-Ion Batteries. *ACS Appl. Mater. Interfaces* 2019, **11**, 42086.

7. Fu, Y.; Wei, Q.; Zhang, G.; Sun, S. Advanced Phosphorus-Based Materials for Lithium/Sodium-Ion Batteries: Recent Developments and Future Perspectives. *Adv. Energy Mater.* 2018, **8**, 1702849.

8. Gusmao, R.; Sofer, Z.; Pumera, M. Black Phosphorus Rediscovered: From Bulk Material to Monolayers. *Angew. Chem. Int. Ed.* 2017, **56**, 8052.

9. Marbella, L. E.; Evans, M. L.; Groh, M. F.; Nelson, J.; Griffith, K. J.; Morris, A. J.; Gray, C. P. Sodiation and Desodiation via Helical Phosphorus Intermediates in High-Capacity Anodes for Sodium-Ion Batteries. *J. Am. Chem. Soc.* 2018, **140**, 7994.

10. Mayo, M.; Griffith, K. J.; Pickard, C. J.; Morris, A. J. Ab Initio Study of Phosphorus Anodes for Lithium- and Sodium-Ion Batteries. *Chemistry of Materials* 2016, **28**, 2011.

11. Chen, T.; Zhao, P.; Guo, X.; Zhang, S. Two-Fold Anisotropy Governs Morphological Evolution and Stress Generation in Sodiated Black Phosphorus for Sodium Ion Batteries. *Nano Lett.* 2017, **17**, 2299.

12. Dahbi, M. *et al*. Black Phosphorus as a High-Capacity, High-Capability Negative Electrode for Sodium-Ion Batteries: Investigation of the Electrode/Electrolyte Interface. *Chem. Mater.* 2016, **28**, 1625.

13. Qian, J.; Wu, X.; Cao, Y.; Ai, X.; Yang, H. High Capacity and Rate Capability of Amorphous Phosphorus for Sodium Ion Batteries. *Angew. Chem.* 2013, **125**, 4731.

14. Yabuuchi, N.; Matsuura, Y.; Ishikawa, T.; Kuze, S.; Son, J. Y.; Cui, Y.-T.; Oji, H.; Komaba, S. Phosphorus Electrodes in Sodium Cells: Small Volume Expansion by Sodiation and the Surface-Stabilization Mechanism in Aprotic Solvent. *ChemElectroChem.* 2014, **1**, 580.

15. Lu, W., Zhi, H. X. Yu, X. Recent progress in phosphorus based anode materials for lithium/sodium ion batteries. *Energy Storage Mater.* 2019, **16**, 290.

16. Qin, X.; Yan, B.; Yu, J.; Jin, J.; Tao, Y.; Mu, C.; Wang, S.; Xue, H.; Pang, H. Phosphorus-based materials for high-performance rechargeable batteries. *Inorg. Chem. Front.* 2017, **4**, 1424.

17. Ferrara, C.; Vigo, E.; Albini, B.: Galinetto, P.; Milanese, C.; Tealdi, C.; Quartarone, E.; Passerini, S.; Mustarelli, P. Efficiency and Quality Issues in the Production of Black Phosphorus by Mechanochemical Synthesis: A Multi-Technique Approach. *ACS Appl. Energy Mater.* 2019, **2**, 2794.

18. Xu, G.-L. *et al.* Nanostructured Black Phosphorus/Ketjenblack–Multiwalled Carbon Nanotubes Composite as High Performance Anode Material for Sodium-Ion Batteries. *Nano Lett.* 2016, **16**, 3955.

19. Liu, H.; Tao, L.; Zhang, Y.; Xie, C.; Zhou, P.; Liu, H.; Chen, R.; Wang, S. Bridging Covalently Functionalized Black Phosphorus on Graphene for High-Performance Sodium-Ion Battery. *ACS Appl. Mater. Interfaces* 2017, **9**, 36489.

20. Haghighat-Shishavan, S.; Nazarian-Samani, M.; Nazarian-Samani, M.; Roh, H.-K.; Chung, K.-Y.; Cho, B.-W.; Kashani-Bozorg, S. F.; Kim, K.-B. Strong, persistent superficial oxidation-assisted chemical bonding of black phosphorus with multiwall carbon nanotubes for high-capacity ultradurable storage of lithium and sodium. *J. Mater. Chem. A.* 2018, **6**, 10121.

21. Wu, X.; Zhao, W.; Wang, H.; Qi, X.; Xing, Z.; Zhuang, Q.; Ju, Z. Enhanced capacity of chemically bonded phosphorus/carbon composite as an anode material for potassium-ion batteries. *J. Power Sources* 2018, **378**, 460.

22. Marino, C.; El Kazzi, M.; Berg, E. J.; He, M.; Villevieille, C. Interface and Safety Properties of Phosphorus-Based Negative Electrodes in Li-Ion Batteries. *Chem. Mater.* 2019, **29**, 7151.

23. Xiao, W.; Sun, Q.; Banis, M. N.; Wang, B.; Liang, J.; Lushington, A.; Li, R.; Li, X.; Sham, T.-K.; Sun, X. Unveiling the Interfacial Instability of the Phosphorus/Carbon Anode for Sodium-Ion Batteries. *ACS Appl. Mater. Interfaces* 2019, **11**, 30763.

24. Nilges, T.; Schmidt, P.; Weihrich, R.; Phosphorus: The Allotropes, Stability, Synthesis and Selected Applications. *Encyclopedia of Inorganic and Bioinorganic Chemistry* (Wiley, New York) 2018.

25. Ruck, M.; Hoppe, D.; Wahl, B.; Simon, P.; Wang, Y.; Seiferty, G. Fibrous Red Phosphorus. *Angew. Chem. Int. Ed.* 2005, **44**, 7616.

26. Johansson I.; Somasundaran, P. Handbook for Cleaning/Decontamination of Surfaces (*Elsevier Science B.V., Amsterdam*) 2007.

27. NIST, X-ray Photoelectron Spectroscopy Database (*NIST Standard Reference Database Number 20, National Institute of Standards and Technology, Gaithersburg MD*) 2000, 20899.

28. Carboni, M.; Manzi, J.; Armstrong, A. R.; Billaud, J.; Brutti, S.; Younesi, Y. Analysis of the Solid Electrolyte Interphase on Hard Carbon Electrodes in Sodium-Ion Batteries. *Chem. Electro. Chem.* 2019, **6**, 1745.

29. Lyu, H.; Gao, B.; He, F.; Ding, C.; Tang, J.; Crittenden J. C. Ball-Milled Carbon Nanomaterials for Energy and Environmental Applications. *ACS Sustainable Chemistry & Engineering* 2017, **5**, 9568.

30. Capone, I.; Hurlbutt, K.; Naylor, A. J.; Xiao, A. W.; Pasta, M. Effect of the Particle-Size Distribution on the Electrochemical Performance of a Red Phosphorus-Carbon Composite Anode for Sodium-Ion Batteries. *Energy Fuels* 2019, **33**, 45651.

31. Huang, Y. *et al.* Interaction of Black Phosphorus with Oxygen and Water. *Chem. Mater.* 2016, **28**, 8330.

32. Sun, J.; Lee, H.-W.; Pasta, M.; Yuan, H.; Zheng, G.; Sun, Y.; Li, Y.; Cui, Y. A phosphorene-graphene hybrid material as a high-capacity anode for sodium-ion batteries. *Nat. Nanotechnol.* 2015, **10**, 980.

33. Ghimbeu, C. M.; Gorka, J.; Simone, V.; Simonin, L.; Martinet, S.; Vix-Guterl, C. Insights on the Na^+ ion storage mechanism in hard carbon: Discrimination between the porosity, surface functional groups and defects. *Nano Energy* 2018, **44**, 327.

34. Li, Z.; Chen, Y.; Jian, Z.; Jiang, H.; Razinik, J. J.; Stickle, W. F.; Neuefeind, J. C.; Ji, X. Defective Hard Carbon Anode for Na-Ion Batteries. *Chem. Mater.* 2018, **30**, 4536.

35. Zhang, B.; Ghimbeu, C. M.; Laberty, C.; Vix-Guterl, C.; Tarascon, J. M. Correlation Between Microstructure and Na Storage Behavior in Hard Carbon. *Adv. Energy Mater.* 2016, **6**, 1501588.

36. Li, W.; Yang, Z.; Li, M.; Jiang, Y.; Wei, X.; Zhong, X.; Gu, L.; Yu, Y. Amorphous Red Phosphorus Embedded in Highly Ordered Mesoporous Carbon with Superior Lithium and Sodium Storage Capacity. *Nano Lett.* 2016, **16**, 1546.

37. Datta, P. K.; Gosh, A.; Mitra, S. Sodium-ion battery anode stabilization. *Nanomaterial for Electrochemical Energy Storage Devices*, ed. Roy, P. and Srivastava, S.K. (*John Wiley & Sons (USA), New York*) 2019, Chap.**7**.

38. Y. Wu, Y.; Liu, Z.; Zhong, X.; Cheng, X.; Fan, Z.; Yu, Y. Amorphous Red Phosphorus Embedded in Sandwiched Porous Carbon Enabling Superior Sodium Storage Performances. *Small* 2018, **14**, 1–8.

39. Tian, W.; Wang, L.; Huo, K.; He, X. Red phosphorus filled biomass carbon as high-capacity and long-life anode for sodium-ion batteries. *J. Power Sources* 2019, **430**, 60–66.

40. Feng, N.; Liang, X.; Pu, X.; Li, M.; Liu, M.; Cong, Z.; Sun, J.; Song, W.; Hu, W. Rational design of red phosphorus/reduced graphene oxide composites for stable sodium ion storage. *J. Alloys Compd.* 2019, **775**, 1270–1276.

Chapter 5:
Autonomous Self-Healing Strategy:
A Case Study of Black Phosphorus Anodes

5.1. Abstract

Autonomic Self-Healing (SH), namely, the ability to repair damages from mechanical stress spontaneously, is polarizing attention in the field of new-generation electrochemical devices. This property is highly attractive to enhance the durability of rechargeable Li-Ion Batteries (LIBs) or Na-Ion Batteries (SIBs), where high-performing anode active materials (silicon, phosphorus, etc.) are strongly affected by volume expansion and phase changes upon ion insertion. Here, we applied a SH strategy, based on the dynamic quadruple hydrogen bonding, to nanosized black phosphorus (BP) anodes for Na-ion cells. The goal is to overcome drastic capacity decay and short lifetime, resulting from mechanical damages induced by the volumetric expansion/contraction upon sodiation/desodiation. Specifically, we developed novel ureidopyrimidinone (UPy)-telechelic systems and related blends with poly(ethylene oxide) as novel and green binders alternative to the more conventional ones, such as polyacrylic acid and carboxymethylcellulose, which are typically used in SIBs. BP anodes show impressively improved (more than 6 times) capacity retention when employing the new SH polymeric blend. In particular, the SH electrode still works at a current density higher than 3.5 A g^{-1}, whereas the standard BP electrode exhibits very poor performances already at current densities lower than 0.5 A g^{-1}. This is the result of better adhesion, buffering properties, and spontaneous damage reparation.

5.2. Introduction

The future next-generation metal (M)-ion batteries [M = Li-Ion Batteries (LIBs) and Na-Ion Batteries (SIBs)] need to be improved in terms of enhanced durability, lower cost per stored energy, and sustainability. Some of the most crucial issues which are detrimental on the battery performances are related to the physical chemistry of the electroactive materials selected as anode components.[1] The electrochemical processes taking place in the anode compartment, in fact, involve dimensional/ structural evolutions which cause degeneration,

damage, and serious cycling failure. This is particular evident in anodes based on silicon[2] or phosphorus,[3] which normally undergo huge volumetric expansion/contraction upon full Li or Na insertion/deinsertion, thereby forcing large material strains. This results in electrode mechanical fracture, leading to cracking, pulverization, loss of electrical contact with the current collector, and even uncontrolled Solid Electrolyte Interphase (SEI) growth. All the previously reported Si- and P-based anodes showed capacity fading higher than 70-80% over the first 10-20 cycles.[2,3] Several approaches were discussed in the literature to enhance the durability of Si and P anodes in order to exploit their high theoretical capacity, such as the use of nanostructures or composites with carbon acting as a buffer agent.[2-6] Very recently, an innovative strategy to overcome such concerns is emerging, which finds inspiration from biology and specifically from the capability of some materials/tissues to self-heal or recover from a physical damage to prevent them from the loss of their vital functions.[7] In this frame, polymers are particularly appealing because of their good self-healing (SH) capabilities involving either physical (*e.g.*, interchain diffusion, phase-separated morphology, and shape memory effects) or chemical (incorporation of covalent, free radical, or supramolecular dynamic bonds) features, which employ a synergistic combination of hydrogen bonds (HBs), Van der Waals forces, and chemical reactions to repair micro-damages, autonomously or even upon external triggering by variation of pH, temperature, pressure, and so forth.[7-11] SH polymers (SHPs) are finding applications as active components in the improvement of electrochemical energy storage devices, including LIBs. For this specific application, several possible recovering strategies were explored, including different healing mechanisms (physical vs chemical), processes, and materials.[12-14] In order to develop new electrodes with high energy density and less irreversible mechanical fractures, SPHs were added chiefly to microparticles of silicon, both pure and as composites with carbon.[15-19] In this frame, SHPs acted as a new concept of binder, properly designed to be multifunctional as (i) a mechanical stabilizer, (ii) a structural support, (iii) wettable by the electrolyte, and also (iv) capable of recovering the physical damage caused by the structural changes.[20] Basically, SHPs were used following two different approaches: (i) as a thin soft layer of randomly branched hydrogen-bonded strands coating the Si electrode[18] or (ii) as a conventional binder surrounding the electrode particles and binding them to the current collector.[21] In both cases, very promising results were obtained in terms of cracks and damages recover upon cycling and, consequently, significant improvements in terms of anode capacity retention.[14,19,22] Among the possible SH mechanisms, such as covalent bonding, supramolecular chemistry, ion-ion interaction, π-π-stacking, and dynamic H-bonding, the latter one received specific

attention in the case of battery application.[14,22-24] In fact, even though H-bonds among neutral systems are not particularly strong, they confer significant mechanical strength due to the high directionality and affinity.[7] This is well evident, especially if multiple H-bonds are combined into a functional unit, for example, ureidopyrimidinone (UPy), which strongly associates with polymers potentially adaptable to the battery components (*e.g.*, polyethers). In this case, the mechanism is dynamic and requires high free volume and fluid-like systems which allow the orientation and approaching of the polymer chains, thus favouring the H−H interactions and consequently the SH mechanism. These supramolecular polymers exhibit low glass transition temperature, *Tg*, resulting in soft systems with high segmental motion, easily modeled, but mechanically strong.[8,11] Furthermore, an SHP based on dynamic bonding is capable of repeated and spontaneous healing without any external stimulus[11,25] even at room temperature, as in the case of UPy-containing brush-like poly(ethylene glycol) (PEG) chains[24] or upon gentle heating, as shown by maleimide-furan-based polymers.[26] If silicon anodes have been widely investigated in terms of SH strategies, very few examples are to date reported about phosphorus but for a work employing inorganic anchoring units to protect the active material surface.[27] In this paper, we describe, for the first time to the best of our knowledge, an autonomic SH strategy to improve the cycling lifetime of black phosphorus (BP) anodes for SIBs. To this aim, a novel H-bonding directed polymer is developed as an electrode binder with the specific role to repair the mechanical damages induced by the BP huge expansion and strain upon cycling. The system is based on PEG telechelic polymers decorated with UPy-chain end functionalities exhibiting the ability to self-recover at room temperature in the absence of external stimuli. The SH capability of the polymer is investigated by means of a multitechnique approach. Its effect on the BP anode electrochemical performances is demonstrated by comparing with similar electrodes including conventional binders, such as polyacrylic acid (PAA) and carboxymethylcellulose (CMC).

5.3. Material and Methods

Compound UPy-NCO 1 was synthesized as reported elsewhere.[28] Di-(OH)-terminated PEGs were purchased with different molecular weights (PEG$_n$, MW = 4000 Da, n = 91; MW = 6000 Da, n = 136; MW = 10,000 Da, n = 227; and MW = 35,000 Da, n = 795) as monodisperse products from different commercial sources and were used as received.

5.3.1. Synthesis of UPyPEG*n*UPy (2-5) Polymers: PEG 2-(6-Isocyanato-exilaminocarbonylamino)-6-metyl-4-[1H]-pyrimidinone

The representative procedure for the synthesis of all the polymers 2-5, sketched in Scheme 1, is reported in detail for the specific polymer 5 (UPyPEG795UPy).
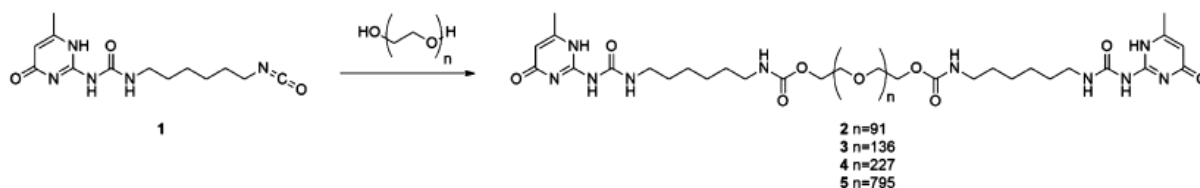
Scheme 2. Synthesis by UPy-Terminated PEG Telechelics (UPyPEGnUPy). Reaction conditions: dry CHCl3, dibutyltin dilaurate (cat.), 60°C, and 48 h.

UPy-NCO 1 (166.4 mg, 0.568 mmol) was added to a solution of PEG795 (5 g, 0.143 mmol) in CHCl3 previously dried over molecular sieves (10 mL) in the presence of a catalytic amount of dibutyltin dilaurate (two drops). The resulting reaction mixture was stirred at 60°C under inert atmosphere for 48 h. The mixture was cooled and filtered off to remove the exceeding UPy-NCO (compound 1). The last purification step was precipitation in hexane. The precipitate was recovered by filtration and washed plentifully with hexane, followed by drying under a reduced pressure to obtain UPyPEG*n*UPy as a white powder (4,9 g, 97%). ^{1}HNMR of UPyPEG795UPy (200 MHz, CDCl3): δ 5.89 (s, 2H, CH=CCH3), 4.07 (d, J = 6.9 Hz, 4H, OCH2(CH2OCH2)CH2O) , 4.02-3.17 (m, 209 3H, OCH2 (CH2OCH2)CH2O), 3.11 (m, 8H, NH(C=O)NHCH2 + CH2NH(C=O)O), 2.15 (s, 6H, CH3C=CH), 1.48 (m, 8H, NHCH2CH2 + CH2 CH2NHC=O) , 1 .34 (m , 8 H , CH2CH2CH2CH2CH2CH2). ^{13}C NMR (75 MHz, CDCl3): δ = 172.8, 156.3, 154.4, 148.1, 106.4, 42.6, 39.5, 30.9, 29.1, 26.0, 19.9, 15.7.

5.3.2. Preparation of SH Blends of (UPyPEG795UPy)-PEO

Three blends of UPyPEG795UPy and PEO (300 kDa) were obtained by mixing UPyPEG795UPy and PEO in deionized water at different volume concentrations 40/60 (40-60), 50/50 (50-50), and 60/40 (60-40) (see Table 1). The final mixture was then cast on a

Teflon foil and dried at 50°C under vacuum in order to obtain homogeneous 110 μm-thick films.

	A/B (vol %)	T_g (°C)	$\Delta H_{m,s}$ (J g^{-1})	X_c (%) from ^{1}H	G' (MPa) as prepared	G' (MPa) restored
UPyPEG$_{795}$UPy (A)		−22.3	184.4			
PEO (B)		−25.6	198.6			
40−60	40/60	−26.7	152.9	24	9.8	9.6
50−50	50/50	−27.1	166.0	34	12.7	16.7
60−40	60/40	−32.7	136.8	30		

Table 1. Glass Transition Temperatures, T_g, Melting Enthalpies, $\Delta H_{m,s}$, and Crystalline Fraction, X_c, (Estimated from ^{1}H and ^{13}C Solid-State NMR Spectra), storage (G') and loss (G'') elastic moduli of the Investigated Blends and Pure Components.

5.3.3. Thermal, Compositional and Mechanical Characterization

Thermogravimetric analyses of the SH polymers were performed by heating aliquots of about 20 mg at 5°C min^{-1} from room temperature up to 250°C under a N$_2$ atmosphere in a Pt crucible by means of a Q5000 thermogravimetric instrument (TA Instruments, USA). Differential scanning calorimetry (DSC) analyses were performed with a Q2000 instrument (TA Instruments, USA) by heating the samples (about 20 mg) from −80 to 150°C at 5°C min^{-1} under a N$_2$ atmosphere in Al crucibles sealed in the glove box. ^{1}H and ^{13}C NMR high-resolution spectra were recorded on Bruker 300 and 400 MHz instruments and calibrated with the solvent residual proton signal. CHCl$_3$ was dried using 4 Å molecular sieves. Solid-state NMR measurements were acquired on a Bruker AVANCE III 400 MHz (9.4 T) equipped with a 4 mm probe at 27° ± 1 °C under MAS condition (10 kHz). 1H one-pulse data were collected after T$_1$ determination to ensure the quantitative measurement condition with the use of 90° pulse of 3 μs and 16 scans; T$_1$ was evaluated with the use of a standard inversion recovery pulse sequence. For all the samples the same experimental conditions (contact time and decoupling scheme) were used. Rotors were filled with the membranes in the same quantity by cutting the membrane in macroscopic pieces (∼2 × 2 mm); this sample preparation was necessary to obtain stable MAS rotation and likely does not change the interchain interactions under investigation. Dynamic mechanical analysis (DMA) measurements were performed on rectangular-shaped samples (35 mm × 10 mm), directly cut from the piece, by a Metravib DMA/25 equipped with a shear jaw for films. The

frequency sweep experiments were carried out in the frequency range between 0.2 and 20 Hz at a constant strain of 0.004% from 20 to 60°C every 10°C. Temperature sweeps were performed at a heating rate of 2°C, over a range between 20 and 60°C, at a dynamic stress of amplitude 4×10^{-3} and a frequency of 1 Hz. For the stress-strain test, the sample was clamped on the tensile module with a separation of 10 mm. The speed rate was fixed at 0.2 mm min^{-1}. Membrane's thickness ranged between 100 and 110 µm.

5.3.4. Anode Preparation and Cell Assembly

Two electrodes were fabricated, which differ for the binder component. The starting slurries were prepared through aqueous processing by mixing proper amounts of BP, carbon (Imerys Super C65), and the polymer binder with a 50:30:20 weight ratio. BP was synthesized via high-energy ball milling, as deeply described elsewhere.[6,29] Raman spectra, SEM images, and XRD patterns of the as-prepared BP and the BP-C mixture used to prepare the anode slurry are reported in Figures 5.1 and 5.3, respectively.
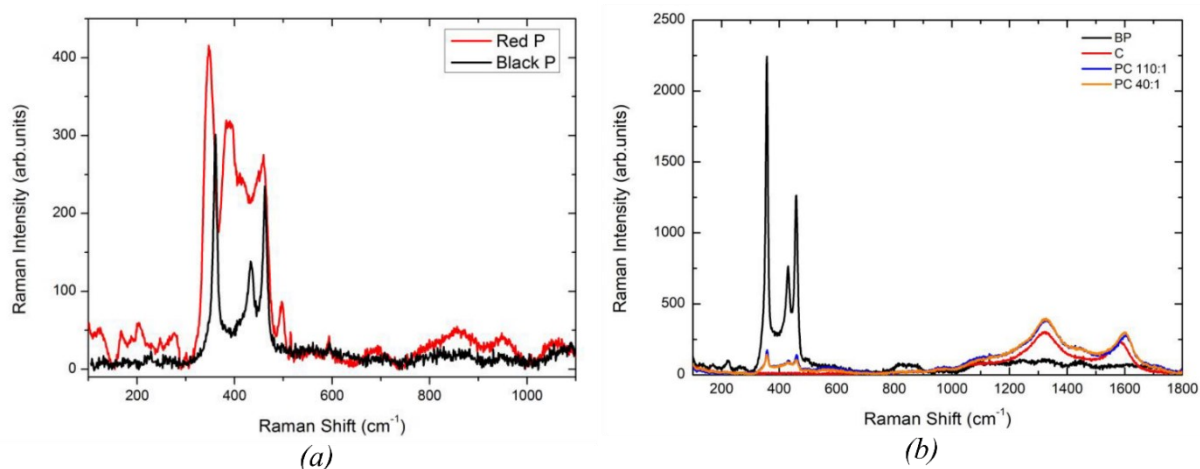
Figure 5.1. Raman spectra of: (a-left) black phosphorus, obtained by high energy ball milling starting from Red Phosphorus (whose corresponding spectrum is the red line) at 500 rpm and milling ball /RP mass ratio of 40/1 for 2 hours; the stars show the typical A_{1g}, B_{2g}, A_{2g} modes for orthorhombic BP; (b-right) black phosphorus including carbon as used to prepare the anode slurry (see the spectra of sample 40:1). Here the spectra of pure BPs and pure Carbon have been added for a sake of comparison.
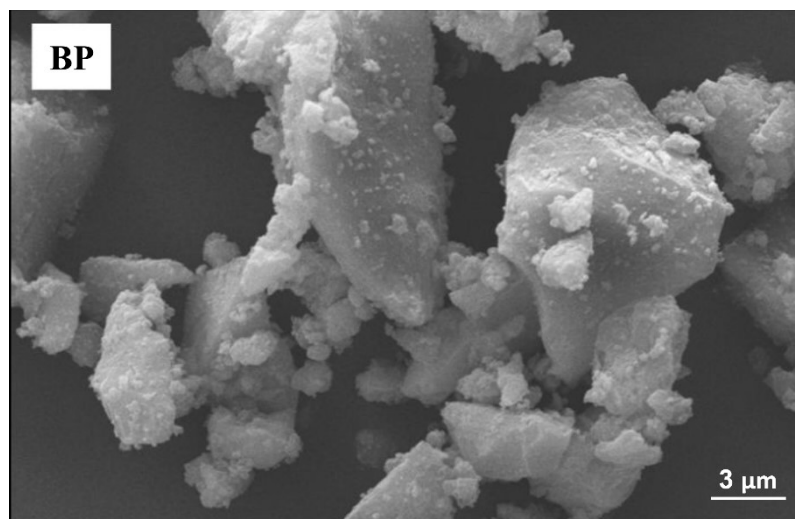
Figure 5.2. SEM image of black phosphorus (BP), obtained by high energy ball milling starting from Red Phosphorus. The image of the BP-C used in the anode is discussed in Ref. 6. Figure reproduced with permission from Ref. 29 Copyright 2019 American Chemical Society.
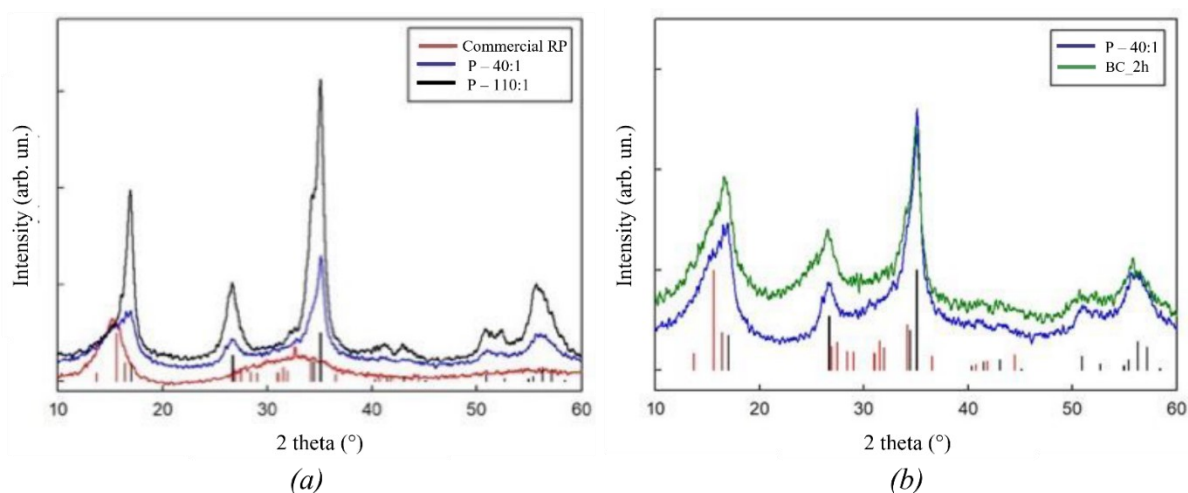

Figure 5.3. XRD patterns of: (a) black phosphorus, obtained by high energy ball milling starting from Red Phosphorus at 500 rpm and milling ball /RP mass ratio of 40:1 and 110:1; (b) black phosphorus including carbon, in the composition as used to prepare the anode slurry. Vertical red and black lines refer to the Bragg intensity related to red phosphorus (RP) and black phosphorus (BP) as reported by PDF cards 44-0906 and 76-1958, respectively. Figure reproduced with permission from Ref. 6 Copyright 2020 IOP Publishing.

Two different binders were used: (i) the SH UPyPEG$_{795}$UPy-PEO blend (50-50) and (ii) a blend of Na-CMC and PAA (1/1 wt/wt). In detail, BP and carbon were initially ball milled for few minutes; in a typical process, the binder was dissolved in excess water, added to the two components, and successively mixed in a planetary ball mill at 200 rpm for 2 h, followed by a 10 min stop and other 2 h of milling in reverse direction. The solid content of the slurries was kept between 12% and 15 wt%. The resulting inks were then cast on an aluminium foil

(UACJ, 15 μm thick) using a doctor blade to obtain a wet film with a thickness of 100 μm that was immediately dried under vacuum at 80°C to avoid moisture and oxygen contamination. The anode was finally cut into 2 cm^2 disks and stored in a glove box (MBraum, O_2, H_2O < 0.5 ppm) before the electrochemical measurements. In the case of electrodes based on the SH blend (50-50), two BP mass loadings were explored, ~1.26 and ~2.5 mg cm^{-2}; in the electrode including CMC-PAA as a binder, the mass loading was 1.6 mg cm^{-2}. Lower loadings were tested for the former system in our previous paper.[6]

5.3.5. Electrochemical Characterization

The electrochemical characterization of the anodes was performed by means of galvanostatic cycling and electrochemical impedance spectroscopy (EIS) by using 2032-type coin cells assembled in an argon-filled glove box (H_2O and O_2 < 0.5 ppm) with Na metal both as a counter and reference electrode. Electrodes were separated with a *Whatman* glass fiber separator (GF/D) soaked in a 1.0 M solution of NaPF$_6$ in Ethylene Carbonate: Propylene Carbonate (EC:PC) (50:50 wt%) with 5 wt% of NaTSFI and 2 wt% of FluoroEthylene Carbonate (FEC). The cells were cycled on a BioLogic BCS-810 battery tester from 0.02 to 2 V at various C-rates (1C = 2596 mAh g^{-1}). All the potentials reported refer to the Na$^+$/Na couple. Rests of 48 h were typically imposed every six cycles in order to evaluate the SH effect on the cycling performances. The impedance on the cells was measured by means of EIS at room temperature by applying an AC voltage of 100 mV in the frequency range of 0.1 Hz to 1 MHz.

5.3.5.1. Electrodes SEM Investigation

SEM analyses on the pristine anode and on *post mortem* were performed using a Tescan Mira3XMU microscope operated at 20 kV and equipped with an EDAX EDX analysis system. The samples were coated with a carbon thin film using a Cressington 208 carbon coater.

5.4. Results

5.4.1. Self-Healing Binder: Material Design and Characterization

As stated before, we used a chemical approach to develop a new binder for anodes in SIBs capable of SH from physical damages upon long cycling and to mitigate the huge volume expansion of the BP anode. Figure 5.4 shows a naïve picture of the SH binder working with a dynamic hydrogen bonding mechanism boosted by the presence of two UPy functional groups in the backbone, which should promote a good adhesion among the BP particles themselves and also to the current collector.

(a)

(b)
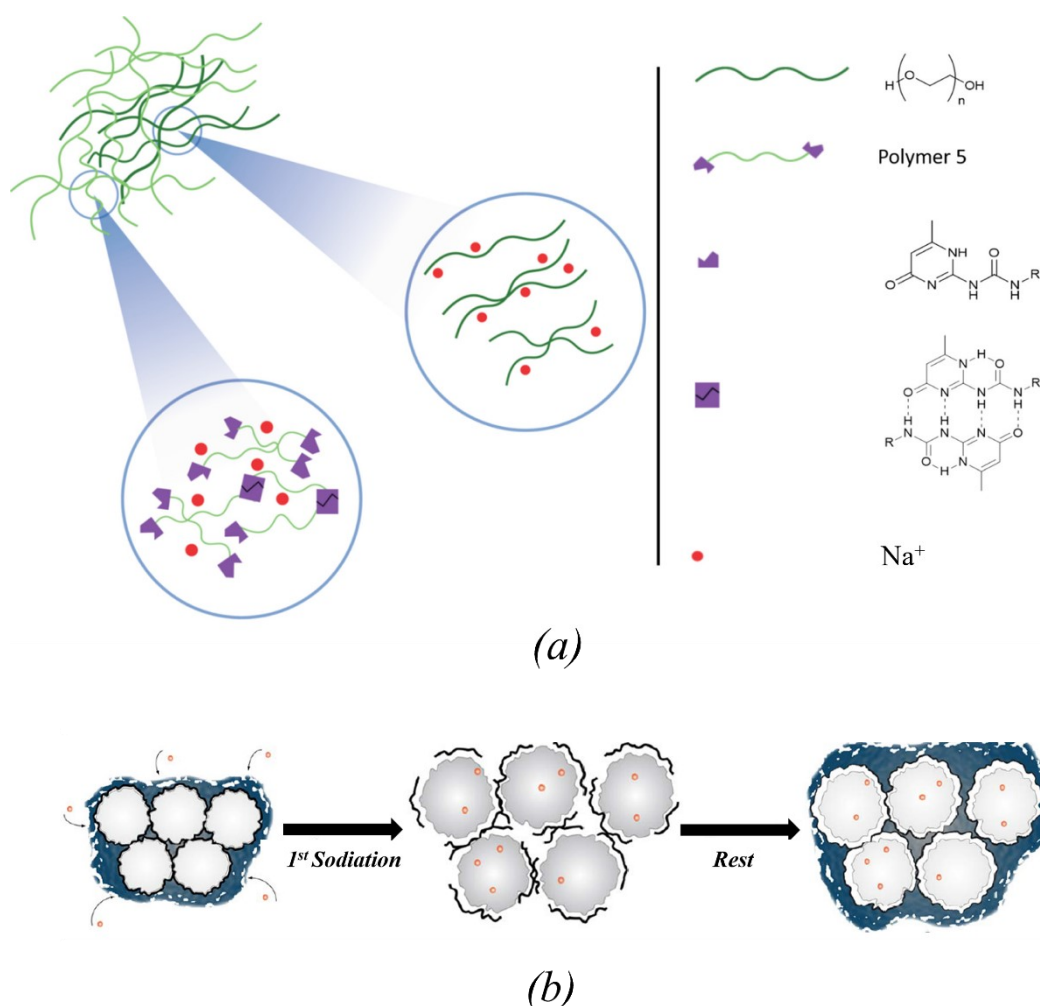
Figure 5.4*. Design and working mechanism of the SH BP anode: **(a)** schematic representation of the binder and **(b)** expected functional reversible behaviour of the UPyPEG$_{795}$UPy-PEO blends. Red point: intercalating Na ions; black lines: repairing polymer backbones; and blue: electrode texture.*

The SH polymer (UPyPEG$_n$UPy) includes PEG units playing a dual role (i) to assist the Na ion transport within the anode and conferring ion-conducting properties to the binder and (ii) to decrease the charge transfer anode resistance, thus resulting in an enhanced electrochemical kinetics.[30] The SH network (UPyPEG$_n$UPy) was further blended with high-molecular weight (MW) polyethylene oxide (MW = 300 kDa), which is physically and chemically affine, in order to achieve better free-standing properties and improve the dispersion of BP and carbon aggregates.

5.4.1.1. Self-Healing UPyPEG$_n$UPy Unit

2-Ureido-4[1H]-pyrimidone (UPy) containing supramolecular polymers were thoroughly discussed [see, for instance, Refs. 7,11,31] in view of their excellent dynamic and supramolecular properties, including UPy-functionalized telechelics. Telechelics are the most classical of supramolecular polymers, where the highly directional physical interactions are applied by replacing some of the covalent bonds with supramolecular ones.[32] Here, the quadruple hydrogen bonding group (UPy), by association via noncovalent interactions, endcaps a preformed short polymer chain, leading to a strong increase of the virtual molecular weight and to a concurrent improvement of its mechanical and rheological properties. Such end-end associations also result in a further enhancement of the SH capability of the supramolecular polymers due to a longer linear chain extension.[33,34] The preformed central segment is typically given by a thermoplastic polymer such as polybutadiene, polystyrene, polyethylene, and so forth. Other polymeric chain segments for UPy-based telechelics, such as PEG, indeed more interesting for application in LIBs and SIBs, are less explored.[35] The SH UPyPEG$_n$UPy polymers were synthetized as detailed in the Materials and Methods section (Scheme 1) by the covalent anchoring of isocyanate-functionalized UPy synthons to the terminal OH groups of PEG$_n$ (1:2 M ratio). In principle, the reaction is simple, but the process must be optimized to minimize the degree of PEG monofunctionalization. Indeed, monofunctional species can work as chain stoppers in the supramolecular polymerization of the difunctional UPy telechelics. The experimental parameters favouring the complete difunctionalization and then the telechelic formation are (i) a prolonged heating (60°C, 48 h); (ii) the optimal molar ratio of the reagents, PEG, and isocyanate 1 (1:4); and the use of hexane as the purification agent. The obtained telechelics

were first characterized by high-resolution NMR and FTIR spectroscopies. Figure 5.5 shows a representative spectrum for the case of the UPyPEG$_{795}$UPy sample. As clearly shown in Figure 5.5a, the UPy end-capping of PEG moieties was successful. Specifically, complete difunctionalization was proven by integration of the unique proton resonances of the UPy moiety at ~6 ppm and the unique proton resonances of the PEG moiety (namely, those of the CH$_2$ groups in the repeating unit) at ~3.5 ppm.
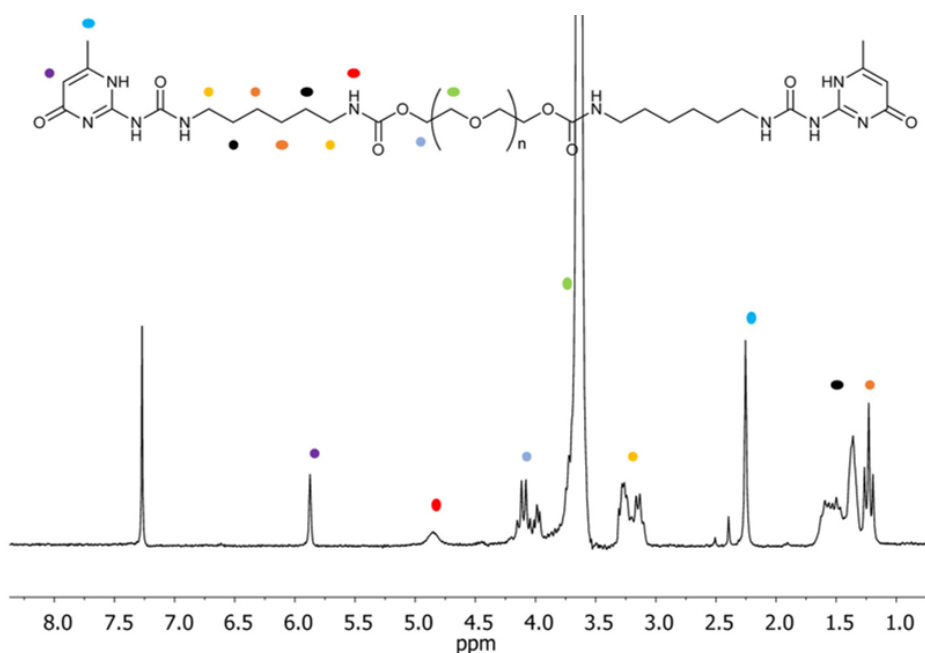

Figure 5.5. ^1H NMR spectrum (300 MHz, 25°C) of polymer 2 in CDCl$_3$.

Furthermore, the polymer purity is proved by the absence of unique proton resonances of the starting material 1 (*e.g.*, the signal of CH$_2$ protons of the isocyanate moieties) as shown in the ^{1}H NMR spectra reported in Figure 5.6.
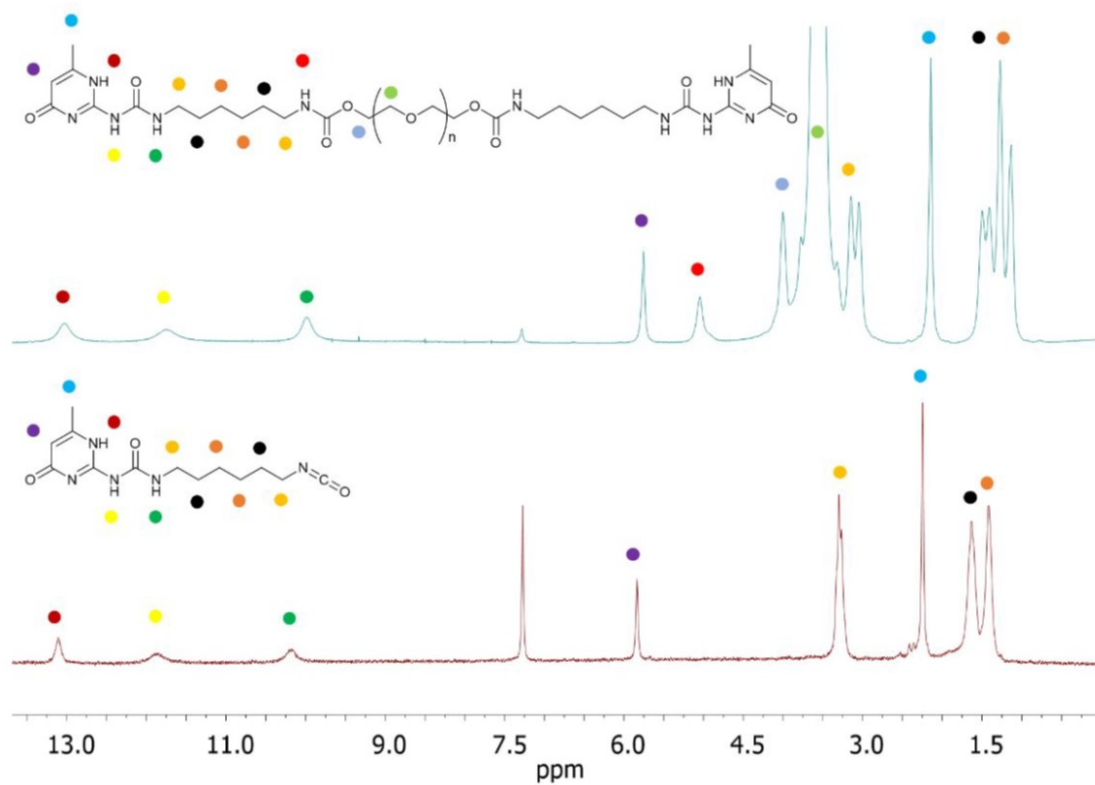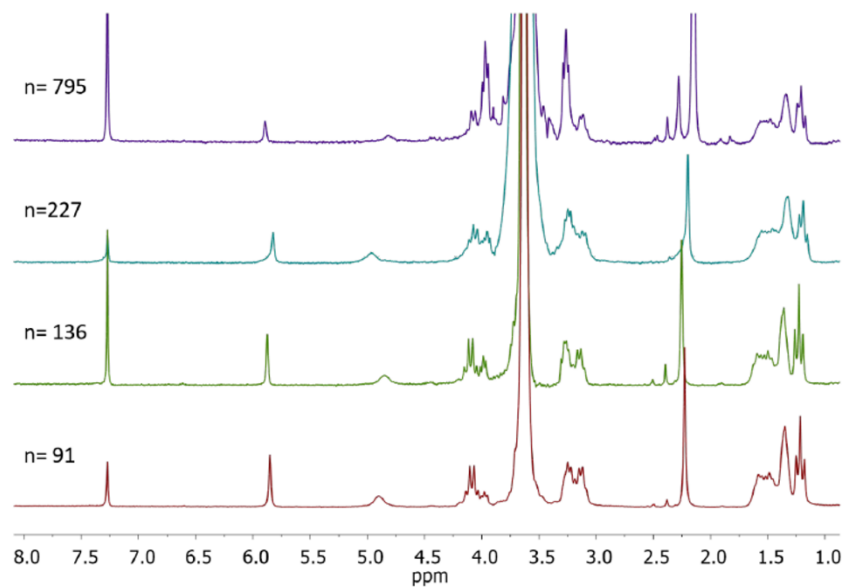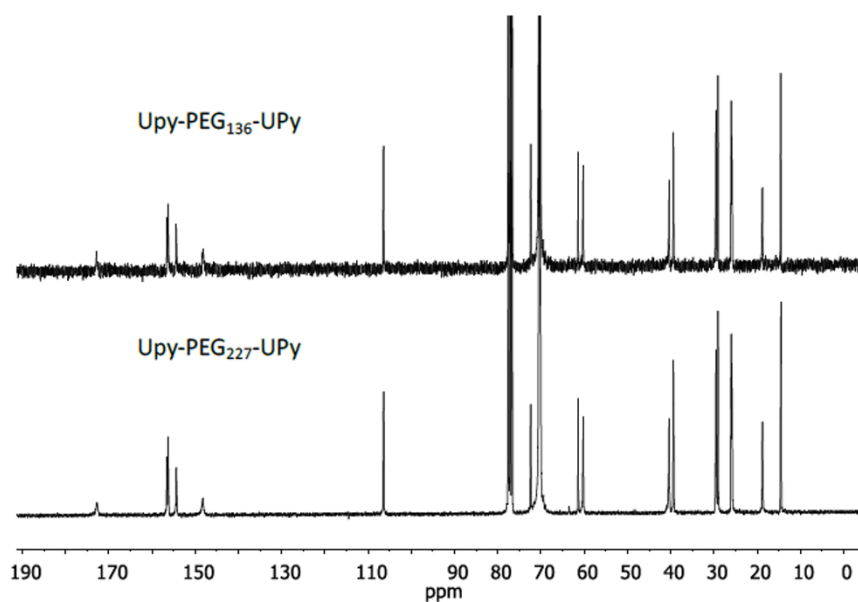
Figure 5.6. *Comparison between the ¹H NMR spectra (300 MHz, 25°C) of reagent 1 and purified polymer 2.*

All the collected spectra of UPyPEG$_n$UPy (namely, polymers 2-5 in Scheme 1) are fully consistent with the proposed structure for each investigated *n*, as shown in Figure 5.7.

(a)

(b)

Figure 5.7. Comparison between (a) the ^1H NMR spectra (200 MHz, 25°C) of purified polymers 2-5 and (b) the ^{13}C NMR spectra of purified polymers 3-4.

A comparison among them also clearly provides evidence of the increasing chain length of the PEG repeating units. FTIR spectra were also collected for each UPyPEG$_n$UPy telechelic to further confirm the expected polymer structure. The spectra do not show the vibrational signal at ~3500 cm^{-1} typical of the OH bond stretching, which is, in contrast, well evident
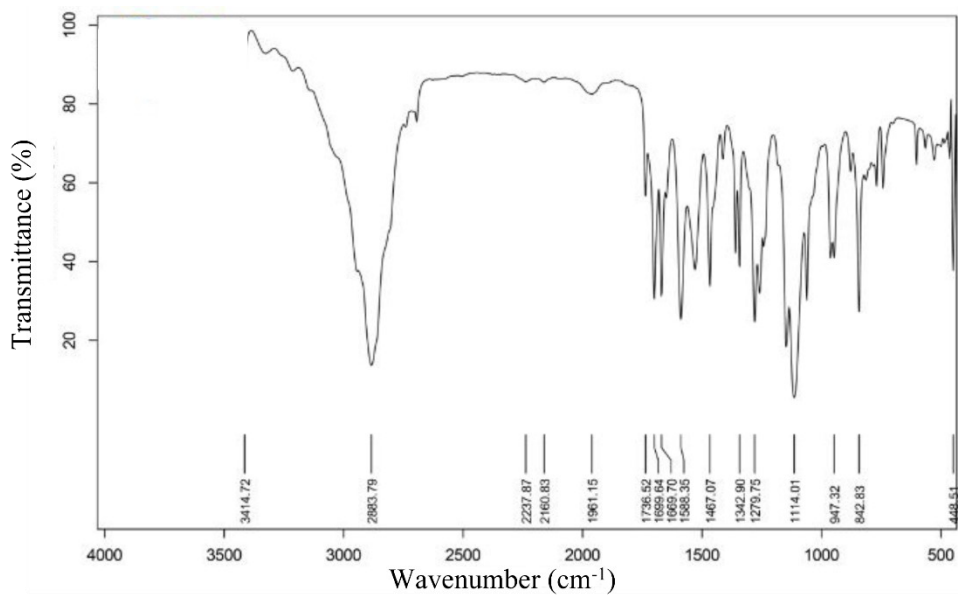
in the case of pure PEG spectrum (Figure 5.8*a-e*). This further confirms the point that the above-described reaction took place through the foreseen mechanism.
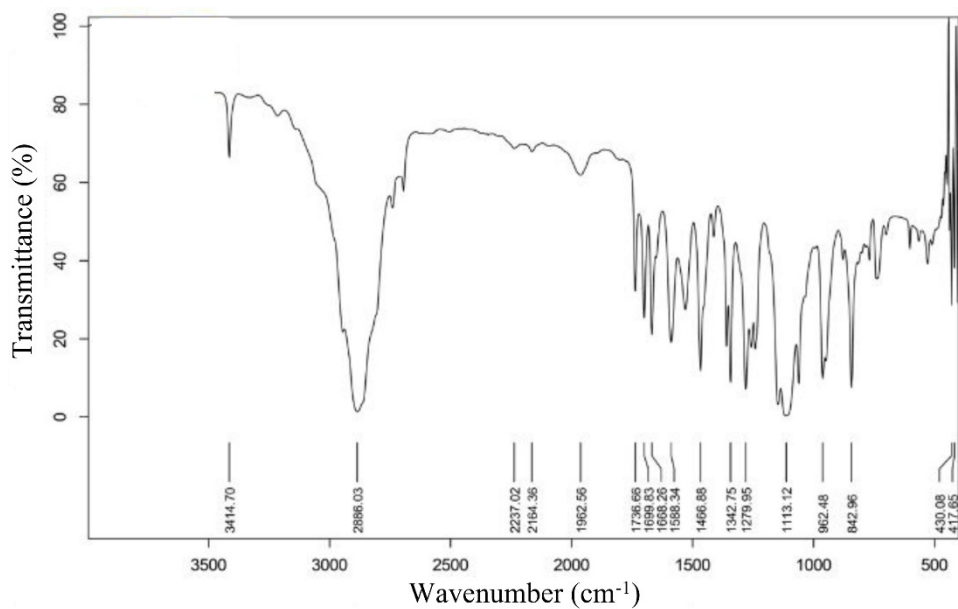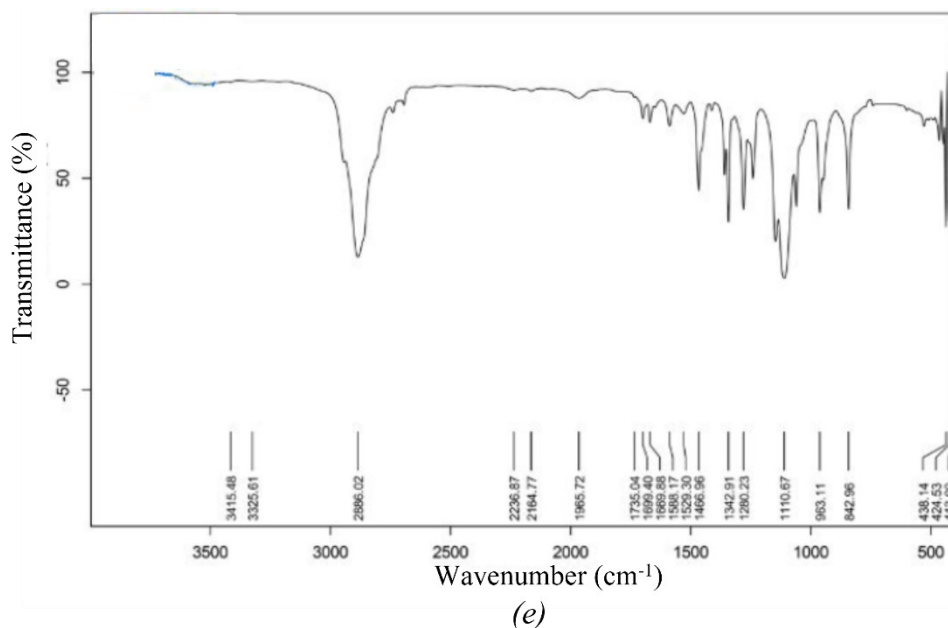

(a)

(b)

(c)

(d)

(e)
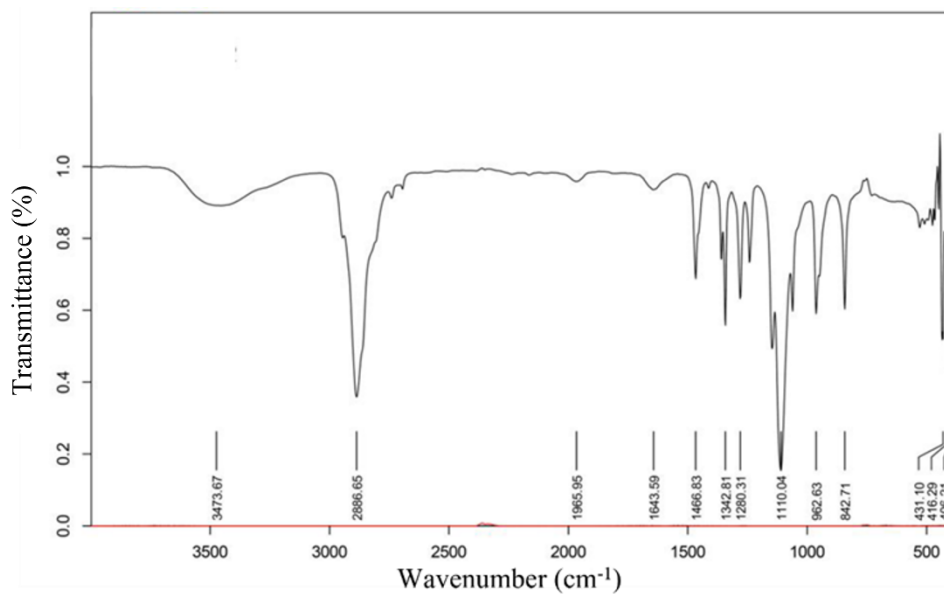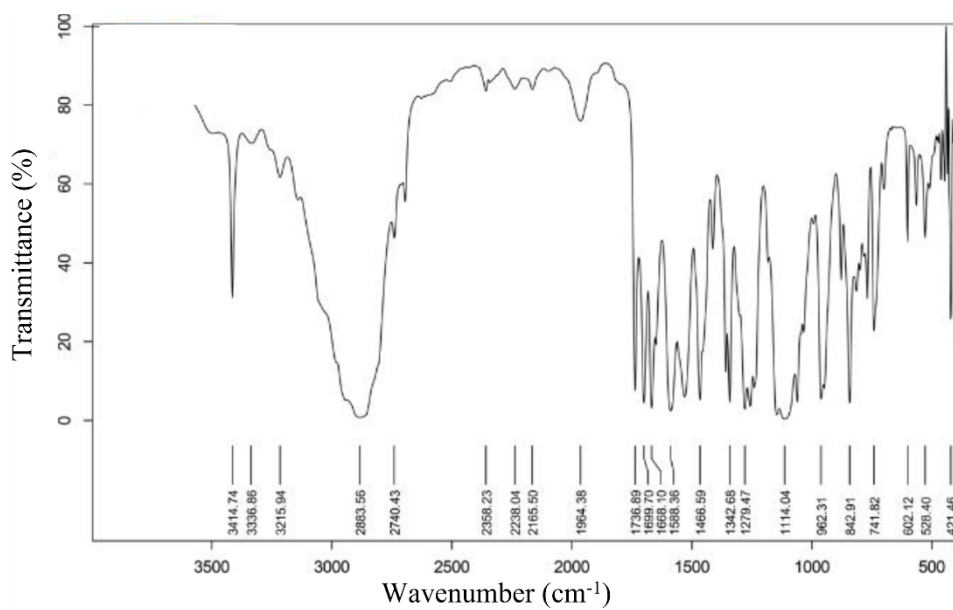
Figure 5.8. *IR spectra of pure PEG$_{227}$ (MW = 10000 Da)* **(a)** *and purified polymers 2, 3, 4 and 5 (respectively* **b, c, d,** *and* **e***).*

In order to select the optimal UPy telechelic in terms of chain dynamics, DSC measurements were carried out on all the synthesized polymers. PEG is a semicrystalline polymer with glass transition temperature, Tg, well below room temperature, and this property is important to assure sufficient chain mobility and then self-repairing ability. Figure 5.9a compares the DSC traces of the UPyPEG$_n$UPy networks at different n values.
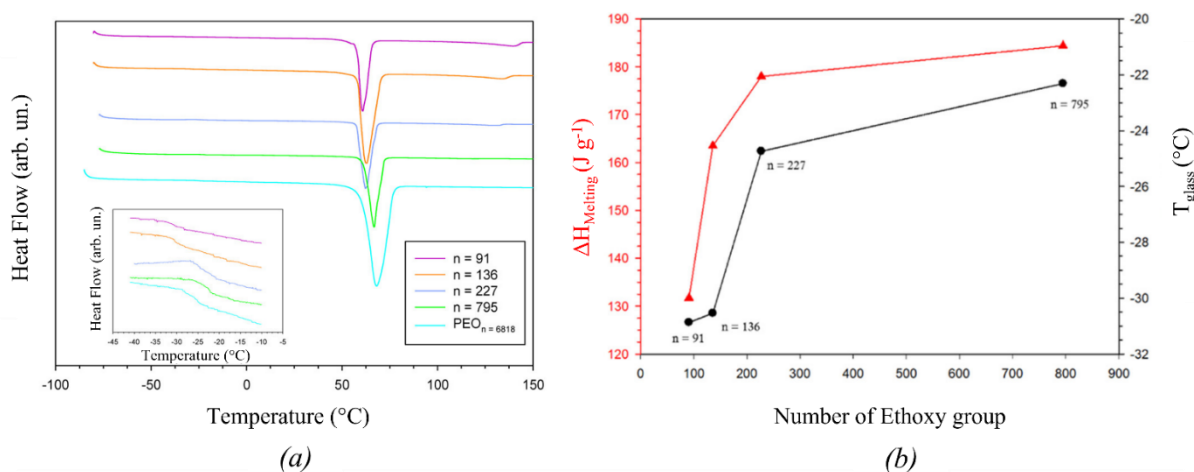

(a)   *(b)*

Figure 5.9. (a) *DSC thermograms of UPyPEG$_n$UPy with different chain lengths compared to that of pure PEO$_{6818}$ (300 kDa). The inset shows the T_g region;* **(b)** *melting enthalpy, $\Delta H_{m,s}$, and glass transition temperature, T_g, for all the investigated UPyPEG$_n$UPy samples.*

117

All the polymers show well-defined glass transition and melting phenomena, whose characteristic temperatures, T_g and T_m, respectively, are influenced by the PEG molecular weight. As expected, both the glass transition temperature and the melting enthalpy increase with n, resulting in an enhancement of polymer stiffness (see Figure 5.9*b*). The UPyPEG$_n$UPy crystalline fraction is obtained from the ratio between the experimental melting enthalpy, $\Delta H_{m,s}$, and the one expected for a fully crystalline sample, assumed to be $\Delta H_m = 206$ J g^{-1}.[36] It increases from 60% to about 85% by increasing *n*, whereas the glass transition temperatures remain below -22 °C even in the case of PEG$_{795}$ (MW = 35 kDa). The thermograms also show another endothermal phenomenon between 120° and 150°C, whose intensity decreases by increasing the PEG chain length. Such a broad signal is frequently observed in PEO-based systems and is assigned to the endothermic mixing between the crystalline PEG-chain undergoing melting around 65°C and the metastable liquid phase originating at the polymer glass transition.[37] The conjunction of these two properties, namely, low T_g and the presence of crystalline domains, is therefore optimal to obtain polymers with high hydrogen bonding dynamics and good mechanical strength. Taking into accounts such results, we opted for UPyPEG$_{795}$UPy (MW = 35 kDa) as the SH UPy-telechelic unit for the blend component. Here, the amorphous phase is enough to allow the rearrangement of the polymer chains and to drive the healing of any cracks autonomously. At the same time, the crystalline phase contributes to the polymer's mechanical properties helpful to contain the large fluctuations of the BP structure in the anode.[22] Finally, thermogravimetric analysis showed that each investigated telechelic is very stable from a thermal point of view with degradation temperature exceedingly at least 180°C, independently on the PEG chain length, as reported in Figure 5.10.
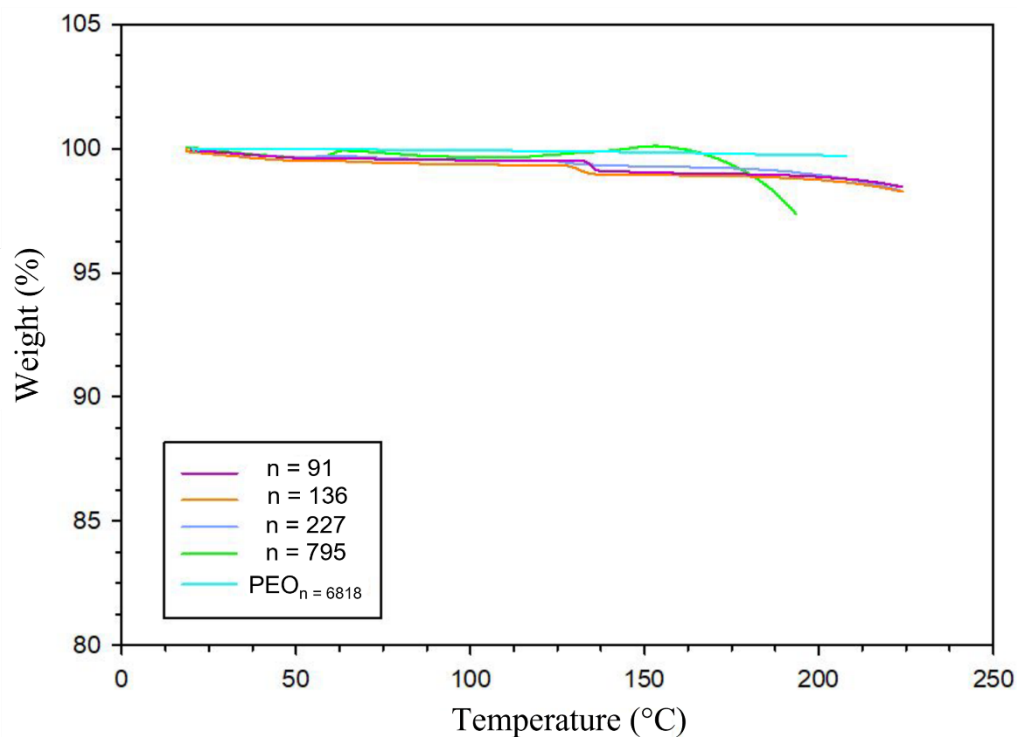
Figure 5.10. *TGA plots of all the investigated UPyPEG$_n$UPy telechelics. The thermogram of pure PEO (300 kDa) is also reported as a comparison.*

5.4.1.2. Self-Healing UPyPEG$_{795}$UPy-PEO Blend

The UPyPEG$_n$UPy polymers have no optimal MW to form films with good freestanding properties. For this reason, the longer telechelic (UPyPEG$_{795}$UPy) was selected to be homogeneously mixed with a higher MW polymer as PEO (300 kDa) to obtain a blend with a double function, namely, (i) SH capability ensured by the telechelic unit and (ii) good free-standing properties allowed by PEO. Specifically, three blends UPyPEG$_{795}$UPy-PEO were prepared by mixing proper amounts of the single components to achieve the volume ratios (v-v) 40-60, 50-50, and 60-40. In the following, the samples will be labelled blend 40-60, blend 50-50, and blend 60-40, respectively (see Table 1). For the sake of clarity, here the first number refers to UPyPEG$_{795}$UPy and the second one to PEO. In order to exclude the SH effects due to the PEO component, the same test was also carried out on a pure PEO film, whose optical microscopy image is reported in Figure 5.11, showing that no crack is repaired even after 5 days of rest time.
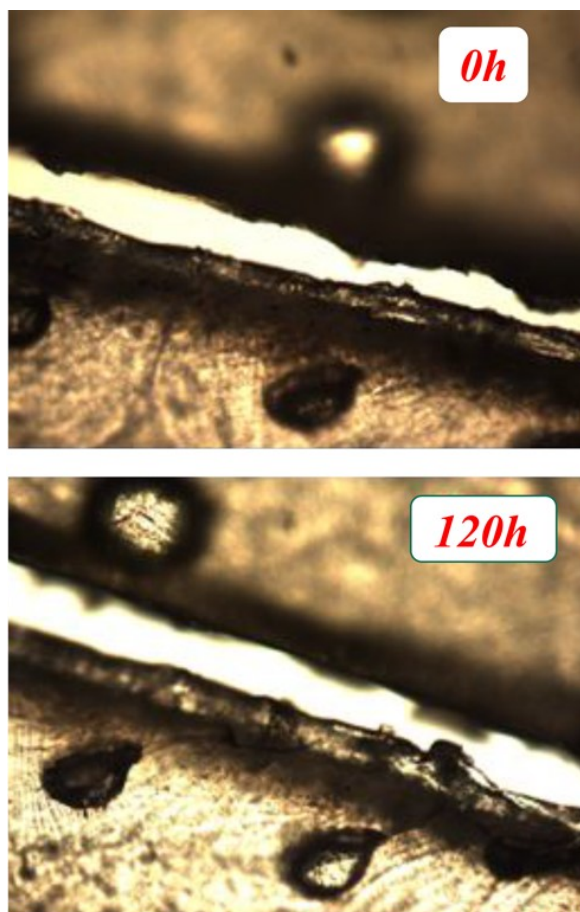
119

Figure 5.11. Optical microscopy images of a PEO (MW=300 kDa) film, as cut and after 120 hours of rest time.

Initially, the SH ability of the blends was qualitatively evaluated by scratching with a razorblade 100 μm-thick films, prepared as described in paragraph 5.3.2, and following their spontaneous self-repairing upon time. Figure 5.12*a* shows the optical microscopy images obtained for all the investigated blends, immediately after cut (i, ii, iii) and after 2 h (i', ii', iii'). In the first two cases, the cracks are fully healed. In contrast, the SH of 60-40 is not recovered at all, as observed by comparing Figure 5.12 iii, iii'.
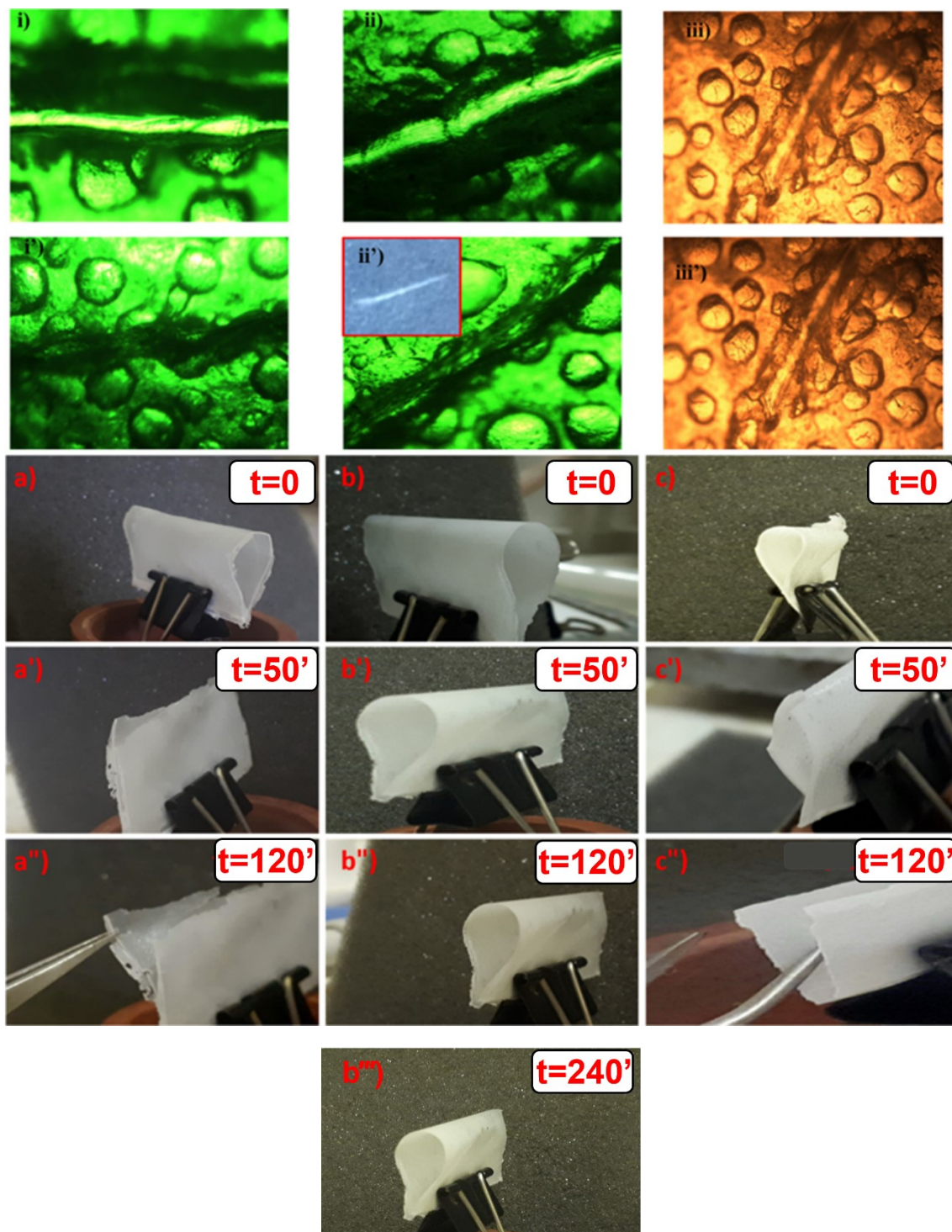
Figure 5.12. *(Up) Optical microscopy images of the UPyPEG$_{795}$UPy-PEO blends: 40-60 (**i, i'**), 50-50 (**ii, ii'**), and 60-40 (**iii, iii'**), just cut (above), and during the SH process (below). (Down) Bending test over time for the blends 40-60 (**a, a'**), 50-50 (**b, b'**), and 60-40 (**c, c'**).*

In order to check the bending resistance of the blends, finally, the films were kept under forced folding for at least 2 h, as shown in Figure 5.12*a-c*. While the samples 40-60 and 60-40 underwent partial or complete rupture, 50-50 did not undergo fracture, remaining well

121

flexible for about 4 h (Figures 5.12*b-b‴*. These findings can be explained by the higher crystallinity observed in the 50-50 sample, resulting in an increased mechanical robustness, as proved by the good agreement of the experimental evidence coming from our multidisciplinary approach (DSC, ^{13}C-^{1}H solid-state NMR, and DMA), whose main results are summarized in Table 1. The repairing ability was also checked in terms of the reconstruction of electric continuity. To this aim, a 50-50-based composite film was prepared including 15 vol% of conductive carbon (KS-10 Timcal). This film was connected to a multimeter and then cut in two pieces in order to follow the evolution with time of the film resistance. Figure 5.13 shows the gradual and full recovery of the composite resistance after the sample crack toward the initial value shown before the rupture.
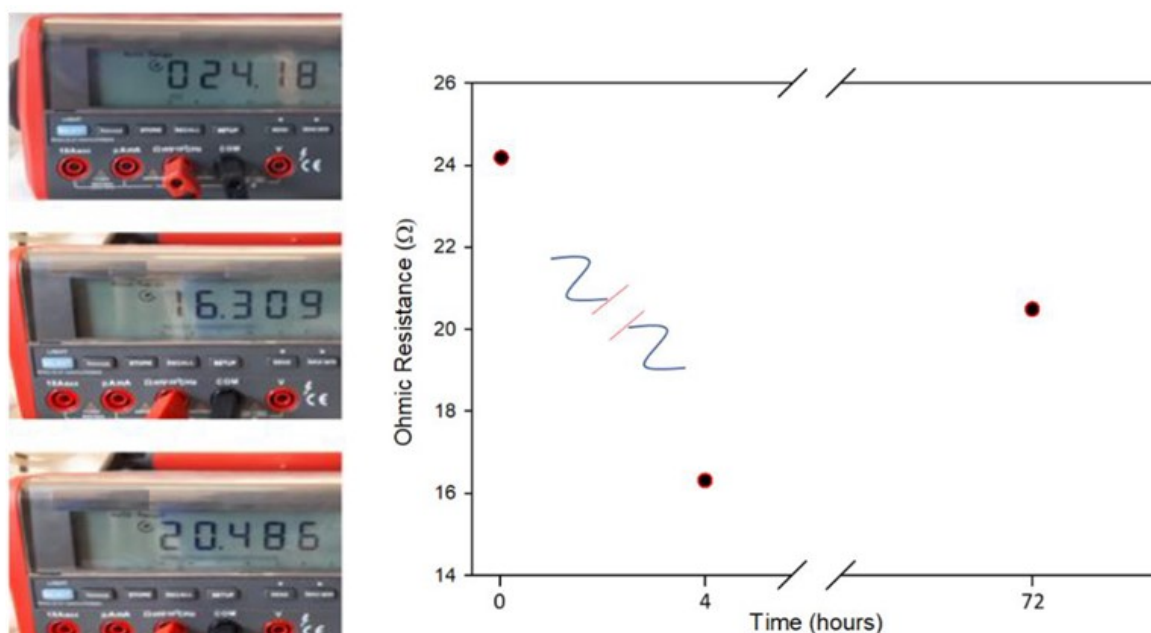

Figure 5.13. *Electric resistance measurements of a composite film based on the B50-50 blend and carbon (15 vol% of Graphite KS-10), before the damage and during the recovering time. The blue and red lines is an illustration of the absence of electric contact caused by the cut.*

Figure 5.14*a* compares the DSC thermograms of the three blends as prepared. Clear glass transition (see the inset) and melting phenomena are observed. While all blends exhibit a single T_g, the melting endotherms are well structured, suggesting a physical mixing of multiple phases with slightly different melting temperatures and enthalpies. Indeed, all the blends exhibit T_g and $\Delta H_{m,s}$ lower than those of pure UPyPEG$_{795}$UPy and PEO components, resulting in semicrystalline systems where the amorphous fraction is more extended and less viscous at ambient temperature. However, 50-50 exhibits melting enthalpies of 10% and

20% higher than 40-60 and 60-40, respectively, which suggests a larger fraction of crystalline domains. As the melting enthalpy of 100% crystalline UPyPEG$_n$UPy is not known, it is not possible to determine the amount of the crystalline fraction from DSC data, and just the trend should be considered.
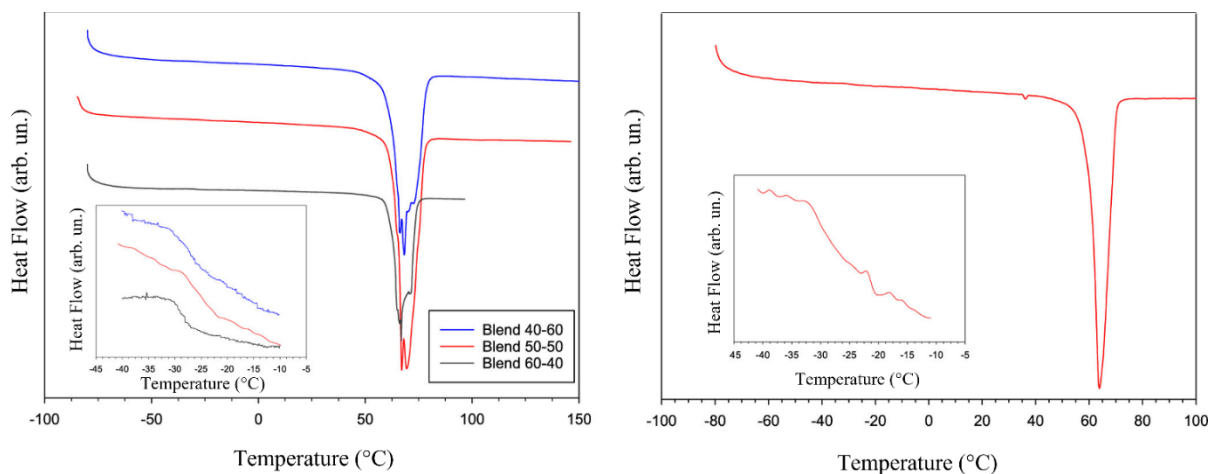

Figure 5.14. (**a**) *DSC thermograms of the UPyPEG$_{795}$UPy-PEO blends 40-60, 50-50, and 60-40 and* (**b**) *of the healed part of the blend 50-50 (see the inset in Figure 12ii'). The glass transition temperatures, T$_g$, are highlighted in the figure insets.*

Figure 5.14*b* reports the DSC plot of the healed part of the 50-50 sample. Here, the several melting peaks undergo coalescence, and the glass transition temperature, $T_g < -34°C$, significantly decreases. Both these phenomena may be related to the formation of new dynamic H-bonds driven by the approaching of the UPy-terminated chains, which physically link the two components into a unique and highly dynamic network. The repaired damage also indicates that the presence of crystalline PEG domains does not interrupt the dynamic hydrogen bonding formation and the related properties. As for the pure components, the blends are also thermally stable at least up to 250°C, as shown by the corresponding TGA plots, reported in Figure 5.15.
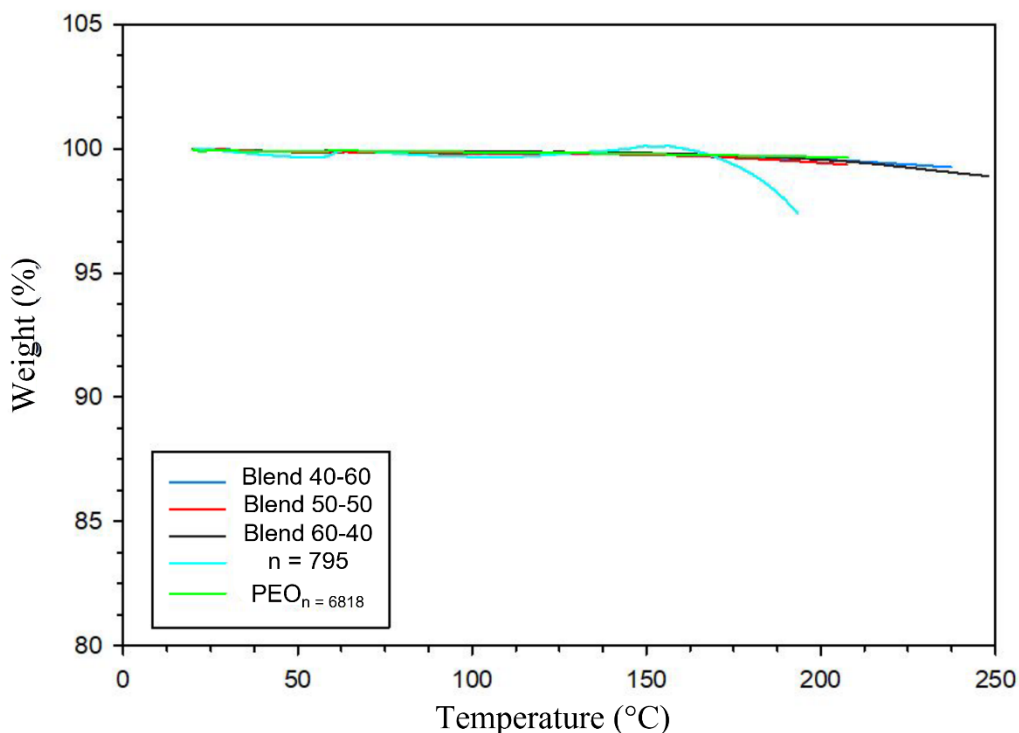
Figure 5.15. *TGA plots of all the investigated UPyPEG$_{795}$UPy-PEO blends. The thermogram of UPyPEG$_{795}$UPy and pure PEO is also reported as a comparison.*

The blends were also investigated by means of solid-state NMR spectroscopy. Figure 5.16*a* shows the ^{1}H one-pulse spectra, which exhibit narrow signals at ~4.1 ppm, overlapped to broader bands centered at the same chemical shift. Smaller features can be observed at ~3.8 ppm and in the range of 1.9-1.3 ppm. The main peak at 4.1 ppm can be associated with the protons of the PEO units ─(CH$_2$─CH$_2$─O)─ present both in the PEO and UPy chains, in good agreement with the attribution reported for the molecule in solution (Figure 5.5), and the narrow and broad contributions can be attributed to signals from the crystalline and amorphous polymer strands, respectively.[37,38] The small feature in the 3.8-3.5 ppm range, which shifts to lower fields with increasing PEO content, can be associated with the ─CH$_2$─ moieties in the UPy-based polymer.
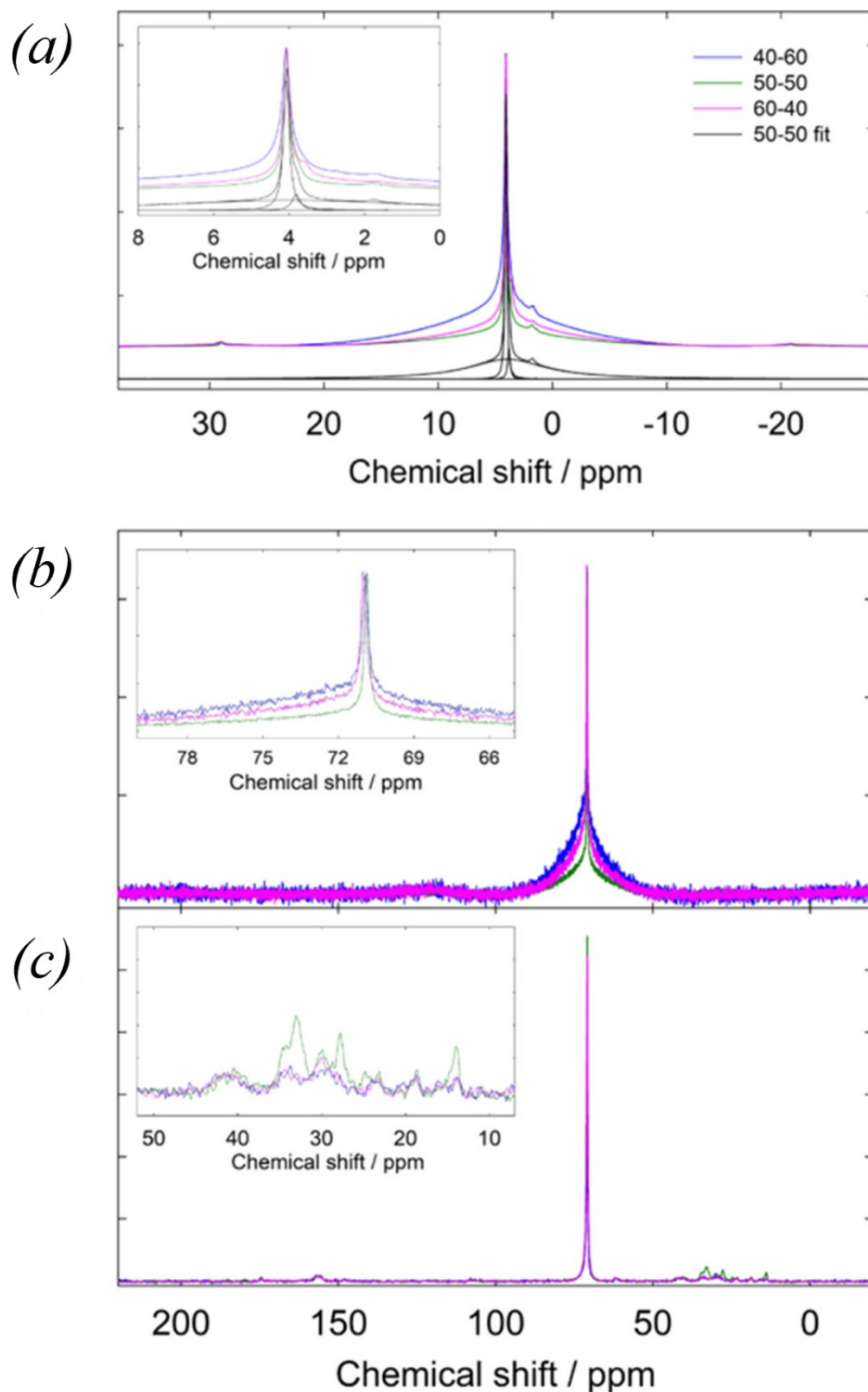
Figure 5.16. (a) *^1H spectra for the pristine blend 40-60 (blue), blend 50-50 (green), and blend 60-40 (pink) compositions;* ***(b)*** *^{13}C spectra for the pristine blend 40-60 (blue), blend 50-50 (green), and blend 60-40 (pink) compositions; and* ***(c)*** *^1H-^{13}C CPMAS spectra for the blend 40-60 (blue), blend 50-50 (green), and blend 60-40 (pink) compositions.*

Finally, the small features in the 2.5-1.3 ppm region can be associated with the terminal methyl groups of the polymer chains, again in good agreement with the attribution reported

in Figure 5.5.[38,39] The remaining protons of the UPy unit could not be observed because of their low concentration. Although the main peaks near 4 ppm are very similar, a closer inspection shows some changes with the membrane composition (see the inset of Figure 5.16a). The main part of the spectrum can be fitted in terms of three Gaussian contributions, two of them centered at 4.1 ppm and the third one ranging in the range 3.8-3.5 ppm, depending on the composition. As previously stated, this third component is associated with the CH_2- moieties of the UPy-based part of the polymer. The two components at 4.1 ppm, in turn, can be attributed to system crystalline and amorphous fractions.[38,39] The best fit performed on the base of this simple model shows that the amorphous/crystalline fraction does not vary linearly with the composition, but the 50-50 sample has the highest content of crystalline domains (see Table 1). This trend has been qualitatively confirmed by the same analysis performed on the ^{1}H-decoupled ^{13}C spectra (Figure 5.16b) on the sharp and broad resonances observed for all the three samples at 71 ppm. Finally, ^{13}C-^{1}H CPMAS spectra, reported in Figure 5.16c, show the same main resonance at 71 ppm due to the $-(CH_2-CH_2-O)-$ moieties in the polymer chains and smaller features associated with the amide (~175 ppm), aromatic rings (152-165 ppm), and aliphatic portions (10-50 ppm) (see Figure 5.16c and the inset).[40] Again, all the spectra are very similar. However, upon normalization to the main resonance, it is possible to observe that the 50-50 sample has a better signal-to-noise ratio than the other two compositions, which is well evident in the aliphatic portion of the spectrum (see the inset). This calls for a higher cross-polarization efficiency, which can be due to different factors, that is, the lower mobility of the interested fragments if the cross-polarization is associated with intrachain mechanisms and/or to the shorter distance among fragments if associated with the interchain ones. Both these mechanisms are compatible with higher crystallinity of this sample, which is associated with a closer packing of the polymeric chains, in agreement with the results obtained from the DSC and DMA analyses. DMA was used to investigate the mechanical properties of 50-50 and 40-60 blends. The 60-40 sample was not considered due to nonefficient SH capability. Figure 5.17 shows the frequency dependence of the storage (G') and loss (G'') elastic moduli for the 50-50 (a) and 40-60 (b) samples, at 20 and 60°C, both pristine (B50-50 and B40-60) and restored (SH-B 50-50 and SH B40-60). In the whole temperature range, all the samples reveal storage modulus higher than the loss one, which highlights their good elasticity.
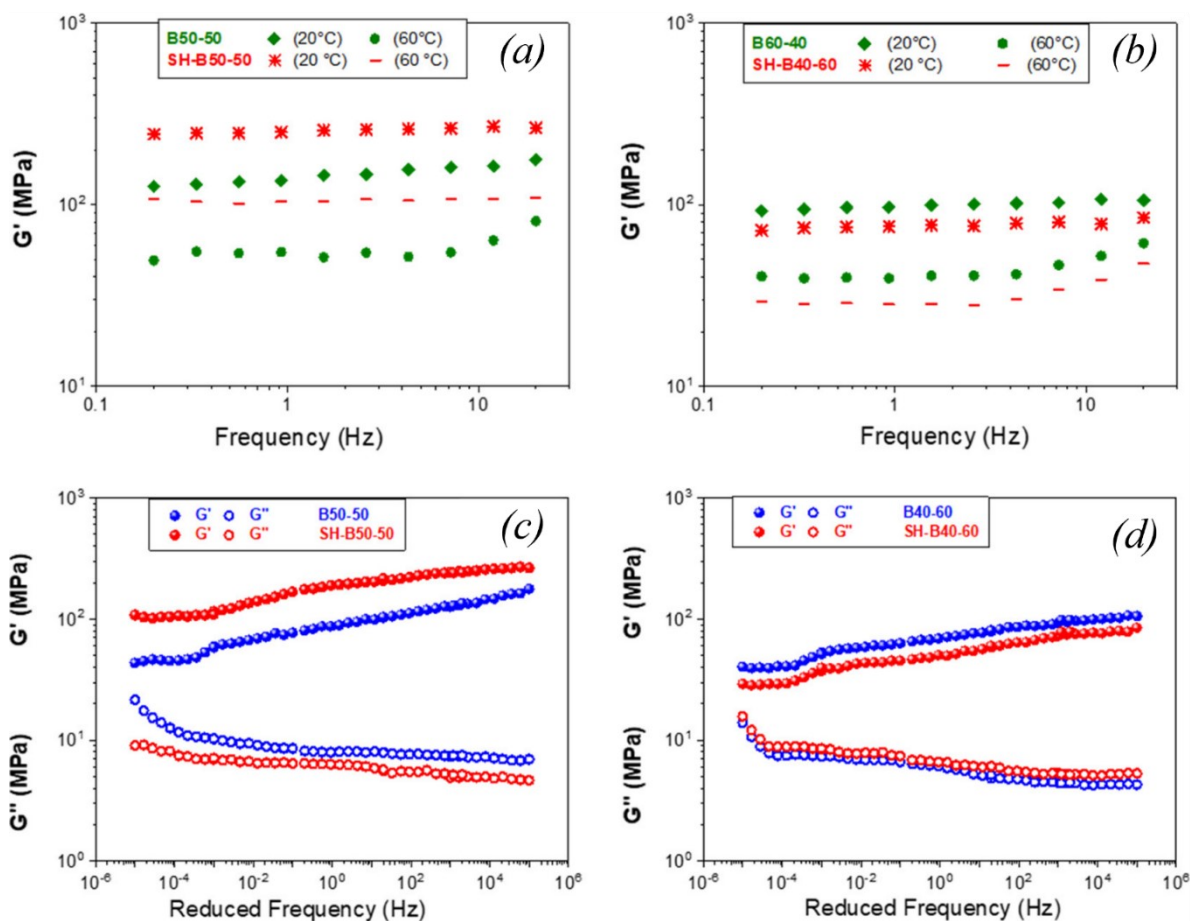
Figure 5.17. (a,b) *Frequency sweep tests, at 20 and 60°C, for the UPyPEG$_{795}$UPy-PEO blends:* ***(a)*** *blend 50-50 both pristine B50-50 and self-healed SH-B50-50 and* ***(b)*** *blend 40-60 both pristine B40-60 and self-healed SH-B40-60.* ***(c,d)*** *Master curves of storage (G') and loss (G") moduli reduced at a reference temperature of 40 °C:* ***(c)*** *blend 50-50 both pristine B50-50 and self-healed SH-B50-50;* ***(d)*** *blend 40-60, both pristine B40-60, and self-healed SH-B40-60.*

Nonetheless, DMA analysis underlines some crucial differences between the samples:

(i)   The G' moduli of 50-50 is 127 MPa at 20°C, which is roughly 30% higher than that of 40-60 gel (96 MPa), thus implying greater mechanical strength of the former blend, in agreement with the higher crystallinity revealed by DSC and NMR;

(ii)   The self-healed 50-50 sample exhibits higher elastic modulus than the pristine film. This is likely due to a larger number of strong HBs between the two components (UPyPEG$_{795}$UPy and PEO) taking place in such a blend;

(iii)   G' decreases upon heating (while G" clearly increases) due to the gradual weakening of the polymer structure. There is also a slight dependence on the

frequency of both modules for some samples, with a reduction in the G'/G" ratio below 10, which is typical of "weak gel"-like systems.[41]

With regard to this last point, a different behaviour is observed in the case of self-healed 50-50 blend, which is able to maintain the mechanical properties of a "strong gel"-like system (both modules independent from ω and with a G'/G" ratio > 10) even at relatively high temperature (*i.e.*, 60°C).[42] In a nutshell, the SH process enhances the mechanical strength as well as the thermostability of the 50-50 blend. Master curves were constructed by using the "Time-Temperature Superposition (TTS)" principle, based on the Williams-Landel-Ferry model.[43] This allows the prediction of the mechanical behaviour of polymers as a function of frequency over time scales that are not experimentally accessible.[44,45] For each sample, the frequency sweeps acquired at five test temperatures (from 20 to 60°C every 10°C) were shifted to the reference temperature of 40°C, allowing to extend the frequency window from 0.01 mHz to 0.1 MHz (Figure 5.17*c,d*). In such a wide frequency range, all the membranes show an elastic solid-like behaviour since the elastic module G' is averagely 10 times larger than the viscous module G". However, both the two 40-60 membranes and the pristine 50-50 one show module values approaching toward the low-frequency region, which is an indication of a weakening of the polymeric film. Accordingly, a clear loss of elasticity occurs to the systems as a consequence of a "strong-weak" network transition. Despite this, no crossover between the moduli was found in the whole frequency range, implying the absence of "gel-sol" transition. This indicates that the blends possess excellent stability over a wide range of time scales, either in undamaged or in self-healed state. These master curves also confirm the exceptional mechanical properties of the 50-50 restored membrane, which maintains a strong gel behaviour on a wide range of time scales. The temperature sweep tests on a heating-cooling cycle are shown in Figure 5.18*a*, where the temperature behaviour of the storage modulus (G'), in the range 25-60°C on the first heating and cooling scan cycle, is displayed. All the samples exhibit a similar behaviour: G' slightly decreases during heating, but it is almost completely recovered on cooling. Actually, a certain hysteresis is observed, which means that more time, less than 1 h, is needed to fully recover the module to its initial value in cooling.
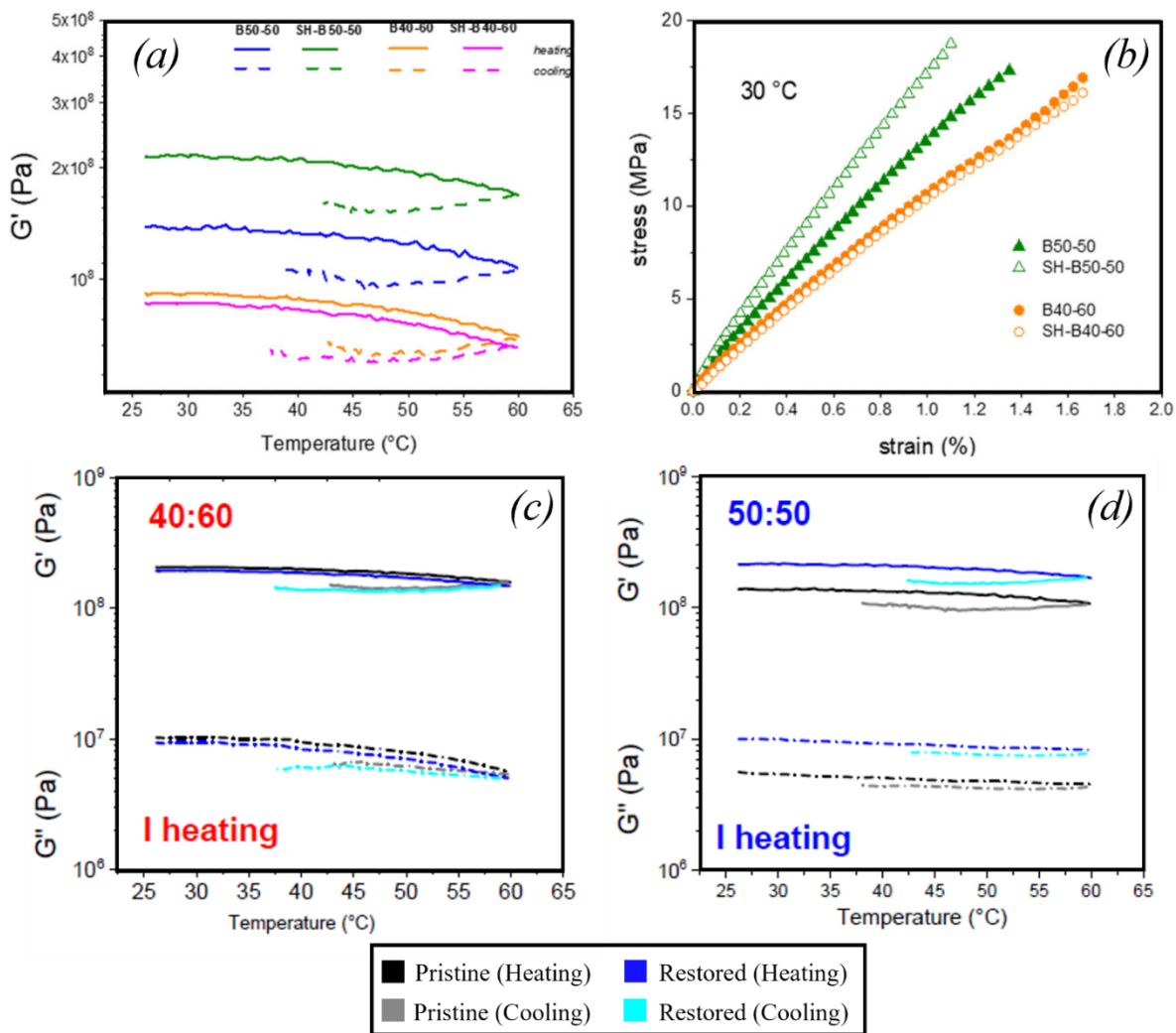
Figure 5.18. (a) *Temperature evolution of the storage moduli (G') from 25 to 60 °C performed on pristine blend 50-50 (B50-50), self-healed blend (SH-B50-50), blend 40-60 (B40-60), and self-healed blend SH-B40-60.* ***(b)*** *Stress-strain plot for blend 50-50, both pristine B50-50 and self-healed SH-B50-50; and blend 40-60, both pristine B40-60 and self-healed SH-B40-60.* ***(c,d)*** *Frequency sweep tests carried out on more thermal cycles from 25°C to 60°C, performed on 50-50, 50-50_restored (self-healed), 40-60 and 40-60_restored (self-healed) membranes.*

Indeed, the mechanical spectra executed on more thermal cycles are practically superimposable (Figure 5.18*c,d*), clearly indicating the thermal reversibility of these systems. Finally, Figure 5.18*b* shows the stress-strain behaviour of the pristine and self-healed 50-50 and 40-60 membranes up to the limit of their respective linearity region. Undamaged blends exhibit similar tensile stress (~17.5 MPa), but the elongation at yield point is higher for 40-60 (1.66%) than for 50-50 (1.33%). Such higher elasticity is likely due to the rubber-like properties of the network. As can be clearly seen, both the healed polymer films can effectively self-recover to their original strain after a healing duration of 24 h at

room temperature. It is worth noting that the self-healed 50-50 polymer can sustain a remarkably higher tensile stress, that is, ~22 MPa, than the undamaged membrane, ~17 MPa. Such a massive increase in membrane strength is clearly compatible with the formation of an efficient hydrogen-bonded crosslinked structure.

5.4.2. Electrochemical Performance

To the best of our knowledge, contrary to the silicon-based anodes, chemical SH of BP-based anodes for LIBs or SIBs has not been explored yet. As described in previous reports, the huge volume expansion (up to 300%) observed in these materials upon cycling is typically managed by means of BP composites with high amount of carbon, which acts as a volume buffer. Such a strategy is in principle promising but causes a decrease of the volumetric energy density and the success depends on several variables, including the type of carbon, anode composition, electrolyte, and additives.[3] This work describes, for the first time, the use of a novel binder with SH ability in the aqueous processing of BP anodes for SIBs. To this aim, the blend 50-50 (namely, UPyPEG$_{795}$UPy-PEO 50-50 volume ratio) was selected as the SH polymeric component of the electrode due to its excellent elastic properties and recovering ability. To properly evaluate the repairing effect of such a binder on the electrochemical behaviour of BP in SIBs, the functional properties of the anode were compared with those observed for the same anode including a conventional CMC-PAA binder. The galvanostatic behaviour was evaluated on coin cells from 0.01 and 2 V *versus* Na$^+$/Na at different current densities by using sodium as the counter electrode. Figure 5.19*a,b* reports the rate performances and the corresponding voltage profiles of the BP anodes made with the SH and the CMC-PAA binders. The BP mass loading in the anode was 1.26 and 1.6 mg cm^{-2}, respectively.
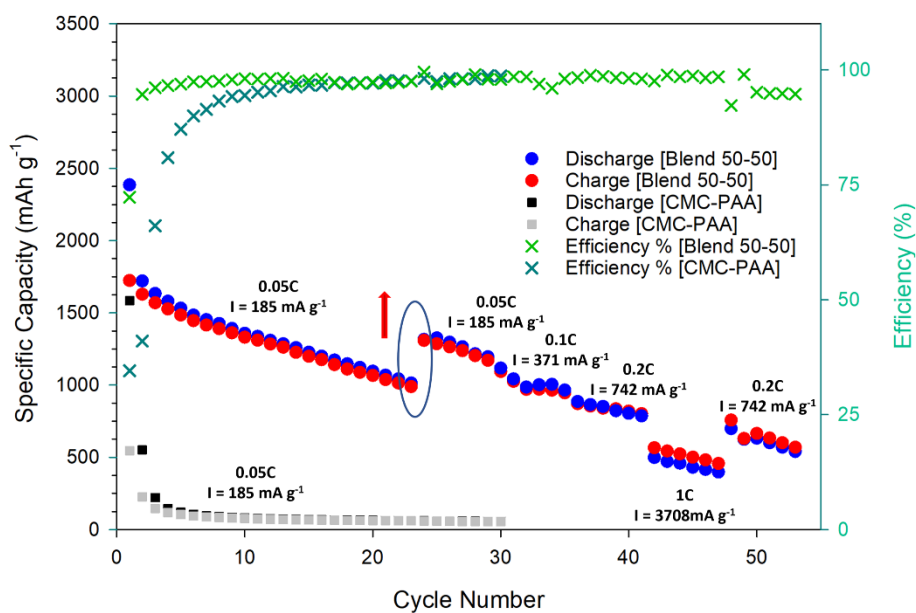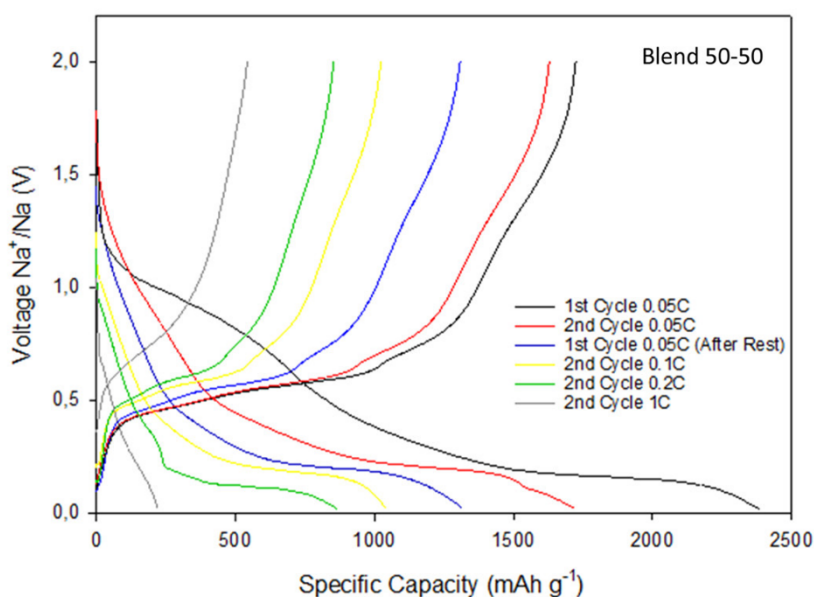
Figure 5.19. (a) *Comparison of the rate performances of two BP anodes (0.05C: I = 185 mA g^{-1}; 0.1C: I = 371 mA g^{-1}; 0.2C: I = 742 mA g^{-1}; and 1C: 3708 mA g^{-1}), including the SH binder (circles, blue: discharge; red: charge; and light green: efficiency) and the conventional CMC-PAA (squares, black: discharge; gray: charge; and dark green: efficiency). The arrow in red and the section delimited by the blue ellipse represent the recovery of specific capacity following 48 hours of rest. **(b)** Voltage profiles of the SH BP anode.*

On cycling, the first cycle discharge (desodiation) capacity is 2450 mAh g^{-1} at 0.18 A g^{-1} (corresponding to a cycling rate of 0.05C based on the theoretical capacity of BP 1C = 2596 mAh g^{-1})[3], very close to the theoretical one for both the anodes. Upon sodiation, both the samples show a typical stepwise process related to the formation of Na$_x$P species, followed

by a pronounced plateau at around 0.3 V *versus* Na metal, due to the final Na$_3$P formation. After the first cycle, the discharge capacity of SH anodes decreases up to 1700 mAh g^{-1}, as typically observed in these systems. However, starting from the second cycle, the cycling stability of the two electrodes is dramatically different. After 25 cycles at the same current density (0.185 A g^{-1}), the BP anode with a 50-50 binder retained ~70% of the initial capacity, proving the SH agent ability to assure stronger adhesion among the phosphorus particles, thus mitigating structural instability. In contrast, the capacity of the anode with a CMC-PAA binder abruptly drops to about 100 mAh g^{-1} after the first five cycles, corresponding to a capacity retention less than 10%, in agreement with what is generally observed for pure BP anodes.[6,46] The impressive stabilizing effects of the 50-50 SH binder is further confirmed when this anode is kept to rest for 48 h (see Figure 5.19*a*). Contrary to the anode with CMC-PAA, after the cycling breaks, the SH anode regains about 80% of the capacity lost during the first 25 cycles at 0.185 Ah g^{-1} (increasing from 1000 mAh g^{-1} to 1500 mAh g^{-1}). This demonstrates the maintenance of a good electric contact upon cycling, which is secured by the autonomic healing of the mechanical cracks through the UPy-driven multiple hydrogen bonding. The repairing ability of the binder also affects the electrode cycling performances. In fact, as the current density increases, the specific capacity only slightly decreases, achieving 1000 and 850 mAh g^{-1} at 0.371 A g^{-1} (0.1C) and 0.742 A g^{-1} (0.2C), respectively, with Coulombic efficiency very close to unit.

Although a definite plateau in the capacity behaviour is not reached, as observed in the case of SH pure Si anodes,[18,22] the binder exhibits an impressive stabilizing effect even at high current densities. In fact, the SH BP anode still works well around 500 mAh g^{-1}. This result is better than those observed in the case of other mitigation strategies, for instance, the introduction of Ge into BP to enhance the elastic softness, for which similar capacity retention was only observed at a 4 times lower current density.[46] Electrodes including different BP amounts were also investigated, namely, 2.5 mg cm^{-2} for B50-50 and 1 mg cm^{-2}, but no significant differences were observed in the electrochemical performances as reported in Figure 5.20 (see also Ref. 6).
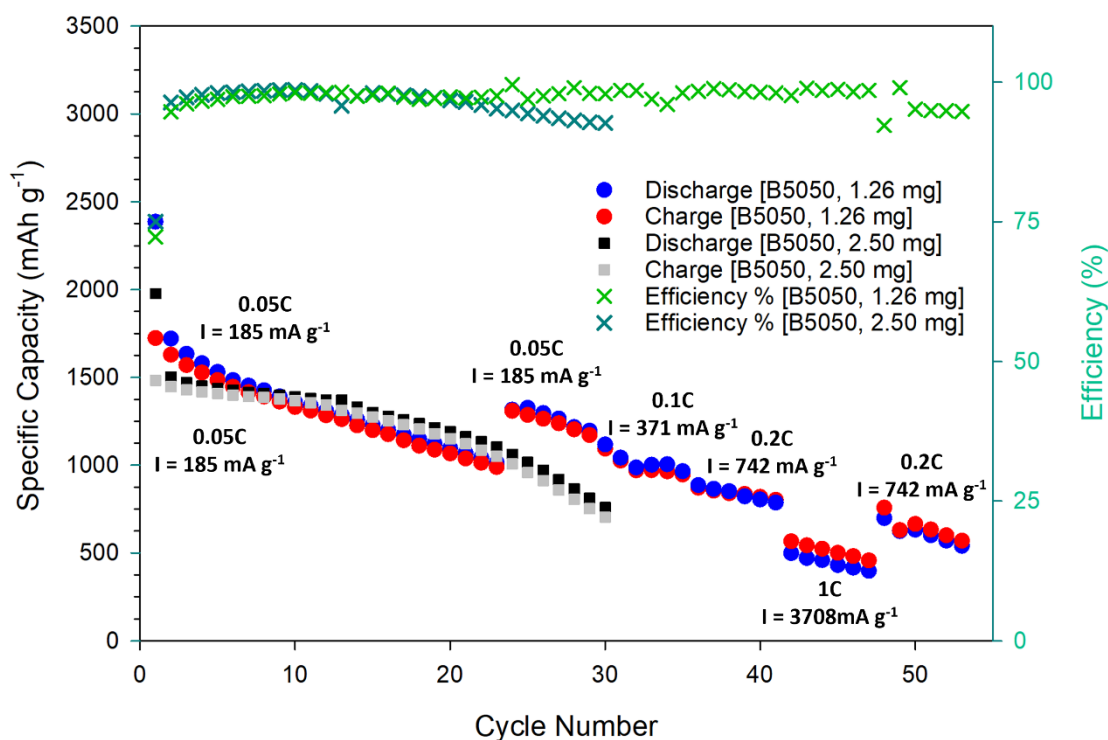
Figure 5.20. *Comparison of the rate performances of two BP anodes, including the self-healing binder with a mass loading of 1.26 mg cm^{-2} (circles, blue: discharge, red: charge; light green: efficiency) and of 2.50 mg cm^{-2} (squares, black: discharge, grey: charge; dark green: efficiency).*

EIS was used to check the SH effect on the interfacial resistances as reported in Figure 5.21. The spectra were obtained at the 20th cycle (i) before, (ii) after the 48 h rest period, and (iii) at the end of the cycling test (see Figure 5.21*b*). The charge transfer resistance is in principle very low in both cases and undergoes further decrease in consequence of the rest from 45 to 15 Ω. This trend indicates the growth on the anode of a stable, thin, and low-resistance SEI, which is able to protect the BP surface avoiding abrupt capacity decays. In the case of CMC-PAA-based BP anode, charge transfer resistances much higher than those measured for the SH electrode were obtained by impedance spectroscopy measurements (Figure 5.21*c*) after electrochemical cycling, namely, 1840 and 1221 Ω, respectively. The spectrum at the end of the cycling test appears more complex, likely because of the formation of one or more different passivation layers, reasonably thicker than what, in contrast, noticed in the B50-50 anode.
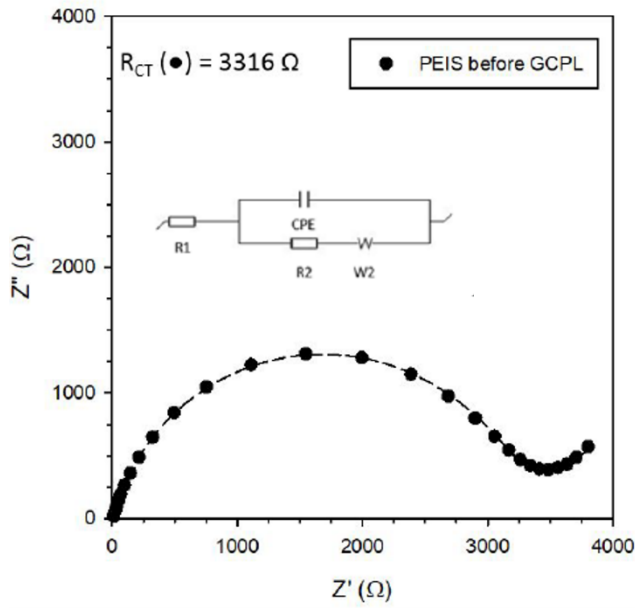
(a)
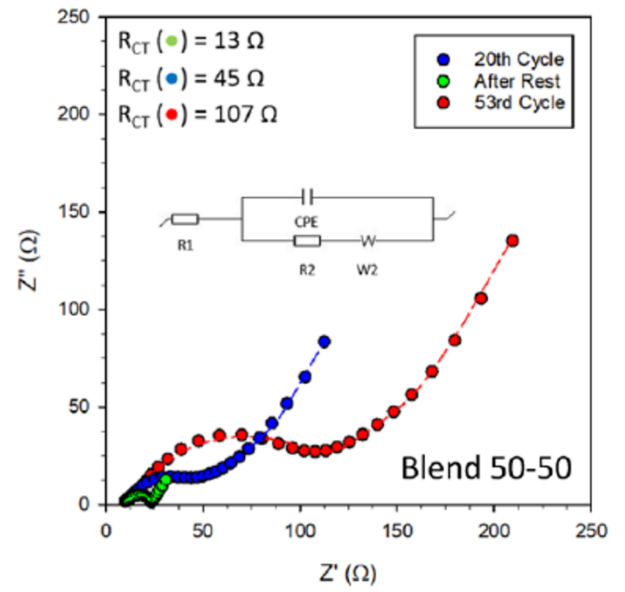
(b)
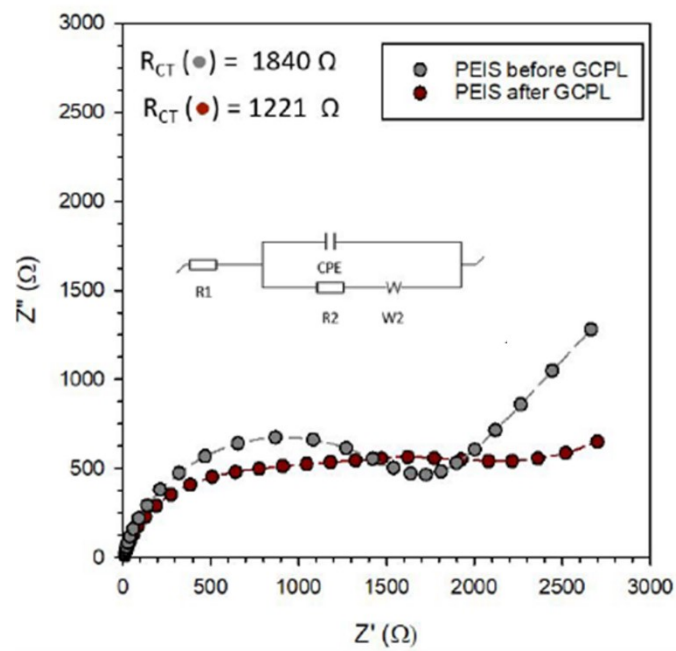
(c)

Figure 5.21. *Nyquist plots collected **(a)** on the SH BP anode before the galvanostatic cycling tests and **(b)** during and at the end of the galvanostatic cycling tests on the SH BP anode. **(c)** Nyquist plots collected on the CMC-PAA BP anode before and at the end of the galvanostatic cycling.*

Finally, both top-view and cross-sectional scanning electron microscopy (SEM) images (Figure 5.22) were collected on the cell before the galvanostatic cycling and at the end of the whole tests (after 55 cycles at different current densities).
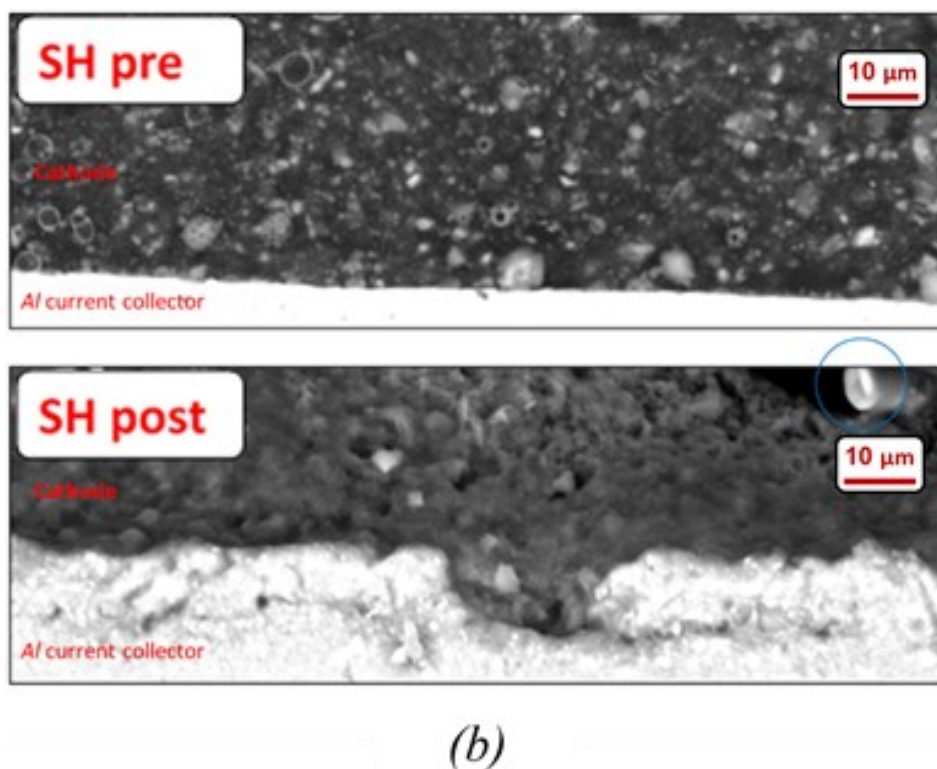

(a)
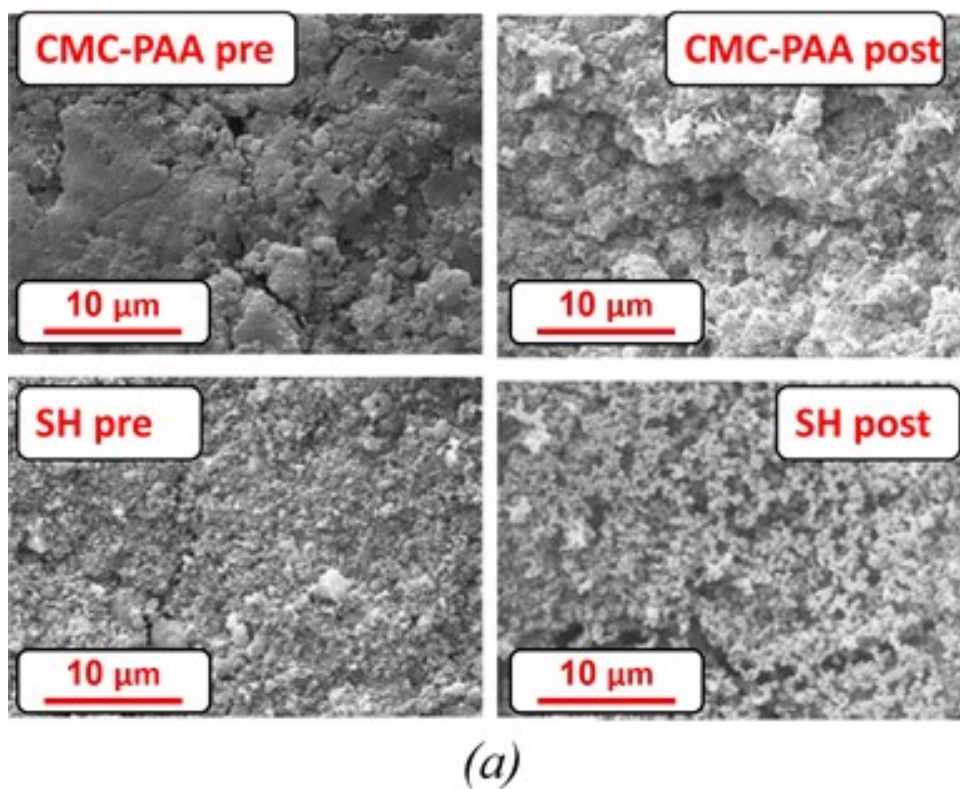
Figure 5.22. (a) Top-view images of the CMC-PAA-based (up) and SH-based (down) BP anode before and after cycling; *(b)* cross-sectional SEM images of the pristine SH-based BP anode (up), and of the same electrode observed after the end of galvanostatic cycling tests (down).

The top-view images (Figure 5.22*a*) provide evidence that the SH anode displays a much more flat and smooth morphology with respect to the CMC-PAA-based electrode, which shows even a much discontinuous surface. This low rugosity is also maintained after electrochemical cycling, where no significant increase of roughness is noted. A texture of small grains distributed on the surface is also present reasonably related to the SEI formation and by products of electrolyte decomposition. The cross-sectional images (Figure 5.22*b*) show that the BP anode including the SH binder is able to preserve the electrode morphology. The cross-section of the pristine anode reveals a slightly porous electrode with a thickness of about 35 μm and a homogeneous distribution of the particle sizes. Despite such low porosity, the Na migration along the anode is still ensured thanks to a polymer chain-assisted mechanism, allowed by the low T_g-PEG-based SH binder, further plasticized by the carbonate liquid electrolytes. Except for a slight increase of porosity, the cycled electrode does not reveal any significant structural degradation or reduction of adhesion with the current collector, which is still very good, contrary to what is observed in the case of CMC-PAA binders where *post mortem* SEM-FIB/EDX revealed serious coating layer

136

detachments from the Al foil, as already shown in our previous paper.[6] In addition, the cycled electrode thickness does not increase, confirming that such a binder prevents the BP anode from irreversible volume expansion thanks to its SH ability.

5.5. Conclusion

For the first time to the best of our knowledge, we have reported on a novel and sustainable polymeric blend with SH ability as a binder in BP-based anodes for SIBs. The repairing reactivity is intrinsic and based on dynamic multiple hydrogen bonding enabled by UPy-telechelic networks. Specifically, we have successfully demonstrated that the SH properties of the binder have remarkable beneficial effects on both cycling performances and stability of the electrode in Na-ion cells. Although additional work is necessary to meet the commercial requirements of SIBs or LIBs, undoubtedly the SH performances of this binder are very promising and will be further explored. In particular, our results lay the groundwork to extend the use of the UPy-telechelic backbones also to other electrochemically active materials suffering huge volumetric changes, even in synergy with other strategies which already proved their ability to improve the structural stability, for example, carbon as a buffering agent.

5.6. Bibliography

1. Choi, J. W.; Aurbach, D. Promise and Reality of Post-Lithium-Ion Batteries with High Energy Densities. *Nat. Rev. Mater*. 2016, **1**, 16013.

2. Casimir, A.; Zhang, H.; Ogoke, O.; Amine, J. C.; Lu, J.; Wu, G. Silicon-Based Anodes for Lithium-Ion Batteries: Effectiveness of Materials Synthesis and Electrode Preparation. *Nano Energy* 2016, **27**, 359−376.

3. Fu, Y.; Wei, Q.; Zhang, G.; Sun, S. Advanced Phosphorus-Based Materials for Lithium/Sodium-Ion Batteries: Recent Developments and Future Perspectives. *Adv. Energy Mater.* 2018, **8**, 1703058.

4. Dou, F.; Shi, L.; Chen, G.; Zhang, D. Silicon/Carbon Composite Anode Materials for Lithium-Ion Batteries. *Electrochem. Energy Rev.* 2019, **2**, 149−198.

5. Li, F.; Xu, J.; Hou, Z.; Li, M.; Yang, R. Silicon Anodes for High-Performance Storage Devices: Structural Design, Material Compounding, Advances in Electrolytes and Binders. *ChemNanoMat* 2020, **6**, 720−738.

6. Quartarone, E.; Eisenmann, T.; Kuenzel, M.; Tealdi, C.; Marrani, A. G.; Brutti, S.; Callegari, D.; Passerini, S. Towards Advanced Sodium-Ion Batteries: Green, Low-Cost and High-Capacity Anode Compartment Encompassing Phosphorus/Carbon Nanocomposite as the Active Material and Aluminum as the Current Collector. *J. Electrochem. Soc.* 2020, **167**, 080509.

7. Wang, S.; Urban, M. W. Self-Healing Polymers. *Nat. Rev. Mater.* 2020, **5**, 562−583.

8. Yang, Y.; Urban, M. W. Self-Healing Polymeric Materials. *Chem. Soc. Rev.* 2013, **42**, 7446-7467.

9. Chakma, P.; Konkolewicz, D. Dynamic Covalent Bonds in Polymeric Materials. *Angew. Chem., Int. Ed.* 2019, **58**, 9682−9695.

10. Li, C. H.; Zuo, J. L. Self-Healing Polymers Based on Coordination Bonds. *Adv. Mater.* 2019, **32**, 1903762.

11. Thangavel, G.; Tan, M. W. M.; Lee, P. S. Advances in Self-Healing Supramolecular Soft Materials and Nanocomposites. *Nano Convergence* 2019, **6**, 18.

12. Cheng, Y.; Xiao, X.; Pan, K.; Pang, H. Development and Application of Self-Healing Materials in Smart Batteries and Supercapacitors. *Chem. Eng. J.* 2020, **380**, 122565.

13. Wang, H.; Wang, P.; Feng, Y.; Liu, J.; Wang, J.; Hu, M.; Wei, J.; Huang, Y. Recent Advances on Self-Healing Materials and Batteries. *ChemElectroChem* 2019, **6**, 1605−1622.

14. Mezzomo, L.; Ferrara, C.; Brugnetti, G.; Callegari, D.; Quartarone, E.; Mustarelli, P.; Ruffo, R. Exploiting Self-Healing in Lithium Batteries: Strategies for Next-Generation Energy Storage Devices. *Adv. Energy Mater.* 2020, **10**, 2002815.

15. Xu, Z.; Yang, J.; Zhang, T.; Nuli, Y.; Wang, J.; Hirano, S.-i. Silicon Microparticle Anodes with Self-Healing Multiple Network Binder. *Joule* 2018, **2**, 950−961.

16. Yang, J.; Zhang, L.; Zhang, T.; Wang, X.; Gao, Y.; Fang, Q. Sef-Healing Strategy for Si Nanoparticles towards Practical Application as Anode Materials for Li-Ion Batteries. *Electrochem. Commun.* 2018, **87**, 22−26.

17. Zhang, G.; Yang, Y.; Chen, Y.; Huang, J.; Zhang, T.; Zeng, H.; Wang, C.; Liu, G.; Deng, Y. A Quadruple-Hydrogen-Bonded Supramolecular Binder for High-Performance Silicon Anodes in Lithium-Ion Batteries. *Small* 2018, **14**, 1801189.

18. Wang, C.; Wu, H.; Chen, Z.; McDowell, M. T.; Cui, Y.; Bao, Z. Self-Healing Chemistry Enables the Stable Operation of Silicon Microparticle Anodes for High-Energy Lithium-Ion Batteries. *Nat. Chem.* 2013, **5**, 1042−1048.

19. Ryu, J.; Kim, S.; Kim, J.; Park, S.; Lee, S.; Yoo, S.; Kim, J.; Choi, N. S.; Ryu, J. H.; Park, S. Room-Temperature Crosslinkable Natural Polymer Binder for High-Rate and Stable Silicon Anodes. *Adv. Funct. Mater.* 2020, **30**, 1908433.

20. Zou, F.; Manthiram, A. A Review of the Design of Advanced Binders for High-Performance Batteries. *Adv. Energy Mater.* 2020, **10**, 2002508.

21. Pan, Y.; Gao, S.; Sun, F.; Yang, H.; Cao, P. F. Polymer Binders Constructed through Dynamic Noncovalent Bonds for High-Capacity Silicon-Based Anodes. *Chem.─Eur. J.* 2019, **25**, 10976−10994.

22. Munaoka, T.; Yan, X.; Lopez, J.; To, J. W. F.; Park, J.; Tok, J. B.-H.; Cui, Y.; Bao, Z. Ionically Conductive Self-Healing Binder for Low Cost Si Microparticles Anodes in Li-Ion Batteries. *Adv. Energy Mater.* 2018, **8**, 1703138.

23. Zhou, B.; Jo, Y. H.; Wang, R.; He, D.; Zhou, X.; Xie, X.; Xue, Z. Self-Healing Composite Polymer Electrolyte Formed via Supramolecular Networks for High-Performance Lithium-Ion Batteries. *J. Mater. Chem. A* 2019, **7**, 10354−10362.

24. Zhou, B.; He, D.; Hu, J.; Ye, Y.; Peng, H.; Zhou, X.; Xie, X.; Xue, Z. A Flexible, Self-Healing and Highly Stretchable Polymer Electrolyte via Quadruple Hydrogen Bonding for Lithium-Ion Batteries. *J. Mater. Chem. A* 2018, **6**, 11725−11733.

25. White, S. R.; Sottos, N. R.; Geubelle, P. H.; Moore, J. S.; Kessler, M. R.; Sriram, S. R.; Brown, E. N.; Viswanathan, S. Autonomic Healing of Polymer Composites. *Nature* 2001, **409**, 794−797.

26. van Gemert, G. M. L.; Peeters, J. W.; Söntjens, S. H. M.; Janssen, H. M.; Bosman, A. W. Self-Healing Supramolecular Polymers In Action. *Macromol. Chem. Phys.* 2012, **213**, 234−242.

27. Kong, W.; Wen, Z.; Zhou, Z.; Wang, G.; Yin, J.; Cui, L.; Sun, W. A Self-Healing High-Performance Phosphorus Composite Anode Enabled by in Situ Preformed Intermediate Lithium Sulfides. *J. Mater. Chem. A* 2019, **7**, 27048−27056.

28. Wang, X.; Li, Y.; Qian, Y.; Qi, H.; Li, J.; Sun, J. Mechanically Robust Atomic Oxygen-Resistant Coatings Capable of Autonomously Healing Damage in Low Earth Orbit Space Environment. *Adv. Mater.* 2018, **30**, 1803854.

29. Ferrara, C.; Vigo, E.; Albini, B.; Galinetto, P.; Milanese, C.; Tealdi, C.; Quartarone, E.; Passerini, S.; Mustarelli, P. Efficiency and Quality Issues in the Production of Black Phosphorus by Mechanochemical Synthesis: A Multi-Technique Approach. *ACS Appl. Energy Mater.* 2019, **2**, 2794−2802.

30. Kwon, Y. H.; Minnici, K.; Huie, M. M.; Takeuchi, K. J.; Takeuchi, E. S.; Marschilok, A. C.; Reichmanis, E. Electron/Ion Transport Enhancer in High Capacity Li-Ion Battery Anodes. *Chem. Mater.* 2016, **28**, 6689−6697.

31. Sharma, A. K.; Caricato, M.; Quartarone, E.; Edizer, S.; Schieroni, A. G.; Mendichi, R.; Pasini, D. Polystyrene-Based Self-Aggregating Polymers Based on UPy Units. *Polym. Bull.* 2012, **69**, 911−923.

32. Folmer, B. J. B.; Sijbesma, R. P.; Versteegen, R. M.; van der Rijt, J. A. J.; Meijer, E. W. Supramolecular Polymer Materials: Chain Extension of Telechelic Polymers Using a Reactive Hydrogen-Bonding Synthon. *Adv. Mater.* 2000, **12**, 874−878.

33. Kautz, H.; van Beek, D. J. M.; Sijbesma, R. P.; Meijer, E. W. Cooperative End-to-End and Lateral Hydrogen-Bonding Motifs in Supramolecular Thermoplastic Elastomers. *Macromolecules* 2006, **39**, 4265−4267.

34. Bobade, S.; Wang, Y.; Mays, J.; Baskaran, D. Synthesis and Characterization of Ureidopyrimidone Telechelics by CuAAC "Click" Reaction: Effect of Tg and Polarity. *Macromolecules* 2014, **47**, 5040−5050.

35. Lange, R. F. M.; Van Gurp, M.; Meijer, E. W. Hydrogen-Bonded Supramolecular Polymer Networks. *J. Polym. Sci., Part A: Polym. Chem.* 1999, **37**, 3657−3670.

36. Afifi-Effat, A. M.; Hay, J. N. Enthalpy and Entropy of Fusion and the Equilibrium Melting Point of Polyethylene Oxide. *J. Chem. Soc., Faraday Trans. 2* 1972, **68**, 656 −661.

37. Quartarone, E.; Mustarelli, P.; Tomasi, C.; Magistris, A. Structure and Transport Properties of PEO−$Li_2O \cdot 3B_2O_3$Mixed-Phase Composites. *J. Phys. Chem. B* 1998, **102**, 9610−9616.

38. Duan, P.; Moreton, J. C.; Tavares, S. R.; Semino, R.; Maurin, G.; Cohen, S. M.; Schmidt-Rohr, K. Polymer Infiltration into Metal-Organic Frameworks in Mixed-Matrix Membranes Detected In Situ by NMR. *J. Am. Chem. Soc.* 2019, **141**, 7589.

39. Liu, T.; Zou, S.; Hang, C.; Li, J.; Di, X.; Li, X.; Wu, Q.; Wang, F.; Sun, P. Mechanically Strong and Tough Hydrogels with PH-Triggered Self-Healing and Shape Memory Properties Based on a Dual Physically Crosslinked Network. *Polym. Chem.* 2020, **11**, 1906−1918.

40. Samiullah, M. H.; Pulst, M.; Golitsyn, Y.; Busse, K.; Poppe, S.; Hussain, H.; Reichert, D.; Kressler, J. Solid State Phase Transitions in Poly(Ethylene Oxide) Crystals Induced by Designed Chain Defects. *Macromolecules* 2018, **51**, 4407−4414.

41. Nicotera, I.; Coppola, L.; Oliviero, C.; Ranieri, G. A. Rheological Properties and Impedance Spectroscopy of PMMA-PVdF Blend and PMMA Gel Polymer Electrolytes for Advanced Lithium Batteries. *Ionics* 2005, **11**, 87−94.

42. Winter, H. H.; Chambon, F. Analysis of Linear Viscoelasticity of a Crosslinking Polymer at the Gel Point. *J. Rheol.* 1986, **30**, 367−382.

43. Williams, M. L.; Landel, R. F.; Ferry, J. D. The Temperature Dependence of Relaxation Mechanisms in Amorphous Polymers and Other Glass-Forming Liquids. *J. Am. Chem. Soc.* 1955, **77**, 3701−3707.

44. Nicotera, I.; Coppola, L.; Oliviero, C.; Russo, A.; Ranieri, G. A. Some Physicochemical Properties of PAN-Based Electrolytes: Solution and Gel Microstructures. *Solid State Ionics* 2004, **167**, 213−220.

45. Nicotera, I.; Coppola, L.; Oliviero, C.; Ranieri, G. A. Spectromechanical Properties of Polymeric Gel Electrolytes and Blends. *Macromol. Symp.* 2007, **247**, 282−294.

46. Kim, D.; Zhang, K.; Cho, M.; Kang, Y.-M. Critical Design Factors for Kinetically Favorable P-Based Compounds toward Alloying with Na Ions for High-Power Sodium-Ion Batteries. *Energy Environ. Sci.* 2019, **12**, 1326−1333.

Chapter 6:
Lithium Intercalation Mechanisms and Critical Role of Multi-Doping in LMO Spinel Type as High-Capacity Cathode Materials for Lithium Ion Batteries

6.1. Abstract

The ever-growing demand for Li-ion batteries requires high-capacity electrode materials that should also be environmentally benign, Co-free, secure, and durable, to achieve an optimal compromise between sustainability and functional performances. Spinel $LiMn_2O_4$ (LMO) is a state-of-the-art material, which, in principle, could satisfy such requirements. However, an undesired cubic-tetragonal phase transition favours Jahn-Teller (J-T) spinel distortion, leading to severe capacity reduction upon cycling below 3 V. Here, we propose a novel dual-doping strategy for LMO, based on the partial substitution of Mn(III) with Fe(III) and Ti(IV) to design new active materials for high-capacity cathodes, namely $LiFe_xMn_{2-x-y}Ti_yO_4$ (LFMT), with Li/Mn ratio ranging between 1 and 1.7. The substitution of Mn with Fe and Ti suppresses the J-T distortion, which is often still evident in the case of Ti-doped LMO. This allows cycling in a wider voltage range (4.8 V-1.5 V), thus resulting in higher capacity and significantly improved stability. The lithiation mechanisms were investigated by combining *ex situ* X-ray diffraction (XRD) and X-ray absorption spectroscopy (XAS analyses). It demonstrated that the only redox-active metal is Mn, while Fe and Ti are electrochemically inactive. The extensive electrochemical lithiation/delithiation of the LFMT compositions brought unprecedented results, which give evidence of stabilizing cation disorder through the formation of Mn-rich and Mn-poor domains, leading to two spinel phases with different Mn:Ti ratios. These insights into the lithiation mechanism pave the way for a better understanding of the doping chemistry and electrochemistry of Mn-based spinels as cathode materials for Li-ion batteries.

6.2. Introduction

The cubic spinel $LiMn_2O_4$ is one of the most traditionally studied active materials for cathodes in Lithium-ion batteries (LIBs). This is due to some unique properties, such as its high abundance of manganese and the absence of Co, resulting in a non-toxic, safe, environmental friendly, and thermally stable material.[1] The interest in the spinel electrodes is predominantly due to their favourable framework, made of a continuous and energetically accessible 3D framework of face-sharing tetrahedra and octahedra through which Li ions can easily diffuse.[2] The electrochemical profile of the $Li/Li_xMn_2O_4$ cell shows two reversible intercalation phenomena, at 4.1 V and 3.0 V vs. Li, each of them resulting in a capacity of 120 mAh g^{-1}.[1] The first plateau is associated with the removal of one lithium ($0 \leq x \leq 1$), whereas the second plateau corresponds to the insertion of a second Li in the spinel phase ($1 \leq x \leq 2$).[1,3] However, it is well known that the spinel cathode can practically use only half of its potential Li capacity and suffers from poor kinetics and a capacity that reduces upon cycling. This problem is more severe at 3 V and slower at 4 V, particularly at elevated temperatures. This is due to a strong synergy between three phenomena: (i) a first-order phase transition (cubic‑tetragonal) occurring at 3 V once the spinel is lithiated beyond the $LiMn_2O_4$ composition; (ii) a structural rearrangement, causing physical destruction induced by a surface Jahn-Teller (J-T) distortion associated with Mn(III) ions; (iii) a chemical dissolution of Mn into the spinel. The latter process is exacerbated especially in the case of slightly acidic electrolytes (for example in presence of HF-based impurities) and is responsible for a disproportionation reaction of extensively lithiated particles with high Mn(III) concentration to give Mn(IV) (in the solid) and Mn(II) (released in the electrolyte).[2] Once dissolved, the manganese ions migrate to the anode where they are reduced to metallic Mn, consuming Lithium and, consequently, decreasing the overall cell capacity.[3] In order to minimize both the disproportionation step and the impact of the J-T distortion, several attempts to dope the spinel were proposed in literature these last decades.[4-13] A first doping strategy concerns the partial Mn(III) substitution with metals such as Al, Mg, Ni, Cr, Co, Fe, Ti. A second approach was to replace some oxygen with fluorine. The cation doping enhances the overall structural stability and decreases the spinel lattice parameter to values lower than 8.23 Å. This seems to be a threshold below which the cycling performances significantly improve.[1,5] Moreover, the substitution of Mn(III) ions with other transition metals also results in an effective improvement of the cycling performances at 4 V. On the

other hand, the anion doping with fluorine favours the reduction of the Mn average oxidation state, inhibiting the capacity loss.[5] One of the most efficient doping strategies in the case of $LiMn_2O_4$ is the partial substitution of Mn(III) with Ti(IV) to form $LiMn_{2-x}Ti_xO_4$.[6,14,15] The bonding energy of Ti-O is higher than that of Mn-O, therefore an enhancement of the structural stability of the spinel is expected. Moreover, it was demonstrated that when Ti(IV) is present in high content in the spinel structure, the removal and intercalation of Li ions is associated with the increase of Mn(IV) and Mn(II), respectively, that are both non-J-T ions. Due to the inhibition of such distortions, the spinel can store about 2 Li^+ occupying the tetragonal *8a* and the octahedral *16c* sites of the structure, resulting in a very high theoretical capacity (308 mAh g^{-1} in the specific case of $LiMnTiO_4$) by using the Mn^{2+}/Mn^{4+} redox couple.[6] The concentration reduction of the J-T active Mn(III) can, in principle, also improve the cycling performances in a wider voltage range up to 4.8 V.[14] However, it may occur that some Mn(II) ions replace Li^+ during the Ti substitution for Mn, with the consequent degradation of the rate capability. For this reason, the Ti doping level needs to be properly modulated and optimized.[14] In this work, a new family of dual-doped $LiFe_xMn_{2-x-y}Ti_yO_4$ and tri-doped $LiCr_xFe_yMn_{2-x-y-z}Ti_zO_4$ spinel was synthesized via sol-gel reaction by modulating the stoichiometry ratio of the transition metals. These systems were investigated as novel active materials for high-energy cathodes in Co-free Li ion batteries more suitable over a wide voltage range, between 1.5 V and 4.8 V. The effect of the partial dual and tri Mn(III) substitution with Cr, Fe and Ti and the potentially synergetic role of such transition metals on the stability of the spinel structure and on the modulation in the amount of Mn(II) ions were investigated by means of electron microscopy, X-ray diffraction and electrochemical characterizations. For LFMT cathodes *ex situ* X-ray spectroscopy (XAS) was also performed to understand the chemistry of each element in the spinel and to address the lithiation/delithiation mechanism as well as the possible presence of oxygen redox activity in such complex systems.

6.3. Material and Methods

6.3.1. Synthesis of LFMT Spinel Active Materials

LFMT powders were synthesized by means of a sol-gel route starting from a mixture of $LiCH_3COO \cdot 2H_2O$, $Mn(NO_3)_2 \cdot 4H_2O$, and $Fe(NO_3)_3 \cdot 9H_2O$ (Sigma Aldrich) in the proper molar ratios, dissolved in distilled H_2O under magnetic stirring at room temperature. A solution of $Ti(i\text{-}OPr)_4$ and acetylacetone (acac) (Ti:acac molar ratio of 1:1.1) was then added under vigorous stirring to the dissolved precursors. Citric acid was finally added as a gelling agent. The solution was heated to 80°C and the resulting gel was dried at 120°C for 2 hours and finally calcined in air at 600°C (temperature ramp of 5°C min^{-1}) for other 2 hours. Several spinels were prepared by changing the stoichiometry of the transition metals, whose compositions are reported in Table 6.1.

	Composition	Li/Mn	Mn/Fe	Mn/Ti	Fe/Ti
LFMTa	$LiFe_{0.53}Mn_{1.00}Ti_{0.47}O_4$	1.0	1.9	2.1	1.1
LFMTb	$LiFe_{0.56}Mn_{0.92}Ti_{0.52}O_4$	1.1	1.6	1.8	1.1
LFMTc	$LiFe_{0.6}Mn_{0.85}Ti_{0.55}O_4$	1.2	1.4	1.5	1.1
LFMTd	$LiFe_{0.74}Mn_{0.58}Ti_{0.68}O_4$	1.7	0.8	0.8	1.1

Table 6.1. Spinel cathode composition as determined by SEM-EDX measurements.

6.3.2. Structural and Morphological Characterization

SEM and Energy Dispersive X-ray Spectroscopy (EDX) were performed using a Tescan Mira3XMU microscope operated at 20 kV and equipped with an EDAX EDX analysis system. The samples were coated with a carbon thin film using a Cressington208 carbon coater. Powder X-rays diffraction carried out by using a Bruker D8 Advance diffractometer in Bragg-Brentano geometry equipped with Ni-filtered Cu Kα radiation. The diffraction patterns of the powder samples as well as the composite cathodes, stuck onto a glass holder, were collected in the 15-65 2θ range, with a scan step of 0.04°, for a total acquisition time of 2 hours. Structural analysis was performed via Rietveld refinements using the GSAS

package.[16] The peak broadening was estimated using WinPLOTR, accounting explicitly for $K\alpha_1$-$K\alpha_2$ wavelengths.[17] The quality of least squares refinement in this case is also indicated by residual functions R_p and R_{wp}, defined as:

$$R_p = \frac{\sum |I_0 - I_C|}{\sum I_0}$$

$$R_{wp} = \sqrt{\frac{\sum w(I_0 - I_C)^2}{\sum W i_0^2}}$$

where I_0 is the experimental intensity and I_C the calculated one.

6.3.3. Cathode Preparation and Cell Assembly

The cathode slurry was prepared by using 70 wt% of active material (LFMT), 20% of Conductive Carbon black (Imerys, Ensaco 350P), and 10% of a binder (polyvinylidene fluoride, PVdF). The solid content of all slurries was kept between 26 wt% and 28 wt%. LFMT and carbon powders were mixed in zirconia jars by a planetary ball mill at 150 rpm for 10 min twice, with a rest period of 5 min. Subsequently, the polymeric binder was added and mixed with a similar procedure. The as prepared mixture was dispersed in N-methylpyrrolidone (NMP) (Sigma-Aldrich) to obtain the slurry, which was cast on a carbon-coated Al foil using a doctor blade with a wet thickness of 300 μm. The casted slurry was dried under vacuum at 80°C to avoid moisture and oxygen contamination. The cathode (active mass ~2 mg cm^{-2}) was finally cut into 2 cm^2 disks and stored in a glove box (MBraum, H_2O and O_2 < 0.5 ppm) before the electrochemical measurements. All the functional tests were performed using a coin cell type (CR2032 – MTI Corp.) assembled in an Ar-filled glove box (H_2O and O_2 < 0.5 ppm). Metallic Li was used as counter electrode. Electrodes were separated with a *Whatman* glass fiber separator, imbied by 120-150 μL of liquid electrolyte, consisting in a solution 1.0 M $LiPF_6$ in Ethylene Carbonate:Dimethyl Carbonate (LP30, EC:DMC, 50:50 vol%) (Sigma-Aldrich).

6.3.4. Electrochemical Characterization

Potentio-electrochemical impedance spectroscopy (PEIS), galvanostatic cycling with potential limitation (GCPL), and potentiodynamic cycling with galvanostatic acceleration PCGA) were performed on $Li/LiM_xMn_yO_4$ cells in a wide voltage range between 1.5 V and 4.8 V at room temperature and different C rates by means of battery tester (Bio-Logic BCS-810). A theoretical capacity of 270 mAh g^{-1} was calculated by taking into account the composition and the redox couple actually involved in the electrochemical process. Electrochemical Impedance Spectroscopy (EIS) was used to measure the bulk conductivity (both ionic and electronic) as well as the transference numbers of ionic and electronic species in the active materials.[20] To this aim, Nyquist plots were collected on a symmetric cell including Platinum-sputtered pellets of the spinel powders ($\sim$1.8 mm thick), sandwiched between two Pt plates. Frequency sweeps between 500 and 0.1 Hz were imposed at 100-150 mV as voltage amplitude by means of a frequency response analyzer (Solartron 1255), coupled with an electrochemical interface (Solartron 1287) in the temperature range 25–300°C. EIS scans between 100 and 0.1 Hz were also collected at 50 mV during the galvanostatic cycling to investigate Li/LFMT cell impedance before and after the functional tests.

6.3.5. *Ex Situ* X-Ray Absorption Spectroscopy Measurements

Ex situ XAS spectra were acquired on LFMT electrodes quenched at four different electrochemical conditions, namely at OCV, at 4.8 V *vs*. Li (in correspondence of the first and the second delithiation), and at 1.5 V *vs*. Li after 60 cycles. The XAS spectra were measured at the Mn, Fe, and Ti $L_{2,3}$ edges and at the O K edge at the APE-HE beamline at the Elettra synchrotron radiation facility in Trieste.[18,19] All the electrodes were first located in the sample holder in an N_2-filled glove box (H_2O and O_2 < 0.5 ppm), and then moved to the ultrahigh-vacuum chamber of the APE-HE beamline, where the spectra were acquired in Total Electron Yield (TEY) mode. In this configuration, the X-rays beam passes through a Si_3N_4 membrane and reaches the sample; the secondary emission is then collected with a picoammeter connected to the sample, measuring the drain current. The collected data were calibrated using a reference for each investigated edge (Mn_3O_4, Fe_2O_3, and TiO_2). All spectra

were background-subtracted, flattening the baseline of the spectra, and normalized to peak integrated area.

6.4. Results

6.4.1. LFMT Active Materials: Morphology, Structure, and Transport Properties

Sol-gel syntheses were attempted using annealing conditions similar to the one used for the synthesis of the spinel-based active materials. Specifically, a greener modified-Pechini route was carried out by using citric acid as complexing agent and nitrates as transition metal (TM) precursors, instead of the conventional chloride, whose removal as impurities is typically more difficult. As summarized in Table 6.1, four compositions were selected, differing in the Li/Mn molar ratio, while the Fe/Ti ratio was kept constant at 1.1. The pristine spinels were first investigated by XRD, SEM, and electrochemical impedance spectroscopy in order to understand the role played by the TMs dual doping on the morphology, crystal structure, and transport properties of each material. Figure 6.1 compares the electron microscopy images for all the synthesized samples.
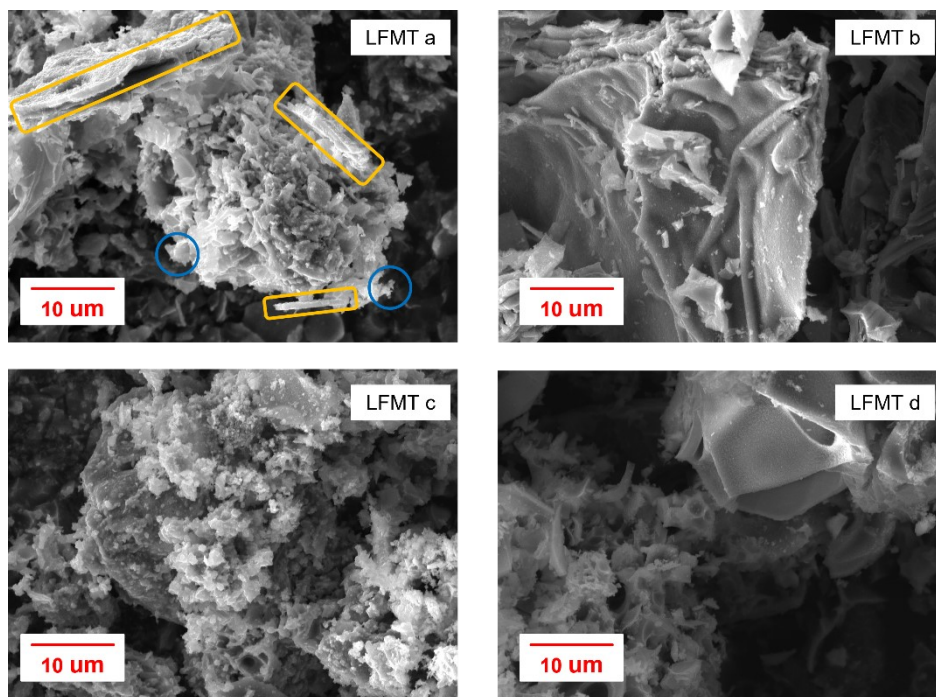
Figure 6.1. *Secondary electrons SEM image of the pristine LFMT sample prepared via sol-gel route and calcination at low temperature.*

The LFMT systems exhibit a lamellar- and flake-like morphology consisting of loose agglomerates showing a large distribution in dimension and connected to each other through a porous network, likely formed during the sol-gel process. The undoped LMO prepared by more conventional solid state reactions presents, in fact, a morphology characterized by closely packed particles, whose size strictly depends on the annealing conditions.[21] Fig. 6.2(I) reports the XRD patterns of the pristine powder samples, whose diffraction peaks can all be indexed according to a single cubic $LiMn_2O_4$ $Fd\bar{3}m$ space group. The corresponding lattice constant, a, computed by Rietveld refinements, is reported in Figure 6.2(II), as a function of the average ionic radius (i.r.) of the cations and is compared to the one of the undoped $Li_{1+x}Mn_{2-x}O_4$ at different degrees of (de)lithiation, as taken from Ref. 3.
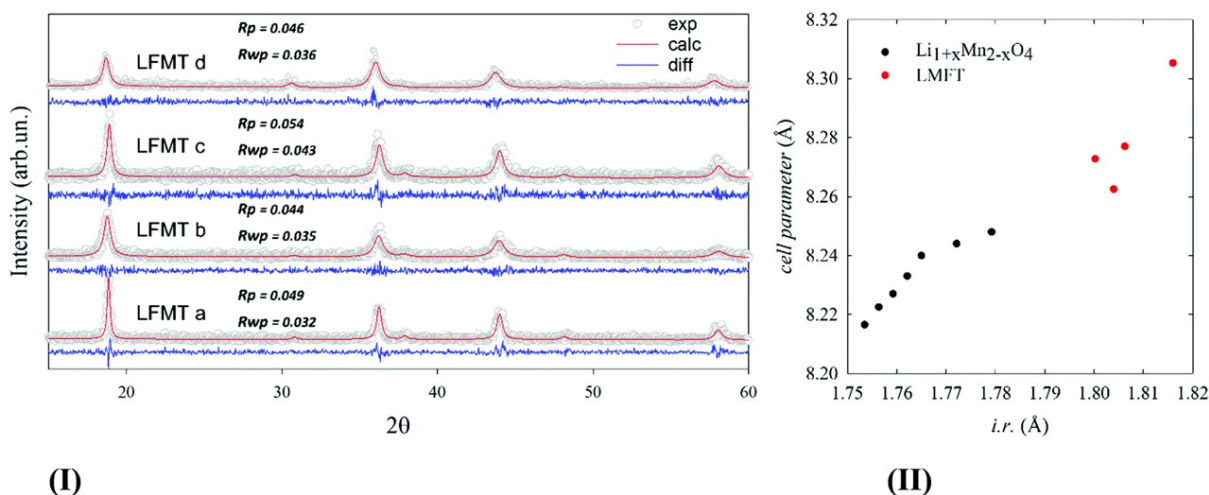
Figure 6.2. (I) *Experimental patterns of powdered specimens collected at room temperature (empty gray circles) and corresponding calculated profile computed by Rietveld refinement (red solid line) based on cubic spinel structural model. The difference curve (blue solid line) is shown below each pattern.;* ***(II)*** *cell parameter of LFMT (red) compared to undoped $Li_{1+x}Mn_{2-x}O_4$ from Ref. 3 plotted as a function of the average ionic radius, i.r., of the cations.*

The ionic radii are calculated based on reference values for tetrahedral and octahedral coordination, as reported by Shannon (see Table 6.2) assuming that Li ions lie in the tetrahedral sites and the other cations in the octahedral ones (no site inversion).[22]

	i.r._T (Å)	*i.r._O (Å)*
Li^+	0.59	0.76
Fe^{3+}	0.49	0.645
Mn^{3+}	-	0.645
Mn^{4+}	0.39	0.53
Ti^{4+}	0.42	0.605
Mn^{2+}	0.66	0.83

Table 6.2. *Ionic radii of the species of interest in tetrahedral (IV) and octahedral (VI) coordination according to Shannon.*

The unit cell expands increasing the Li/Mn molar ratio. As to the undoped $Li_{1+x}Mn_{2-x}O_4$, such expansion is attributed to the formation of Mn(IV) cations taking place to compensate the charge when Li ions substitute for Mn(III).[5] In particular, the cell expansion up to 8.31 Å gives indirect evidence of the partial Ti/Mn substitution. Indeed, Ti(IV) is bigger than

Mn(IV) in octahedral coordination, whereas Fe(III) has negligible effect, having the same size as Mn(III). The LFMT transport properties were evaluated by means of electrochemical impedance spectroscopy using ionically blocking electrodes. $LiMn_2O_4$ is a well-known mixed conductor with predominant Li-ion conduction, whose electronic and ionic impedances are not very different.[21] For this reason, it is, in principle, easy to recognize the single components and to extrapolate the ionic and electronic resistances (and consequently the transference numbers, t_e and t_{Li^+}) from the relative values of the intercepts upon the real impedance axis at higher and lower frequencies, respectively.[20] Figure 6.3, shows, as an example, a typical impedance spectrum of a LFMT pellet as collected using a 2-electrode cell. The Nyquist plot typically shows two semicircles. The first represents a parallel combination of the electronic resistance, R_e, and geometrical capacitance, giving clear evidence of a significant electronic leakage through the sample. This is confirmed by the absence of the typical capacitive tail at lower frequencies. The second semicircle is due to the parallel combination of the ionic resistance, R_i, and the geometrical capacitance at high frequency.
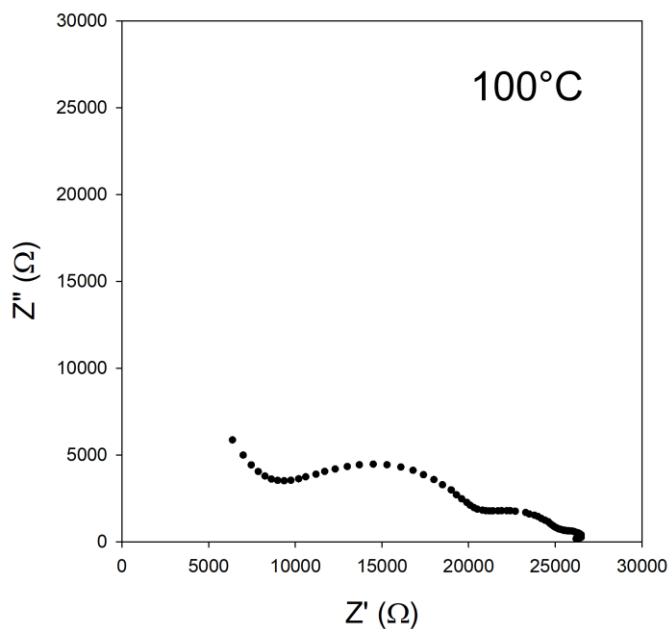

Figure 6.3. Impedance spectrum of a LFMTc pellet, recorded/obtained at 100°C.

In some cases, as for the example reported in Figure 6.3, also the contribution of the grain boundary was recognized in the intermediate frequency domains, that was readily isolated. The ionic and electronic resistances were used to calculate the conductivity and transference numbers, as clearly described in detail in Ref. 19. Both transport components were studied as a function of the Li/Mn molar ratio and of the temperature. Figure 6.4(I) shows the behaviour of σ_i and σ_e for the LFMT systems *vs* the Li/Mn ratio in the spinel phase. The Li^+ conduction decreases almost linearly by increasing the Li/Mn ratio. This is an expected result, since fewer lattice sites are gradually available for the lithium ionic diffusion when more Li cations are present.[23] The conductivity values are in fair agreement with what is usually reported for the $LiMn_2O_4$ systems (Li/Mn = 0.5) (*e.g.* $\sigma_{i,100°C} \sim 10^{-5}$ S cm^{-1}), as well as the activation energy calculated by the Arrhenius plots (Figure 6.4(II)), ranging between 0.32 eV and 0.49 eV.[21]
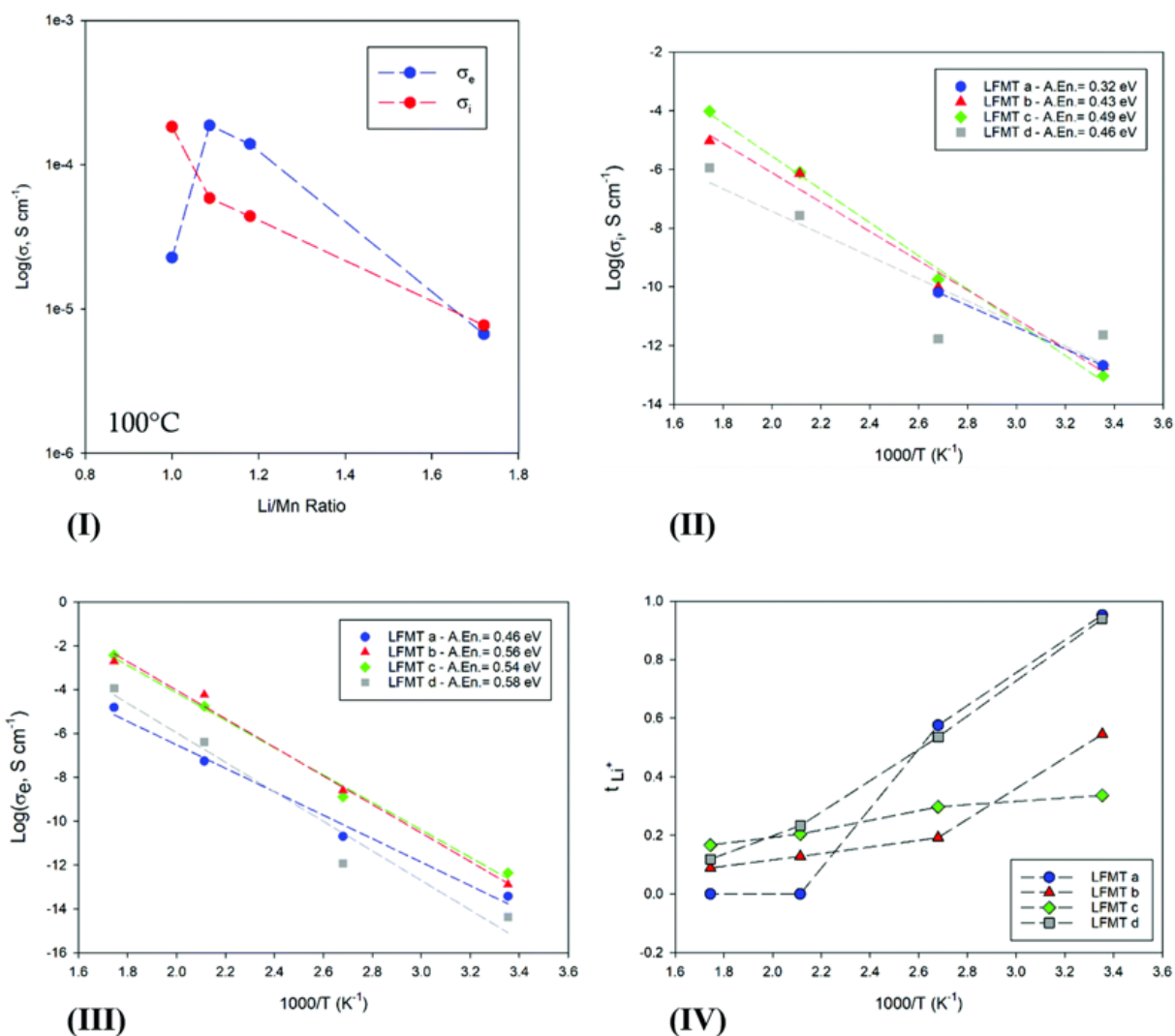
***Figure 6.4. (I)** Ionic (red) and electronic (blue) conductivity behaviour at 100°C vs. the Li/Mn ratio; **(II)** Ionic and **(III)** electronic conductivity behaviour against temperature; **(IV)** Li ion transport number, t_{Li+}, vs. T, for the investigated LFMTa-d active materials. In **Figure 6.4(II)**, σ_i values up to 100°C are only reported for LFMTa, since the conductivity is fully electronic at higher temperature.*

The electronic conductivity changes as a function of the Li/Mn ratio with a more complex trend (see Figure 6.4(III)). $\sigma_{e,100°C}$ increases with the Li/Mn ratio, achieving the maximum value of 0.2 mS cm^{-1} for the sample LFMTb for which the ratio is 1.1. This behaviour is in very good agreement with what is reported in the literature for the electronic transport of LiMn$_2$O$_4$.[21,24] The spinel exhibits semiconducting characteristics related to the electron hopping between mixed-valence Mn, being 2.73 Å the calculated critical cation-cation separation in the octahedral configuration.[21] Smaller lattice constant allows a more extended overlapping of the wave functions of neighbouring Mn with different oxidation states, which consequently results in an enhanced electronic conductivity. In general, the obtained value

154

for the electronic conductivity, exceeding 0.1 mS cm^{-1} around the curve maximum, are very satisfactory and significantly higher than $LiMn_2O_4$. The improved transport is likely due to a sound compromise between an optimal structure for the electron hopping and a good charge carrier concentration related to a proper composition of the dopant TMs. Electronic activation energy, E_{ae}, higher than the ionic one, was determined from the Arrhenius plots reported in Figure 6.4(III), with values in the range 0.46-0.58 eV between 25 and 300°C. Figure 6.4(IV) and Figure 6.5, finally show the Li$^+$ and electron transference numbers, respectively t_{Li^+} and t_e, vs T, as calculated by the respective Nyquist plots.
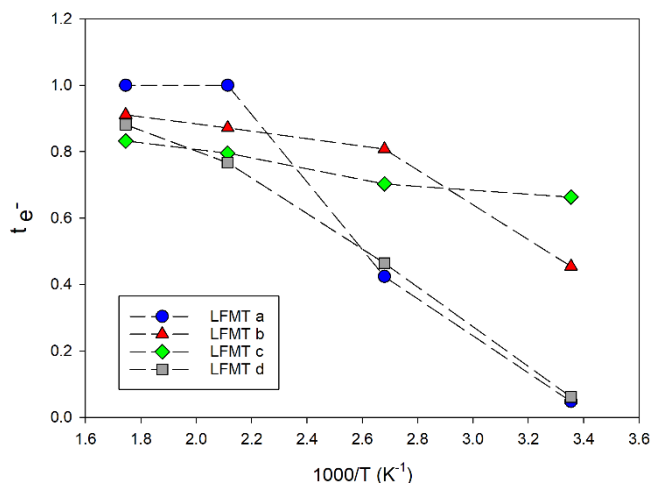

Figure 6.5. *Electron transference numbers t_e, vs T, as calculated by the respective Nyquist plots.*

The curve clearly evidences as the semiconductor character of the materials remarkably increases with the temperature for each composition, reaching an almost fully electronic transport at 300°C. At room temperature, only spinels with the smaller lattice constant (LFMTb and LFMTc) exhibit a significant faction of the electronic component, with transference numbers, t_e, of 0.7 and 0.5, respectively.

6.4.2. LFMT Cathodes: Electrochemical Performance

All LFMT spinels were investigated as cathode materials and tested in terms of their functional properties, as described in the relative paragraph. Figure 6.6(I),(II) reports the

155

SEM images and the XRD patterns, respectively, obtained for all the cathodes. The morphological features of the aforementioned electrodes are quite similar to those of the as realized active materials. From the structure analysis, it is possible to note the presence of a single spinel phase for the pre-cycled electrode, in agreement for the pristine materials, while a variation is evident at the end of the cycling process.
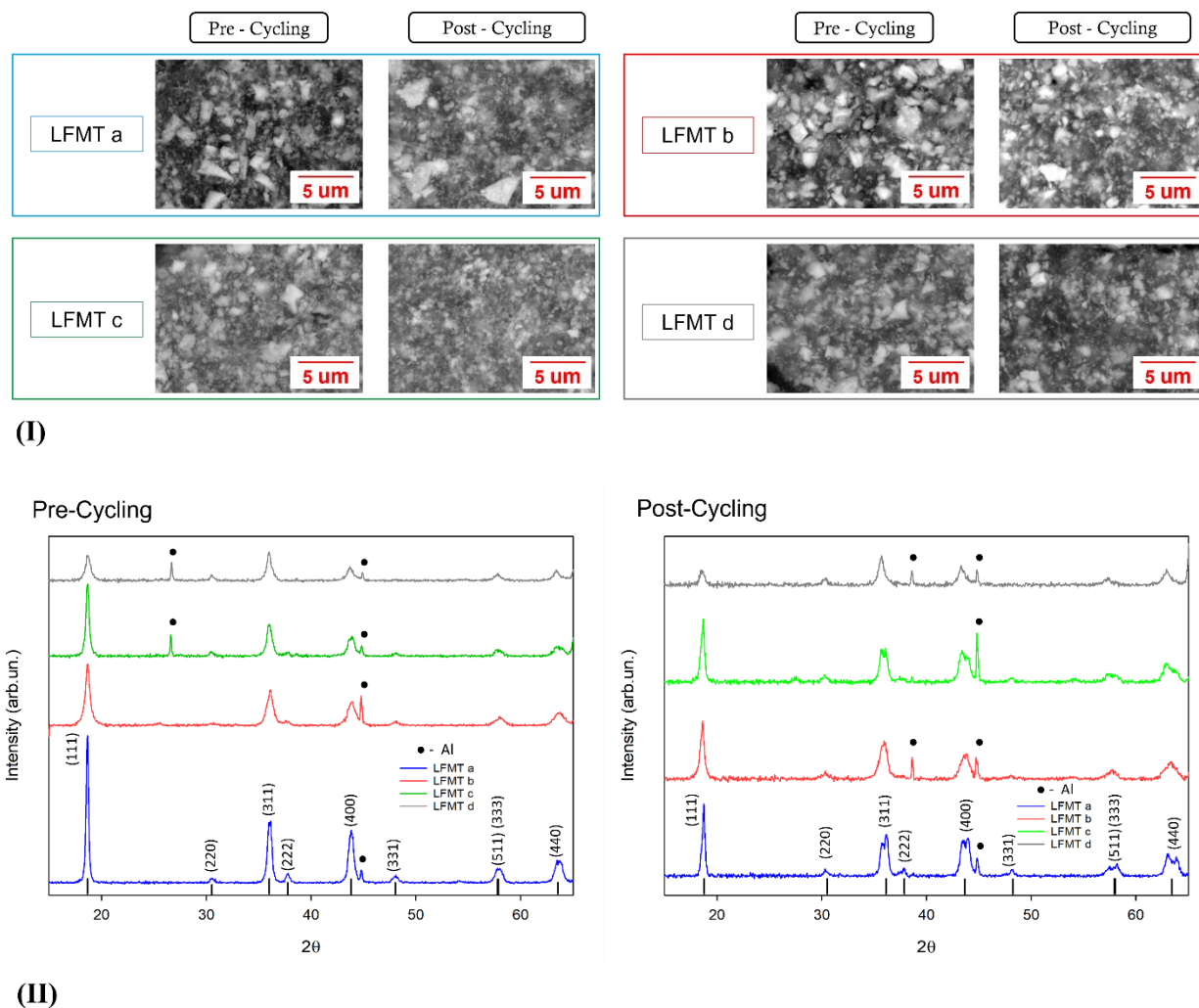

Figure 6.6. (I) (Back-scattered) SEM images of the LFMT electrodes pre- and post-cycling and (II) XRD patterns of the pre-cycled (left) and post-cycled LFMT electrodes (right). The star ● in plots indicates the Al signal coming from the current collector.

The LFMT electrochemical performances were investigated against Li as counter-electrode between 1.5 V and 4.8 V at different current rates, starting from the OCV (~3.1 V). The spinels exhibit qualitatively similar voltage profiles (see Figure 6.7).
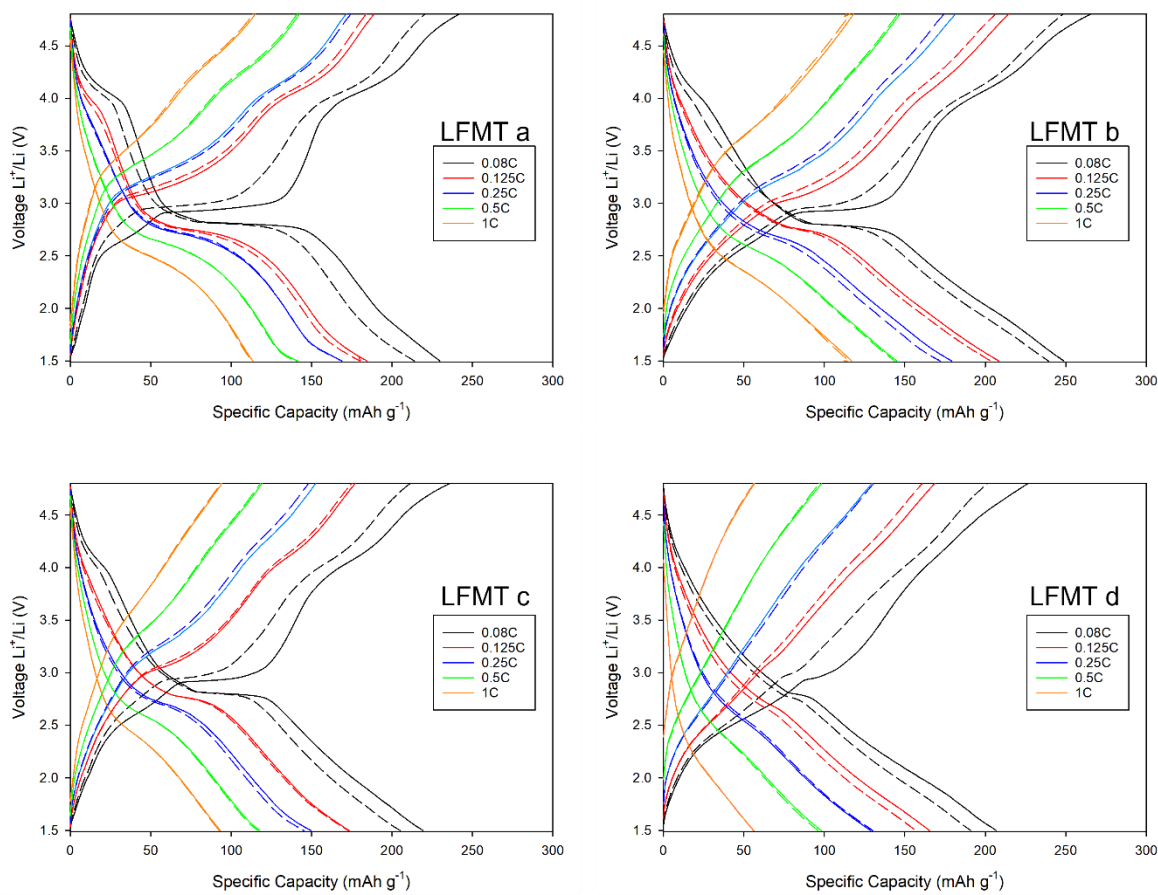
156

Figure 6.7. Voltage profiles of the 2nd (solid line) and 5th (dotted line) cycles at each investigated C rate.

Two main plateaus are clearly evident even upon long cycling, one sharper at 2.8 V-3.0 V and one broader, characteristic of the Li^+ extraction from the tetrahedral *8a* sites, at around 4 V. One exception is represented by LFMTd, whose first charge does not reach the cut-off voltage of 4.8 V, probably because of unfavoured kinetics as a consequence of low content of Mn (Li/Mn = 1.7) and therefore also of Mn(IV). The electrochemical phenomena of the doped spinels are therefore very different from those ones expected for the undoped spinel. They are better evidenced in the dQ/dV curves shown in Figure 6.8 for all the compositions, where the lithiation/delithiation reactions at ∼3.0 V and 4.0 V are associated with two peaks, describing the redox processes involving Mn.
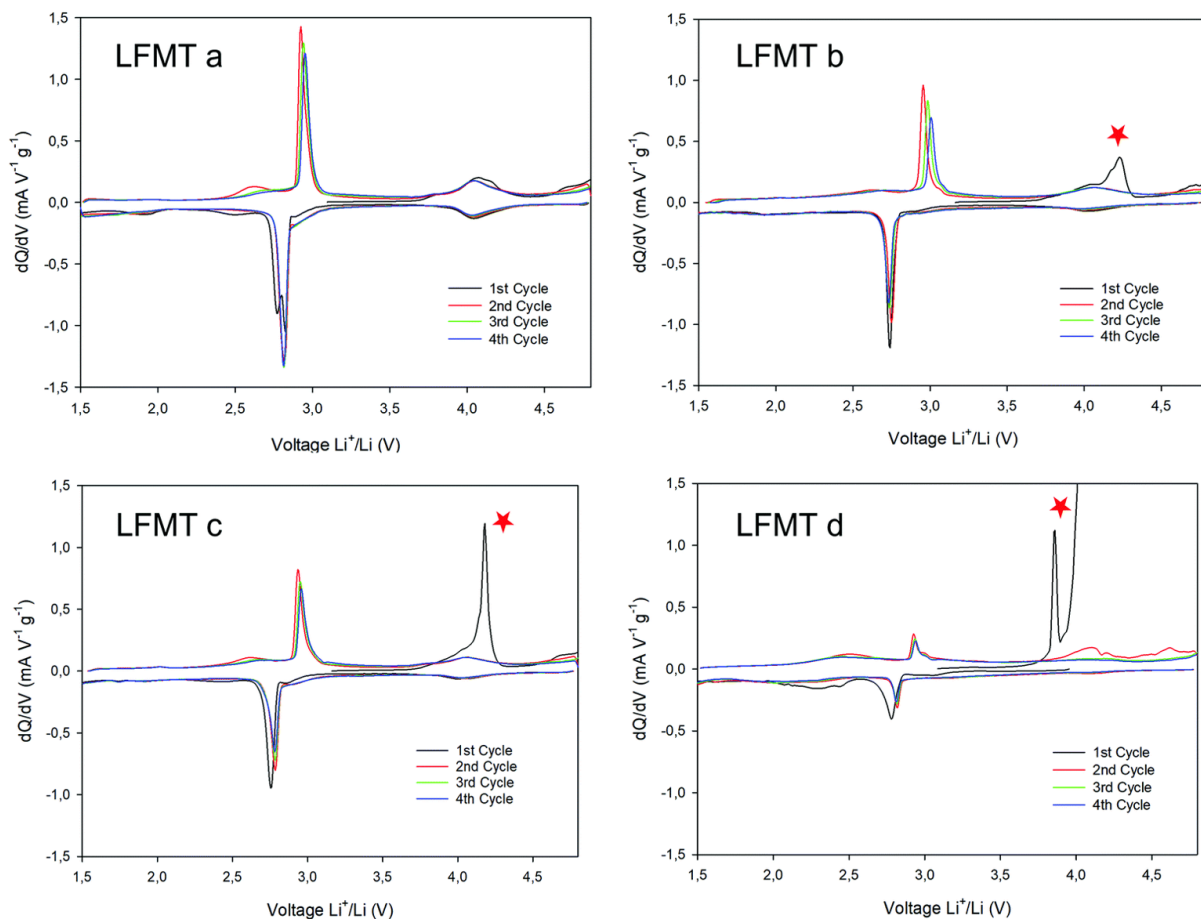
Figure 6.8. dQ/dV plots of LFMTa–d-based cathodes collected in the voltage range between 4.8 V and 1.5 V by means of PCGA experiments at 0.05C.

The first process is ascribed to Mn(III)/Mn(II) transition and the second to Mn(IV)/Mn(III) step. As already stated above, the availability of the whole Mn(IV)/Mn(II) redox couple is responsible for the significantly higher specific capacity observed in the doped spinels over LMO, achieving in some cases values higher than 250 mAh g^{-1} (0.08C) and high energy density > 0.8 Wh kg^{-1}, when cycled in a wide voltage range (4.8 V-1.5 V). The peak at 3 V is narrower than the corresponding signal observed for the undoped $LiMn_2O_4$ spinel, suggesting the hindering of the cubic-tetragonal phase transition typical of the LMO system, as confirmed by the *ex situ* XRD discussed in the following. The Mn(III)/Mn(IV) occurring around 4 V is a single broad signal, indicating a one-step reaction, contrary to what was observed for the undoped spinel, where two couples of sharp redox peaks are obtained between 3.5 V and 4.8 V. These peaks can be theoretically attributed to the 2-step transition: one from $LiMn_2O_4$ to $Li_{0.5}Mn_{0.5}^{III}Mn_{1.5}^{IV}O_4$ and the other from $Li_{0.5}Mn_{0.5}^{III}Mn_{1.5}^{IV}O_4$ to a fully delithiated system (Mn_2O_4).[4] The intensities of both peaks, around 3 V and 4 V, decrease

158

coherently with the Mn content in the spinel, as better shown in Figure 6.9, reporting the behaviour of the 1st cycle-specific capacity as a function of the Li/Mn ratio.
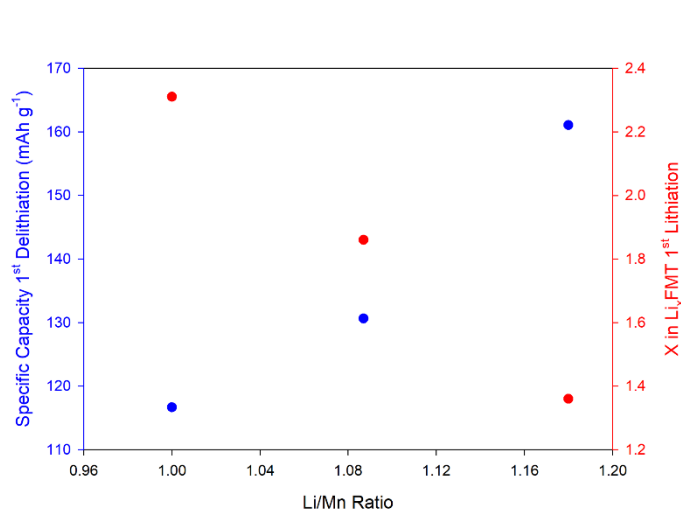

Figure 6.9. *1st Delithiation Capacity (blue) and Lithium stoichiometry, x, (red) as a function of the Li/Mn molar ratio in LFMTa-c cathodes.*

The rate capability is reported in Figure 6.10 for all the compositions. The best functional behaviour was obtained for LFMTa and LFMTb, exhibiting discharge capacities between 230-250 mAh g^{-1} and 130 mAh g^{-1} in the current density range 21-270 mA g^{-1}, respectively.

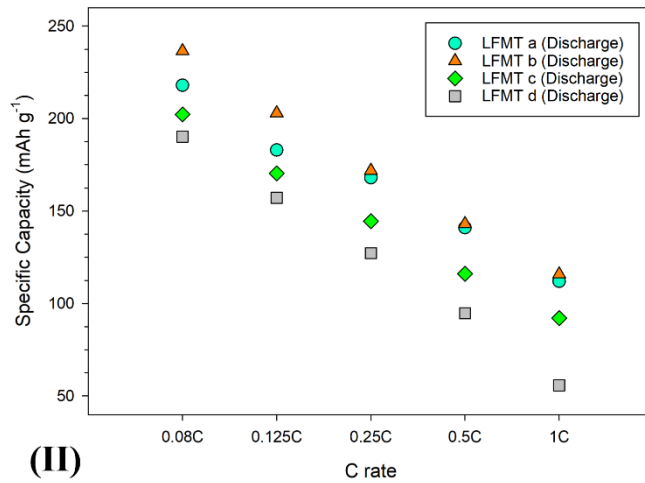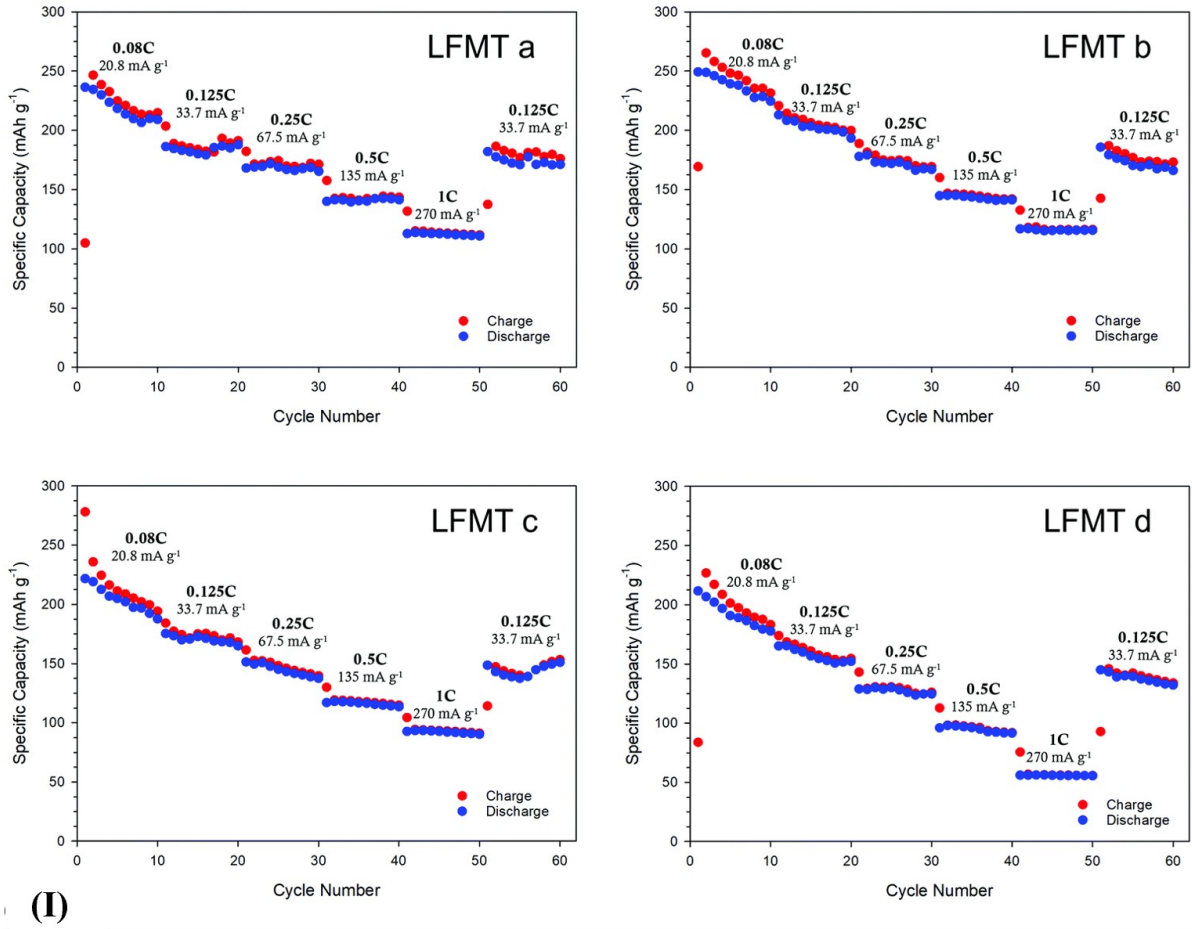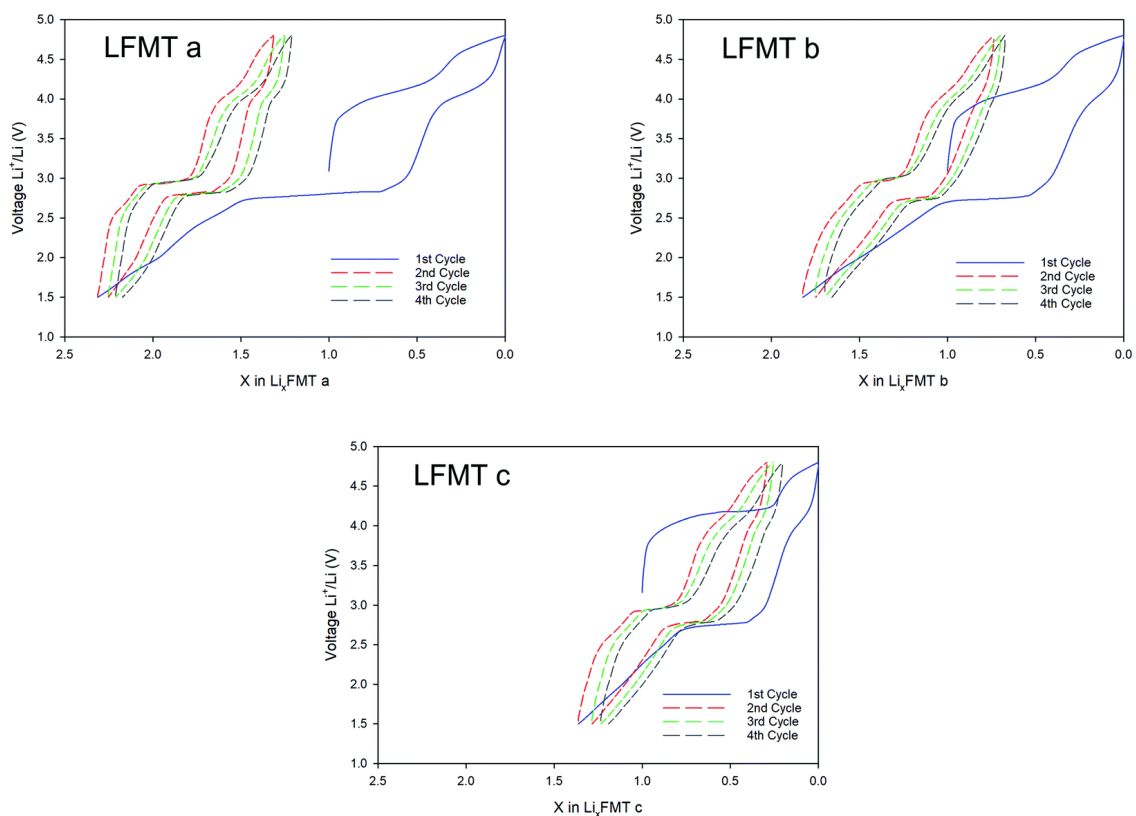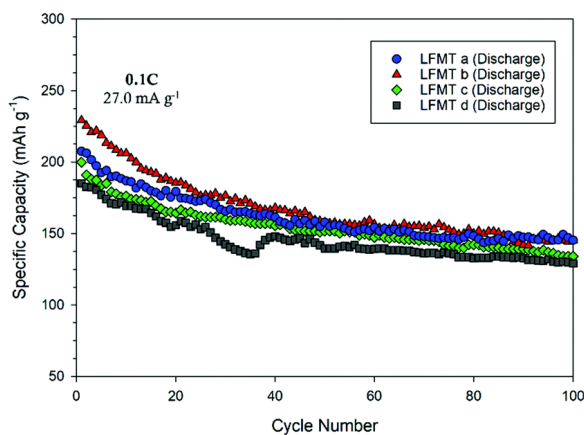**Figure 6.10. (I)** *Rate performances of LFMTa–d cathodes cycled from 4.8 V to 1.5 V at different current densities.* **(II)** *Average discharge capacity behaviour as a function of C rate in LFMTa-d cathodes.*

Lower performances were in contrast achieved by cells including LFMTd, especially at higher current densities where C_{disch} values < 60 mAh g^{-1} were delivered at 1C. However, in

each composition, the charge/discharge processes are almost reversible. The coulombic efficiency is very close to 1 after the initial 3 cycles and mostly at higher C rates, suggesting that the doped spinels have a stable structure during lithium-ion intercalation/deintercalation. The amount of Li ions that de/intercalate from/into the spinels was estimated by the voltage profile at low current density (0.05C), as reported in Figure 6.11(I). Here the redox plateaus at about 4 V and 2.8 V-3.0 V are clearly evident. During the lithiation step, the Li^+ equivalents progressively inserted through the reduction of the Mn redox couple are strictly dependent on the type of spinel. In particular, they change linearly by increasing the Li/Mn ratio (*e.g.* nominally from 1.0 to 2.3 for LFMTa), as better shown in Figure 6.9. The plot also shows that, except for the first cycle, the mechanism involved upon lithiation/delithiation is almost symmetric, suggesting very good coulombic efficiency. After the first cycle, the amount of exchanged Li is always x = 1, both on charge and discharge (see Figure 6.11(I)).
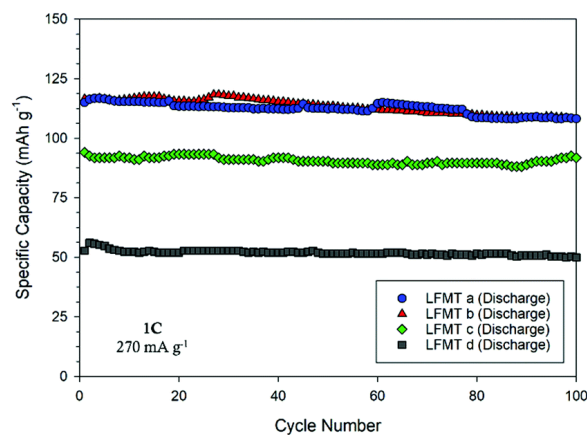
Figure 6.11. (I) *Voltage-composition profiles of the LFMTa–d cathodes during the first charge-discharge cycle with a voltage window 1.5 V-4.8 V vs. Li/Li⁺ at 0.05C rate;* ***(II)*** *discharge capacity upon 100 cycles at a current density of 27 mA g⁻¹ and* ***(III)*** *270 mA g⁻¹.*

The voltage profiles and the dQ/dV plots also reveal the presence of a plateau at around 4.3 V-4.4 V during the first oxidation step, which gradually becomes more intense as the Mn content in the spinel decreases (red star in Figure 6.8). This signal may be ascribed to an irreversible anionic redox activity that leads to O_2 loss, as a consequence of the oxidation of

162

structural O^{2-}, possibly at surface sites, as it is often observed in literature both in layered and spinel-like cathodes.[13,25,26] Despite the fact that O_2 evolution is in some cases valuable, this process does not contribute, if not marginally, to the delithiation capacity, which in contrast stems from the Mn(IV)-Mn(II) reduction. On the other hand, the anionic redox activity may affect to some extent the cathode capacity retention upon prolonged cycling, inducing potential structural changes. Figure 6.11(II) shows the cell stability upon cycling for all the spinels at 27 mA g^{-1} for 100 cycles. All the compositions show an initial capacity very close or even exceeding 200 mAh g^{-1} (LFMTa = 207 mAh g^{-1}; LFMTb = 229 mAh g^{-1}; LFMTc = 199 mAh g^{-1}; LFMTd = 185 mAh g^{-1}). However, after 20 cycles, the capacity loss increases with the entity of the irreversible O_2 release. Indeed, capacity retention higher than 78% is obtained in the case of LFMTa where the irreversible phenomenon is absent or negligible, whereas more severe losses are observed when the oxygen evolution is more pronounced, such as for LFMTc and LFMTd (capacity retention of about 68%). At higher current densities (270 mA g^{-1}), the spinel-based electrodes show higher stability with negligible capacity reduction and coulombic efficiency higher than 98% (Figure 6.11(III)). However, very different values of specific capacity are obtained, which remarkably decrease when the irreversible anionic redox phenomena are more intense and when the Mn stoichiometry (Mn_{2-x-y}) in the spinel significantly deviates from unity. In particular, capacity higher than 125 mAh g^{-1} is delivered by the cells including the LFMTa and LFMTb spinels, whose cycling behaviour is only marginally affected by O_2 loss at high voltage. However, despite capacity reductions are still evident at low C rates, the Mn multi-substitution with transition metals appear to be a very good strategy in order to significantly enhance the long-term stability of the spinel-based cathodes. As well known, in fact, undoped LMO shows severe capacity reduction upon cycling, that might exceed 49% even at very lower current densities, because of the J‑T distortion. The O_2 release may be somehow suppressed or limited by using proper additives in the liquid electrolytes. Different amounts of Succinic Anhydride (SA) (4 wt% and 6 wt%) were added to the selected electrolyte and used in the LFMTa-based cathode in order to evaluate its possible role on the cycling performances. From the Figure 6.12(I) showing the dQ/dV plot for the cell including a 4 wt% of succinic anhydride, there is no evidence of the peak at high voltage, ascribed to the O_2 formation. Furthermore, a significant reduction of the capacity fade is observed particularly at low C rate, when slightly higher amounts of additive are added (*e.g.* 6 wt%) (Figure 6.12(II)).
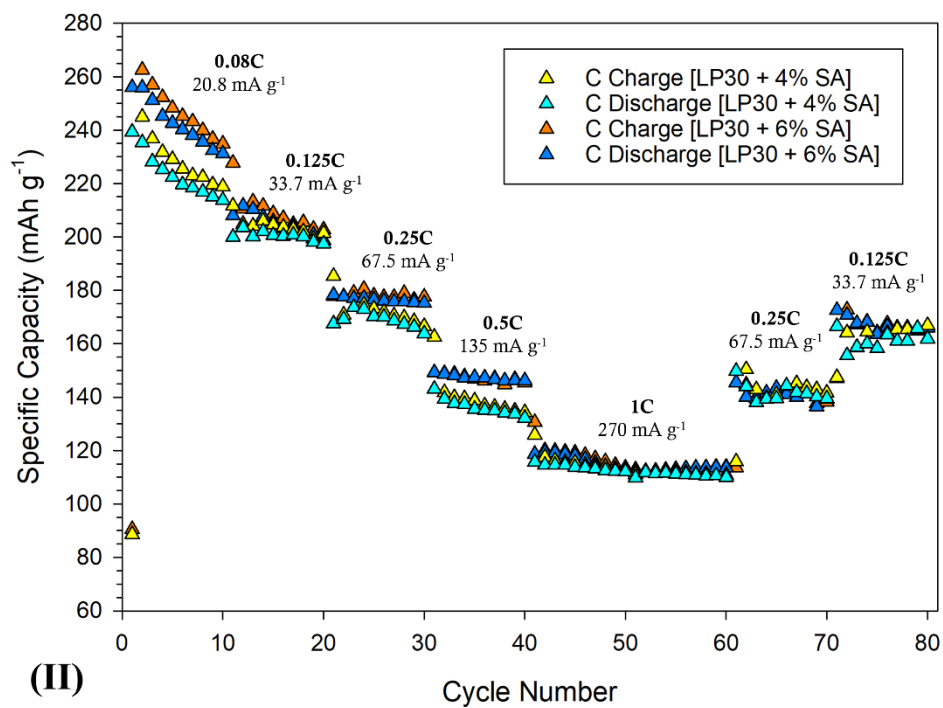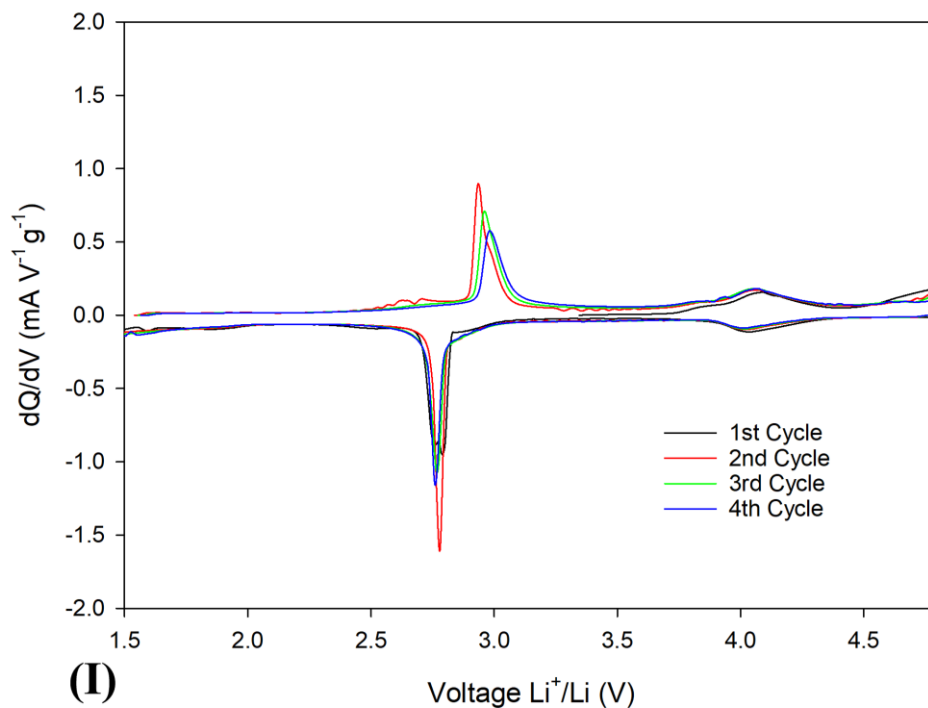
Figure 6.12. (I) *dQ/dV plots of LFMTa cathode with LP30 + 4 wt% of succinic anhydride as electrolyte.* **(II)** *Galvanostatic cycling at different C rate of the cell LFMTa/electrolyte/Li. Electrolyte: LiPF₆ 1.0M in EC:DMC (50:50 vol%) + 4 wt% (cyano/yellow) and 6 wt% (blue/orange) of succinic anhydride.*

6.4.3. LFMT Cathodes: Spectroscopic Investigation – *Ex Situ* XAS

The chemical environment and TM oxidation states were studied by means of XAS through *ex situ* experiments carried out on the LFMTc cathode (selected as case study), whose cycling was stopped at specific voltages, namely at OCV, delithiated up to 4.8 V, and lithiated up to 1.5 V (see Figure 6.8). Figure 6.13 shows the corresponding XAS spectra at the Ti, Mn, and Fe $L_{2,3}$ edges and at the O K edge for these samples. At the $L_{2,3}$ edges of the TM, the peaks in the XAS spectra arise from dipole allowed electronic transitions from 2p to 3d states. At the O K edge, the initial states are of 1s character, and therefore dipole allowed electronic transitions probe final states with p character.
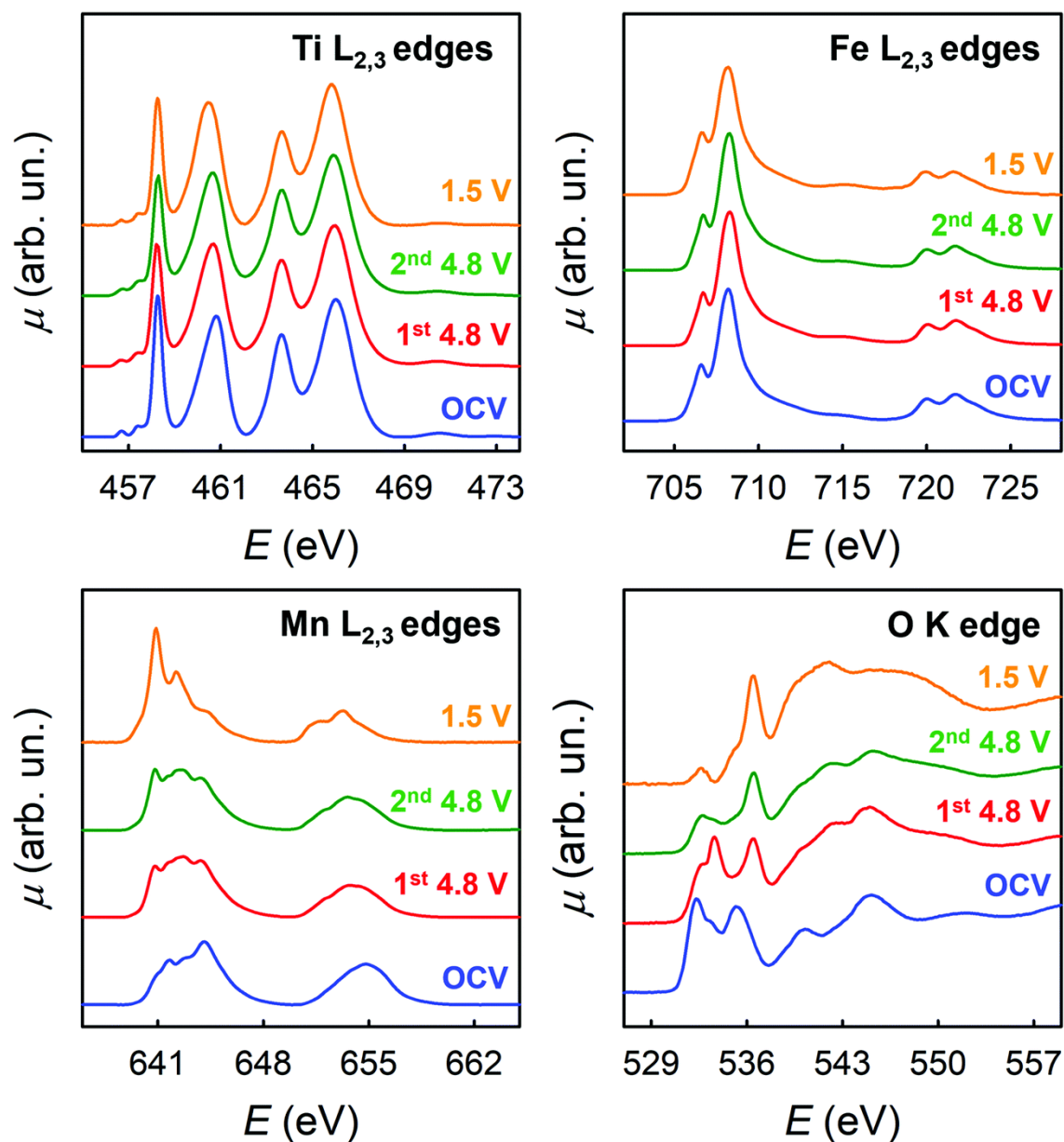
Figure 6.13. X-ray absorption spectra at the Fe, Mn and Ti L$_{2,3}$ edges and at the O K edge on LFMTc cathode at different potentials.

Therefore, the spectra of Figure 6.13 probe in principle all the valence states of the material and can detect their modifications in the lithiation process. However, the detailed interpretation of the L$_{2,3}$ edges of TMs is complicated by the presence of multiplet interactions. As a general consideration, it is possible to state that the 3d metal L$_{2,3}$ edges are sensitive to orbital occupancy (oxidation state) and local geometry, while the O K edge gives a more complete picture of the valence states. In addition, concerning the 3d TMs, the analysis will be here limited to the L$_3$ edge, as the states involved at the L$_2$ edge change only for the different values of the J quantum number. The spectra at the Ti L$_{2,3}$ edges are easily discussed, as the spectral shape in all the experimental conditions is unequivocally attributed

to Ti(IV) in an octahedral environment (see Figure 6.14(I)).[27] Ti(IV) has the d^0 electronic configuration, and therefore the multiplets arising from the $2p^5 3d^1$ final state are easily discussed. The octahedral crystal field split the Ti 3d states into threefold degenerate t_{2g} states, and twofold degenerate e_g states. Thus, the peak at ~460 eV is attributed to the electronic transitions from the Ti 2p to Ti t_{2g} states, while the peak at ~463 eV is attributed to Ti 2p to Ti e_g states.[28,29]
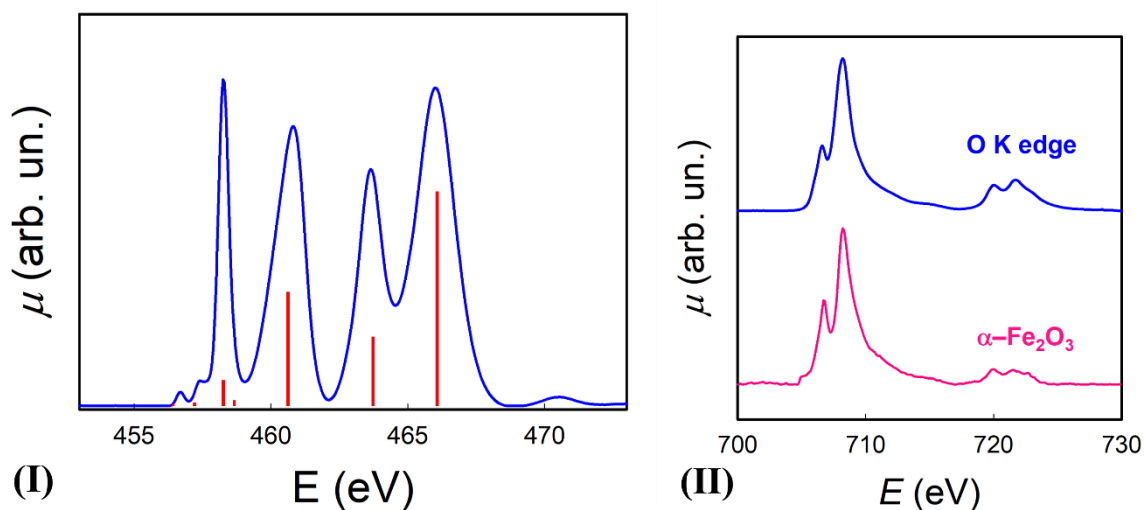

Figure 6.14. (I) *Ti L$_{2,3}$ edges of sample LFMTc at OCV (blue line). The red bars are the multiplets calculated by means of the XTM4XAS program,[30] including crystal field, charge transfer, and spin-orbit coupling effects and assuming Ti in Oh environment; (II) XANES spectra at the Fe L$_{2,3}$ edges of LFMTc at OCV (blue line) and Fe$_2$O$_3$ (pink line), taken as reference.*

The spectra at the Fe $L_{2,3}$ edges are in principle more difficult to be interpreted, as the electronic configurations of Fe in the different oxidation states give rise to a multiplicity of final states. However, for all the experimental conditions we note a strong resemblance of the Fe $L_{2,3}$ edges with that of Fe_2O_3 (see Figure 6.14(II)). It is therefore concluded that in all the samples, Fe is present mainly as Fe(III) in an octahedral environment. Concerning the spectra at the Mn $L_{2,3}$ edges, the spectral shape which is found in the different experimental conditions is indicative of a complex behaviour. The spectrum at OCV shows a marked peak at ~644 eV, which, by comparison with literature data,[31] is attributed to Mn(IV). The other spectral features arise from Mn in different oxidation states, indicating that in all the experimental conditions Mn is found in a mixed oxidation state, which renders the interpretation less straightforward than for Fe and Ti, and does not allow a meaningful interpretation in terms of multiplet analysis. Some more specific remarks are however

possible. In particular: (i) both spectra at 4.8 V show a clear decrease in the peak at 644 eV; simultaneously, the $L_{2,3}$ edges develop into a spectral shape which is strongly resembling that of the Mn_3O_4 spinel.[31] Therefore, at this potential, the Mn oxidation state is assigned to a value close to 2.7, even if the presence of residual Mn(IV) cannot be excluded. (ii) at 1.5 V, a strong peak close in energy to 641 eV develops. This peak is attributed to Mn(II) by comparison with the spectrum of MnO.[31] This clearly indicates that a large amount of Mn is reduced from Mn(III) to Mn(II) at this potential. Therefore, the results for the TM $L_{2,3}$ edges show that Ti and Fe are inert during the lithiation process, while Mn participates with both the Mn(IV)/Mn(III) and Mn(III)/Mn(II) redox couples. The oxygen K edge spectra which are shown in Figure 6.13 show notable differences. This is quite surprising, as the O K edge XANES of TM oxides, where the TM is in octahedral coordination, usually show impressive similarities due to the hybridization of the TM 4s, 4p, and 3d states with the 2p states of oxygen.[32,33] Typically, the first two peaks in the O K edge XANES are due to electronic transitions from the oxygen 1s orbital to oxygen 2p orbitals hybridized with TM 3d orbitals with t_{2g} and e_g symmetry.[32,33] Here, we note that there is a marked shift towards higher energies when passing from OCV conditions to 4.8 V. This shift is similar to that observed in the literature comparing the spectra of MnO_2 and Mn_2O_3.[31] This is a confirmation of the presence of Mn(IV) in OCV conditions. Additional differences are found by comparing the two spectra at 4.8 V. For the sample after the second delithiation (green plot in Figure 6.13), the peaks at ~533-534 eV show a marked decrease in intensity when compared to 1st delithiation (red plot). The intensity of this transition is mainly influenced by two factors: the degree of hybridization between oxygen and TM states (covalence of the TM-O bond) and the filling of the TM 3d states with t_{2g} symmetry.[32,33] Recalling the results of the TM $L_{2,3}$ edges, where almost no changes are found comparing the spectra of these specific samples (green and red plots), a difference in the occupation of TM 3d states seems very unlikely. Thus, we are left with the different hybridization as a cause of this noticeable decrease in intensity. The decrease is even more evident for the spectrum at 1.5 V. This further decrease cannot be due to the reduction of Mn(III) to Mn(II) which is detected at the Mn $L_{2,3}$, as the $3d^4$ and $3d^5$ electronic configurations do have the same occupancy for the t_{2g} states. Therefore, the degree of the TM-O bond should be involved also in this process.

6.4.4. LFMT Cathodes: *Ex Situ* XRD Investigation

To unravel the mechanism responsible for the spinels cycling performances, the structural evolution was studied during the first charging (delithiation) cycle, the second charge/discharge cycle, and also after extended cycling by means of *ex situ* XRD experiments. This has been performed selecting the LFMTc composition as a case study, due to its sharp irreversible anion redox activity. Figure 6.15 shows the patterns collected after stopping the cycle at a few defined voltages. The pattern of the spinel before electrochemical cycling is also included for the sake of comparison. The Rietveld refinement confirms that the specimen is a single phase with lattice parameter 8.272 Å (see Table 6.2).
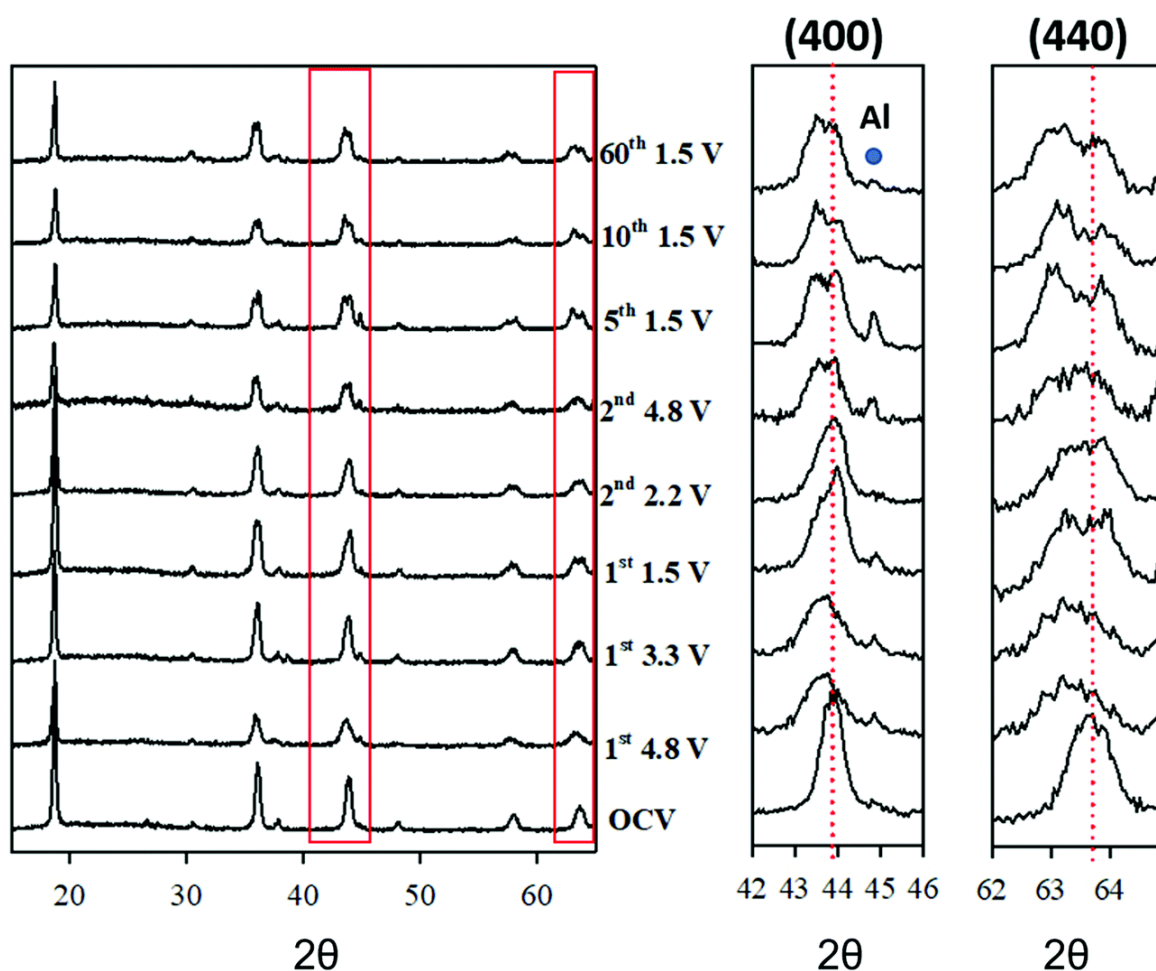

Figure 6.15. *Ex situ experimental XRD patterns during electrochemical cycling of the LFMTc cathode. The 400 and 440 reflections are highlighted in the insets. The red dotted lines refer to the peak position before cycling.*

The lattice parameter and the FWHM of the 400 reflection, taken as a reference, are reported in Table 6.3. Initially, the spinel was delithiated by charging up to 4.8 V from the OCV. The diffraction pattern collected at 4.8 V reveals a clear lattice expansion and a broadening of all reflections. A similar trend was observed in undoped $Li_{1-x}Mn_{2+x}O_4$. However, in that case, the change in Li concentration was balanced by adjusting the fraction of Mn.

Cycle #	Voltage (V)	$a_{spinel1}$ (Å)	$a_{spinel2}$ (Å)	FWHM$_{(400)}$ (deg)
OCV	3.1	8.2728(7)		0.605(7)
1	4.8	8.302(2)		1.000(2)
1 dis	3.3	8.251(4)	8.310(5)	0.663(8)
1	1.5	8.250(3)	8.330(5)	0.78(3)
2 ch	2.2	8.250(10)	8.322(10)	0.77(2)
2	4.8	8.253(7)	8.326(8)	0.88(2)
5	1.5	8.250(3)	8.346(4)	0.90(2)
10	1.5	8.248(4)	8.339(5)	0.92(2)
60	1.5	8.251(4)	8.339(5)	0.88(2)

Table 6.3. Lattice parameter, a, and FWHM of the 400 reflection for the XRD patterns collected for LFMTc cathode at different steps of the electrochemical cycling

The current behaviour, instead, cannot be interpreted as a simple extraction of Li^+ ions from the spinel, as this would result in a cell contraction, rather than expansion, as usually reported on Li-based compounds.[34-36] The origin of this peculiar behaviour can be understood by monitoring the XRD patterns during the electrochemical cycling. Indeed, during the first lithiation, at 3.3 V (see Figure 6.15), the spinel peaks split into two separated contributions. The same applies likely at 4.8 V, where the extensive peak broadening (see Table 6.3), hinting at the presence of significant disorder, hinders the observation of the peak splitting. The following point collected while recharging at 2.2 V after the first full lithiation down to 1.5 V, exhibits still a two-phase system. Since then, a clear phase separation is observed throughout the electrochemical process, the split being less apparent at high voltage, due to important disordering: after 60 cycles, the split is still evident. A careful analysis of the XRD data excludes that such peak splitting may be ascribed to the cubic/tetragonal phase transition, which is typical of LMO spinel, that was also observed in the case of Ti-doped LMO composition.[6] In our case, the split is consistent with the coexistence of two spinel

phases, with different composition, and, therefore, different lattice parameter. Here we refer to "Spinel 1" and "Spinel 2" for the spinel phases with smaller and larger unit cell volume, respectively. We, here, briefly discuss the character of this phase separation. It is first noted that different phases have been reported to form upon lithiation/delithiation in similar systems. *Chen et al.* suggested the formation of a rock salt phase, which distorts irreversibly into a tetragonal system.[6] Even when the rock salt phase has the same lattice spacing (half unit cell) as spinel, some high intensity reflections observed in the spinel phase are missing. In particular, the splitting of the high angle reflection (333/511, 58° with CuKα radiation) is not consistent with the formation of secondary rock salt phase. Neither are the splits consistent with a tetragonal distortion, since not all the peaks would be affected, as for instance the 111 reflection, which is instead observed to split (see Figure 6.6(II)). Therefore, we can exclude the formation of a rock salt phase or a tetragonal distortion. Eventually, *Levi et al.* suggested the occurrence of a layered, rhombohedral phase, presenting diffraction pattern very similar to the spinel, which was observed upon delithiation of $LiMn_2O_4$.[36] *Gummow et al.* demonstrated that the spinel and layered phase can be distinguished by the occurrence of few minor peaks (220 and 422 in the spinel setting), which are observed only in the spinel and whose intensity depends on the cation distribution between the two sites.[37] The 220 reflection is actually observed only for the Spinel 2 phase, while the 422 reflection has a too low intensity. However, assuming that the Li^+ ions occupy only the tetrahedral sites without inversion, the 220 reflection shows negligible intensity. Having no direct proof of the formation of a rhombohedral phase, we consider more reliable the formation of two different spinel phases, with different cation distribution and thus different lattice parameter. More importantly, the combination of the two phases led to reliable fits (see Figure 6.16).
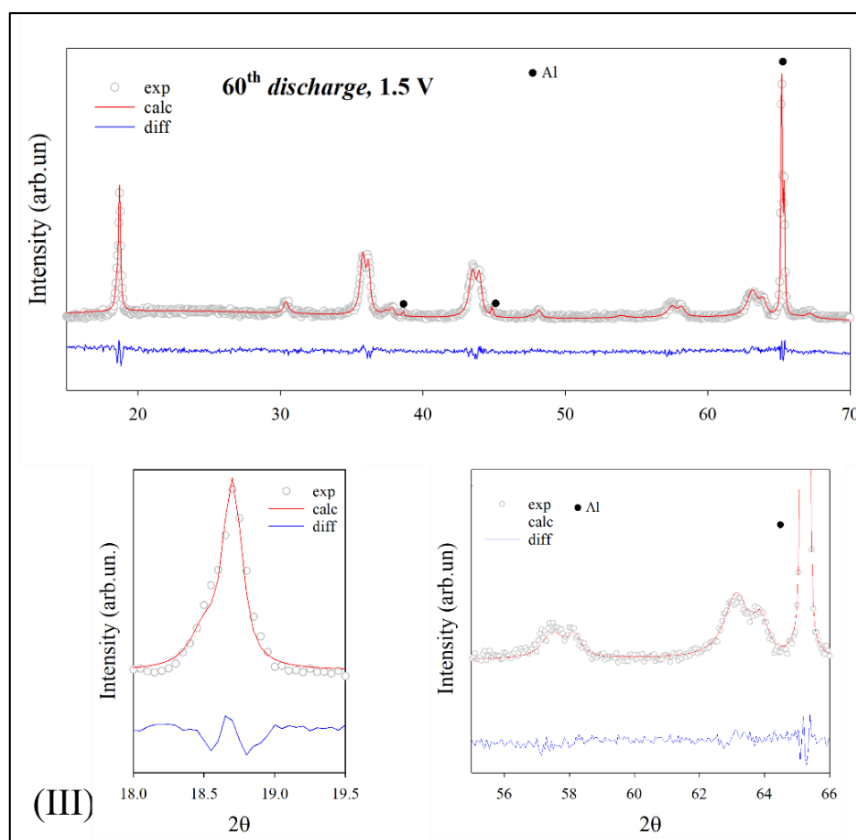
Figure 6.16. *Rietveld refinements of specimen LFMTc discharged at 1.5 V after (I) 5, (II) 10 and (III) 60 electrochemical cycles, plotted full range and zoomed into different regions. (Empty dots:experimental data, red solid line: calculated profile, blue solid line: difference curve. Full cycles highlight the signal of the Al support of the electrode.)*

The two phases exhibited a different behaviour upon cycling (see Table 6.3). The lattice parameter of Spinel 1 is constant ~8.25 Å upon cycling, while Spinel 2 expands adding Li, from ~8.31 Å to ~8.34 Å. In particular, during the first discharge, the lattice parameter expands from ~8.31 A at 3.3 V to ~8.33 Å at ~3.1 V, then it contracts to ~8.32 Å at 2.2 V. The point at 4.8 V is, again, likely biased by the peak broadening. The following lithiations cause the unit cell to expand up to ~8.34 Å. This suggests that Spinel 2 is the phase electrochemically active. Unfortunately, Fe, Mn, and Ti have very similar scattering factors, hence it is not possible to resolve their distribution between the two phases. However, the presence of Li (or Li vacancies) has a strong impact on the intensity of the XRD patterns of the spinel. In this respect, the Spinel 1 phase shows the typical cation arrangement of a normal spinel, with Li (or vacancies) on the tetrahedral sites, and transition metals on the octahedral site. Conversely, the Spinel 2 phase shows significantly lower scattering from octahedral sites, thus suggesting the presence of Li^+ ions. The presence of large Li^+ ions in coordination VI (0.76 Å) is likely the reason for the larger cell volume observed for the

173

Spinel 2 phase.[22] On the basis of this cation distribution, we estimated that Spinel 2 phase is in large excess (roughly 3:1), this ratio only slightly changing upon cycling.

6.3.2.5. Lithiation/Delithiation Mechanism Investigatio

Figure 6.17 sketches a possible redox mechanism that may be proposed on the basis of the information coming from the electrochemical, spectroscopic, and structural investigations. The redox process occurs with the cooperation of a structural modification of the LFMT-based spinels, accompanied by the irreversible phenomena taking place at high voltage during the first charge. By considering the results from the differential capacity and XAS, it is possible to conclude that Mn(IV)/Mn(III) and Mn(III)/Mn(II) are the only redox couple involved in the extraction/ intercalation of Li ions from/into the cathode. No further electrochemical process can be observed in the dQ/dV plots and this is confirmed by XAS spectra at the Ti $L_{2,3}$ and Fe $L_{2,3}$ edges, which do not evolve upon cycling. Hence, Fe and Ti are electrochemically inactive in these systems, even during the initial cycling step.
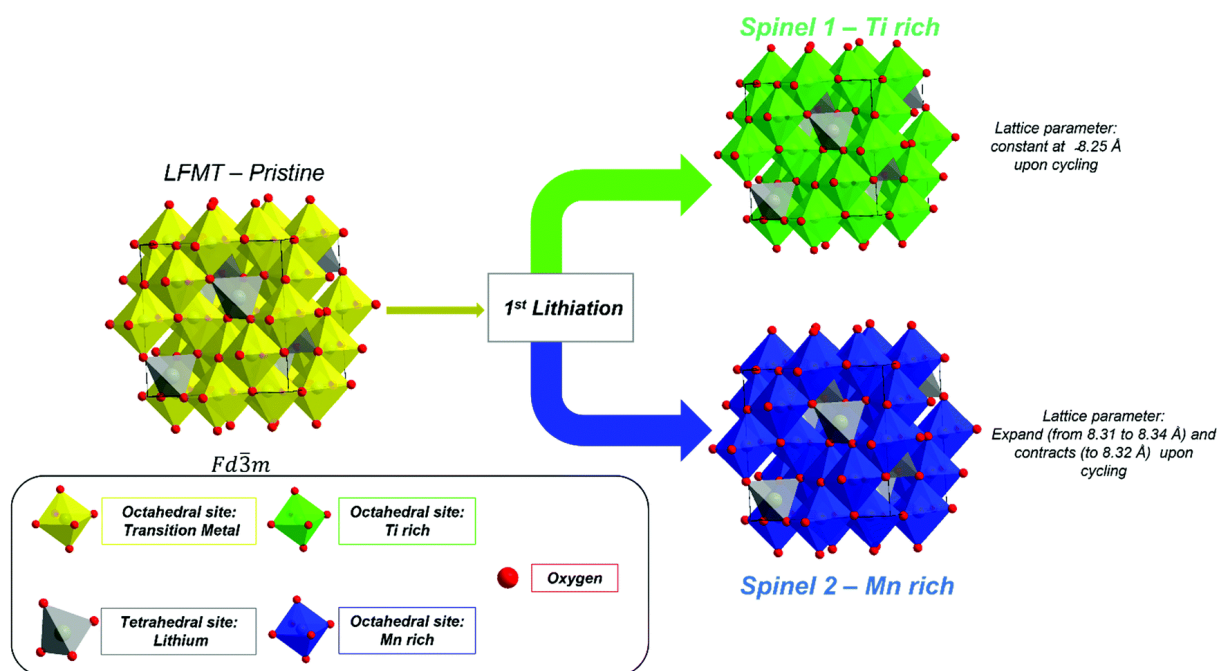

Figure 6.17. *Lithiation mechanism of the LFMTa–d cathodes.*

Therefore, these transition metals act only as stabilizers of the spinel structure in terms of suppression of the J-T distortion and to lowering the J-T active Mn(III) concentration. In particular, the partial substitution of Mn with Fe(III) contributes to further hinder the cubic to tetragonal phase transition, which is sometimes still observed in the LiMnTiO4-based spinels,[6,14] reasonably increasing the overall configurational entropy of the spinel. At 4.4 V upon delithiation, an irreversible phenomenon takes places, which is likely related to an irreversible anionic redox process leading to the structural O^{2-} oxidation to O_2^{2-n} and consequent evolution of O_2 in the gas phase. This irreversible step appears to be strictly related to the Li/Mn ratio, increasing its intensity by reducing the Mn amount in the spinel. The oxygen loss is reasonably compensated in terms of charge by the redox processes involving Mn in all its oxidation state and specifically a subsequent reduction Mn(IV)-Mn(III)-Mn(II) occurring at high voltage. This hypothesis is confirmed by the XAS measurements: the *ex situ* spectrum at the Mn $L_{2,3}$ edge collected at 4.8 V during the first delithiation reveals the unexpected presence of Mn(II) in addition to Mn(III) and a small fraction of Mn(IV) (Figure 6.14), not detected in the spectra obtained at OCV. The extensive Li insertion/extraction in a wide voltage range (4.8 V-1.5 V) induces a structural transformation upon cycling, as evidenced by ex situ XRD. As discussed before, all diffraction patterns collected after the first delithiation up to 4.8 V reveal a peak splitting, which is coherent with the formation of two spinel phases with an estimated 25/75 volume ratio (Spinel 1/Spinel 2). This structural modification is in good agreement with the SEM-EDX analysis. Figure 6.18 and Figure 6.19 show the SEM images and the corresponding EDX map for cathodes at OCV, delithiated at 4.8 V, and lithiated at 1.5 V at different selected cycles.

OCV | **1st Charge 4.8V** | **2nd Charge 4.8V**

10th Discharge 1.5V | **60th Discharge 1.5V**
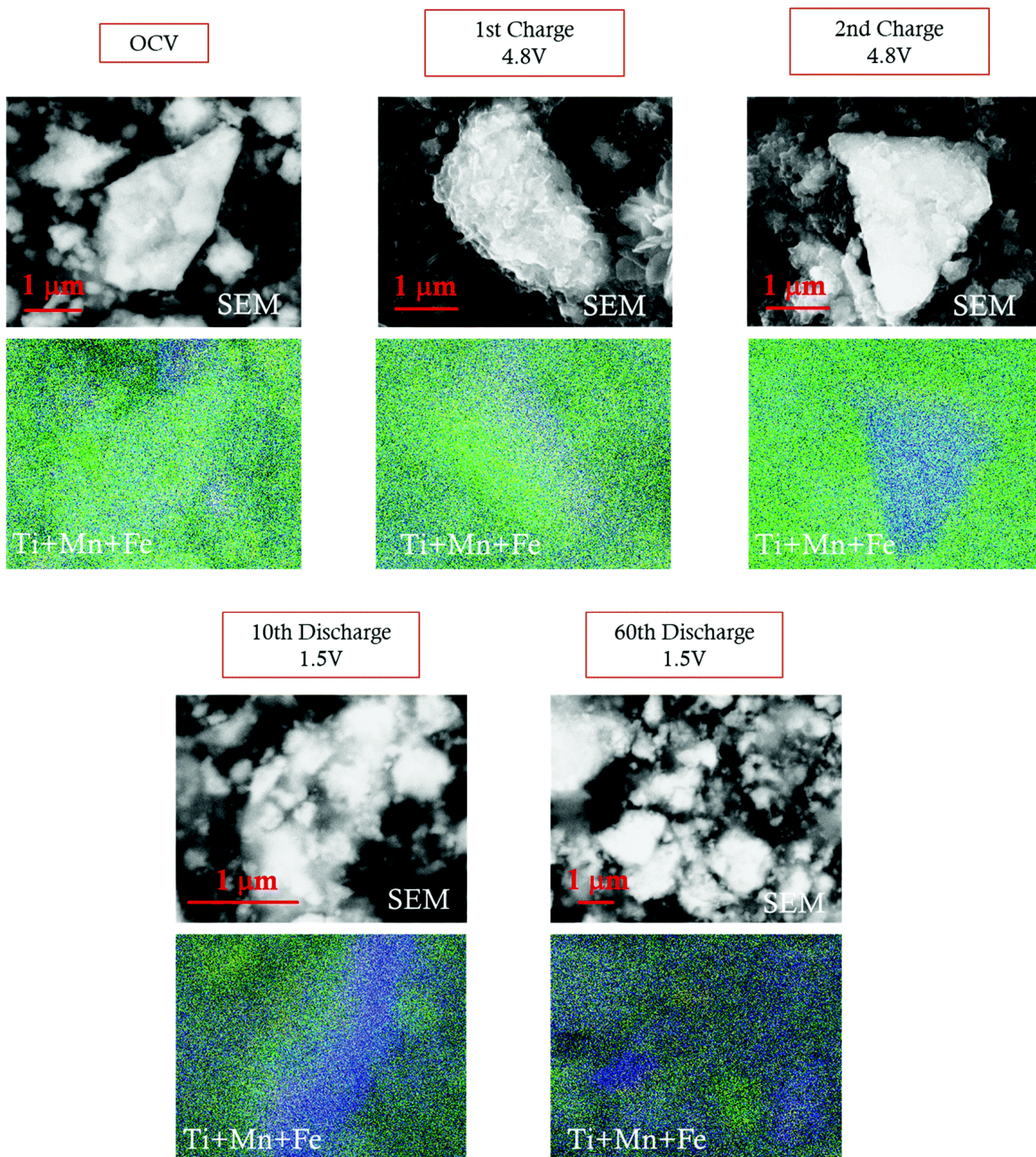
Figure 6.18. SEM images and SEM-EDX maps of the LFMTc cathode before and after galavanostatic cycling. Fe (yellow); Mn (blue); Ti (green).
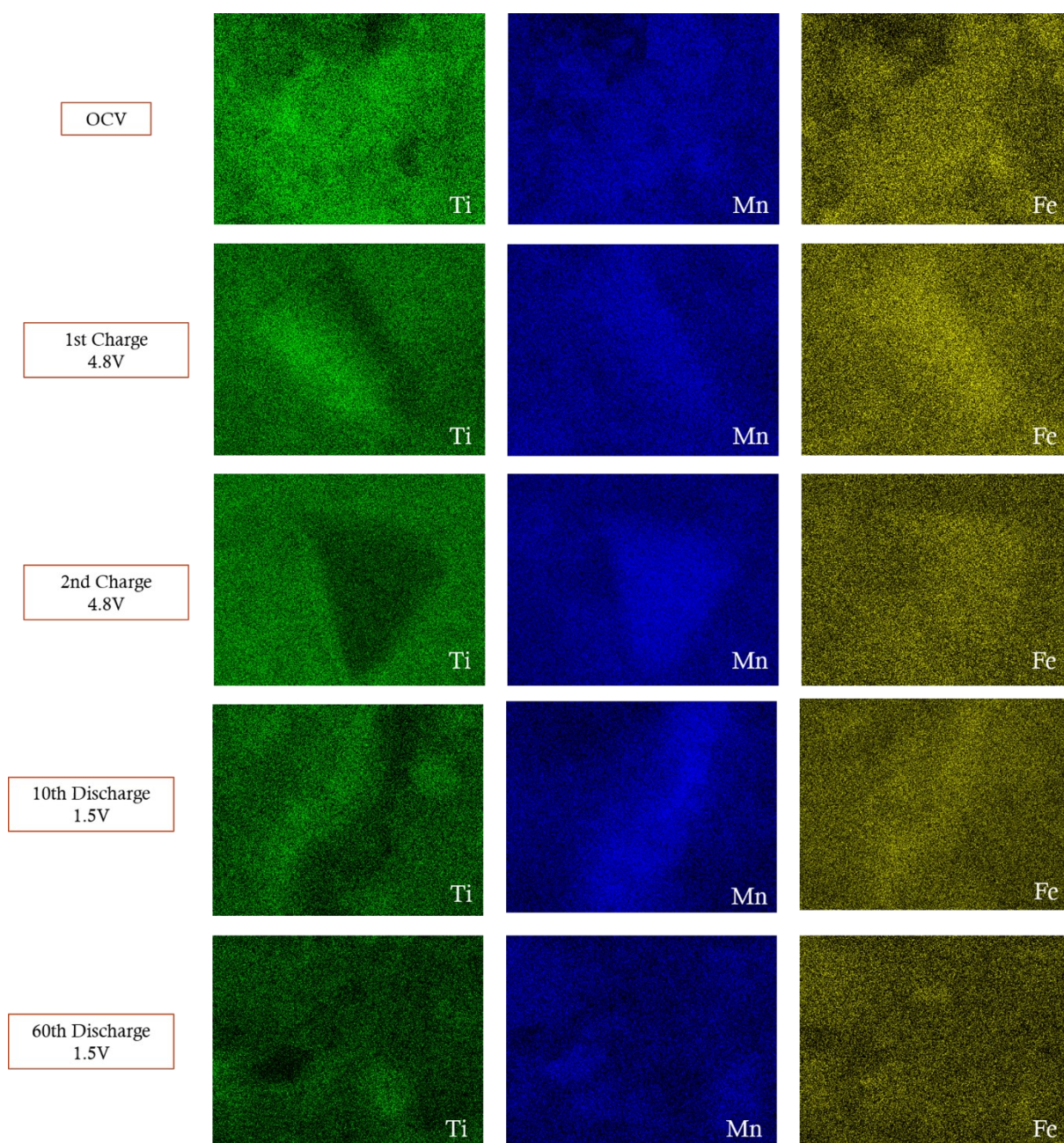
Figure 6.19. EDX TMs mapping images of the cathodes frozen at OCV, delithiated at 4.8 V and lithiated at 1.5 V at different selected cycles.

The concentration maps show that, while Fe remains well distributed throughout all the samples, independently from the voltage and cycle, the Mn and Ti distribution is inhomogeneous, and two separated domains, one Mn-rich (blue) and the other Ti-rich (green), are clearly noticeable. Similar evidence was reported in the literature in the case of Mg-doped $LNi_xMn_{2-x}O_4$ spinels, whose initial Ni-Mn ordering is lost during Li insertion due to extensive Ni and Mn migration, achieving Ni-rich and Ni-poor domains in distorted

177

tetragonal phases with different Ni/Mn ratios.[38] While a rough quantification of the volume ratio of the different spinel phases may be attempted, a reliable estimation of their composition is not possible, because of the close scattering factors of the involved TMs. The two spinel phases individuated by XRD were investigated in terms of variations of the lattice parameters upon cycling (Figure 6.20).
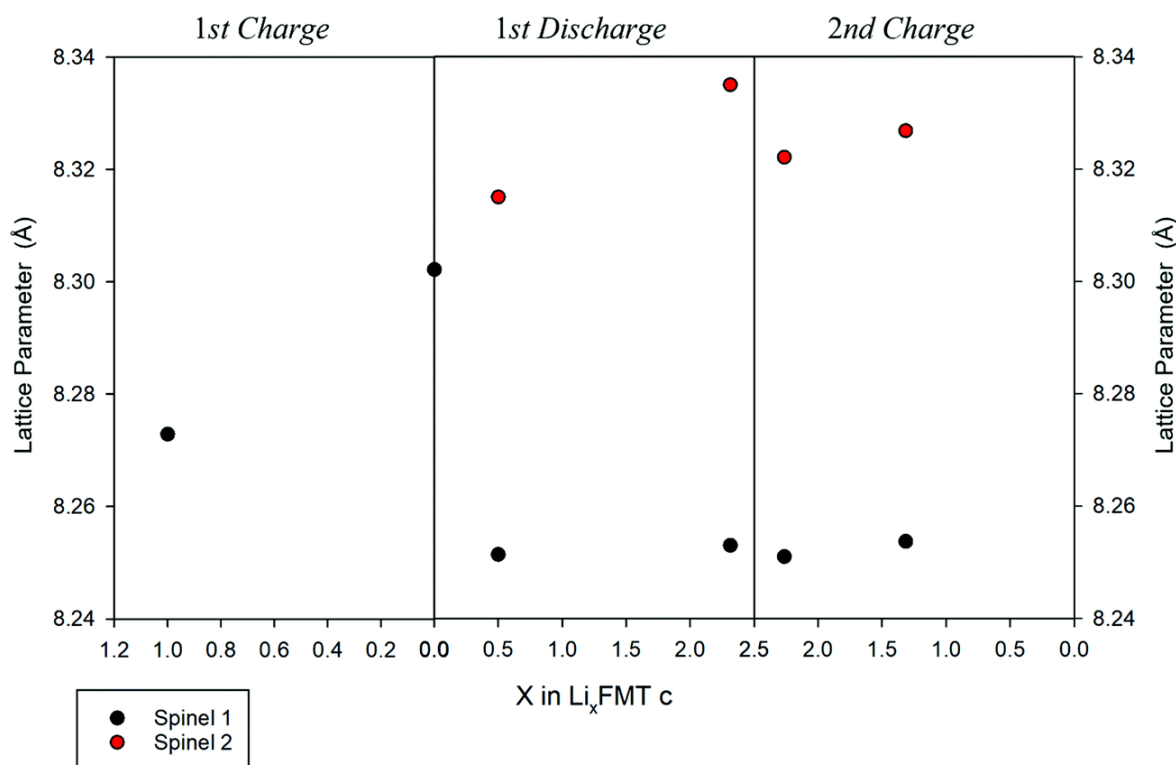
Figure 6.20. Variation of the lattice parameter, a, upon cycling vs. the Li composition in the LFMTc cathode.

Indeed, the Ti-rich Spinel 1 is reasonably electrochemically inactive (or poorly active), since its lattice volume does not change upon Li intercalation/extraction, showing a constant parameter *a* (8.25 Å) during the 1st discharge and 2nd charge. In contrast, the Mn-rich Spinel 2 appears to be the active materials. This conclusion is nicely proved by the change of its lattice parameter a upon cycling, as determined by *ex situ* XRD measurements. Indeed, during the first delithiation (1st charge, Figure 6.20) an increase of the lattice parameter with respect to the OCV is noticeable at 4.8 V, thus suggesting a volume expansion of the spinel. The lattice expansion is even more evident after the 1st lithiation at 1.5 V (Figure 6.20, 1st discharge), when the Spinel 2 is richer in Li and Mn is almost entirely present as the larger Mn(II) ion, as confirmed by the XAS investigation. During the 2nd charge, the lattice

178

parameter of the Spinel 2 decreases with respect the fully lithiated state, indicating a lattice contraction, as expected in case of Li deintercalation.[36] The unit cell of Spinel 2 is further expanded up to 8.34 Å and contracted upon cycling, demonstrating its electrochemically capability to intercalate and deintercalate Li with excellent reversibility.

6.5. Conclusion

We analyzed, for the first time, the microstructure, local environment, and electrochemistry of new $LiFe_xMn_{2-x-y}Ti_yO_4$ compositions with different Li/Mn ratios. The redox mechanism of these materials was clarified. An easy and fast sol-gel synthesis produced a family of spinels with Li/Mn ratio ranging between 1.0 and 1.7, all presenting the cubic $Fd\bar{3}m$ structure of $LiMn_2O_4$ with lattice parameter, a, increasing with the Li/Mn ratio. Fe/Ti dual-doped spinels show higher electronic conductivity and electronic transport number than undoped $LiMn_2O_4$, achieving values that exceed 0.2 mS cm^{-1} and 0.7 mS cm^{-1} at 90°C, respectively, in case of compositions presenting smaller lattice parameters. XAS investigation demonstrated that the only electrochemically active redox couples involve Mn, while both Fe(III) and Ti(IV) do not change their oxidation state upon cycling. Two electrochemical phenomena are clearly observed, one ascribed to Mn(IV)/Mn(III) at around 4 V, and the second one at 3 V, which is assigned to the Mn(III)/Mn(II) transition. The exchange of more than 2 Li ion through the whole Mn(IV)/Mn(II) redox couple is observed in the LFMT spinels during Li intercalation/deintercalation, providing specific capacity significantly higher than what observed for the undoped spinel (> 250 mAh g^{-1} during the first delithiation step). Extensive galvanostatic cycling between 1.5 and 4.8 V also demonstrated the presence of irreversible anion redox activity during the first charge, whose entity increases with the Li/Mn ratio in the spinel. The disorder induced by multiple doping stabilizes the spinel phase, hindering the cubic-tetragonal transition upon prolonged Li intercalation/deintercalation. Such effect results in an unusual behaviour through the modification of the LFMT spinel into two different spinel phases with 3:1 mass ratio. The first phase is electrochemically active and shows Mn-rich domains, while the other, including Ti-rich domains, is electrochemically inert, as proved by the lattice parameter variation and SEM-EDX maps upon cycling. By suppressing the spinel Jahn‑Teller distortion, the substitution of Mn(III) with Ti and Fe lowers the concentration of J-T Mn(III),

which is responsible for the severe capacity fade in the undoped spinel. Such stabilizing effect, favoured by the synergistic presence of Fe and Ti, results in remarkably reduced capacity fade at low current density (< 28% after 100 cycles at 27 mA g^{-1}) and to an excellent stability and reversibility in case of higher C rate (270 mA g^{-1}). The encouraging functional performances of these new LFMT spinels and the resulting structure-property relationship may be an important guide to design an ever-wider range of spinel materials with enhanced stability against J-T distortion as new cathodes for sustainable, greener and Co-free Li-ion batteries.

6.6. Bibliography

1. Tarascon, J. M.; McKinnon, W. R.; Coowar, F.; Bowmer, T. N.; Amatucci, G.; Guyomard, D. Synthesis Conditions and Oxygen Stoichiometry Effects on Li Insertion into the Spinel $LiMn_2O_4$. *J. Electrochem. Soc.* 1994, **141**, 1421‑1431.

2. Thackeray, M. M. Manganese oxides for lithium batteries. *Prog. Solid State Chem.* 1997, **25**, 1‑71.

3. Whittingham, M. S. Lithium Batteries and Cathode Materials. *Chem. Rev.* 2004, **104**, 4271‑4301.

4. Zhang, X.; Yang, M.; Zhao, X.; Wang, Y.; Wang, M.; Ma, L. The spinel phase $LiMnTiO_4$ as a potential cathode for rechargeable lithium ion batteries. *J. Mater. Sci.: Mater. Electron.* 2015, **26**, 6366‑6372.

5. Amatucci, G. G.; Pereira, N.; Zheng, T.; Tarascon, J.-M. Failure Mechanism and Improvement of the Elevated Temperature Cycling of $LiMn_2O_4$ Compounds Through the Use of the $LiAl_xMn_{2-x}O_{4-z}F_z$ Solid Solution. *J. Electrochem. Soc.* 2001, **148**, A171.

6. Chen, R.; Knapp, M.; Yavuz, M.; Heinzmann, R.; Wang, D.; Ren, S.; Trouillet, V.; Lebedkin, S.; Doyle, S.; Hahn, H.; Ehrenberg and H.; Indris, S. Reversible Li+ Storage in a $LiMnTiO4$ Spinel and Its Structural Transition Mechanisms. *J. Phys. Chem. C* 2014, **118**, 12608‑12616.

7. Wang, H. C.; Lu, C. H. Dissolution behavior of chromium-ion doped spinel lithium manganate at elevated temperatures. *J. Power Sources* 2003, **119–121**, 738‑742.

8. Chen, R.; Knapp, M.; Yavuz, M.; Ren, S.; Witte, R.; Heinzmann, R.; Hahn, H.; Ehrenberg, H.; Indris, S. Nanoscale spinel $LiFeTiO_4$ for intercalation pseudocapacitive Li^+ storage. *Phys. Chem. Chem. Phys.* 2015, **17**, 1482‑1488.

9. Liu, Q.; Wang, S.; Tan, H.; Yang, Z.; Zeng, J. Preparation and Doping Mode of Doped $LiMn_2O_4$ for Li-Ion Batteries. *Energies* 2013, **6**, 1718-1730.

10. Xu, G.; Liu, Z.; Zhang, C.; Cui, G.; Chen, L. Strategies for improving the cyclability and thermo-stability of $LiMn_2O_4$-based batteries at elevated temperatures. *J. Mater. Chem. A* 2015, **3**, 4092.

11. Song, D.; Ikuta, H.; Uchida, T.; Wakihara, M. The spinel phases $LiAl_yMn_{2-y}O_4$ (y=0, 1/12, 1/9, 1/6, 1/3) and $Li(Al,M)_{1/6}Mn_{11/6}O_4$ (M=Cr, Co) as the cathode for rechargeable lithium batteries. *Solid State Ionics* 1999, **117**, 151‑156.

12. Ebin, B.; Gürmen, S.; Arslan, C.; Lindbergh, G. Electrochemical properties of nanocrystalline $LiFe_xMn_{2-x}O_4$ (x = 0.2-1.0) cathode particles prepared by ultrasonic spray pyrolysis method. *Electrochim. Acta* 2012, **76**, 368‑374.

13. Cai, Z.; Ji, H.; Ha, Y.; Liu, J.; Kwon, D.-H.; Zhang, Y.; Urban, A.; Foley, E. E.; Giovine, R.; Kim, H.; Lun, Z.; Huang, T.-Y.; Zeng, G.; Chen, Y.; Wang, J.; McCloskey, B. D.; Balasubramanian, M.; Clément, R. J.; Yang W.; Ceder, G. Realizing continuous cation order-to-disorder tuning in a class of high-energy spinel-type Li-ion cathodes. *Mater.* 2021, **4**, 3897‑3916.

14. Wang, S.; Yang, J.; Wu, X.; Li, Y.; Gong, Z.; Wen, W.; Lin, M.; Yang, J.; Yang, Y. Toward high capacity and stable manganese-spinel electrode materials: A case study of Ti-substituted system. *J. Power Sources* 2014, **245**, 570‑578.

15. Jayapal, S.; Mariappan, R.; Sundar, S.; Piraman, S. Electrochemical behavior of $LiMn_{2-X-Y}Ti_xFe_yO4$ as cathode material for Lithium ion batteries *J. Electroanal. Chem.* 2014, **720–721**, 58‑63.

16. Hervás, P.; Millares, R. *CWL Publ. Enterp. Inc., Madison* 2004, **vol. 2004**, p. 352.

17. T. Roisnel, T.; Rodríguez-Carvajal, J. WinPLOTR: a windows tool for powder diffraction pattern analysis. *Mater. Sci. Forum* 2001, **378–381**, 118‑123.

18. Panaccione, G.; Vobornik, I.; Fujii, J.; Krizmancic, D.; Annese, E.; Giovanelli, L.; MacCherozzi, F.; Salvador, F.; De Luisa, A.; Benedetti, D.; Gruden, A.; Bertoch, P.; Polack, F.; Cocco, D.; Sostero, G.; Diviacco, B.; Hochstrasser, M.; Maier, U.; Pescia, D.; Back, H.; Greber, T.; Osterwalder, J.; Galaktionov, M.; Sancrotti M.; Rossi, G. Advanced photoelectric effect experiment beamline at Elettra: A surface science laboratory coupled with Synchrotron Radiation. *Rev. Sci. Instrum.* 2009, **80**, 043105.

19. Castán-Guerrero, C.; Krizmancic, D.; Bonanni, V.; Edla, R.; Deluisa, A.; Salvador, F.; Rossi, G.; Panaccione, G.; Torelli, P. A reaction cell for ambient pressure soft x-ray absorption spectroscopy. *Rev. Sci. Instrum.* 2018, **89**, 054101.

20. Huggins, R. A. Simple method to determine electronic and ionic components of the conductivity in mixed conductors a review. *Ionics* 2002, **8**, 300‑313.

21. Guan, J.; Liu, M. Transport properties of LiMn2O4 electrode materials for lithium-ion batteries. *Solid State Ionics* 1998, **110**, 21‑28.

22. Shannon, R. D. Revised Effective Ionic Radii and Systematic Studies of Interatomic Distances in Halides and Chalcogenides. *Acta Crystallogr., Sect. A: Cryst. Phys., Diffr., Theor. Gen. Crystallogr.* 1976, **32**, 751‑767.

23. Goodenough, J. B. Design considerations. *Solid State Ionics* 1994, **69**, 184‑198.

24. Goodenough, J. B. Metallic oxides. *Prog. Solid State Chem.* 1971, **5**, 145‑399.

25. Luo, M.; Zheng, S.; Wu, J.; Zhou, K.; Zuo, W.; Feng, M.; He, H.; Liu, R.; Zhu, J.; Zhao, G.; Chen, S.; Yang, W.; Peng, Z.; Wu, Q.; Yang, Y. Identifying the anionic redox activity in cation-disordered $Li_{1.25}Nb_{0.25}Fe_{0.50}O_2$/C oxide cathodes for Li-ion batteries. *J. Mater. Chem. A* 2020, **8**, 5115‑5127.

26. Hu, E.; Yu, X.; Lin, R.; Bi, X.; Lu, J.; Bak, S.; Nam, K.-W.; Xin, H. L.; Jaye, C.; Fischer, D. A.; Amine, K.; Yang, X.-Q. Evolution of redox couples in Li-and Mn-rich cathode materials and mitigation of voltage fade by reducing oxygen release. *Nat. Energy* 2018, **3**, 690‑698.

27. Brydson, R.; Sauer, H.; Engel, W.; Thomass, J. M.; Zeitler, E.; Kosugi, N.; Kuroda, H. Electron energy loss and X-ray absorption spectroscopy of rutile and anatase: a test of structural sensitivity. *J. Phys.: Condens. Matter* 1989, **1**, 797‑812.

28. Van Der Laan, G.; Kirkman, I. W. The 2p absorption spectra of 3d transition metal compounds in tetrahedral and octahedral symmetry. *J. Phys.: Condens. Matter* 1992, **4**, 4189‑4204.

29. Laskowski, R.; Blaha, P. Understanding the $L_{2,3}$ x-ray absorption spectra of early transition elements. *Phys. Rev. B: Condens. Matter Mater. Phys.* 2010, **82**, 1‑6.

30. Stavitski, E.; De Groot, F. M. F. The CTM4XAS Program for EELS and XAS Spectral Shape Analysis of Transition Metal L edges. *Micron* 2010, **41**, 687– 94.

31. Gilbert, B.; Frazer, B. H.; Belz, A.; Conrad, P. G.; Nealson, K. H.; Haskel, D.; Lang, J. C.; Srajer, G.; De Stasio, G. Multiple scattering calculations of bonding and X-ray absorption spectroscopy of manganese oxides. *J. Phys. Chem. A* **2003**, 107, 2839‑2847.

32. Frati, F.; Hunault, M. O.-J. Y.; de Groot, F. M.-F. Oxygen K-edge X-ray absorption spectra. *Chem. Rev.* 2020, **120**, 4056‑4110.

33. de Groot, F. M.-F.; Grioni M.; J. C. Fuggle, J. C. Oxygen 1s x-ray-absorption edges of transition-metal oxides. *Phys. Rev. B: Condens. Matter Mater. Phys.* 1989, **40**, 5715‑5723.

34. Mohanty, D.; Kalnaus, S.; Meisner, R. A.; Safat, A. S.; Li, J.; Payzant, E. A.; Rhodes, K.; D.; Wood L.; Daniel, C. Structural transformation in a $Li_{1.2}Co_{0.1}Mn_{0.55}Ni_{0.15}O_2$ lithium-ion battery cathode during high-voltage hold. *RSC Adv.* 2013, **3**, 7479‑7485.

35. Zhu, W.; Liu, D.; Trottier, J.; Gagnon, C.; Mauger, A.; Julien C. M.; Zaghib, K. In-situ X-ray diffraction study of the phase evolution in undoped and Cr-doped $Li_xMn_{1.5}Ni_{0.5}O_4$ (0.1≤ x≤ 1.0) 5-V cathode materials. *J. Power Sources* 2013, **242**, 236‑243.

36. Levi, E.; Levi, M. D.; Salitra, G.; Aurbach, D.; Oesten, R.; Heider U.; Heider, L. In situ XRD study of Li deintercalation from two different types of $LiMn_2O_4$ spinel. *Solid State Ionics* 1999, **126**, 109‑119.

37. Gummow R. J.; Thackeray, M. M. Characterization of LT-$Li_xCo_{1-y}Ni_yO_2$ Electrodes for Rechargeable Lithium Cells. *J. Electrochem. Soc.* 1993, **140**, 3365‑3368.

38. Wagemaker, M.; Ooms, F. G.-B.; Kelder, E. M.; Schoonman, J.; Kearley G. J.; Mulder, F. M. Extensive Migration of Ni and Mn by Lithiation of Ordered $LiMg_{0.1}Ni_{0.4}Mn_{1.5}O_4$ Spinel. *J. Am. Chem. Soc.* 2004, **126**, 13526‑13533.

Chapter 7:
Enhanced Janus Gel Polymer Electrolyte

7.1. Abstract

Cell failure at material level due to internal short circuit is extremely difficult to detect and mitigate. Among the cell components, separators are primarily responsible for internal shorting. This issue can be induced by external causes such as mechanical deformation and overcharging, but also electrochemical phenomena leading to dendrite growth which usually penetrate the separator. A promising route to engineering a robust separator consists in the use of a ceramic filler (alumina o zirconia) in order to improve thermal shrinkage resistance and also to obtain a physical obstruction to dendrite proliferation. However, such separators are able to just delay the dendrite penetration, resulting in an even more violent and dangerous failure subsequent to the shorting event. Here, a novel composite Janus separator was designed with tunable properties such as mechanical strength, ionic and electronic conductivity. The composite separator was realized with two different layers: an electronically insulating one composed of PVdF-HFP (poly(vinylidene fluoride-*co*-hexafluororpropylene)) and Al-LLZO ($Li_{6.24}La_3Zr_2Al_{0.24}O_{11.98}$) and a second electroconductive layer constituted of PVdF-HFP:Al-LLZO:N-CQDs (Nitrogen-Carbon Quantum Dots). The Janus separator was characterized by potentiodynamic electrochemical impedance spectroscopy (PEIS) and galvanostatic cycling in order to evaluate the performance and stability in a NMC811| *Separator* | $Li_{(m)}$ coin cell configuration. A neat PVdF-HFP and a single layer PVdF-HFP:Al-LLZO separators were also characterized for comparison. Also, the Janus separator was investigated through SEM analysis in order to estimate eventual mechanical damages and dendrite penetration. When single layer PVdF-HFP:Al-LLZO separator was tested, at the 114th cycle a sudden and evident failure occurred, while for the PVdF-HFP separator the most problematic behavior was represented by the poor electrochemical performance that leads to a capacity loss of 26 %. The obtained Janus separators realized through blade casting result in a homogeneous film with a thickness of ~35-40 μm, comparable to separators in commercial applications, and with good wettability and electrolyte uptake. Electrochemical characterization evidences the maintenance of excellent reversibility of electrochemical phenomena, good stability, and overall efficiency

for even more than 130 cycles with a capacity loss of about 11% with no significant evidence of short circuit events and dendrite penetration, as further confirmed by SEM images. The composite Janus separator demonstrated an interesting compromise between improved capability to hinder short circuit events and mitigate the dendrite penetration and good overall electrochemical performances.

7.2. Introduction

Lithium metal batteries (LMBs) are expected to play an increasingly important role in automotive sector during the next decades.[1] However, the industrial development of LMBs requires to overcome a series of issues regarding materials and interfaces.[2] Indeed, more rigid constraints are required on the electrolyte design with respect to lithium ion batteries (LIBs): in addition to high conductivity, chemical and electrochemical stability against the electrodes, low flammability, and environmental sustainability,[3] the electrolytes for LMBs must be able to block the formation of lithium dendrites, *e.g.*, by forming a stable solid electrolyte interface (SEI) towards the metal anode, and/or by constituting a rigid barrier by themselves.[4,5] Among the solutions proposed in the literature, Janus separators (JSs) could play a major role.[6] These membranes take their name from the ancient Roman god Janus "two-faced" and are characterized by having two faces with different chemical-physical and functional properties. The Janus concept was recently applied both to LIBs and beyond-lithium batteries. On the LIBs side, *Oh et al.* demonstrated dual (ion/electron)-conductive/chemically active (*i.e.*, able to chelate heavy metal ions) Janus membrane (JM) based on a hetero-layered nanofiber matrix architecture.[7] Later, *Zhang et al.* reported JM for acid scavenging and manganese ions trapping in $LiMn_2O_4$ LIBs. These separators were made of interpenetrating hydroxyapatite/bacterial cellulose fibres, integrated with a nanofibrous poly(mphenylene isophthalamide) (PMIA) support membrane by electrospinning.[8] On the beyond-lithium batteries side, a great deal of work was devoted to the improvement of lithium-sulphur cells, by developing JMs with the double aim to stabilize the lithium metal interface and (most importantly) to block/reduce polysulphides shuttle.[9-19] *Zhou et al.* developed JMs contain a single sodium ion-conducting side and a functional low-dimensional material (MXene)-coated side. When employed in room temperature sodium-sulfur batteries, these JMs showed improved performances in enhancing electrolyte

186

wettability, inhibiting polysulfide diffusion and sodium dendrite growth.[20] On the side of LMBs, *Xu et al.* reported a polymeric one-side conductive JM with quasi-oriented pores, prepared via directional ice-templating and phase inversion from electrically conducting polyaniline (PANI) and insulating polyvinyl alcohol (PVA). The basic idea was that PANI surface could reduce locally concentrated currents promoting the formation of an even and stable Solid Electrolyte Interface (SEI) layer, so solving uneven germination of lithium dendrites and low coulombic efficiency. At the same time, the pores that are oriented nearly perpendicular to the separator surface, would improve affinity to the electrolyte and shorten ion diffusion pathways.[21] *Xie et al.* used two molecular sieves, MCM-41 and SAPO-34, as functional modification layers to design JMs for LMBs.[22] Due to the presence of Li-philic groups and the confinement effect of its pores, MCM-41 could provide fast transportation channels for Li^+ ions and ensure their uniform distribution. The SAPO-34 is highly selective for Li ions and could work as an "ion rectifier" to redistribute Li ions. Finally, *Gonzales et al.* discussed an interesting "fail safe" mechanism for internal short circuit to mitigate thermal runaway and catastrophic battery failure.[23] They fabricated a nanocomposite JM, encompassing a PVdF-HFP gel polymer electrolyte (GPE), SiO_2 and carbon nanotubes (CNTs) as fillers, with a fully electronically insulating layer towards the anode and a partially electronically conductive (PEC) layer facing the cathode. In our work, we moved from the *Gonzales et al.* results to prepare Janus Separators (JSs) by means of a simpler approach. In fact, we did not exploit a phase inversion method to prepare the polymer matrix, to avoid dibutyl phthalate as plasticizer, rather we employed a standard solvent casting procedure with NMP. In addition, we substituted SiO_2 with modified Al-doped Lithium Lanthanum Zirconate Oxide (Al-LLZO), starting from a commercial batch. The ceramic was treated through a solvothermal reaction with ethylene glycol in order to: i) obtain a more homogeneous morphology in terms of ceramic grains size; ii) introduce nanospheres of polymer on the ceramic grain, so providing further paths for the Li^+ conduction; ii) favour a better filler dispersion thanks to an improved chemical affinity with the separator. For what concern the carbon component, we synthetized Nitrogen doped-Carbon Quantum Dots (N-CQDs) to be added on the separator layer exposed to the cathode side. The final Janus Separator was finally composed by a two-layers system: 1) an electronically insulating layer made of Al-LLZO:PVdF-HFP, (EI-L) interfaced with the lithium metal side and 2) a layer made of Al-LLZO:PVdF-HFP + 5 wt% N-CQDs (EC-L) in contact with the cathode side. As stated, the main advantage of JSs is the possibility of implementing different functional properties on the two sides of the separator. Herein, the layer on the anode side offers a

greater resistance towards the formation of lithium dendrites. The layer on the cathode side provides better interface properties (less ohmic resistance) towards the electrode thanks to the presence of an electron-conducting phase. Al-LLZO:PVdF-HFP monolayer and a neat PVdF-HFP separators were also tested in order to evaluate the individual contribution of each layer to the Janus Separator. Additionally, an analogue separator with a conductive layer with 5 wt% of commercial Multiwalled-Carbon Nanotubes (MW-CNTs) was realized and tested. All the separators were then activated with a standard electrolyte solution, so obtaining a gel polymer electrolyte (GPE).

7.3. Material and Methods

7.3.1. Solvothermal Treatment of Al-doped Lithium Lanthanum Zirconate Oxide

For the solvothermal treatment 1 g of Al-LLZO (Sigma Aldrich) was added to 25 mL ethylene glycol (EG). The mixture was stirred vigorously for 5 h to obtain a homogeneous suspension. Subsequently, the precursor solution was placed in a Teflon-lined stainless solvothermal reactor and heated at 200°C for 5 h. The as obtained product was collected by centrifugation, washed with deionized water and ethanol repeatedly, and then dried in vacuum at 40 °C overnight.

7.3.2. Synthesis of Nitrogen-Carbon Quantum Dots (N-CQDs)

The N-CQDs were synthesized by means of a hydrothermal synthesis. In a glass becher were dissolved 0.70 g of citric acid and 0.25 g of dicyandiamide, both purchased from Sigma Aldrich, in 4 mL of tri-distilled water and sonicated for 30 minutes. Then the as realized mixture was transferred into a Teflon-lined stainless-steel hydrothermal reactor and heated at 180°C for 3 hours, then cooled to room temperature naturally. The product resulted in a brownish solution that was cleaned in order to obtain a homogeneous and stable N-CQDs suspension. Specifically, dichloromethane (DCM) was added to remove the remaining organic compounds, the solution was centrifugated at 9000 rpm to separate the aqueous phase (brown, top part) to the DCM one (transparent, bottom part). The water phase

suspension was centrifugated at 12000 rpm for 15 minutes that lead to the formation of a precipitate. The as obtained supernatant was characterized by Transmission Electron Microscopy (TEM) and then, previous filtration, it undergoes a two-step drying by means of a freeze-dryer and subsequently stored in a vacuum desiccator to avoid contact with moisture.

7.3.3. Morphological Characterization

TEM micrographs of N-CQDs were obtained by keeping aside a small quantity of the brownish solution prior to freeze-drying. The analysis was performed in a JEOL JEM-1200 EX II microscope operating at 100 kV, equipped with a tungsten filament as electron source. The sample was prepared by placing 30 µL of the N-CQDs solution on a grid and letting the solvent evaporate under ambient condition. The particle size distribution was calculated using the software *ImageJ*.

7.3.4. Preparation of Composite Layers (Al-LLZO:PVdF-HFP / Al-LLZO:PVdF-HFP:N-CQDs / Al-LLZO:PVdF-HFP:MW-CNTs layers)

For what concern the undoped single layer, PVdF-HFP and the as prepared Al-LLZO were combined in a weight ratio of 3:2 and mixed in zirconia jars by a planetary ball mill at 150 rpm for 10 min four times, with a rest period of 5 min. For the realization of the conductive layer, for both N-CQDs and MW-CNTs (with a length in the range of 10-20 µm and an outer diameter of 30-50 nm), the procedure was similar to the one previously discussed with the only difference that in a first milling step at 150 rpm for 10 min twice (rest of 5 min) PVdF-HFP and Al-LLZO were mixed; subsequently an amount, of 5 wt%, of carbon source was added to proceed with a second milling step with the same parameters. The as obtained mixture was dispersed in N-methylpyrrolidone (NMP) (Sigma-Aldrich) to obtain a slurry, which was cast on glass using a doctor blade with a wet thickness of 150 µm. The casted slurry was dried overnight at room temperature. The resulting film with an average thickness of ~35–40 µm was cut in disks of 2 cm^2 for the single layerwere stored in a glove box (MBraum, H_2O and O_2 < 0.5 ppm) before the production of the final Janus Separators.

7.3.5. Preparation of Janus Separators

For the realization of the Janus Separators, previously described single layers with and without carbon component were merged by a heat plates press for 10 min at 90°C with a constant pressure of 400 psi. The as obtained JS film with an average thickness of ~40 μm was cut into 2 cm^2 disks and stored in a glove box (MBraum, H_2O and O_2 < 0.5 ppm) before the electrochemical measurements.

7.3.6. Cathode Preparation and Cell Assembly

The cathode slurry was prepared by using 70 wt% of active material (NMC 811), 20 wt% of Conductive Carbon black (Imerys, Ensaco 350P), and 10 wt% of a binder (polyvinylidene fluoride, PVdF). The solid content of all slurries was kept between 26 wt% and 28 wt%. NMC 811 and carbon powders were mixed in zirconia jars by a planetary ball mill at 150 rpm for 10 min twice, with a rest period of 5 min. Subsequently, the polymeric binder was added and mixed with a similar procedure. The as prepared mixture was dispersed in N-methylpyrrolidone (NMP) (Sigma-Aldrich) to obtain the slurry, which was cast on a carbon-coated Al foil using a doctor blade with a wet thickness of 300 μm. The casted slurry was dried under vacuum at 80°C to avoid moisture and oxygen contamination. The cathode (active mass ~1.6 mg cm^{-2}) was finally cut into 2 cm^2 disks and stored in a glove box (MBraum, H_2O and O_2 < 0.5 ppm) before the electrochemical measurements. All the functional tests were performed using a coin cell type (CR2032 – MTI Corp.) assembled in an Ar-filled glove box (H_2O and O_2 < 0.5 ppm). Metallic Li was used as counter electrode. Electrodes were separated with the different as obtained separators, imbied by 40-50 μL of liquid electrolyte, consisting in a solution 1.0 M $LiPF_6$ in Ethylene Carbonate:Dimethyl Carbonate (LP30, EC:DMC, 50:50 vol%) (Sigma-Aldrich) with 2 wt% of Vinylene Carbonate (VC) and 1 wt% of 1,3,2-Dioxathiolane 2,2-dioxide Vinylene Carbonate (VC) (Ethylenesulfate) as additives.

7.3.7. Electrochemical Characterization

The potentio-electrochemical impedance spectroscopy (PEIS) and galvanostatic cycling with potential limitation (GCPL) were performed on NMC811| *Separator* |Li$_{(m)}$ cells in a voltage range between 3.0 V and 4.3 V at room temperature and for two cycle at 0.25C (current density of 50 mA g^{-1}), two cycles at 0.5C (current density of 100 mA g^{-1}) and N cycles at 1C (current density of 200 mA g^{-1}) until failure by means of battery tester (Bio-Logic BCS-810). A theoretical capacity of 200 mAh g^{-1} was calculated by taking into account the composition and the redox couple actually involved in the electrochemical process. Potentiodynamic Electrochemical Impedance Spectroscopy (PEIS) scans between 100 and 0.1 Hz were also collected at 50 mV to investigate NMC811| *Separators* |Li$_{(m)}$ cell impedance before and after the functional tests.

7.3.8. SEM Investigation

SEM analyses on the pristine and *post mortem* separators were performed using a Tescan Mira3XMU microscope operated at 20 kV and equipped with an EDAX EDX analysis system. The samples were coated with a carbon thin film using a Cressington 208 carbon coater.

7.4. Results

7.4.1. Modified Al-doped Lithium Lanthanum Zirconate Oxide

As previously described, the treatment of commercial Al-LLZO was performed by solvothermal reactor with ethylene glycol. The purposes were dual: i) improving the morphology of the pristine lithium stuffed garnet in order to obtain a more homogeneous network of spherical-like particles and, ii) realizing a capping to decorate the grain with nanospheres of polymer; in both cases those modifications aim at improving the polydispersity of the Al-LLZO when mixed with PVdF-HFP in the chosen casting solvent. Figure 7.1 compares the electron microscopy images, obtained through secondary electrons mode, with two different magnifications. The as received Al-LLZO powder (Figure 7.1*a,a'*)

results in a more inhomogeneous and jagged shape that could lead to defects and imperfections in thinner films like the ones necessary to realize an optimal separator. After the solvothermal treatment the resulting sample shown a more uniform and spherical-like morphology, as reported in Figure 7.1*b,b'*.
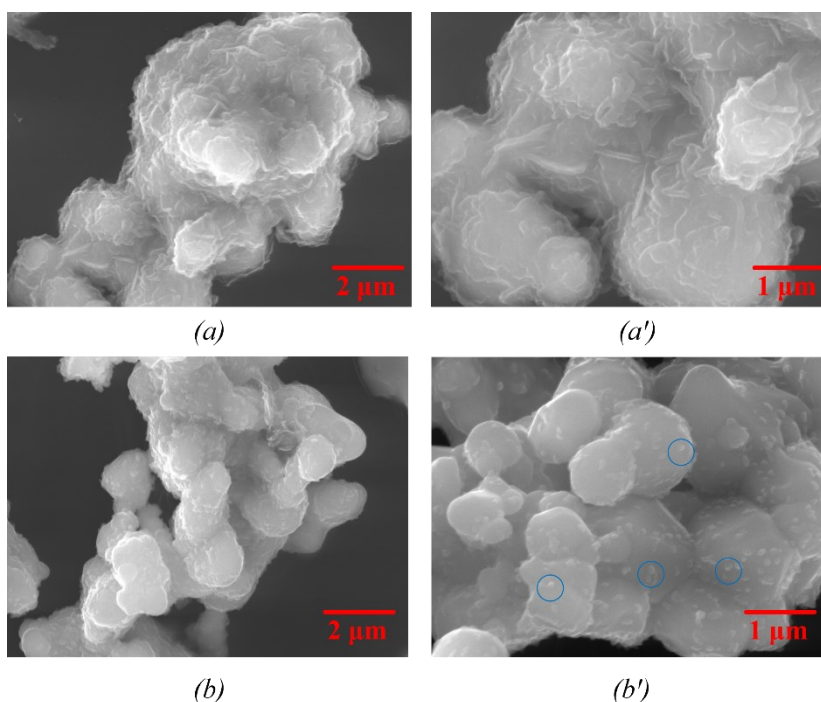

Figure 7.1. SEM images at different magnification of the (a-a') pristine Al-LLZO commercial powder and of the (b-b') Al-LLZO after solvothermal treatment with ethylene glycol.

In addition, it is possible to see in the image at higher magnification (Figure 7.1*b'*) that the grain is decorated with aggregate of polymer (blue circle). Both aspects, as previously stated, will increase the compatibility and dispersity index of the material with the other components that lead to the realization of thin homogeneous films without visible aggregates or defects.

7.4.2. Nitrogen-Carbon Quantum Dots (N-CQDs): TEM analysis

A small amount of the N-CQDs solution, prior to freeze-drying, was analysed by TEM micrographs in order to evaluate the morphology and dimension of the synthesized quantum dots. As reported in Figure 7.2, it is possible to note the as obtained N-CQDs appear to be uniform and with an average dimension of ~5 nm.
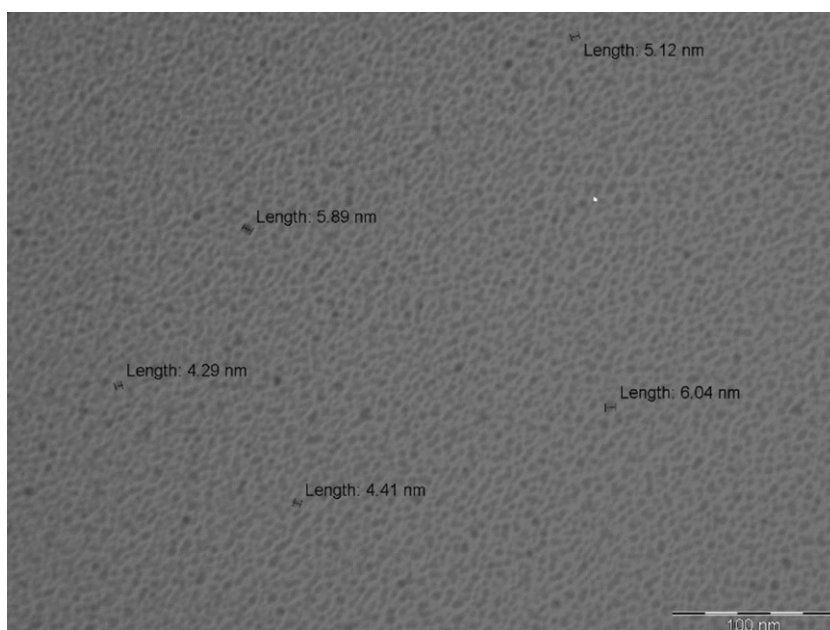
Figure 7.2. TEM image of Nitrogen-Carbon Quantum Dots (N-CQDs).

7.4.3. Electrochemical Performance

All realized separators were investigated and tested in terms of their functional properties, as described in the relative paragraph. As reported in Figure 7.3*a,a'* there are substantial differences in the cycling behaviour of the investigated separators. The neat PVdF-HFP shows an important discharge capacity loss upon cycling that is also evident for the Single Layer with a loss of 26 % and 16% (in the range between 5 to 113 cycles), respectively. Concerning the Janus separator, the electrochemical performance is notable increased, leading to a constant working capacity discharge of ~150-160 mAh g^{-1} up to 130 cycle with a less evident capacity loss, (< 9%) between cycles 5 and 113.
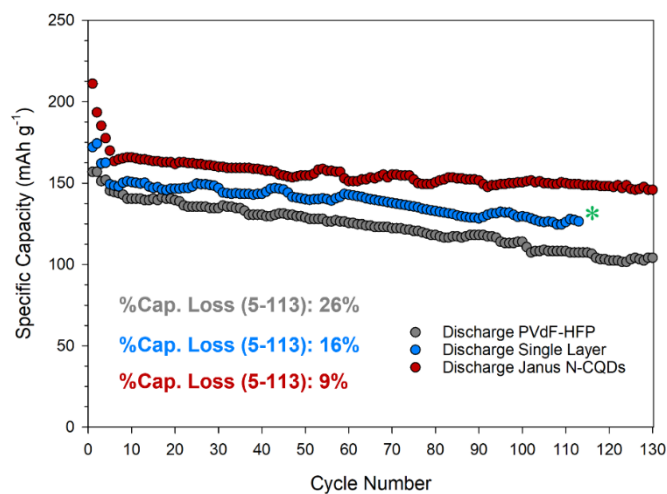
(a)
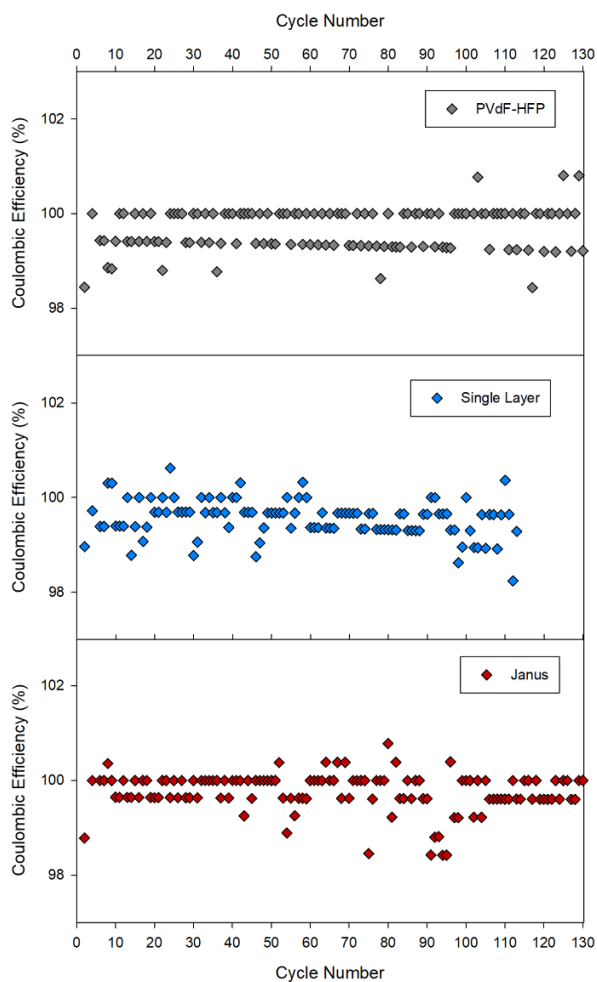
(b)

Figure 7.3.(a) *Discharge capacity upon cycling with relative capacity loss calculated between 5th and 113th cycle and* **(b)** *Coulombic efficiency (%) for the neat PVdF-HFP, Single Layer and Janus separators. (The green "*" indicates the short circuit event occurred for the Single Layer Separator)*

194

For all the investigated cells, the Coulombic efficiency was always very near to 100% (as reported in Figure 7.3*b*). Additionally, it is important to highlight the divergence in the voltage profile behaviour upon cycling. The neat PVdF-HFP separator shows a stable cycling at a current density of 200 mA g^{-1} (1C) with an important loss in both charge and discharge capacity from the 50th cycle (Charge Capacity = 130 mAh g^{-1}, Discharge Capacity = 129 mAh g^{-1}) to the 130th cycle (Charge and Discharge Capacity of ∼104 mAh g^{-1}) (see Figure 7.4*a*.)
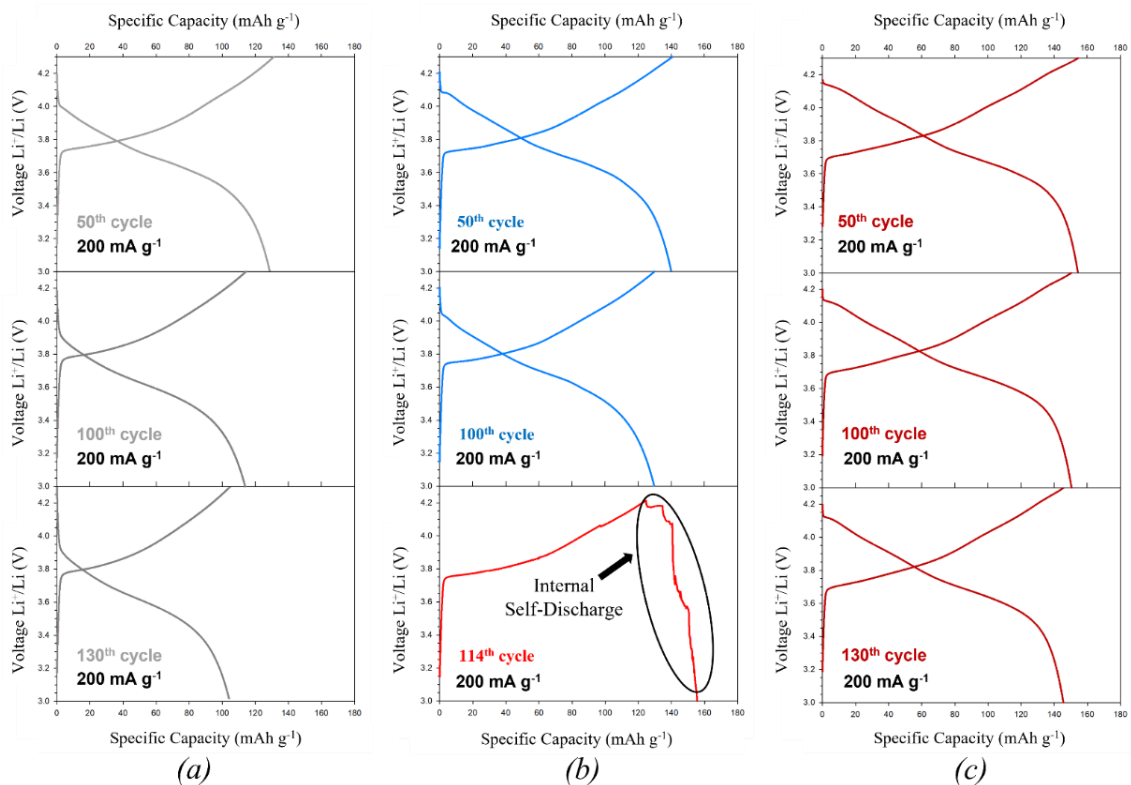

Figure 7.4. Selected voltage profile recorded at 1C (200 mA g^{-1}) at different cycles for (a) neat PVdF-HFP, (b) Single Layer, and (c) Janus separator.

The analysis concerning the Single Layer separator shows slightly improved cycling performance in Coulombic efficiency respect to the neat PVdF-HFP at both 50th and 100th cycle (50th: Charge and Discharge Capacity of ∼140 mAh g^{-1}; 100th : Charge and Discharge Capacity of ∼129 mAh g^{-1}) until a sudden drop of cell potential during charge in the 114th cycle, which is an evidence of an internal self-discharge due to a short circuit event, as reported in Figure 7.4*b*. In contrast, Figure 7.4*c* shows that no sudden voltage drops or the presence of undesired phenomena in the charge/discharge profile were recorded in case of

195

the JS. Also, the cell with the beforementioned separator shows enhanced performance and stability up to 130 cycles with a final discharge capacity of 146 mAh g^{-1}. EIS was used to check the interfacial resistances of the different separators (see Figure 7.5a,b). The spectra were obtained before and at the end of the cycling test. The charge transfer resistance is in principle very low in all cases and undergoes further decrease for the neat PVdF-HFP from 69 to 11 Ω, probably due to the growth of a stable, thin, and low-resistance CEI (Cathode Electrolyte Interphase).
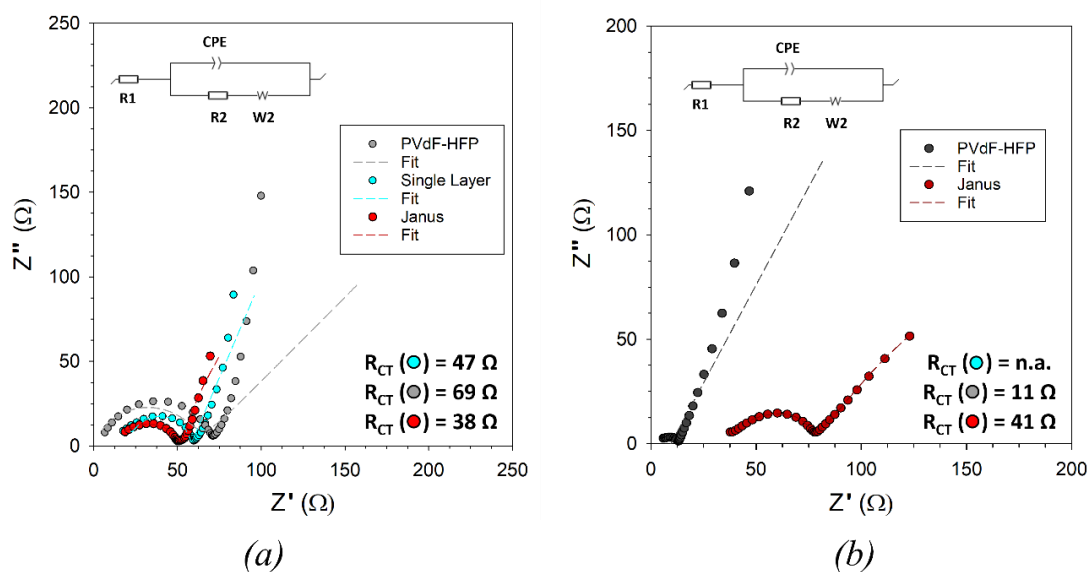

Figure 7.5. *Nyquist plots collected **(a)** before and **(b)** after the galvanostatic cycling tests.*

The evolution spectra for the Janus Separator show a negligible variation in the R_{CT} value (from 38 to 41 ohm) with a Warburg element at low frequencies due to diffusion process in solid/liquid phase. The Single Layer PEIS spectra after cycling test are not available by virtue of the short circuit that occurred. For further investigation, the Janus Separator composed by a conductive layer with 5 wt% of N-CQDs was compared to one sample with analogue weight percentage of MW-CNTs realized by the same procedure. Despite a similar behaviour in the Coulombic efficiency (slightly lower for the JS MW-CNTs) (see Figure 7.6b), the discharge capacity, reported in Figure 7.6a,b, results notably higher at every cycle for the JS with N-CQDs up to 130 cycles.
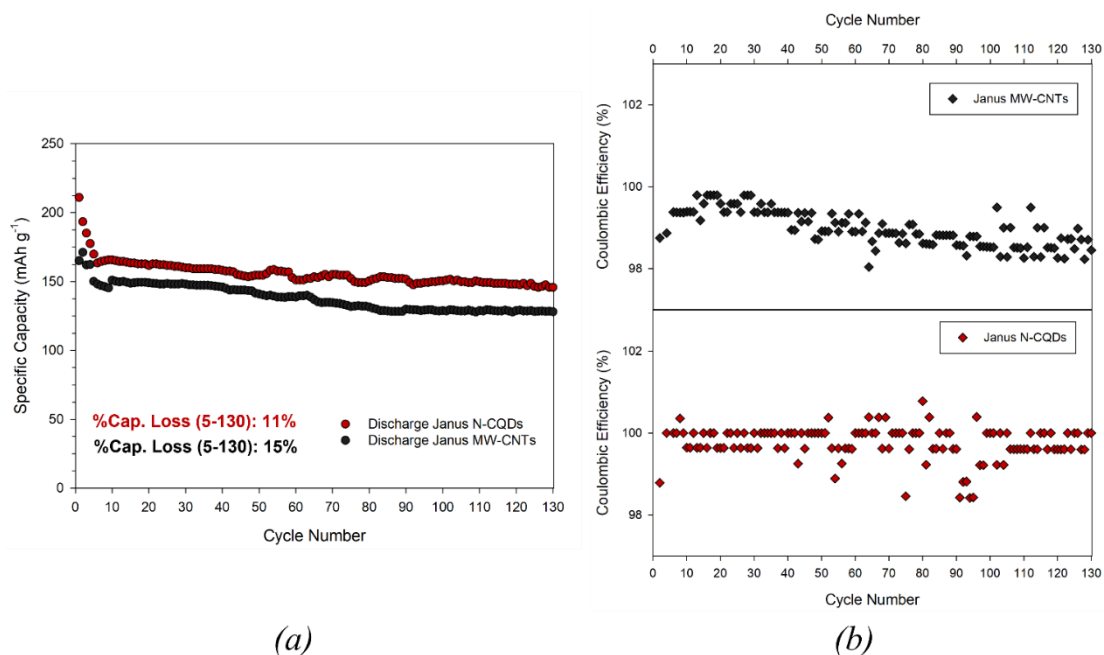
Figure 7.6. (a) *Discharge capacity upon cycling with relative capacity loss calculated between 5th and 130th* *cycle and* **(b)** *Coulombic efficiency (%) for Janus separators realized with conductive layer including a 5 wt% of Nitrogen-Carbon Quantum Dots (N-CQDs) or Multiwalled-Carbon Nanotubes (MW-CNTs).*

The performances are pretty different also in case of capacity loss that results to be higher for the separator realized with MW-CNTs in comparison to the Janus N-CQDs one, with values of 15% and 11%, respectively.

7.4.4. *Post Mortem* SEM Investigation

Post mortem analyses were performed on the Single Layer and Janus N-CQDs separators by means of scanning electron microscopy. In top view images for the Singe Layer, as reported in Figure 7.7a,b showing the sides facing lithium metal and cathode, respectively, it is notable the presence of a significant amount of damages, probably due to degradation phenomena and lithium penetration, confirmed by the electrochemical behaviour evidenced in paragraph 7.4.3.
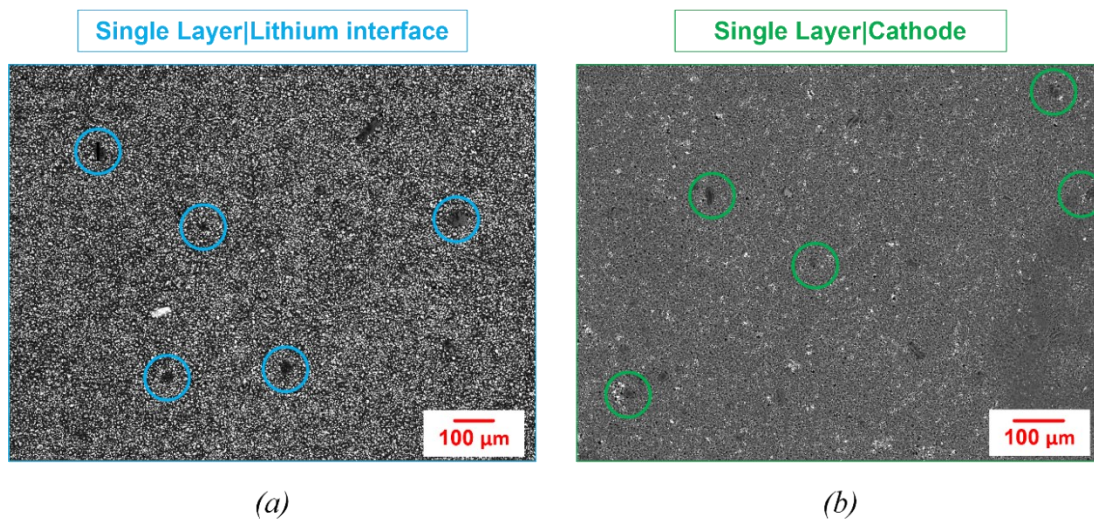
*Figure 7.7. Backscattered Electron (BSE) SEM images of post mortem Single Layer separator on both **(a)** the side in contact with lithium metal and **(b)** the one facing the cathode.*

As concerning the Janus Separator reported in Figure 7.8, the investigation was focused not only on the sides facing the cathode and anode, but also on the internal interfaces between the two different layers, with and without N-CQDs, (see Figure 7.8*a*).
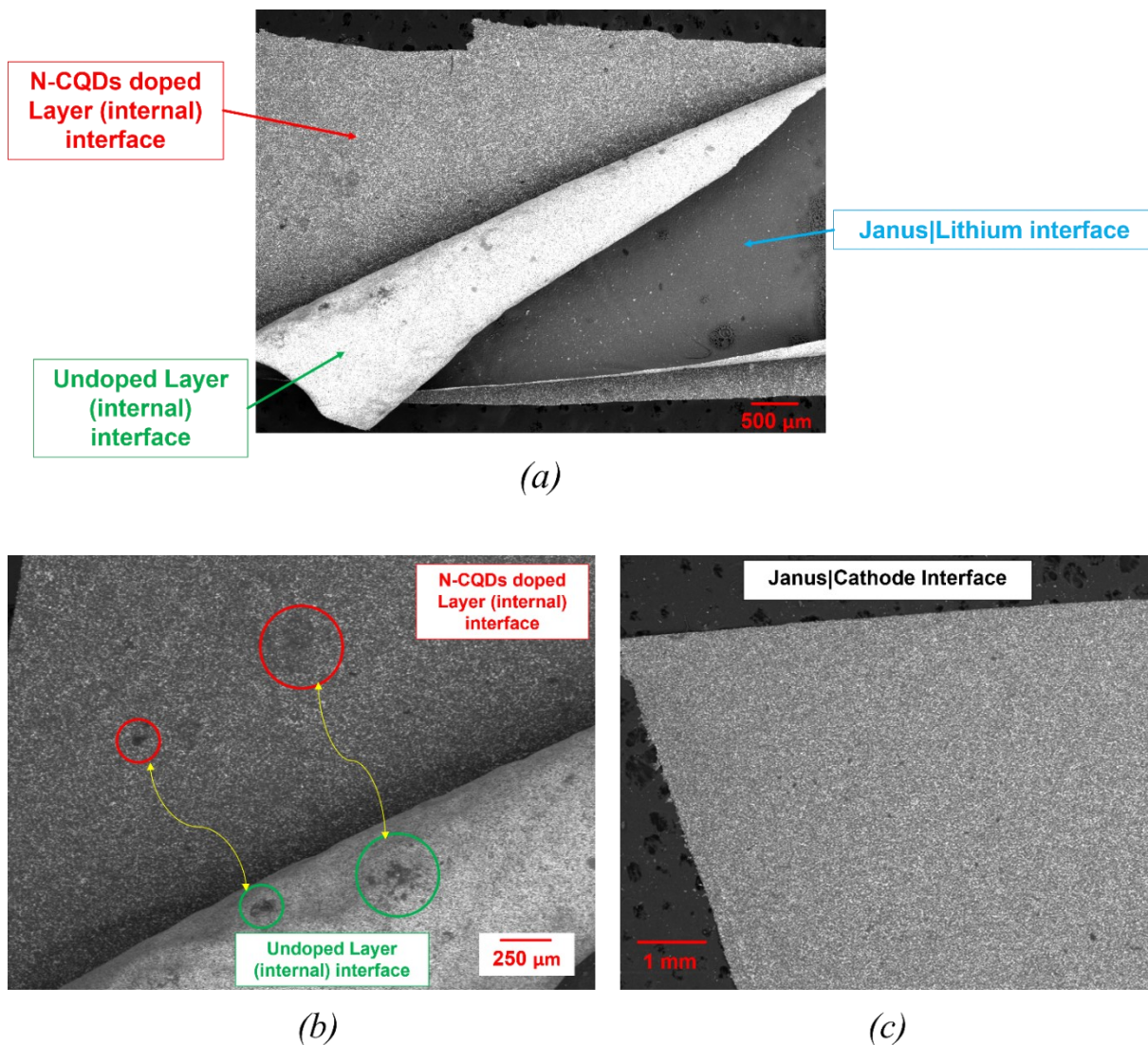
Figure 7.8. *Backscattered Electron (BSE) SEM images of post mortem Janus separator facing **(a, b)** the lithium metal, both internal interface at different magnification and **(c)** the side in contact with the cathode.*

Figure 7.8*b* shows evident damages on both sides likely due to the stress caused by the lithium deposits. However, it is worthy of note that such deposits penetrate the Single Layer of the JS but not pierce trough the electron conductive layer. This aspect seems to be also confirmed by the top view image of the JS facing the cathodic compartment, (Figure 7.8*c*), where no detectable damages are noticeable.

7.5. Conclusion

We investigated a new Janus Separator for application in lithium metal batteries. The as realized JS consisted of two layers: an ion conductive one composed by modified Al-LLZO in a PVdF-HFP matrix facing the lithium metal, and a mixed ion-electron conducting one facing the cathode. The performance of the Janus Separators were compared with those obtained in case of film of pure PVdF-HFP, Single Layer separator and finally with a Janus separator including Multiwalled-Carbon Nanotubes in place of the nitrogen QCD. In principle, the stability tests show that all the separators demonstrate optimal cycling reversibility. However, the Janus N-CQDs separator achieved better electrochemical capacity with a significantly reduced capacity loss ($\sim$11 %) up to 130 cycles and without notable short circuit event, in contrast to what was demonstrated for the Single Layer separator. SEM *post mortem* analysis performed on JS showed that the N-QCD layer intercepted the dendrites growth, allowing to suppress the short circuits occurring in the Single Layer separator.

For further investigation, Dynamic Mechanical Analysis (DMA) to clarify the mechanical properties of the as realized separators are already in progress. Also, separators with different thicknesses and/or with higher wt% loading of Nitrogen-Carbon Quantum Dots will be tested in order to correlate these parameters to the electrochemical performance and also to improve the ability of dendrites suppression. This approach allows to tailor the features of the separators in order to improve safety and performance of the cell.

7.6. Bibliography

1. Bruce, P.G.; Freunberger, S.A.; Hardwick, L.J.; Tarascon, J.-M. Li-O and Li-S batteries with high energy storage. *Nat. Mater.* 2012, **11**, 19-29.

2. Lin, D.; Liu, Y.; Cui, Y. Reviving the lithium metal anode for high-energy batteries. *Nat. Nanotechnol.* 2017, **12**, 194-206.

3. Quartarone, E.; Mustarelli, P. Electrolytes for solid-state lithium rechargeable batteries: Recent advances and perspectives. *Chem. Soc. Rev.* 2011, **40**, 2525-2540.

4. Liu, B.; Zhang, J.-G.; Xu, W. Advancing Lithium Metal Batteries. *Joule* 2018, **2**, 833-845.

5. Tikekar, M.D.; Choudhury, S.; Tu, Z., Archer, L.A. Design principles for electrolytes and interfaces for stable lithium-metal batteries. *Nat. Energy* 2016, **1**, 16114.

6. Quartarone, E.; Mustarelli, P. Emerging Trends in the Design of Electrolytes for Lithium and Post-Lithium Batteries. *J. Electrochem. Soc.* 2020, **167**, 050508.

7. Oh, Y.-S.; Jung, G.Y.; Kim, J.-H.; Kim, J.-H.; Kim, S.H.; Kwak, S.K.; Lee, S.-Y. Janus-Faced, Dual-Conductive/Chemically Active Battery Separator Membranes. *Adv. Funct. Mater.* 2016, **26**, 7074-7083.

8. Zhang, C.; Lan, X.; Liu, Q.; Yu, L.; Li, Y.; Hu, X. Bi-functional Janus all-nanomat separators for acid scavenging and manganese ions trapping in $LiMn_2O_4$ lithium-ion batteries. *Mater. Today Phys.* 2022, **24**, 100676.

9. Li, Z.; Han, Y.; Wei, J.; Wang, W.; Cao, T.; Xu, S.; Xu, Z. Suppressing Shuttle Effect Using Janus Cation Exchange Membrane for High-Performance Lithium-Sulfur Battery Separator. *ACS Appl. Mater. Interfaces* 2017, **9**, 44776-44781.

10. Kong, L.; Fu, X.; Fan, X.; Wang, Y.; Qi, S.; Wu, D.; Tian, G.; Zhong, W.-H.A. Janus nanofiber-based separator for trapping polysulfides and facilitating ion-transport in lithium-sulfur batteries. *Nanoscale* 2019, **11**, 18090-18098.

11. Zhou, Z.; Chen, B.; Fang, T.; Li, Y.; Zhou, Z.; Wang, Q.; Zhang, J.; Zhao, Y. A Multifunctional Separator Enables Safe and Durable Lithium/Magnesium–Sulfur Batteries under Elevated Temperature. *Adv. Energy Mater.* 2020, **10**, 1902023.

12. Wu, X.; Liu, N.; Guo, Z.; Wang, M.; Qiu, Y.; Tian, D.; Guan, B.; Fan, L.; Zhang, N. Constructing multi-functional Janus separator toward highly stable lithium batteries. *Energy Storage Mater.* 2020, **28**, 153-159.

13. Chen, M.; Chen, Z.; Fu, X.; Zhong, W.-H. A Janus protein-based nanofabric for trapping polysulfides and stabilizing lithium metal in lithium-sulfur batteries. *J. Mater. Chem. A* 2020, **8**, 7377-7389.

14. Tricoli, A.; Liu, B.; Taheri, M.; Torres, J.F.; Fusco, Z.; Lu, T.; Liu, Y.; Tsuzuki, T.; Yu, G. Janus conductive/insulating microporous ion-sieving membranes for stable Li-S batteries. *ACS Nano* 2020, **14**, 13852-13864.

15. Gao, G.-K.; Wang, Y.-R.; Wang, S.-B.; Yang, R.-X.; Chen, Y.; Zhang, Y.; Jiang, C.; Wei, M.-J.; Ma, H.; Lan, Y.-Q. Stepped Channels Integrated Lithium–Sulfur Separator via Photoinduced Multidimensional Fabrication of Metal–Organic Frameworks. *Angew. Chem. Int. Ed.* 2021, **60**, 10147-10154.

16. Zheng, S.; Zhu, X.; Ouyang, Y.; Chen, K.; Chen, A.-L.; Fan, X.; Miao, Y.-E.; Liu, T.; Xie, Y. Metal-Organic Framework Decorated Polymer Nanofiber Composite Separator for Physiochemically Shielding Polysulfides in Stable Lithium-Sulfur Batteries. *Energy Fuels* 2021, **35**, 19154-19163.

17. Pei, H.; Yang, C.; Wu, Q.; Zhou, X.; Xie, X.; Hwang, B.; Ye, Y. Ion-selective aramid nanofiber-based Janus separators fabricated by a dry-wet phase inversion approach for lithium-sulfur batteries. *J. Mater. Chem. A* 2022, **10**, 5317-5327.

18. Li, Y.; Gao, T.; Ni, D.; Zhou, Y.; Yousaf, M.; Guo, Z.; Zhou, J.; Zhou, P.; Wang, Q.; Guo, S. Two Birds with One Stone: Interfacial Engineering of Multifunctional Janus Separator for Lithium–Sulfur Batteries. *Adv. Mater.* 2022, **34**, 2107638.

19. Xiao, R.; Yang, S.; Yu, T.; Hu, T.; Zhang, X.; Xu, R.; Wang, Y.; Guo, X.; Sun, Z.; Li, F. A Janus Separator for Inhibiting Shuttle Effect and Lithium Dendrite in Lithium−Sulfur Batteries. *Batter. Supercaps* 2022, **5**, e202100389.

20. Zhou, D.; Tang, X.; Guo, X.; Li, P.; Shanmukaraj, D.; Liu, H.; Gao, X.; Wang, Y.; Rojo, T.; Armand, M.; Wang, G. Polyolefin-Based Janus Separator for Rechargeable Sodium Batteries. *Angew. Chem. Int. Ed.* 2020, **59**, 16725-16734.

21. Xu, L.; Daphne Ma, X.Y.; Wang, W.; Liu, J.; Wang, Z.; Lu, X. Polymeric one-side conductive Janus separator with preferably oriented pores for enhancing lithium metal battery safety. *J. Mater. Chem. A* 2021, **9**, 3409-3417.

22. Xie, H.; Hao, Z.; Xie, S.; Ye, Y.; Zhang, W.; Sun, Z.; Jin, S.; Ji, H.; Chen, J. Molecular sieve-based Janus separators for Li-ions redistribution to enable stable lithium deposition. *Nano Res.* 2022, in press. DOI: 10.1007/s12274-022-4181-1.

23. Gonzalez, M.S.; Yan, Q.; Holoubek, J.; Wu, Z.; Zhou, H.; Patterson, N.; Petrova, V.; Liu, H.; Liu, P. Draining Over Blocking: Nano-Composite Janus Separators for Mitigating Internal Shorting of Lithium Batteries. *Adv. Mater.* 2020, **32**, 1906836.

Chapter 8:
3D Cu Current Collector for Advanced Anode-less Li Batteries

8.1. Abstract

One of the areas of greatest interest in reducing greenhouse gas (GHG) emissions and the use of fossil fuels is the transport sector. A possible solution is the use of electric vehicles that can contribute significantly to mitigate the climate change issues. Nowadays, the main means energy generation and storage is lithium-ion batterie, but inherent limitations delay their application in electric vehicles (EV). Possible alternatives to face energy demand include the use of lithium-metal batteries which, despite several advantages, show various challenges such as the low coulombic efficiency, huge volumetric expansion, and dendrite formation leading also to safety issues. To overcome these drawbacks, the development of materials to optimise lithium deposition behaviour during charge and discharge processes are investigated as possible solutions. Here we reported a simple and effective process to realized 3D Cu current collectors having different patterned structure with increased surface area. The investigated 3D collectors demonstrated stable and low voltage hysteresis at different current densities and a cycle life stability of over 300 h. The evaluation in a full cell showed good capacity retention at moderate current and high and stable coulombic efficiency, thus showing a promising future application in next-generation devices.

8.2. Introduction

The climatic conditions associated with greenhouse gas (GHG) emissions have reached increasingly dangerous levels in recent decades, which can be seen in the evident global warming. To address and remedy the emission of these gases, generated as unwanted by-products of the combustion of fossil fuels for energy, the International Energy Agency (IEA) has presented a roadmap called the 'Net-Zero Emissions by 2050 (NZE) Scenario', aimed at achieving this goal globally, which would be compatible with a 50% probability of limiting the average global temperature increase to 1.5°C through an accelerated transformation of

the energy sector in different fields.[1] The study takes a detailed look at the physical energy infrastructure in place today, including different types of fuel supply, power generation and end uses such as industry and transport. As of 2020, more than 60% of greenhouse gas emissions regarding transport mode in the world are attributable to road transport. Therefore, an important approach to limiting emissions is the development of technology that can replace fossil fuels in vehicles; the most promising way forward is electric vehicles (EVs). One of the crucial factors in improving the performance of electric vehicles and ensuring their competitiveness is the development of EV technologies. In the battery field, technology has evolved from lead-acid batteries to nickel, through ZEBRA and finally to lithium ion batteries. The devices manufactured must meet specific characteristics, such as high energy and power density, light weight, cost-effectiveness, safety, and durability.[2] At the state of the art, lithium-ion battery technology has one obvious limitation for possible use in electric vehicles, which is its limited energy density. Nowadays, considering the most commonly used anode, graphite, the theoretical specific capacity is only 372 mAh g^{-1}. Over the years, numerous attempts and anodic materials, such as phosphor-silicon compounds and transition metal oxides,[3,4] have been investigated in order to increase the effective energy density of LIBs, but although they succeeded in achieving this goal, all solutions presented some constant problems such as high volumetric expansion during charge and discharge cycles and high electrochemical potentials. An alternative possibility is also the use of lithium metal anodes. It possesses numerous advantages such as a high mass specific capacity (3860 mAh g^{-1}), a very low electrochemical potential of -3.04 V *vs* standard hydrogen electrode, and a low density (0.534 g cm^{-3}). But even then, lithium metal is not exempt of problems, the main ones being low coulombic efficiency, huge volumetric expansion, and dendrite formation. This last aspect, during cycling, can cause numerous fractures both within the solid electrolyte interface (SEI) and also the penetration of the separator, resulting in significant short-circuit events, which are of considerable danger from the point of view of the safety of the storage device.[5,6] Recently, there has been a focus on realizing anode current collectors with a larger surface area and/or a high degree of porous structures, in accordance with Sand's law, which states that the time for dendrite nucleation is inversely proportional to the square current density of the anode surface. Therefore, increasing the surface area can delaying the formation of lithium dendrites.[7] Starting from the fact that the most common and widely used current collector for lithium ion batteries is copper foil, due to its excellent conductive and mechanical properties, numerous studies have been directed towards the realisation of collectors based on this transition metal with an increased surface area. To

achieve this result, some studies have focused to the development of porous Cu collectors from chemical dealloying processes or by copper micro-channels structures.[8-10] However, the beforementioned and other methods present in the literature involve multiple steps with high costs, not suitable for a possible industrial scale-up and in addition to the use of potentially harmful reagents.[11] Additive manufacturing 3D printing has recently gained considerable attention as an efficient method for the fabrication of complex, self-standing metal structures to address the beforementioned issues. Specifically, 3D patterned Cu current collectors were manufactured by using a low-cost 3D printing device and a copper water-based colloid, followed by a post processing thermal treatment. The as obtained 3D patterned Cu current collectors provide an enhanced surface area thus leading to low local current densities and an increase of sites for lithium nucleation. The electrochemical results show, in symmetric cells, a cycle life of over 300 h with a hysteresis overpotential between ~10 mV and ~16 mV at a current density of 2 mA cm^{-2} and a good capacity retention and coulombic efficiency in full cells. The 3D-printing extrusion method has proven its efficiency, reproducibility, and suitability for large-scale production of improved anodes for lithium-metal batteries, which has also been confirmed by promising results in terms of electrochemical performance.

8.3. Material and Methods

8.3.1. Inks Preparation

The inks included water as the only solvent, powder of the desired material – with content around 88 wt% of copper – and a polymeric additive to control the stability and the rheological properties. Copper was purchased from New Linbraze (cat. n. CU105-2). Figure 8.1 shows SEM images of the powder used in this work. Copper - as per the supplier's specifications - shows a maximum particle size of about 50 μm with a more regular spherical shape and the presence of some satellites on the particle surface.
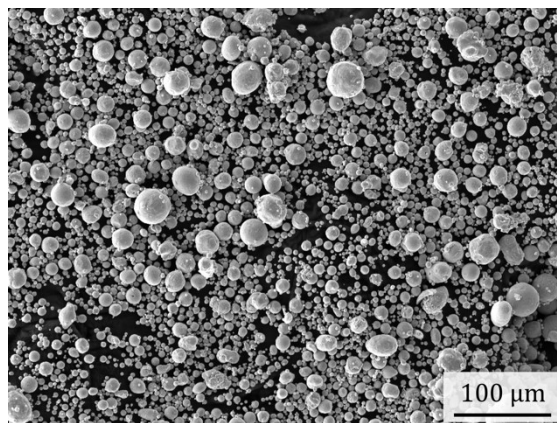
Figure 8.1. SEM images of the metallic copper powders used in this study.

The polymeric additive used in our formulation is polyethylene oxide *co*-polypropylene oxide-*co*-polyethylene oxide (Pluronic® F-127, Sigma Aldrich cat. n. P2443, MW 12600) prepared as a water solution at 25 wt%. All inks were homogenised using a syringe-to-syringe mixing procedure developed in a previous study.[12] In short, it consists of mixing all components of the mixture directly in the syringe of the extruder (30 ml Nordson EFD), at a temperature below 10°C, without any preliminary operations. This approach eliminates any loss of both powder and solvent, allowing optimal print reproducibility and avoiding any cleaning operation.

8.3.2. Printing Apparatus

The current collector meshes have been realized using an in-house modified 3D printer from *e3d* (ToolChanger & Motion System Bundle). SMC provided all the pneumatic components required to control the extrusion of the inks. They include three-port pilot-operated poppets (VP342R-5YO1-02FA), precise pressure regulators (IR2020-F02-A), high-precision digital pressure switches (ISE20-P-01-L), and high noise reduction silencers (ANB1-02/03). Upstream, we placed a pressure relief three-port valve (VHS40-F04A) and a filter regulator with backflow function (AW40-F04*-B) to stabilize the airflow inlet. The colloids were extruded at a pressure of around 1.5 bar through conical needles, presenting an aperture of 0.4 mm (*Nordson* Optimum® SmoothFlow™ 7018298). The open-source software *Ultimaker Cura Slicer* was chosen to set all the printing parameters such as speed, extrusion width and infill type. The last parameter was used to create the different electrode patterns.

The objects, printed on a thin graphite sheet, were allowed to air dry to remove most of the water present and then placed in a high-temperature furnace for the sintering procedure (see Figure 8.2).
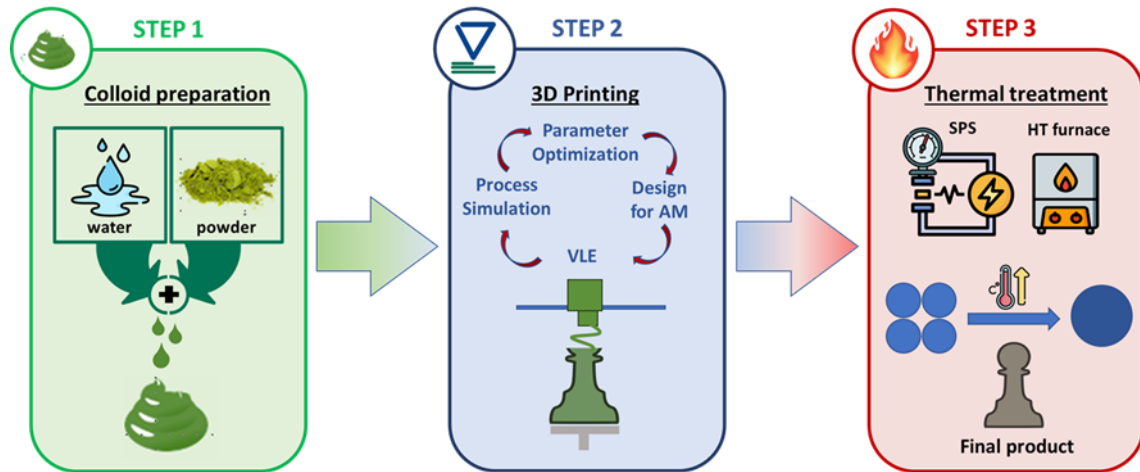

Figure 8.2. Schematic representation of the Cu current collector realization.

8.3.3. Thermal Treatments

Copper samples undergo the same thermal treatments performed in a high-temperature tube furnace (Carbolite Gero TF1-1600). Thermal treatment includes three steps: debinding, chemical reduction, and sintering. The debinding was typically performed using a 1°C min^{-1} ramp from room temperature to *300°C* under air atmosphere. It was then followed by a chemical reduction step, which involved a 6 h ramp to 600°C followed by a 6 h dwell at the same temperature in Ar/10% H_2 atmosphere. Finally, sintering was performed at 1000°C for 6 h, also in Ar/10% H_2 atmosphere.

8.3.4. Morphological Characterization

Surface topography and sample roughness were measured by atomic force microscopy (AFM) with AP06 KLA Tencor stylus profilometer, equipped with a stan-dard silicon tip (radius 2 μm). A force of 0.50 mg was imposed on the silicon tip. Root mean quare roughness values and 3D images were obtained by an Apex ver. 5.0.3.4960 software. Analytical time

for each specimen was about 65 h. For each analysed sample, scans of 6.5 μm × 6.5 μm and 4.0 μm × 4.0 μm, for 3D and plane current collectors, respectively. The measurement has been carried out with a scan sampling rate ranging of 20 Hz.

One crucial challenge was to correctly determine the increment of surface area compared to a flat disk with the same diameter. High surface area plays a key role in the efficiency of the electrochemical system, it determines [13-16]

1. The maximum lithium quantity and therefore the capacity, both specific and areal.
2. High current charge/discharge cycles and so, high-power density system.
3. The stability and uniformity of the lithium layer deposited on the electrode and the dendritic growth suppression during charge/discharge cycles.
4. Lower overpotential in lithium plating and stripping improving the reversibility of the process.

8.3.5. Cathode Preparation

The cathode slurry was prepared by using 75 wt% of active material $LiFePO_4$ (LFP, Hydro-Québec), 15 wt% Conductive Carbon (Timcal-Imerys, ENSACO 350P) and 10 wt% binder (polyvinylidene fluoride, PVdF). The solid content of the slurry was maintained in the range of 26 - 28 wt%. LFP and Carbon were initially mixed in Zirconia jars by planetary ball mill at 150 rpm for 10 min, followed by 5 min break and another 10 min of milling in reverse direction. Subsequently, it was dispersed in a solution of PVdF in N-methylpyrrolidone (NMP, Sigma-Aldrich) to obtain the slurry, which was cast on a carbon-coated aluminium foil using a doctor blade with 300 μm wet thickness. The cathode was finally dried under vacuum at 80°C and finally cut into 2 cm^2 disks and stored in a glove box (MBraum, O_2, $H_2O < 0.5$ ppm) before the electrochemical measurements.

8.3.6. Electrochemical Characterization

The Li electrodeposition was studied by means of galvanostatic stripping/plating experiments performed at room temperature on Li|Electrolyte|3D-Cu@Li symmetric 2032-type coin cells by a battery tester (Arbin, model BT-2000). The electrolyte was 1 M Lithium bis(fluorosulfonyl)imide (LiFSI) in EC:DMC (50:50 vol.%)) and a Celgard 2500 polypropylene membrane served as separator.

The rate performance of Cu current collectors was, while 10 mAh cm^{-2} Li was plated onto them before cycling, tested through periodically cycling (1 hour each half-cycle) at fixed current densities ranging between 0.5 and 8 mA cm^{-2} before performing a 5 recovery cycles at the initial current density of 0.5mA cm^{-2}. The coulombic efficiency was calculated based on the ratio of the charge capacity over discharge capacity.

For long-term stability, symmetric cells were tested with the Cu current collectors as the working electrodes and Li metal foil as the counter electrode. Before cycling 12 mAh cm^{-2} of Li was plated on the current collectors at 0.55 mA cm^{-2}. Then the cells were cycled at 2 mA cm^{-2} current density for 1 hour at half-cycle.

In full cells testing, half-cell was first assembled and discharged to plate 40 mAh cm^{-2} of Li on the current collectors. Then the pre-plated Cu current collector (both 3D and Plane) were used as anode, while LiFePO$_4$ served as the cathode. Electrodes were separated with a *Whatman* glass fiber separator, imbibed of liquid electrolyte, consisting in a solution 1 M LiPF$_6$ in Ethylene Carbonate: Dimethyl Carbonate (LP30, EC:DMC, 50:50 vol.%) (Sigma-Aldrich).The LFP|3D-Cu@Li full cells were cycled on a Biologic BCS 810 battery tester from 3V to 4.3V. All the potentials reported refer to the Li$^+$/Li couple. The impedance on the cells was measured by means of EIS at room temperature by applying an AC voltage of 50 mV in the frequency range of 0.1 Hz to 1 MHz. For comparison cells with Li metal as counter electrode were assembled the with the same features and tested for evaluate the goodness in electrochemical performance of our 3D Cu current collector. All the functional tests were performed using a coin cell type (CR2032 - MTI Corp.) assembled in an Ar-filled glove box (H$_2$O and O$_2$ < 0.5 ppm).

8.3.7. ICP Analysis

ICP-OES was performed by a Thermo Scientific CAP 7400 Duo, equipped with a quartz torch, a charge injection detector and a Cetac ASX-560 autosampler. The Li quantification was carried out in the axial mode, with a LOD of 100 ppb and 670.78 nm as wavelength, by an external standard calibration curve. ICP grade standards 1000 mg L^{-1} (Merck) were diluted to 1-5-10 mg L^{-1} and then acidified to a final concentration of 1% nitric acid (from ultrapure 65% HNO$_3$, Merck). The measurements conditions were as in the following: nebulization gas flow: 0.5 L min^{-1}; power RF: 1150 W; cooling gas flow: 12 L min^{-1}; auxiliary gas flow: 0.5 L min^{-1}; peristaltic pump speed: 50 rpm; frequency: 500 Hz; intake

flow: 1.5 L min^{-1}. The Li quantification was carried out on 3D Square Pattern (P4) and Plane current collector at two different plating time (9h and 18h), with a current density of 0.55 mA cm^{-2}, for both samples. Each investigated current collector was soaked in 5 mL of nitric acid (ultrapure 65% HNO$_3$, Merck) into a 50 mL polyethylene Falcon flask. 5 mL of MilliQ water were added to each flask, obtaining a final volume of 10 mL.

8.4. Results

8.4.1. Morphological Characterization

The as realized Cu current collectors (Figure 8.3) were firstly characterized by the morphological point of view in order to evaluate homogeneity, reproducibility and difference in the selected pattern.
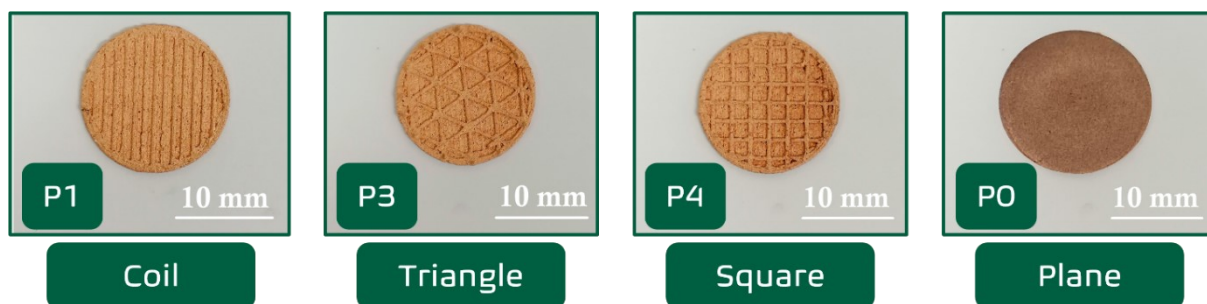

Figure 8.3. *Investigated 3D pattern and flat current collectors.*

As its notable from Figure 8.4 showing 3D image of the Cu current collectors some inhomogeneity within the same pattern can be detected due to the preparation method and treatment.
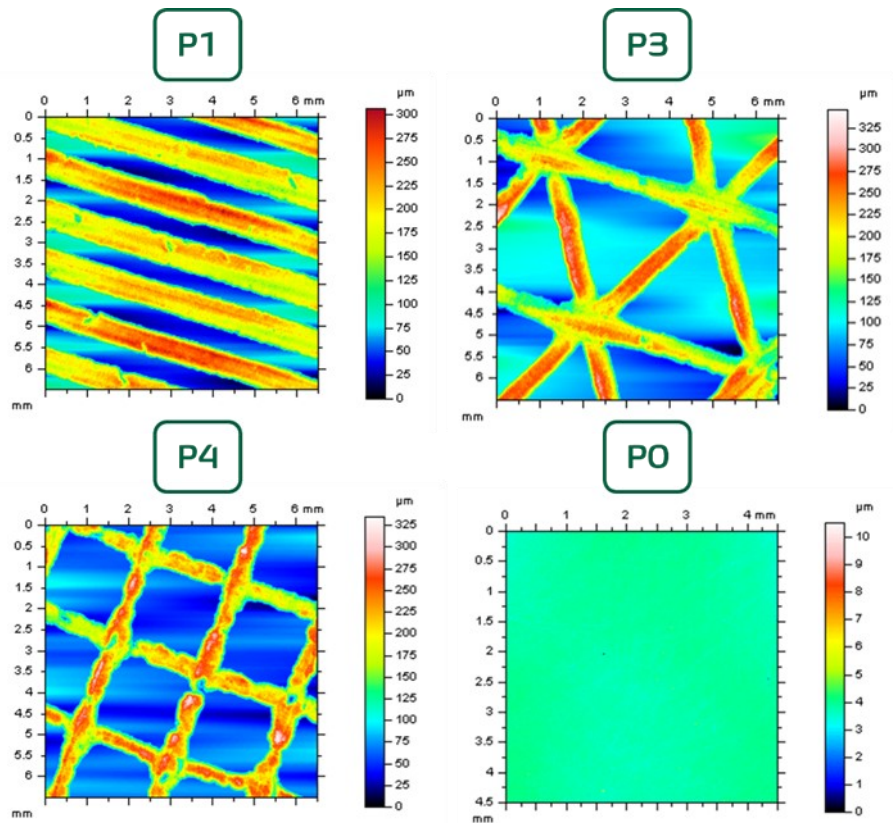
Figure 8.4. Profilometric images of the realized 3D (P1, P2, P3) and Plane (P0) current collectors.

However, between the different collector we obtain comparable average heights. From this analysis, it was also possible to derive roughness profiles, reported in Figure 8.5. The results show that P4 has a significantly higher roughness.
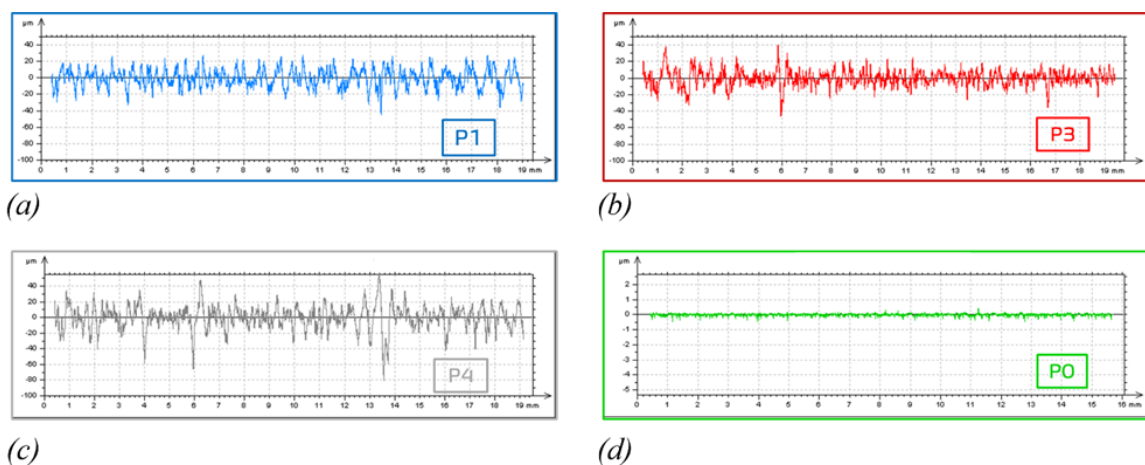

Figure 8.5. Roughness profile for (a) Coil, (b) Triangle, (c) Square and (d) Plane realized Cu current collectors.

Since the profilometer at our disposal gave us only a roughness value and not the actual scanned area, we have resorted to a mathematical model. As can be seen from Figure 8.6 heights can also be represented graphically.
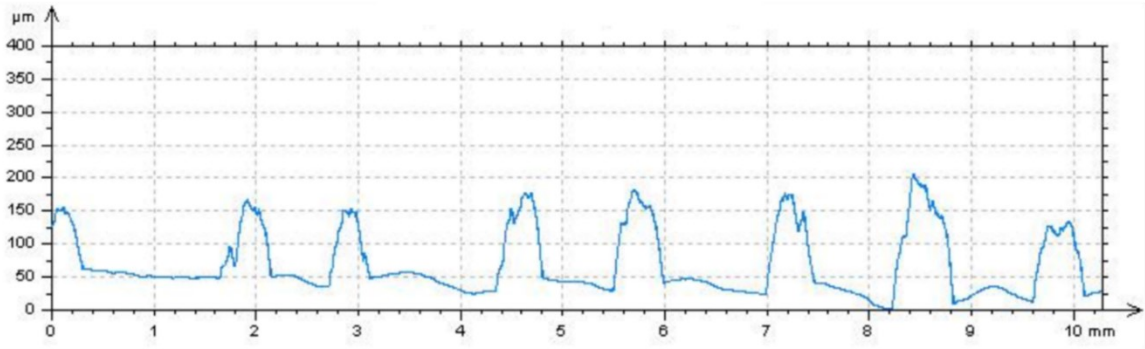

Figure 8.6. Graph showing measured heights obtained by the profilometer 3D scanning.

By using the provided data and correctly estimating lines length with ImageJ software (National Institute of Health), printing line are generally assumed as (400 ± 40 µm) x (100 ± 15 µm) parallelepipeds. This area is then added to the exposed area of the bottom layer, displayed in blue in Figure 8.3 which is also estimated with ImageJ.

To this surface area, calculated on a macrometric level, a micrometric value due to roughness is added. It is estimated by longitudinal scanning a printed line, then converting the results to a 16bit image (Figure 8.7) used to model the corresponding flat surface of the same extent.
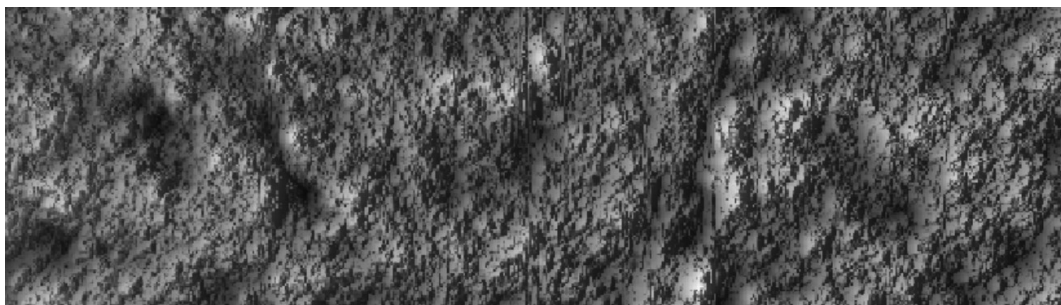

Figure 8.7. 16bit image used to model the increase in surface area caused by the evident amount of roughness derived from the scan of the surface of a printing line.

By combining the two contributions, a multiplier coefficient is found. Compared to a flat disk of the same diameter we have obtained an increment of ~80%. Of this percentage, around a quarter is due to pattern influence and the rest to roughness.

8.4.2. Lithium Stripping/Plating Performance

To investigate the Li stripping/plating cycling stability, symmetric cells with 3D Cu and Plane Cu current collector as working electrode and Li metal foil as the counter electrode were assembled. Previous cycling, 10 mAh cm^{-2} Li was plated onto both type of collector. The rate performance of symmetric cells was tested by cycling over a current density range from 0.5 mA cm^{-2} to 8 mA cm^{-2} for 1 h for each half cycle (Figure 8.8).
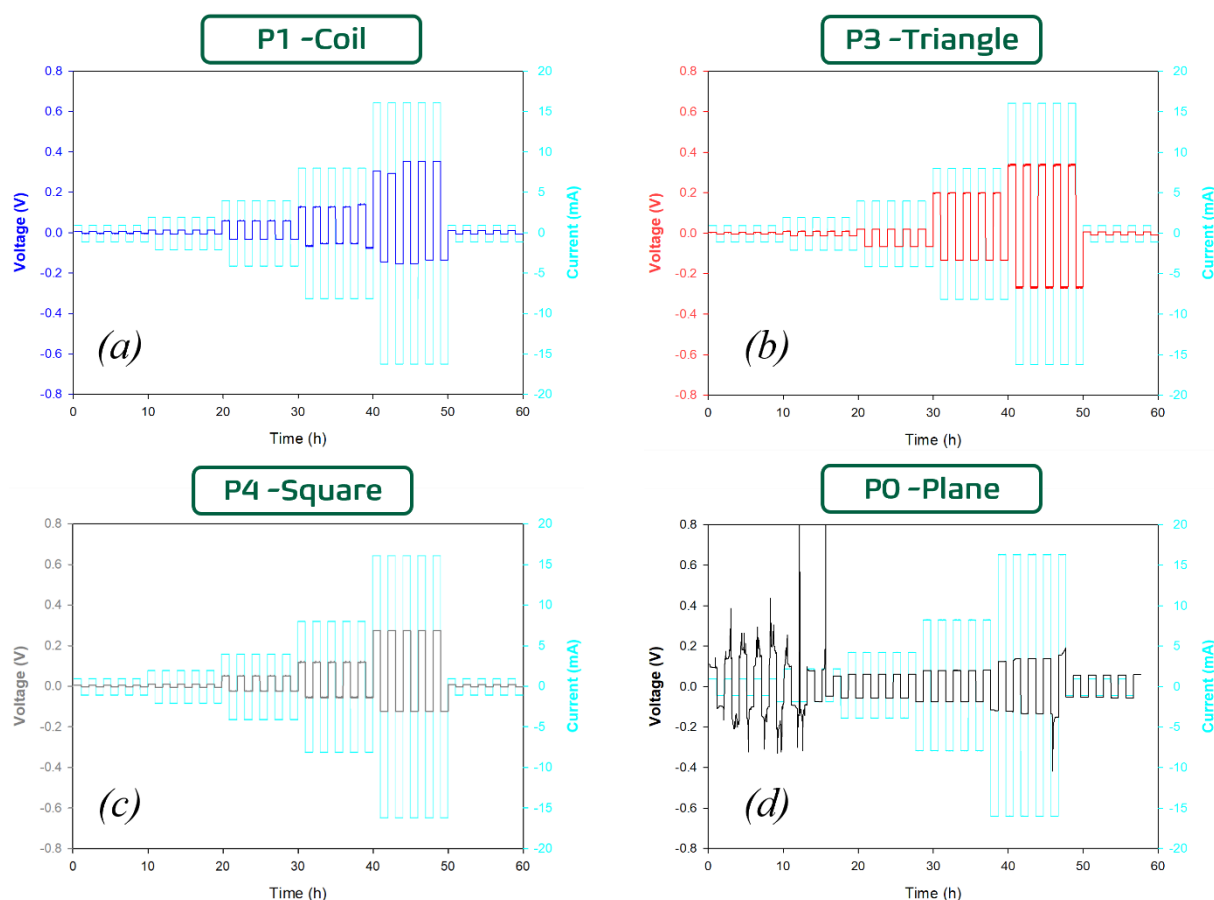

Figure 8.8. *Rate performance of 3D (P1, P3 and P4) and plane (P0) current collectors with Li stripping/plating for 2 hours in each cycle.*

The voltage hysteresis of 3D Cu increases with the increasing of the applicated current but remains relatively low and stable during cycling at the same current density (Figure. 8.8*a-c*); on the other hand, the Plane Cu current collector shows a higher and unstable voltage profile at the beginning of the cycling going through a constant voltage response until high current densities value where the voltage returns to a more unconventional behaviour as

214

reported in Figure 8.8*d*. Among 3D current collectors the better voltage response was demonstrated by the P4 with a more ohmic behaviour according to the increasing in current density and also a stable voltage hysteresis in the cycles within the same imposed current. The better result achieved by the P4 current collector is further displayed by the Coulombic Efficiency (CE) values of the rate performance test (Figure 8.9). The resulting CE of P1 and P3 demonstrated a significant unstable behaviour in all the investigated current values. Those instability is even more pronounced in the P0 collectors.
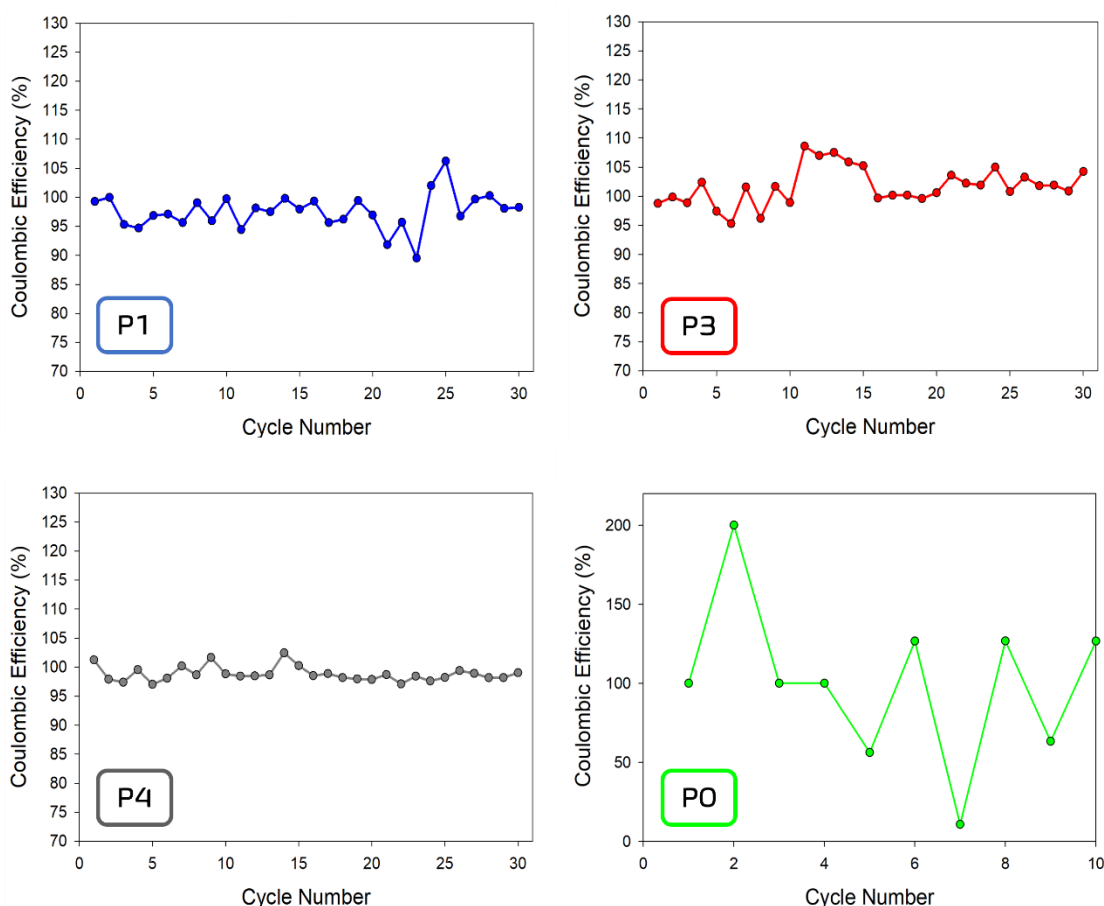

Figure 8.9. *Coulombic efficiency evaluation of the P1 (blue), P3 (red), P4 (grey), and P0 (green) collectors at different current densities from 0.5 mA cm^{-2} to 8 mA cm^{-2} and 5 recovery cycles at the initial current density of 0.5mA cm^{-2}.*

In comparison, P4 achieves an average CE of ~100% with values that show only slightly fluctuation even at higher current densities. Further electrochemical investigation was performed in order to evaluate the stability over a higher number of working hours by stripping and plating lithium until failure. Even in this case the collectors were previously

plated with 12 mAh cm^{-2} of Li. Voltage – time profiles of 3D Cu (Figure 8.10) display a stable trend over 300h with difference in the voltage hysteresis behaviours upon lithium stripping/plating. P1 shows the greatest instability, during the first 50 hours a decidedly non-symmetrical hysteresis profile has showed before stabilising until around 200 hours and then undergoing a slight increase in potential but maintaining a good hysteresis. P2 despite some fluctuations in the early cycle maintained a better voltage hysteresis of ~16 mV until 230 hours. However, it is evident that P4 shows the least instability during the first cycles, necessary for the formation of SEI, and maintains a hysteresis with values of ~10 mV for the greatest number of hours.
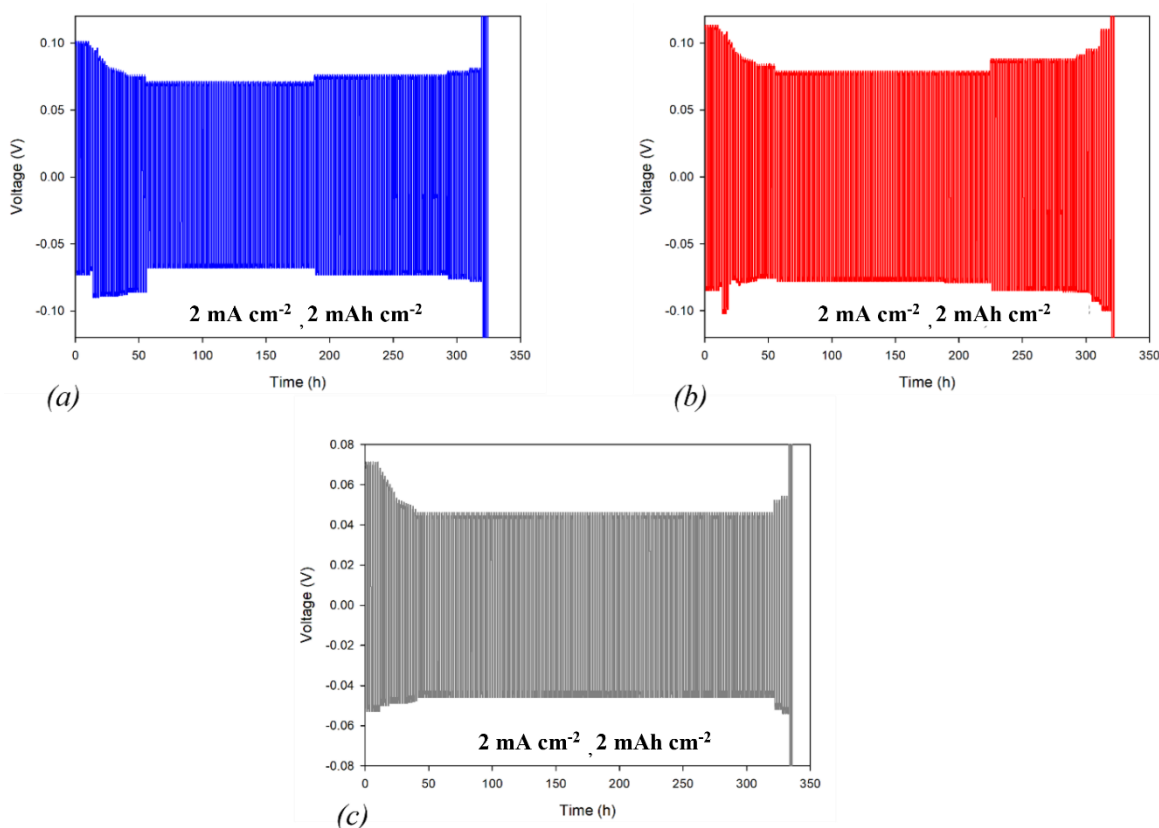
Figure 8.10. *Electrochemical performance of the symmetric cells with 3D-Cu@Li for the* **(a)** *P1,* **(b)** *P3 and* **(c)** *P4 current collectors.*

The symmetric cell with 3D-P4@Li exhibits the lowest overpotential over a long cycle life at moderate current density of 2 mA cm^{-2}. This evidence it even more notable by the comparison between the three investigated copper current collectors, reported in Figure 8.11.
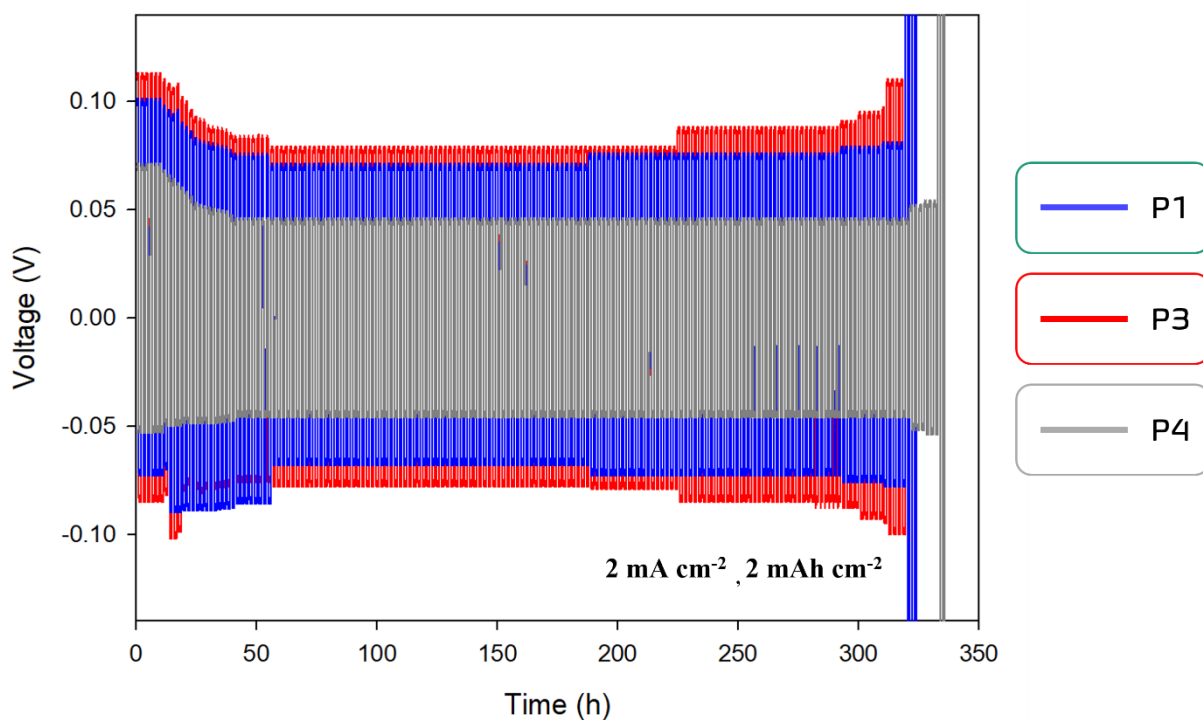
Figure 8.11. Comparison of long-term cycling performance of the 3D-Cu current collectors.

8.4.3. Electrochemical Performance

To further explore the practical possible application of the 3D Cu current collectors, full cell was assembled with P4, which has showed to be the collector with the best characteristic and performance. For comparison a cell with Li metal was also realized.
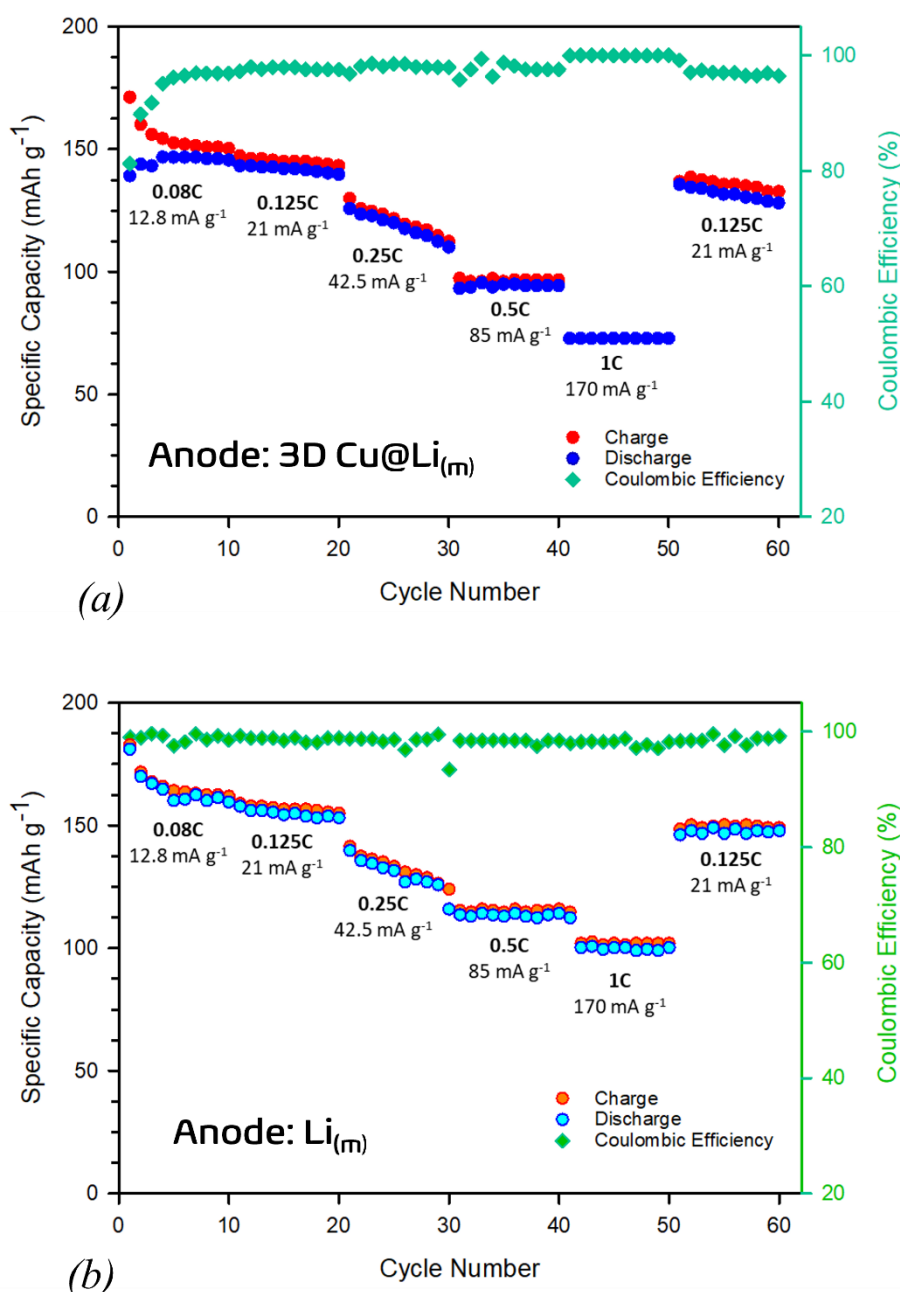
Figure 8.12. Rate capability of the (a) LFP|3D-P4@Li and (b) LFP|Li foil full cells.

In the rate capability reported in Figure 8.12, 3D-P4@Li exhibits good capacitance values and coulombic efficiency for low and moderate current densities while maintaining values fully comparable with the cell made from lithium metal. However, at 1C the three-dimensional current collectors delivered a capacity of $\sim$65 mAh g^{-1} (see Figure 8.12a). This evident decrease in performance at high current densities is probably due to kinetic factors and/or the lower amount of lithium.

8.4.4. ICP Analysis

Following the electrochemical results obtained in the rate performance test, it was decided to proceed with quantifying the actual amount of lithium deposited on a three-dimensional collector. The collector used for this analysis was P4, as it was the same one used operationally in the complete cell. Also, for comparison, a P0 collector was also analysed. Regarding cells that normally used lithium metal as an anode/counter-electrode, the average lithium content is ~38 mg. The results of ICP-OES analyses carried out on both samples at two different plating time (9h and 18h) are reported in Tables 8.1 and 8.2.

	Plating Time (h)	Theoretical Li (mg L^{-1})	Li (mg L^{-1})	Yields
P4 sample 1	9	257.6	132.27	51.3%
P4 sample 2	9	257.6	133.12	51.7%
P4 sample 3	18	515.2	320.45	61.2%
P4 sample 4	18	515.2	321.10	61.3%

Table 8.1. Results from ICP analysis of the P4 Cu current collectors.

	Plating Time (h)	Theoretical Li (mg L^{-1})	Li (mg L^{-1})	Yields
P0 sample 1	9	257.6	7.04	2.7%
P0 sample 2	9	257.6	8.36	3.2%
P0 sample 3	18	515.2	24.36	4.7%
P0 sample 4	18	515.2	23.48	4.6%

Table 8.2. Results from ICP analysis of the P0 Cu current collectors.

The quantitative data evidence that the amount of lithium that is deposited is significantly less than expected, the plating process actually achieves yields of ~50% to 60%. Moreover,

this trend is observed for both plating times analysed with tests performed in duplicate. It should also be noted that for the P0 collector, this yield drops considerably to values of ~2% to 5%.

8.5. Conclusion

In summary, 3D Cu current collectors with different pattern were successfully developed by in-house modified 3D printer. The realised collectors showed themselves to be promising anodes for lithium metal batteries with high and stable coulombic efficiency. Consequently, a cycle life of more than 300 hours and a significant low voltage hysteresis of ~16 mV and ~10 mV for P1-P3 and P4, respectively, in symmetric cells. Finally, the use of 3D copper collector could enhance safety due to the greater surface area and roughness as well as the decrease in local current densities that could delaying the lithium dendrite formation and lead to the formation of a stable SEI layer. Furthermore, in full cells they demonstrated good capacity at moderate current densities and high coulombic efficiency indicating potential to be promising anodes for lithium metal batteries in next generation energy storage applications. As prospects, we will investigate further modulation of the current collector structure by increasing surface area and porosity. Also, different amounts of lithium deposited by plating and different more complex patterns will be investigated in order to enhance even more the performance and stability of this class of materials.

8.6. Bibliography

1. Bistline, J. E. T. Roadmaps to net-zero emissions systems: Emerging insights and modeling challenges. *Joule* 2021, **5**, 2551-2563.

2. Catenacci, M., Verdolini, E., Bosetti,V., Fiorese, G. Going electric: expert survey on the future of battery technologies for electric vehicles. *Energy Policy* 2013, **61,** 403-413.

3. Bruce, P.G.; Freunberger, S.A.; Hardwick, L.J.; Tarascon, J.-M. Li-O and Li-S batteries with high energy storage. *Nat. Mater.* 2012, **11**, 19-29.

4. Weng, W.; Lin, J.; Du, Y.; Ge, X.; Zhou, X.; Bao, J. Template-free synthesis of metal oxide hollow micro-/nanospheres via Ostwald ripening for lithium-ion batteries. *J. Mater. Chem. A*. 2018, **6**, 10168–10175.

5. Cheng, X.-B.; Zhang, R.; Zhao, C.-Z.; Zhang, Q. Toward safe lithium metal anode in rechargeable batteries: a review. *Chem. Rev.* 2017, **117**, 10403–10473.

6. Koo, D.; Ha, S.; Kim, D.-M.; Lee, K. T. Recent approaches to improving lithium metal electrodes. *Curr. Opin. Electrochem.* 2017, **6**, 70–76.

7. Brissot, C.; Rosso, M.; Chazalviel, J.-N.; Baudry, P.; Lascaud, S. *In situ* study of dendritic growth inlithium/PEO-salt/lithium cells. *Electrochim. Acta* 1998, **43**, 1569–1574.

8. Ma, X.; Liu, Z.; Chen, H. Facile and scalable electrodeposition of copper current collectors for high-performance Li-metal batteries. *Nano Energy* 2019, **59**, 500–507.

9. Yun, Q.; He, Y. B..; Lv, W.; Zhao, Y.; Li, B.; Kang, F.; Yang, Q. H. Chemical dealloying derived 3D porous current collector for Li metal anodes. *Adv. Mater.* 2016, **28**, 6932–6939.

10. Wang, S. H.; Yin, Y. X.; Zuo, T. T.; Dong, W.; Li, J. Y.; Shi, J. L.; Zhang, C. H.; Li, N. W.; Li, C. J.; Guo, Y. G. Stable Li metal anodes via regulating lithium plating/stripping in vertically aligned microchannels. *Adv. Mater.* 2017, **29**, 1703729.

11. Shi, Y.; Wang, Z.; Gao, H.; Niu, J.; Ma, W.; Qin, J.; Peng, Z.; Zhang, Z. A self-supported, three-dimensional porous copper film as a current collector for advanced lithium metal batteries. *J. Mater. Chem. A* 2019, **7**, 1092–1098.

12. Airoldi, L.; Brucculeri, R.; Baldini, P.; Pini, F.; Vigani, B.; Rossi, S.; Auricchio, F.; Anselmi-Tamburini, U.; Morganti, S. 3D Printing of Copper Using Water-Based Colloids and Reductive Sintering. *3D Printing and Additive Manufacturing* 2021.

13. Zhang, D.; Dai, A.; Fan, B.; Li, Y.; Shen, K.; Xiao, T.; Hou, G.; Cao, H.; Tao, X.; Tang, Y. Three-Dimensional Ordered Macro/Mesoporous Cu/Zn as a Lithiophilic Current Collector for Dendrite-Free Lithium Metal Anode. *ACS Appl. Mater. Interfaces* 2020, **12 (28)**, 31542–31551.

14. Yang, Y.; Yuan, W.; Zhang, X.; Ke, Y.; Qiu, Z.; Luo, J.; Tang, Y.; Wang, C.; Yuan, Y.; Huang, Y. A Review on Structuralized Current Collectors for High-Performance Lithium-Ion Battery Anodes. *Applied Energy* 2020, **276**, 115464.

15. Eom, J.-Y.; Choi, S. H.; Kang, J.-H.; Eom, G. H.; Moon, J.; Park, M.-S. Rational Design of a 3D Li-Metal Electrode for High-Energy Lithium Batteries. *ACS Appl. Energy Mater. 2021*, **4 (2)**, 1936–1941.

16. Wang, J.; Sun, Q.; Gao, X.; Wang, C.; Li, W.; Holness, F. B.; Zheng, M.; Li, R.; Price, A. D.; Sun, X.; Sham, T.-K.; Sun, X. Toward High Areal Energy and Power Density Electrode for Li-Ion Batteries via Optimized 3D Printing Approach. *ACS Appl. Mater. Interfaces* 2018, **10 (46)**, 39794–39801.

Appendix

In the following chapter, a list of achievements during the three years of Ph.D. including publications, participation in congresses and awards.

Publication

Publication Related to the Ph.D.

- Quartarone, E., Eisenmann, T., Kuenzel, M., Tealdi, C., Marrani, A.G., Brutti, S., **Callegari, D.**, Passerini, S. Towards advanced sodium-ion batteries: green, low-cost and high-capacity anode compartment encompassing phosphorus/carbon nanocomposite as the active material and aluminum as the current collector. *Journal of the Electrochemical Society* (2020)

- Mezzomo, L., Ferrara, C., Gabriele, B., **Callegari, D**., Quartarone, E., Mustarelli, P., Ruffo, R. Exploiting Self-Healing in Lithium Batteries: Strategies for Next-Generation Energy Storage Devices. *Advanced Energy Materials* (2020)

- Ghigna, P., Airoldi, L., Fracchia, M., **Callegari, D.**, Anselmi Tamburini, U., D'Angelo, P., Pianta, N., Ruffo, R., Cibin, G., Oliveira de Souza, D., Quartarone, E. Lithiation Mechanism in High-Entropy Oxides as Anode Materials for Li-Ion Batteries: An *Operando* XAS Study. *ACS Applied Materials and Interfaces* (2020)

- **Callegari, D.**, Colombi, S., Nitti, A., Simari, C., Nicotera, I., Ferrara, C., Mustarelli, P., Quartarone, E. Autonomous Self-Healing Strategy for Stable Sodium-Ion Battery: A Case Study of Black Phosphorus Anodes. *ACS Applied Materials and Interfaces*, (2021)

- **Callegari, D.**, Coduri, M., Fracchia, M., Ghigna, P., Braglia, L., Anselmi Tamburini, U., Quartarone, E. Lithium intercalation mechanisms and critical role of multi-doping in $LiFe_xMn_{2-x-y}Ti_yO_4$ as high-capacity cathode material for Lithium-ion batteries. *Journal of Materials Chemistry C*. (2022)

- Morina, R., Baroni, R., **Callegari, D.**, Quartarone, E., Mustarelli, P. Nanocomposite Janus Gel Polymer Electrolytes for Lithium Metal Batteries. *Batteries.* (2022)

- Fracchia, M., **Callegari, D.**, Coduri, M., Anselmi Tamburini, U., Manzoli, M., Quartarone, E. Ghigna, P. Electrochemical performance of high and medium entropy oxides for lithium batteries. *Front. Energy Res.* (2022)

Other Articles Published during the Ph.D.

- **Callegari, D.**, Bonizzoni, S., Berbenni, V., Quartarone, E., Mustarelli, P. Is It Possible to Obtain Solvent-Free, Li^+-Conducting Solid Electrolytes Based on Pure PVdF? Comment on "Self-Suppression of Lithium Dendrite in All-Solid-State Lithium Metal Batteries with Poly(vinylidene difluoride)-Based Solid Electrolytes. *Advanced Materials* (2020)

- Sommi, P., Vitali, P., Coniglio, S., **Callegari, D.**, Barbieri, S., Casu, A., Falqui, A., Vigano', L., Vigani, B., Ferrari, F., Anselmi Tamburini, U. Microvilli Adhesion: An Alternative Route for Nanoparticle Cell Internalization. *ACS Nano*. (2021)

- *Morina, R., ***Callegari, D.***, Merli, D., Alberti, G., Mustarelli, P., Quartarone, E. Cathode active material recycling from spent lithium batteries: a green (circular) approach based on deep eutectic solvents. *ChemSusChem.* (2021)

- Vitulo, P., Zanoletti, M., Morina, R., **Callegari, D.**, Quartarone, E., Viola, R., Comoretto, D., Dulio, S., Mustarelli, P., Patrini, M. The Electrical Response of Real Dielectrics: Using the Voltage Ramp Method as a Straightforward Diagnostic Tool for Polymeric Composites. *Materials* (2022)

- Montalbano, M., **Callegari, D.**, Anselmi Tamburini, U., Tealdi, C. Design of Perovskite-Type Fluorides Cathodes for Na-Ion Batteries: Correlation between Structure and Transport. *Batteries*. (2022)

Conferences

Nanoinnovation2020: Energy Storage Technologies: Batteries, Supercaps and Electrolyzers
Rome, 15 – 18 October 2020

- o Oral Presentation – Title: Recycling and recovery of Critical Raw Materials from spent Li-ion Batteries

XIII INSTM National Conference – Advanced Materials and Green Processes for a Sustainable Society
Sestriere, 23 – 26 January 2022

- o Oral Presentation – Title: Synthesis and Characterization of $LiFe_xMn_yTi_zO_4$ as Novel Cathodes for High Energy Density Lithium-Ion Batteries

Award

Award Italian Chemical Society (Division of Electrochemistry), the International Society of Electrochemistry and INSTM

- • Best Oral Presentation - "XIII INSTM National Conference - Advanced Materials and Green Processes for a Sustainable Society" (Session 3: MATERIALS AND TECHNOLOGIES FOR ELECTROCHEMICAL ENERGY STORAGE)